Volume 96, Number 4, July–August 1991
Journal of Research of the National Institute of Standards and Technology

Contents

Articles

Conference Reports

News Briefs

Volume 96, Number 4, July-August 1991
Journal of Research of the National Institute of Standards and Technology

[J. Res. Natl. Inst. Stand. Technol. **96**, 391 (1991)]

General Analytic Correction for Probe-Position Errors in Spherical Near-Field Measurements

Volume 96 Number 4 July-August 1991

L. A. Muth

National Institute of Standards and Technology,
Boulder, CO 80303

A general theoretical procedure is presented to remove known probe-position errors in spherical near-field data to obtain highly accurate far fields. We represent the measured data as a Taylor series in terms of the displacement errors and the ideal spectrum of the antenna. This representation is then assumed to be an actual near field on a regularly spaced error-free spherical grid. The ideal spectrum is given by an infinite series of an error operator acting on data containing errors of measurement. This error operator is the Taylor series without the zeroth-order term. The *n*th-order approximation to the ideal near field of the antenna can be explicitly constructed by inspection of the error operator. Computer simulations using periodic error functions show that we are dealing with a convergent series, and the error-correction technique is highly successful. This is demonstrated for a triply periodic function for errors in each of the spherical coordinates. Appropriate graphical representations of the error-contaminated, error-corrected and error-free near fields are presented to enhance understanding of the results. Corresponding error-contaminated and error-free far fields are also obtained.

Key words: computer simulations; error correction; spherical far fields; spherical near fields.

Accepted: April 3, 1991

1. Introduction

A recently developed analytic technique that can correct for probe-position errors in planar near-field measurements to arbitrary accuracy [1,2] is also applicable to spherical near-field data after appropriate modifications. The method has been used successfully to remove probe-position errors in the planar near field, leading to more accurate far-field patterns, even if the maximum error in the probe's position is as large as 0.2 λ. Only the error-contaminated near-field measurements and an accurate probe-position error function are needed to be able to implement the correction. It is assumed that the probe-position error function is a characteristic of the near-field range and has been obtained using state-of-the-art laser positioning and precision optical systems. The method also requires the ability to obtain derivatives of the error-contaminated near field *defined* on an error-free regular grid with respect to the coordinates. In planar geometry the spatial derivatives are obtained using fast Fourier transforms (FFT) [1,2]; in spherical geometry the derivatives of Hankel functions for radial errors, and the derivatives of the spherical electric and magnetic vector basis functions for errors in the θ and ϕ coordinates are needed.

2. General Analytic Procedure

Let $b(x)$ and $\hat{b}(x; \delta x)$ be the error-free and error-contaminated near fields at position x, and δx the probe-position error function. Here the position vector x can be given in planar (Cartesian), cylindrical, or spherical coordinates. Then,

$$\hat{b}(x;\delta x)=(1+T)b(x), \tag{1}$$

where T is a differential error operator. Since real measurements are taken on an *irregular* grid, $x+\delta x$, the measured values can be represented in terms of an *unknown* error-free near field $b(x)$ and the Taylor series expansion of this field around the regular grid x. Thus, the error operator is nothing but the Taylor series operator without the leading zeroth-order term. The exact functional form of T depends on the coordinate system used in representing the near field. To solve for the error-free near field eq (1) can be inverted to yield

$$b(x)=(1+T)^{-1}\hat{b}(x;\delta x), \tag{2}$$

which can then be expanded to any arbitrary order in δx. First, we expand eq (2) as

$$b(x)=(1-T+TT-TTT+TTTT-\dots)\hat{b}(x;\delta x), \tag{3}$$

and observe that

$$T=t_1+t_2+t_3+t_4\dots+t_k+\dots. \tag{4}$$

In general, the kth-order term in the Taylor series T has the form $t_k=\frac{1}{k!}(\delta s)^k\frac{\partial^k}{\partial s^k}$, (5)

where, in Cartesian coordinates, s is x, y or z, in cylindrical coordinates s is ρ, ϕ or z, and in spherical coordinates s is r, θ, or ϕ. Equation (4) can now be used to arrange the terms in eq (3) in an ascending order of approximation. Thus, to fourth-order in δs

$$\begin{aligned}b(x)=(1&\\ -t_1-t_2-t_3-t_4&\\ +t_1t_1+t_1t_2+t_1t_3+t_2t_1+t_2t_2+t_3t_1&\\ -t_1t_1t_1-t_1t_2t_1-t_1t_1t_2-t_2t_1t_1&\\ +t_1t_1t_1t_1)\,\hat{b}(x;\delta x).&\end{aligned} \tag{6}$$

The explicit functional forms of T, t_k, and eq (6) in Cartesian geometry (planar scanning) can be found in [1,2], where the question of convergence of the nth-order expansion has also been discussed.

The following observations about the structure of eq (6) are worthwhile:

(a) The first line of the equation is the *zeroth-order* approximation to the *ideal* near field and corresponds to the first term in eq (3).
(b) Each subsequent term in eq (3) gives rise to all the terms on a subsequent line in eq (6). For example, the term TTT gives rise to all the triple product terms in eq (6); all other terms originate from another term in eq (3).
(c) The sum of subscripts in each of the terms in eq (6) is 4 or less, indicating that we have written down a *fourth-order* approximation.
(d) All possible combinations of subscripts occur, subject to the constraint in (c).
(e) Fifth- or higher-order approximations can be quickly written down using observations (b), (c), and (d) as guidelines.

Finally, we make the following nontrivial observation: $b(x)$ and $\hat{b}(x;\delta x)$ in eq (6) are both defined on a mathematically *regular* grid, even though originally the error-contaminated near field was obtained on an *irregular* grid. This shift in the definition of the error-contaminated field is an essential mathematical step in the error-correction procedure under consideration. The redefinition becomes important when *exact* derivatives of the error-contaminated near field on a *regularly* spaced grid are required; *by definition*, such derivatives can be obtained mathematically, but cannot be obtained experimentally. (In Cartesian geometry, or for planar near fields, derivatives can be obtained using Fourier techniques [1,2].)

The terms in eq (6) are differential operators acting on the error-contaminated near field $\hat{b}(x;\delta x)$. Terms such as t_1t_3 and t_3t_1 will yield different contributions as can be seen from the explicit expressions in Cartesian coordinates for probe-position errors in the z coordinate. Thus,

$$t_1t_3\hat{b}=\frac{1}{3!}\,\delta z\frac{\partial}{\partial z}(\delta z)^3\frac{\partial^3\hat{b}}{\partial z^3} \tag{7}$$

and

$$t_3t_1\hat{b}=\frac{1}{3!}(\delta z)^3\frac{\partial^3}{\partial z^3}\,\delta z\frac{\partial\hat{b}}{\partial z}, \tag{8}$$

which show that different derivatives act on different functions in the two cases. Further, the derivatives of the error function δz as required by each of the terms in eq (6) cannot be measured and are only defined mathematically [1,2], subject to the constraint that each term satisfy Maxwell's equations.

2.1 Simultaneous Errors in Two or More Coordinate Variables

The discussion so far has assumed that probe-position errors occur in only one coordinate variable at a time. In fact, simultaneous errors in more than one coordinate can be treated easily by generalizing eqs (4) and (6). This is accomplished by redefining t_k in eq (5). We simply write

$$t_1 = t_1^{(1)} + t_1^{(2)} + t_1^{(3)}, \tag{9}$$

where the superscript indicates one of the three coordinates in use. These are just the three first-order terms that appear in the usual Taylor series expansion of any function of three variables. The definition of the second-order expression also needs to be augmented the same way, but additional terms must be included to account for the contribution from mixed derivatives. The general t_2 term is now written as

$$t_2 = \sum_s t_2^{(s)} + \sum_{s' \neq s} t_{11}^{(s,s')} \tag{10}$$

where $t_{11}^{(s,s')}$ is

$$t_{11}^{(s,s')} = \partial s \, \partial s' \frac{\partial^2}{\partial s \, \partial s'} \, . \tag{11}$$

Again these are just the second-order terms in the usual Taylor series expression. The definition of the third- and higher-order terms t_k in eqs (4) and (6) can be generalized the same way, and when these general expressions are substituted into eq (6), we obtain the expression for the error-corrected near field in the presence of simultaneous errors in more than one coordinate. Obviously the number of terms in eq (6) quickly increases with the order of correction and with the number of error-contaminated coordinates considered.

3. Spherical Error Correction

In spherical scanning, near-field data are obtained on the surface of a sphere of radius r_0 at regular $\Delta\theta$ and $\Delta\phi$ intervals. The center of rotation is fixed and the probe points toward this center at every point of the spherical grid. At each point two measurements are taken, corresponding to the θ and ϕ components of the measured electric field.

To study the error-correction technique we will consider probe-position errors in a single spherical coordinate only. We also assume that the orientation of the probe is always correct, meaning that the probe points to the center of rotation independent of the position of the probe. To obtain error-correction expressions for errors in the r, θ, or ϕ coordinates the explicit form of t_k has to be substituted into eqs (4) and (6). Thus, for errors in the radial coordinate, the kth-order Taylor series term is

$$t_k = \frac{1}{k!} (\delta r)^k \frac{\partial^k}{\partial r^k} \, . \tag{12}$$

Similar expressions can be immediately written down for errors in the θ and ϕ coordinates:

$$t_k = \frac{1}{k!} (\delta \theta)^k \frac{\partial^k}{\partial \theta^k} \tag{13}$$

and

$$t_k = \frac{1}{k!} (\delta \phi)^k \frac{\partial^k}{\partial \phi^k} \, . \tag{14}$$

These error functions depend on the coordinates: $\delta r = \delta r(r_0, \theta, \phi)$, $\delta\theta = \delta\theta(r_0, \theta, \phi)$, and $\delta\phi = \delta\phi(r_0, \theta, \phi)$ for fixed r_0. This must be kept in mind when spherical versions of the expressions shown explicitly in eqs (7) and (8) are evaluated. When eqs (12), (13), and (14) are substituted into eq (6) we obtain the error-corrected spherical near field in terms of the error-contaminated (measured) spherical near field.

3.1 Spherical Near Fields

In spherical geometry, we really have two independent near fields, which are the θ and ϕ components of the electric field E measured by an ideal dipole. The tangential electric field E_t, with wavenumber k, can be expressed [3] in terms of an infinite sum of products of spherical Hankel functions of the first kind $h_n^{(1)}(kr)$ and spherical vector basis functions $X_{nm}(\theta, \phi)$. We can write (using $\hat{r}$ for the unit vector in the radial direction)

$$E_t(r, \theta, \phi) = \sum_n \sum_m \Big[\alpha_{nm}^{(h)} h_n^{(1)}(kr) \, X_{nm}(\theta, \phi) + \alpha_{nm}^{(e)} g_n^{(1)}(kr) \, \hat{r} \times X_{nm}(\theta, \phi) \Big] , \tag{15}$$

where, with $x \equiv kr$,

$$g_n^{(1)}(x) = \frac{1}{x} \frac{\mathrm{d}}{\mathrm{d}x} [x h^{(1)}(x)] . \tag{16}$$

The near-field quantities b and $\hat{b}$ in eq (6) are identified with either the θ or ϕ component of E_t and $\hat{E}_t$, respectively, where $\hat{E}_t$ is the error-contaminated electric field. Only one set of electric coefficients $\alpha_{nm}^{(e)}$ and one set of magnetic coefficients $\alpha_{nm}^{(h)}$ appear in eq (15), and the error-correction procedure corrects both components of the measured spherical field simultaneously.

To obtain the coefficients α_{nm} in eq (15) we use the explicit definitions and orthogonality relations obeyed by the vector basis functions X_{nm} [3]. These are $\sqrt{n(n+1)}\, X_{nm}(\theta,\phi)=LY_{nm}(\theta,\phi)$, where $L=-i(r\times\nabla)$ is the the well-known angular momentum operator widely used in quantum mechanics, and the spherical harmonics $Y_{nm}(\theta,\phi)=P_{nm}(\theta)$ $\exp(im\phi)$, where P_{nm} are associated Legendre functions. In component form,

$$\sqrt{n(n+1)}\,X_{nm}(\theta,\phi)=-\left(m\frac{Y_{nm}}{sin\theta},\, i\frac{\partial Y_{nm}}{\partial\theta}\right). \qquad (17)$$

The orthogonality properties are [3]

$$\int_0^{2\pi}\int_0^{\pi} X^*_{nm}\cdot X_{n'm'}\sin\theta\mathrm{d}\theta\mathrm{d}\phi=\delta_{n'n'}\delta_{m'm'} \qquad (18)$$

with a similar relationship for $\hat{r}\times X^*_{nm}$, and

$$\int_0^{2\pi}\int_0^{\pi} X^*_{n'm'}\cdot\hat{r}\times X_{nm}\sin\theta\mathrm{d}\theta\mathrm{d}\phi=0 \qquad (19)$$

for all n, n', m, m', where $\delta_{nn'}$ is the Kronecker delta. The coefficients can now be obtained [3] using eqs (15), (18) and (19):

$$\alpha^{(h)}_{nm}h^{(1)}_n(kr)=\int_0^{2\pi}\int_0^{\pi} E_t(r,\theta,\phi)\cdot X^*_{nm}\sin\theta\mathrm{d}\theta\mathrm{d}\phi \qquad (20)$$

and

$$\alpha^{(e)}_{nm}g^{(1)}_n(kr)=$$

$$\int_0^{2\pi}\int_0^{\pi} E_t(r,\theta,\phi)\cdot\hat{r}\times X^*_{nm}\sin\theta\mathrm{d}\theta\mathrm{d}\phi. \qquad (21)$$

With eqs (18), (19), (20) and (21), any spherical near field, error-free or error-contaminated, can be cast into the form of eq (15), and given a set of coefficients α_{nm}, a spherical vector function can always be constructed using eq (15). Consequently, each of the terms appearing in eq (6) and any factor t_k in eq (6) can be evaluated in spherical coordinates. On a regular grid the summation can be accomplished using an efficient FFT summation, but on an irregular grid the sum must be evaluated directly, or by a Taylor series as described in [1,2].

To obtain the coefficients $\alpha^{(h)}_{nm}$ numerically we rewrite eq (20) as

$$2\alpha^{(h)}_{nm}h^{(1)}_n(kr)=$$

$$2\pi\int_{-\pi}^{\pi}\tilde{E}^m_t(r,\theta)\cdot\tilde{X}^*_{nm}(\theta)|sin\ \theta|\mathrm{d}\theta. \qquad (22)$$

Here the factor 2π is the result of the ϕ integral and the factor 2 on the left is introduced to offset the effect of extending the range of integration in θ. $\tilde{E}^m_t(r,\theta)$ and $\tilde{X}_{nm}(\theta)$ are the ϕ-transforms of $E_t(r,\theta,\phi)$ and $X_{nm}(\theta,\phi)$, respectively, extended into the range $[-\pi,0]$. The integrand in eq (22) is now an even function of θ, and can be expanded in a Fourier series,

$$\tilde{E}_t{}^m(r,\theta)\cdot\tilde{X}^*_{nm}(\theta)|\sin\theta|=\sum_l c_l^{nm}e^{-il\theta} \qquad (23)$$

where the coefficients c_l^{nm} can be obtained by Fourier transforming the data. Since only the coefficient c_0^{nm} will survive the term by term integration of the sum in eq (23), we immediately obtain from eqs (22) and (23)

$$\alpha^{(h)}_{nm}h^{(1)}_t(kr)=2\pi^2\cdot c_0^{nm}. \qquad (24)$$

Similar expressions can be written for $\alpha^{(e)}_{nm}$ in eq (21).

3.2 Derivatives of Spherical Near Fields

To evaluate the terms and factors appearing in eq (6) in spherical coordinates, we must be able to obtain first- and higher-order derivatives of arbitrary spherical near fields with respect to any of the spherical coordinates. Derivatives with respect to ϕ are the simplest, since the ϕ dependence is only through the factors $\exp(im\phi)$ in the vector basis functions. Hence, a kth-order derivative with respect to ϕ will merely alter the coefficients in eq (15) according to the substitution,

$$\alpha_{nm}\rightarrow(im)^k\alpha_{nm}, \qquad (25)$$

after which the summation can be performed without change to the summation procedure in use. Radial derivatives are only somewhat more complicated; we obtain kth-order derivatives of Hankel functions with respect to x after repeated differentiation of the recursion relation [3],

$$(2n+1)\frac{\mathrm{d}h^{(1)}_n(x)}{\mathrm{d}x}=nh^{(1)}_{n-1}(x)-(n+1)h^{(1)}_{n+1}(x). \qquad (26)$$

After substitution of derivatives of Hankel functions in place of the functions themselves in eq (15), the existing summation procedure can be used without modification to obtain radial derivatives of the components of the near field. However, derivatives with respect to θ cannot be accomplished with ease, since no simple recursion relationship exists that can be utilized in a straighforward manner in a computer algorithm. To obtain θ derivatives we have to use Fourier series. If we assume that the θ dependence of the components (denoted by superscript s) of $\boldsymbol{E}_t$ has been written in the form

$$\sum_l c_l^{(s)} e^{il\theta} \tag{27}$$

then the kth-order θ derivative is

$$\sum_l (il)^k c_l^{(s)} e^{il\theta}. \tag{28}$$

The coefficients $c_l^{(s)}$ can be obtained using a fast transform; after modification of the coefficients by the factors $(il)^k$, the same FFT can be used to perform the summation indicated in eq (28). Since the data must be periodic with a period of 2π for analysis by an FFT, a near field defined on the θ interval $[0,\pi]$ must be extended to the interval $[0,2\pi]$ or $[-\pi,\pi]$ using the symmetry properties of the basis functions [4,5].

3.3 Data Analysis

As is evident from the discussion in the preceding sections, we need efficient numerical procedures for two basic computational problems arising from eq (15):

(i) Given a spherical vector function $\boldsymbol{E}_t(\theta,\phi)$, we must be able to *analyze* it to obtain the coefficients α_{nm}, and
(ii) Given a set of coefficients α_{nm}, we must be able to *synthesize* the spherical vector function $\boldsymbol{E}_t(\theta,\phi)$ by performing the sum.

Focusing on a specific term of the full error-correction expression as given in eq (6), we can appreciate the role of these two computational procedures. We have, for the case of errors in the r coordinate,

$$t_1 t_2 \hat{b} = \frac{1}{2}\, \delta r \frac{\partial}{\partial r} (\delta r)^2 \frac{\partial^2}{\partial r^2} \hat{b}\ (r,\theta,\phi), \tag{29}$$

where $\hat{b}$ now stands for the components of $\hat{\boldsymbol{E}}_t$. The following six steps must be executed to evaluate this expression numerically:

1. We analyze the components of $\hat{\boldsymbol{E}}_t$ to obtain coefficients α_{nm}, as defined in eq (15).
2. We obtain the second-order radial derivatives of the components of $\hat{\boldsymbol{E}}_t$ by performing the summation in eq (15) using second-order derivatives of the radial functions.
3. We multiply the result by the function $(\delta r)^2$, thereby obtaining a new spherical near field.
4. We analyze the fields obtained in step (3) to get a new set of coefficients α_{nm}, as defined in eq (15).
5. We obtain the first-order radial derivatives of the components of $\hat{\boldsymbol{E}}_t$ by performing the summation in eq (15) using first-order derivatives of the radial functions.
6. We multiply the result in step (5) by 0.5 δr to obtain the part of the error-corrected spherical near field denoted by $t_1 t_2 \hat{b}$ in eq (6).

Similar sequences of steps will correctly evaluate any and all of the terms in eq (6) to obtain the ideal error-free near field. The procedure is highly recursive, and a few well designed subroutines can provide the result of the extensive and complex computational task called for in eq (6). The procedure is the same for errors in the θ and ϕ coordinates.

3.4 Computer Simulations

Computer simulations were performed for probe-position errors in a single spherical coordinate only; simultaneous errors in two or three coordinates were not considered. The following sequence of steps were performed for errors in each of the spherical coordinates:

1. We start with an error-free spherical near field and analyze it to obtain its expansion coefficients α_{nm} [(see eq (15)].
2. We define a probe-position error function $|\delta \mathbf{x}| = \delta s(\theta,\phi)$ to be studied, and choose its amplitude.
3. We construct an error-contaminated near field by performing the summation in eq (15) at the *irregular* grid points $\mathbf{x}+\delta\mathbf{x}$. This requires a direct sum at each point of the grid, since no efficient method of summing is known to exist on an irregular grid.
4. We perform the computations in eq (6) to obtain the error-corrected near field. The steps

taken to accomplish this were outlined above in some detail (see eq (29) and the brief discussion following it).

(5) We calculate error-free, error-contaminated, and error-corrected far fields.

(6) We compare error-free, error-contaminated, and error-corrected fields to study the effectiveness of the error correction.

3.5 Results and Discussion

The near field used in all the simulations was generated by a microstrip array antenna consisting of four 16×16 element subpanels operating at 3.3 GHz. The scan radius was 128 cm. Figures 1a and 1b show perspective plots of the amplitudes of the θ and ϕ components of the error-free near field. The near field was obtained by summing the terms in eq (15) with $n = 30$, after the original near-field data were analyzed to obtain coefficients up to $n = 87$. With $n = 30$, direct summations on irregular grids could be performed in about 6 hours on a personal computer. Figures 2a and 2b show perspective plots of the amplitudes of the θ and ϕ components of the error-free far field.

We chose periodic probe-position error functions of the form

$$\delta s(\theta,\phi) = A \cos^2 \alpha\theta \cos^2 \beta\phi, \qquad (30)$$

where $s = r$, θ, or ϕ, and $\alpha = \beta = 3$. For errors in the radial coordinate we chose $A = 0.1\ \lambda \approx 1$ cm, and for errors in the angular coordinates, we chose $A = 0.01\ \lambda$, which corresponds to a maximum angular error of 3.6°. The magnitude of these errors are unrealistic, since, on the NIST spherical near field scanner, the probe's position errors are estimated to be less than $\delta r \approx 0.1$ cm, and $\delta\theta \approx \delta\phi \approx 0.5°$. Periodic probe-position errors were chosen, because such errors in the near field could lead to large errors in the far field. This is a well known phenomenon in planar near-field to far-field transformations [6,7]. The procedure, however, could be easily performed with nonperiodic error functions.

The results of the simulations are presented in the figures 3–26: perspective plots of ratios of error-contaminated and error-free fields are presented for errors in the three coordinates separately, followed by perspective plots of ratios of error-corrected and error-free fields. Similar plots are presented for the far fields. Both amplitudes and phases are shown for all cases.

An examination of the plots immediately reveals the success of the error correction. By comparing the amplitudes of the error-contaminated and error-corrected ratios, we immediately observe insignificant levels of residual errors almost everywhere on the sphere. The same quantitative observation can be made about the phase difference plots, where the residual error in the error-corrected phases approaches 0. The following additional qualitative observations are worthwhile:

(i) The correction is most successful in the forward hemisphere, especially around the main beam at $\theta = 0$ in all cases. This is true for both the near and the far field.

(ii) The correction is least successful in the back hemisphere, especially around $\theta = \pm 180°$, where the data are ill-determined and small in amplitude.

(iii) There are no large regions on the sphere where the correction technique fails.

(iv) At isolated points the correction seems to be less successful as evidenced by peaks in the perspective plots. These points correspond to deep nulls in the original error-free near field, and, consequently, can be understood as artifacts of the ratio field, rather than some more serious problem with the technique.

(v) The radial error function $\delta r(\theta,\phi)$ clearly shows up in figures (3b) and (4b), as expected, since we have essentially plotted the phase of the ratio of Hankel functions of the form $\exp(ikr)/r$ at $r + \delta r(\theta,\phi)$ and r, with $\delta r \leqslant r$.

(vi) The three-lobe structure of the periodic error function over an angular interval of 180° in θ and ϕ shows up clearly in all the error-contaminated plots, as expected. This structure also shows up in the error-corrected plots, indicating that the error-correction procedure is a systematic global reduction of the error without altering the functional form of the error. This agrees with the structure of eq (6).

Both the qualitative and quantitative features of the results show that the error correction outlined in this study can be very useful in providing more accurate spherical near-field data to determine accurate far fields of antennas.

4. Suggestions for Further Study

Here we have demonstrated the effectiveness of a novel error-correction technique that removes probe-position errors in r, θ, or ϕ from spherical near-field data. For completeness, the technique should be applied when errors in all three coordinates are present simultaneously. This is the most realistic case. Such a *complete* error-correction technique would be computationally more complicated and extensive, but in principle not more difficult, and should also be effective and successful. Finally, more realistic probe-position error functions should be used, and the correction technique should be applied to real error-contaminated spherical data. The success of this error-correction technique is especially desirable at higher frequencies, where the realistic amplitudes of the probe-position errors on a spherical near-field range are a significant part of the wavelength.

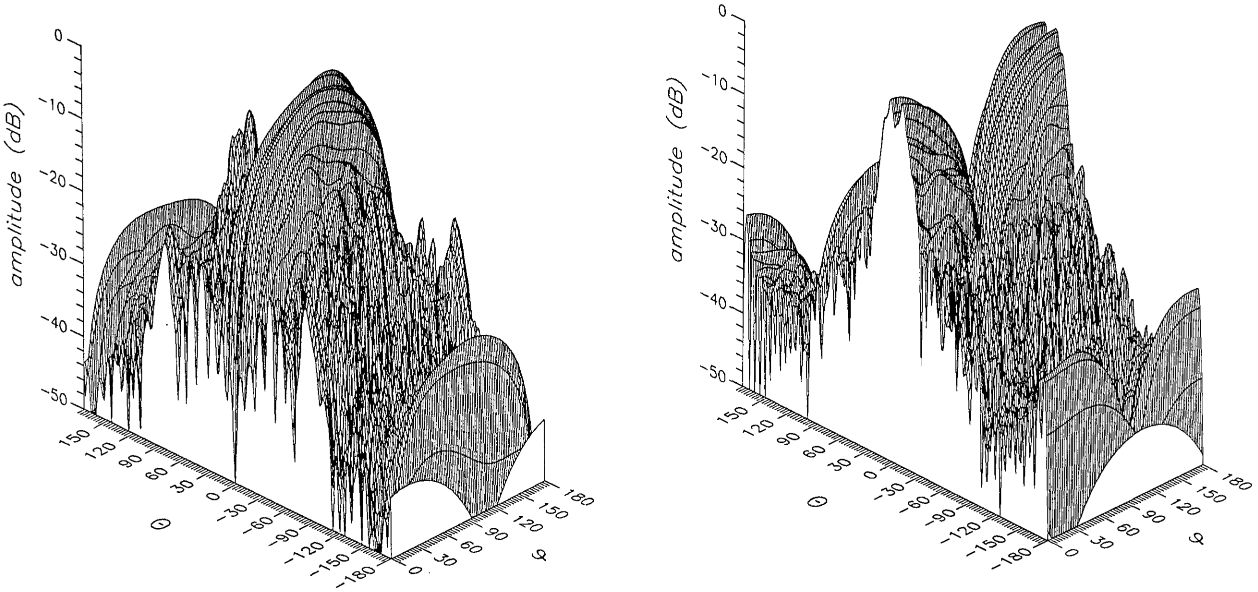

(a) (b)

Figure 1. The amplitude of the error-free near field at 3.3 GHz, (a) the θ and (b) the ϕ component.

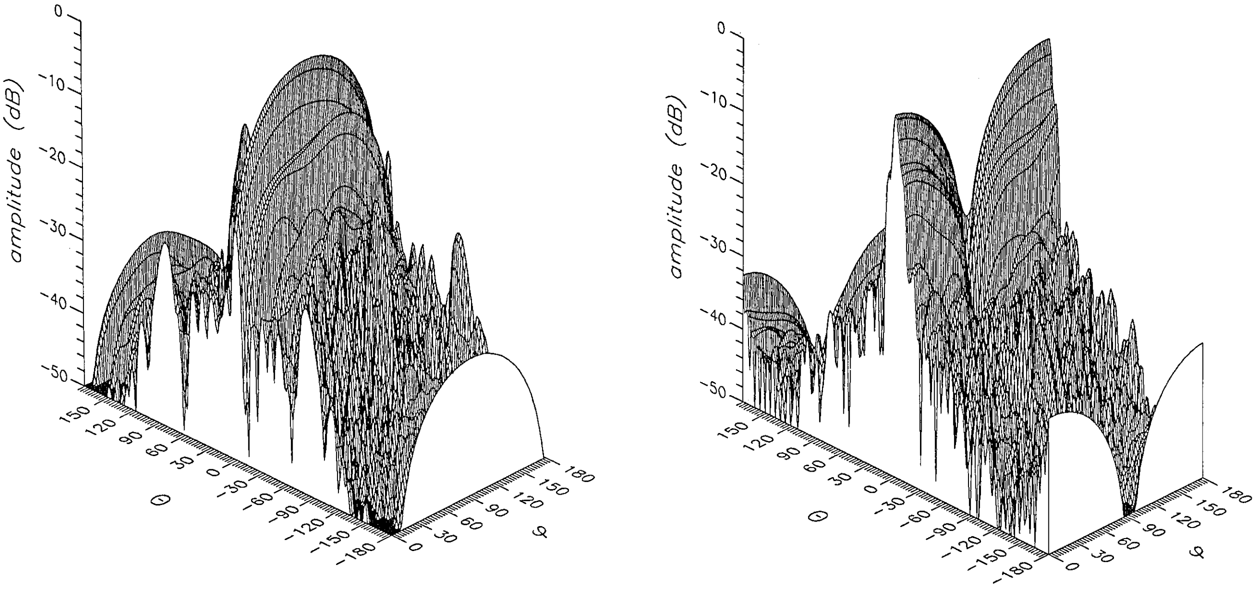

(a) (b)

Figure 2. The amplitude of the error-free far field at 3.3 GHz, (a) the θ and (b) the ϕ component.

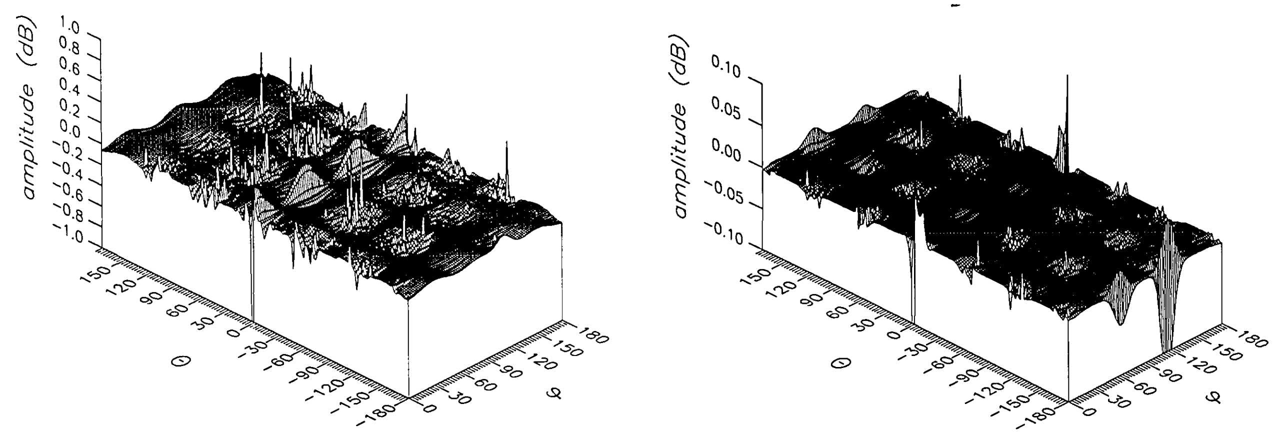

(a) (b)

Figure 3. The amplitudes of the θ components of the ratios of (a) the error-contaminated and (b) the error-corrected near fields to the error-free near field in the case of errors in the r coordinate.

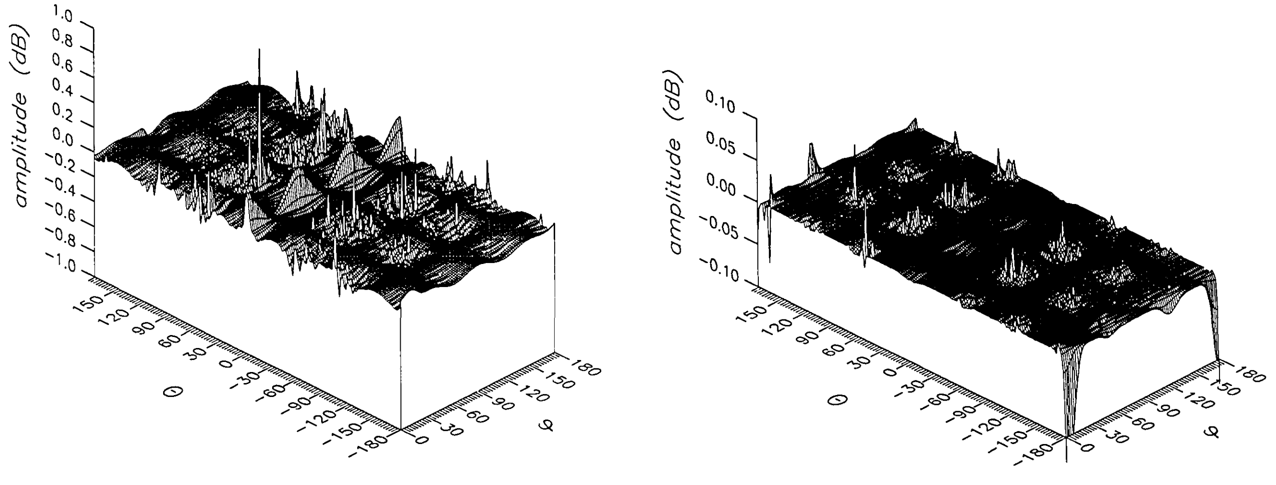

(a) (b)

Figure 4. The amplitudes of the ϕ components of the ratios of (a) the error-contaminated and (b) the error-corrected near fields to the error-free near field in the case of errors in the r coordinate.

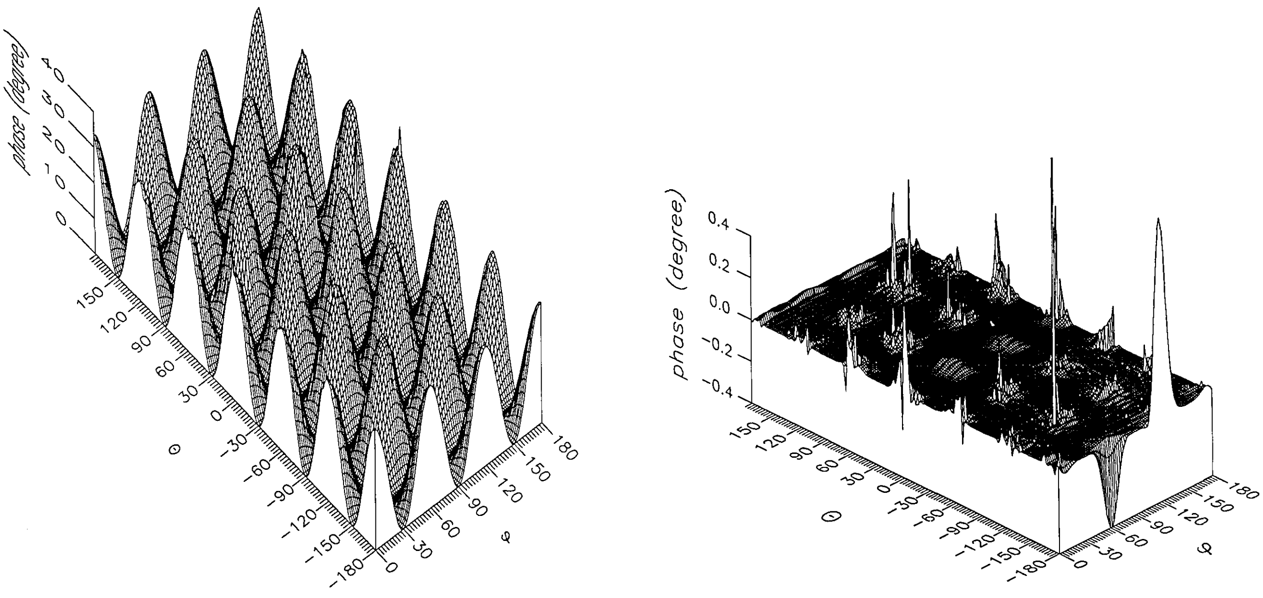

(a) (b)

Figure 5. The phase of the θ components of the ratios of (a) the error-contaminated and (b) the error-corrected near fields to the error-free near field in the case of errors in the r coordinate.

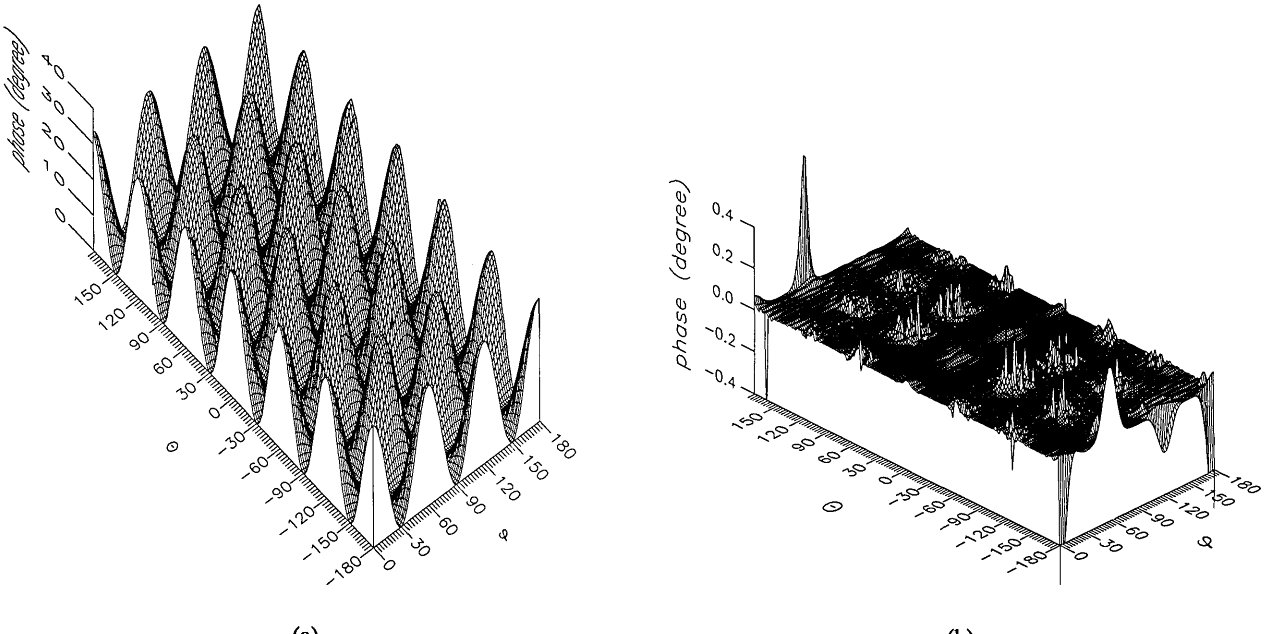

(a) (b)

Figure 6. The phase of the ϕ components of the ratios of (a) the error-contaminated and (b) the error-corrected near fields to the error-free near field in the case of errors in the r coordinate.

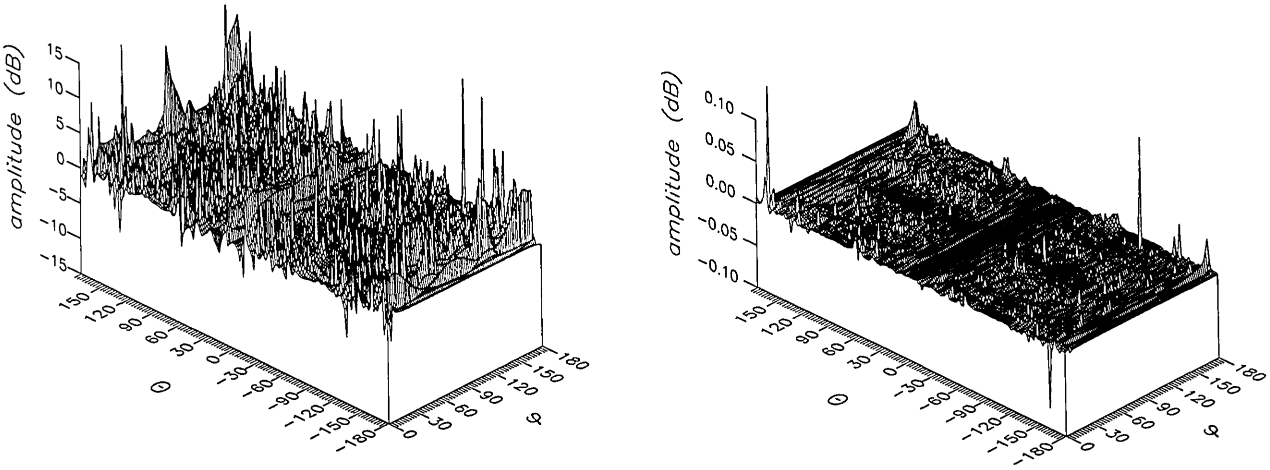

(a)

(b)

Figure 7. The amplitudes of the θ components of the ratios of (a) the error-contaminated and (b) the error-corrected far fields to the error-free far field in the case of errors in the r coordinate.

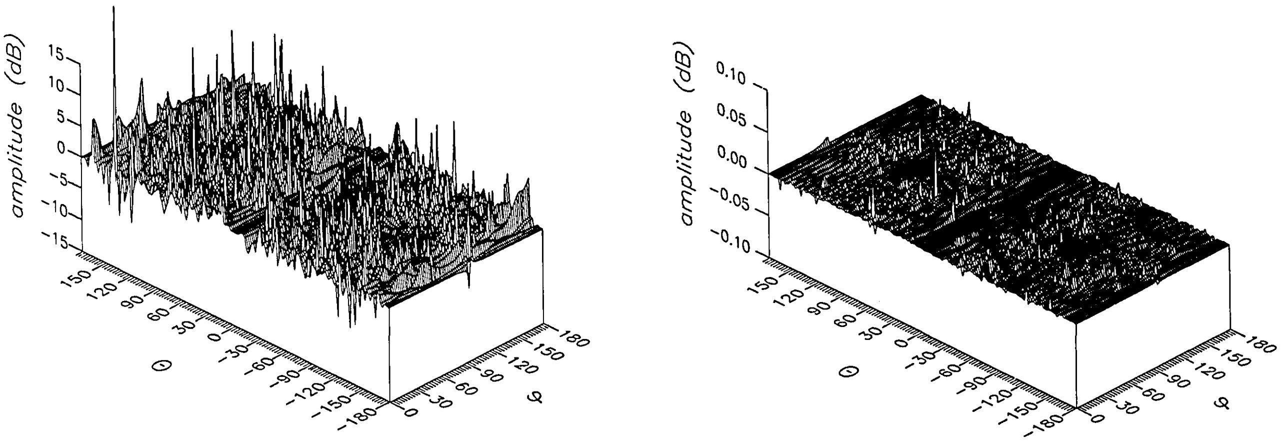

(a)

(b)

Figure 8. The amplitudes of the ϕ components of the ratios of (a) the error-contaminated and (b) the error-corrected far fields to the error-free far field in the case of errors in the r coordinate.

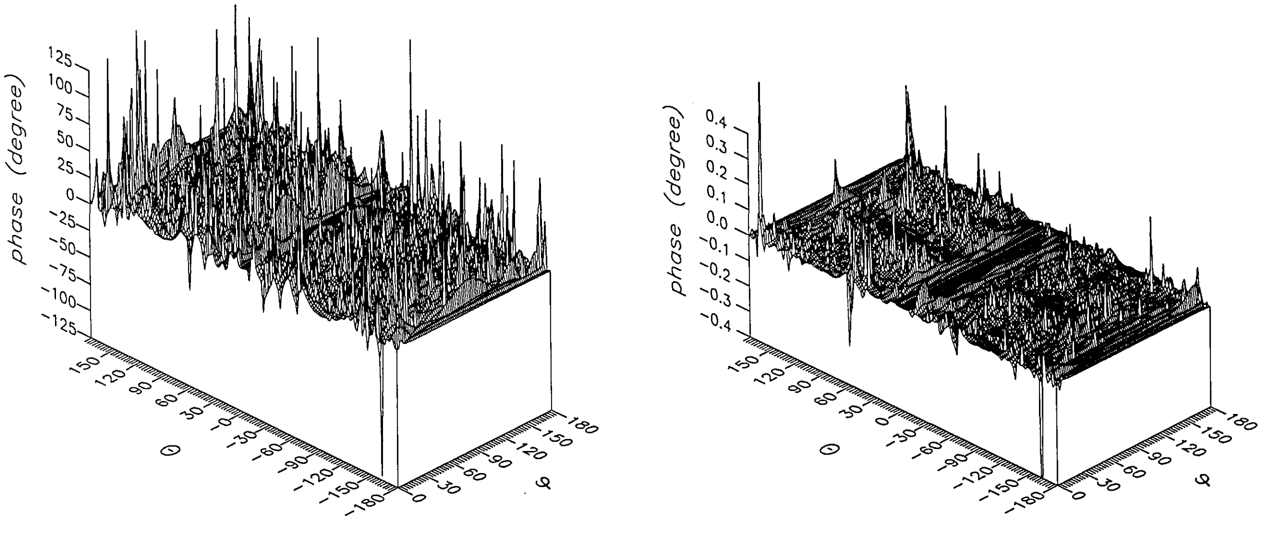

(a) (b)

Figure 9. The phase of the *θ* components of the ratios of (a) the error-contaminated and (b) the error-corrected far fields to the error-free far field in the case of errors in the *r* coordinate.

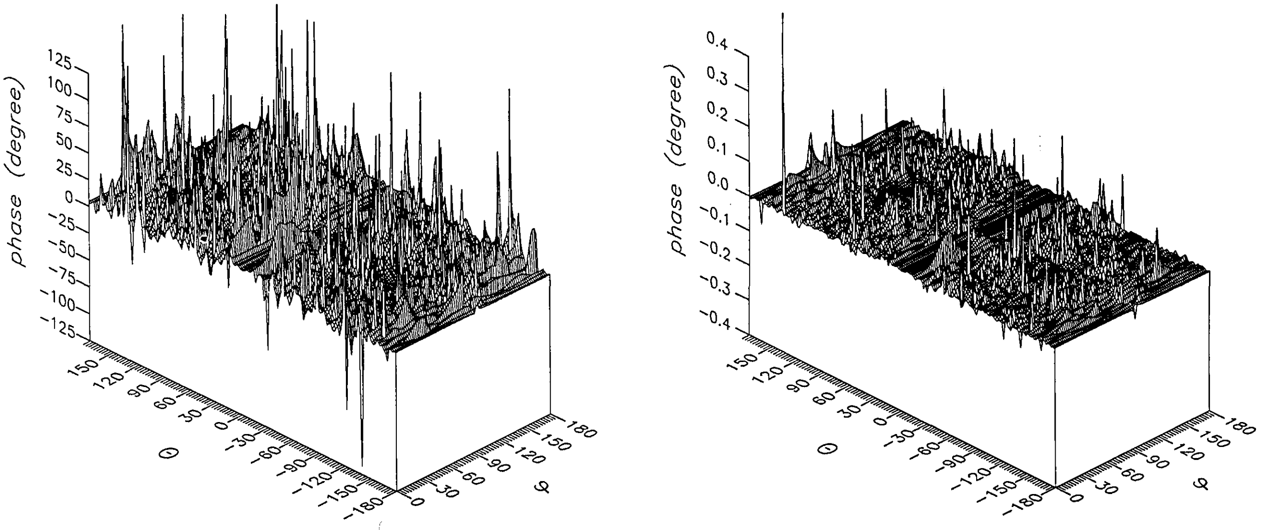

(a) (b)

Figure 10. The phase of the *ϕ* components of the ratios of (a) the error-contaminated and (b) the error-corrected far fields to the error-free far field in the case of errors in the coordinate.

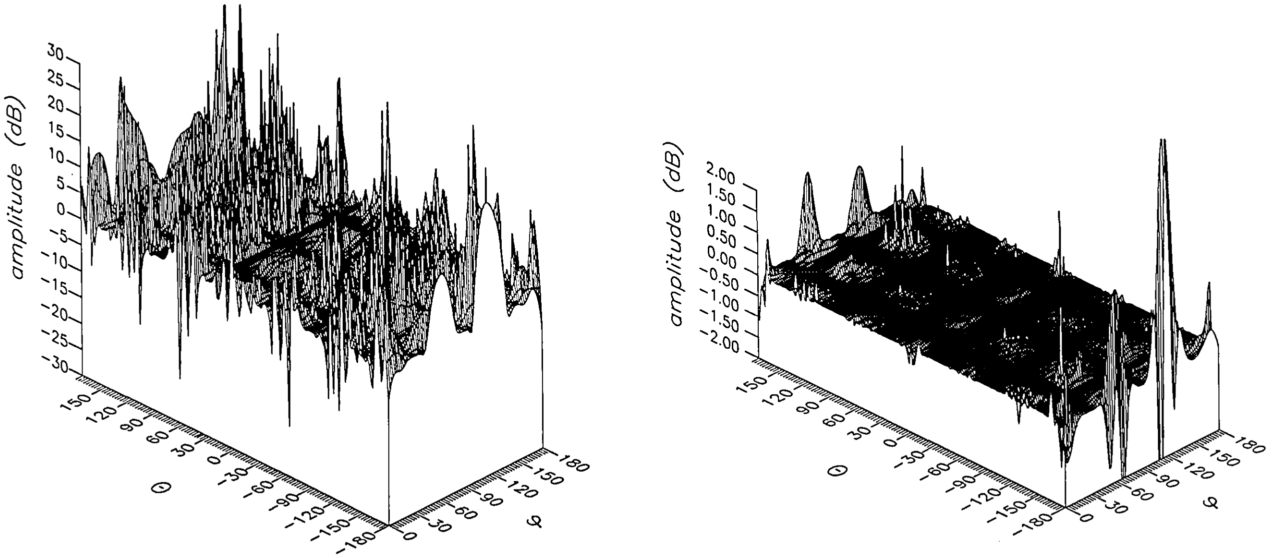

(a) (b)

Figure 11. The amplitudes of the θ components of the ratios of (a) the error-contaminated and (b) the error-corrected near fields to the error-free near field in the case of errors in the θ coordinate.

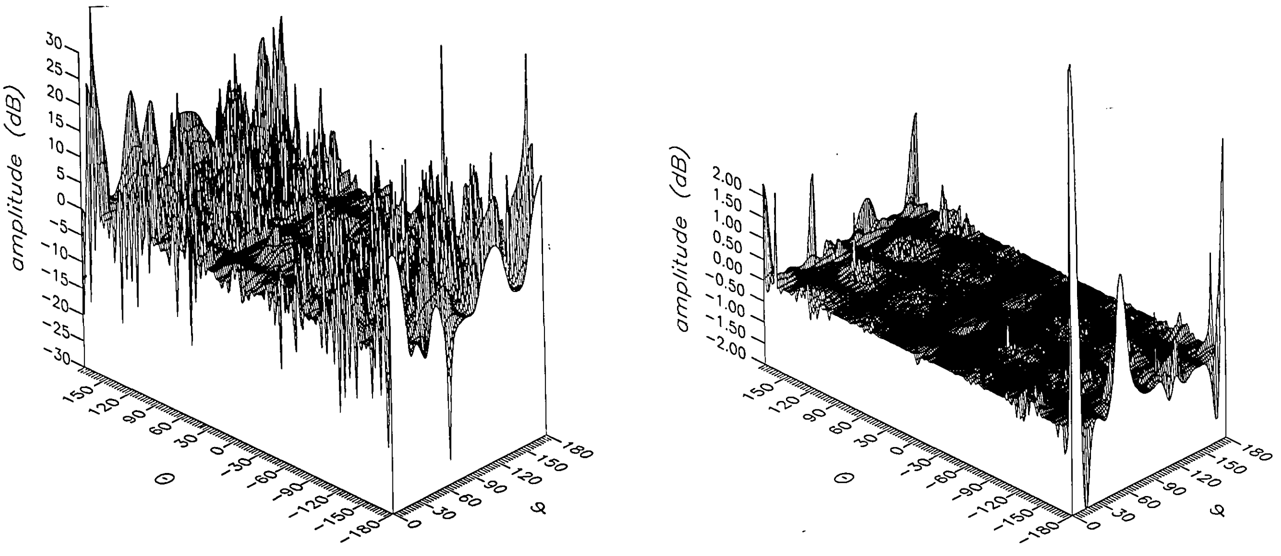

(a) (b)

Figure 12. The amplitudes of the ϕ components of the ratios of (a) the error-contaminated and (b) the error-corrected near fields to the error-free near field in the case of errors in the θ coordinate.

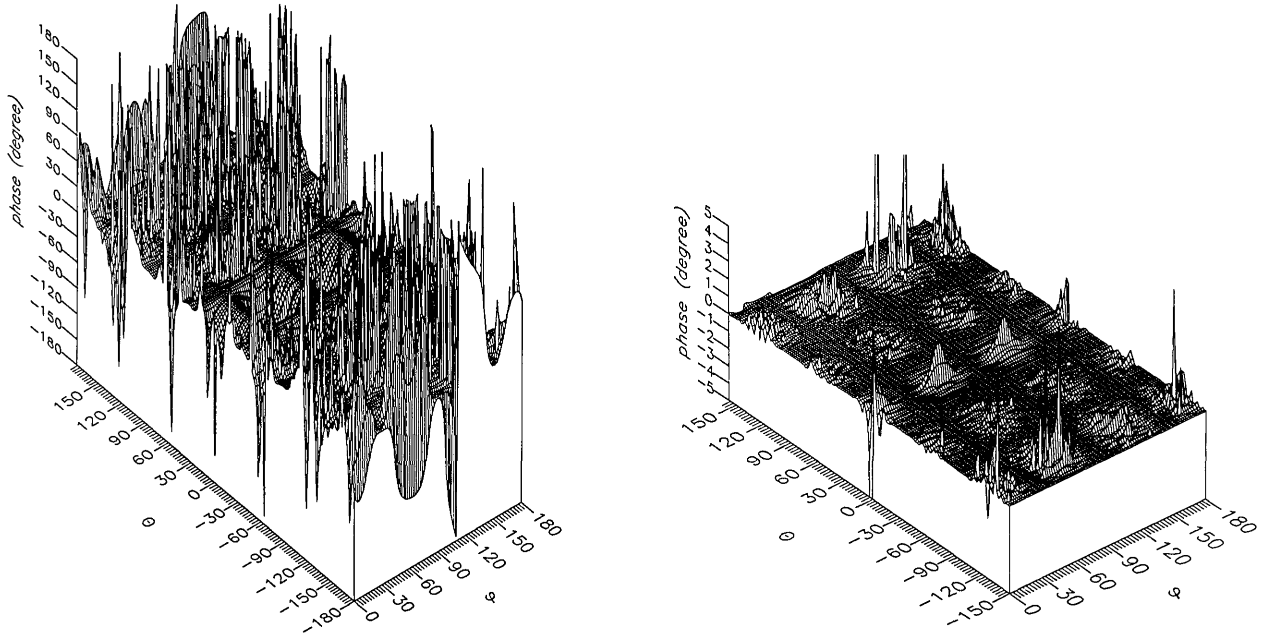

(a) (b)

Figure 13. The phase of the θ components of the ratios of (a) the error-contaminated and (b) the error-corrected near fields to the error-free near field in the case of errors in the θ coordinate.

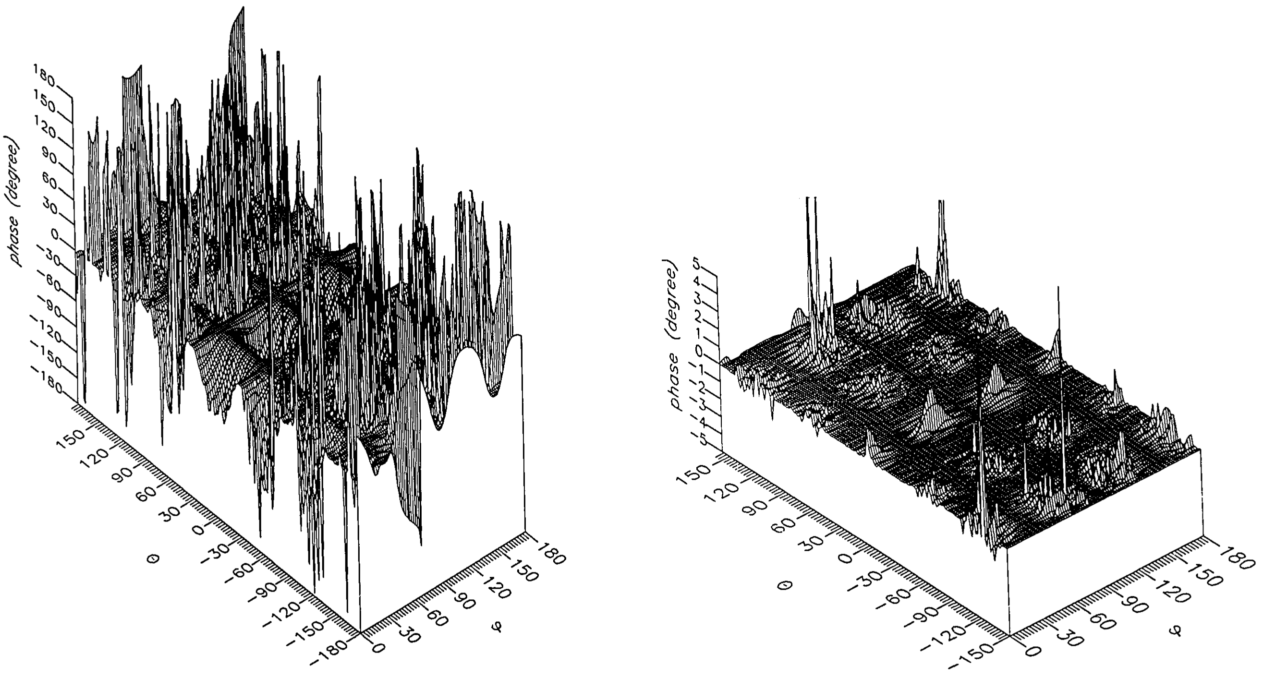

(a) (b)

Figure 14. The phase of the ϕ components of the ratios of (a) the error-contaminated and (b) the error-corrected near fields to the error-free near field in the case of errors in the θ coordinate.

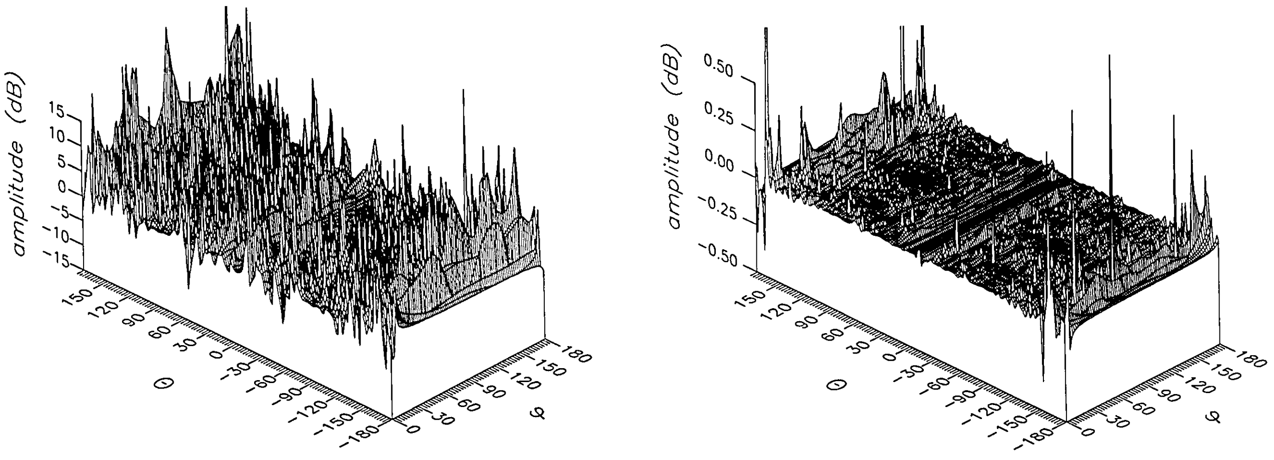

(a) (b)

Figure 15. The amplitudes of the *θ* components of the ratios of (a) the error-contaminated and (b) the error-corrected far fields to the error-free far field in the case of errors in the *θ* coordinate.

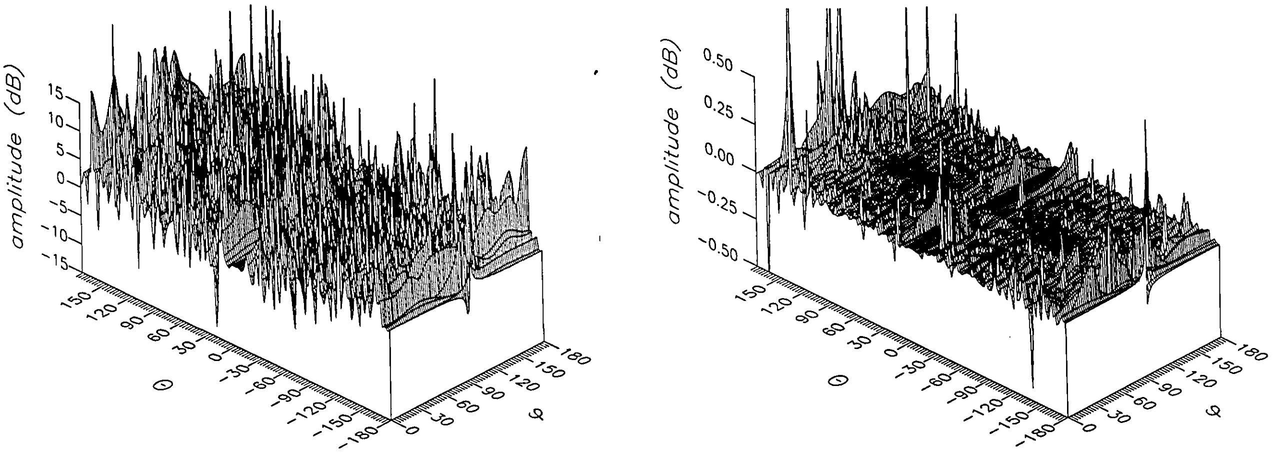

(a) (b)

Figure 16. The amplitudes of the *ϕ* components of the ratios of (a) the error-contaminated and (b) the error-corrected far fields to the error-free far field in the case of errors in the *θ* coordinate.

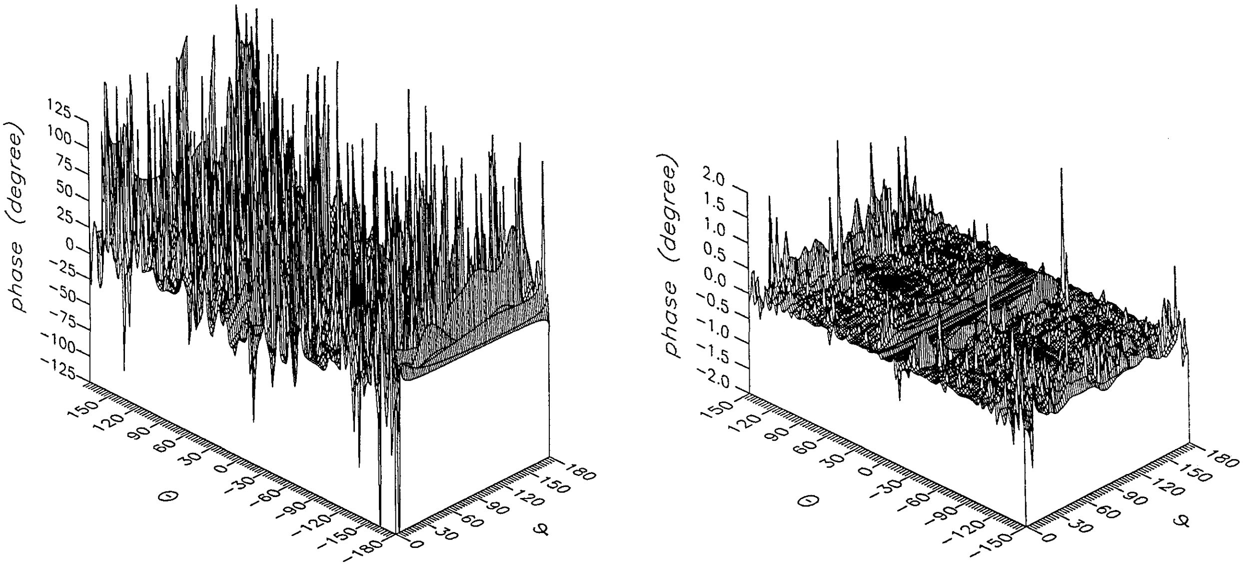

(a) (b)

Figure 17. The phase of the θ components of the ratios of (a) the error-contaminated and (b) the error-corrected far fields to the error-free far field in the case of errors in the θ coordinate.

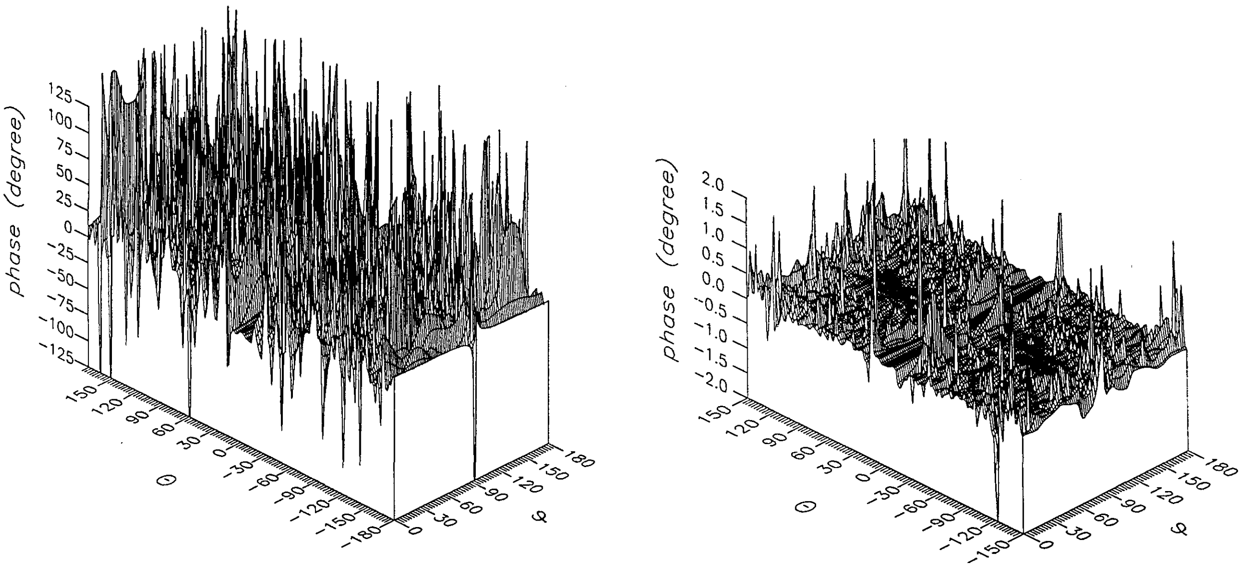

(a) (b)

Figure 18. The phase of the ϕ components of the ratios of (a) the error-contaminated and (b) the error-corrected far fields to the error-free far field in the case of errors in the θ coordinate.

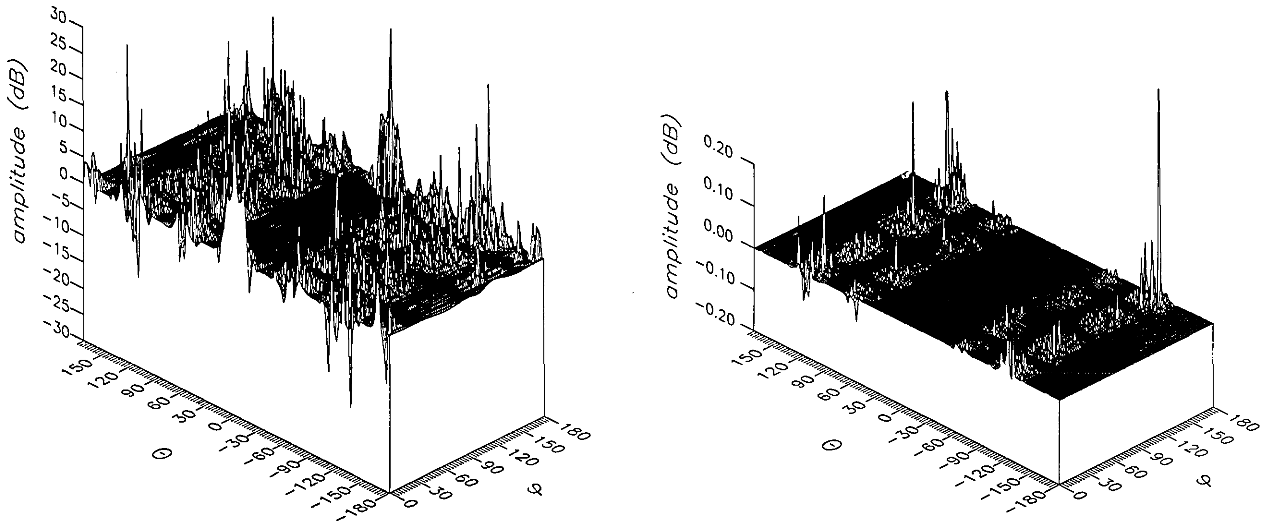

(a) (b)

Figure 19. The amplitudes of the θ components of the ratios of (a) the error-contaminated and (b) the error-corrected near fields to the error-free near field in the case of errors in the ϕ coordinate.

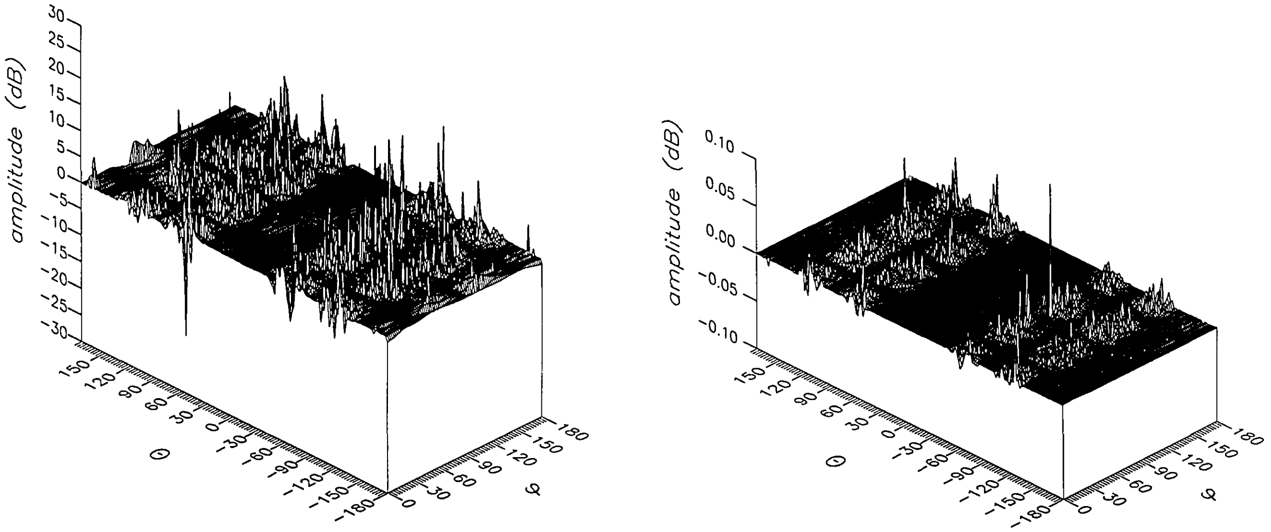

(a) (b)

Figure 20. The amplitudes of the ϕ components of the ratios of (a) the error-contaminated and (b) the error-corrected near fields to the error-free near field in the case of errors in the ϕ coordinate.

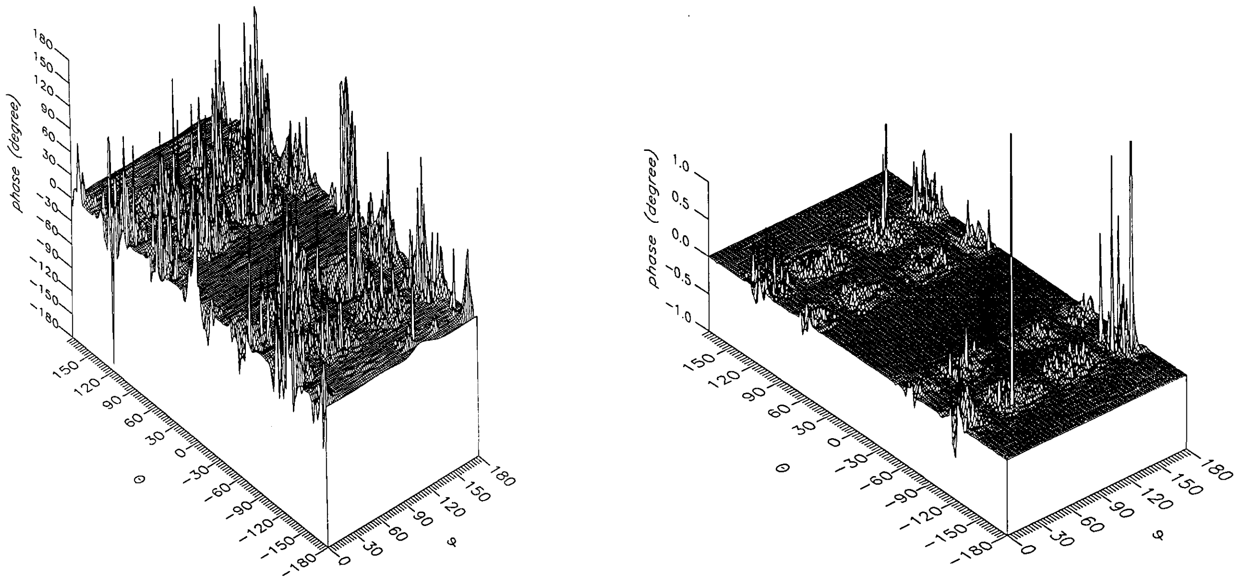

(a) (b)

Figure 21. The phase of the θ components of the ratios of (a) the error-contaminated and (b) the error-corrected near fields to the error-free near field in the case of errors in the ϕ coordinate.

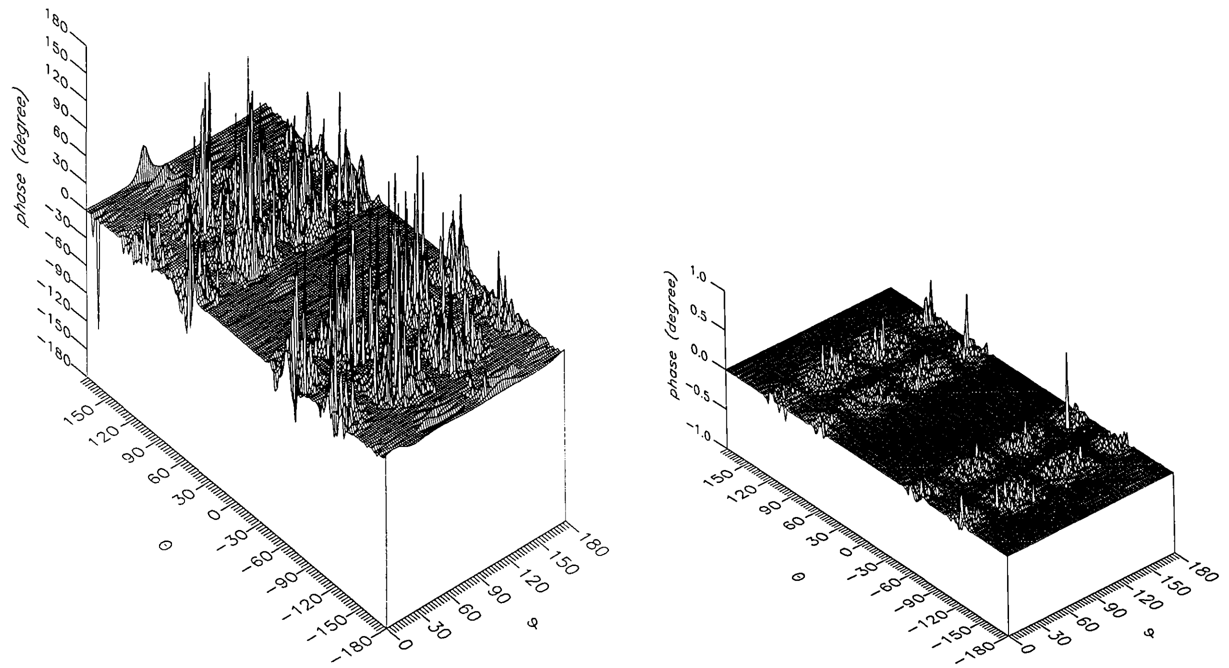

(a) (b)

Figure 22. The phase of the ϕ components of the ratios of (a) the error-contaminated and (b) the error-corrected near fields to the error-free near field in the case of errors in the ϕ coordinate.

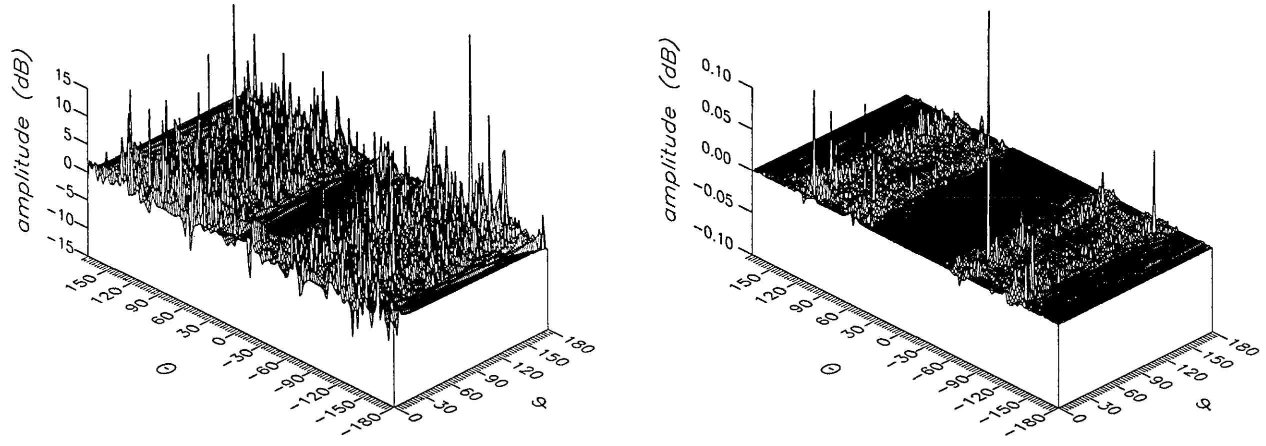

(a) (b)

Figure 23. The amplitudes of the *θ* components of the ratios of (a) the error-contaminated and (b) the error-corrected far fields to the error-free far field in the case of errors in the *φ* coordinate.

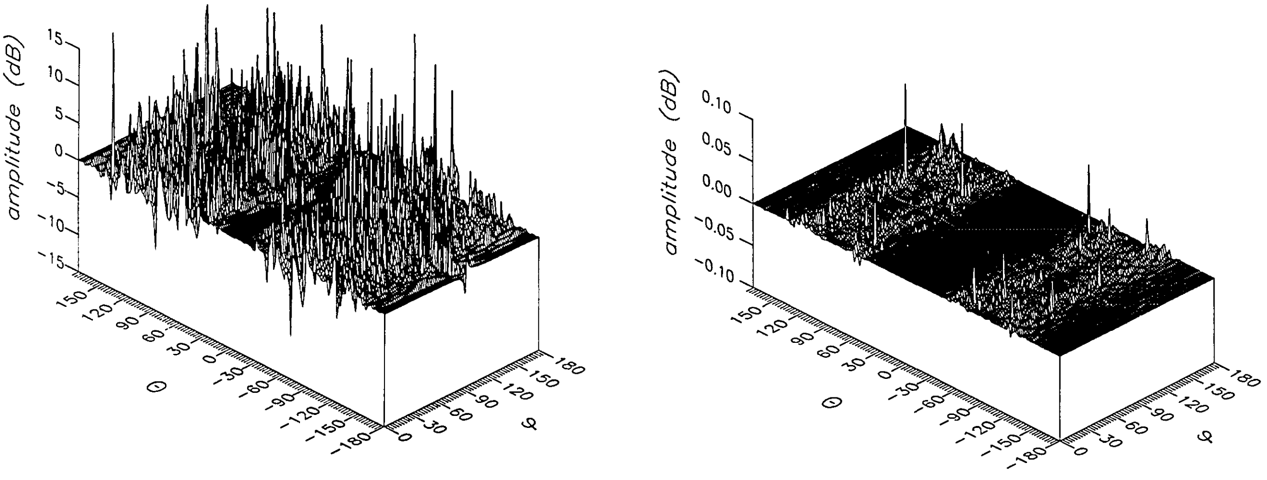

(a) (b)

Figure 24. The amplitudes of the *φ* components of the ratios of (a) the error-contaminated and (b) the error-corrected far fields to the error-free far field in the case of errors in the *φ* coordinate.

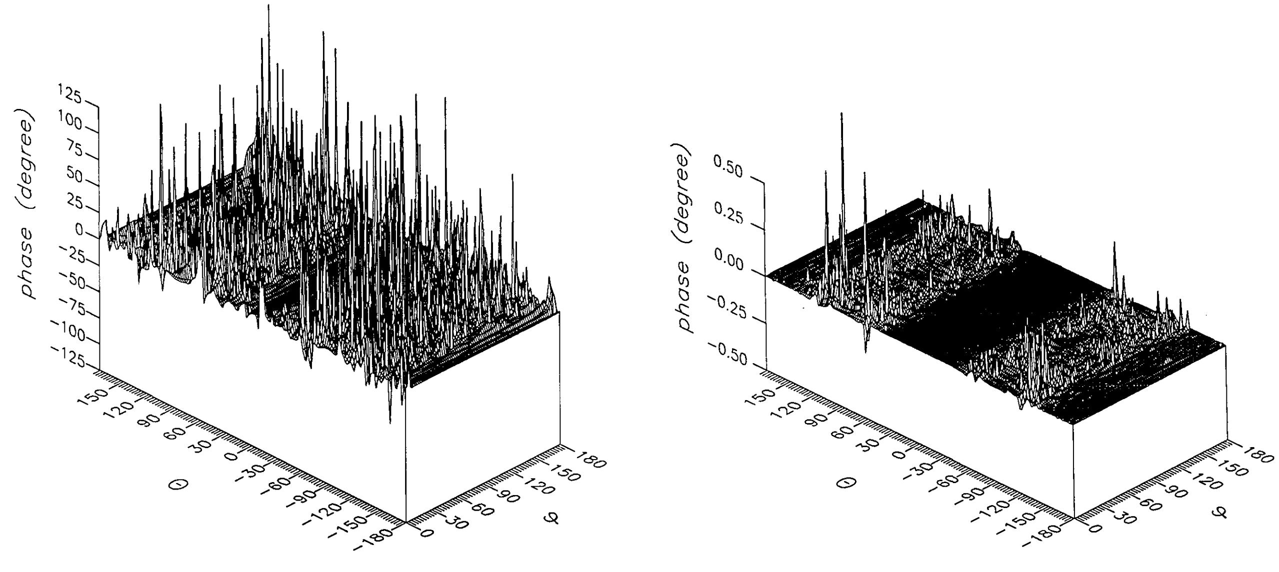

(a) (b)

Figure 25. The phase of the θ components of the ratios of (a) the error-contaminated and (b) the error-corrected far fields to the error-free far field in the case of errors in the ϕ coordinate.

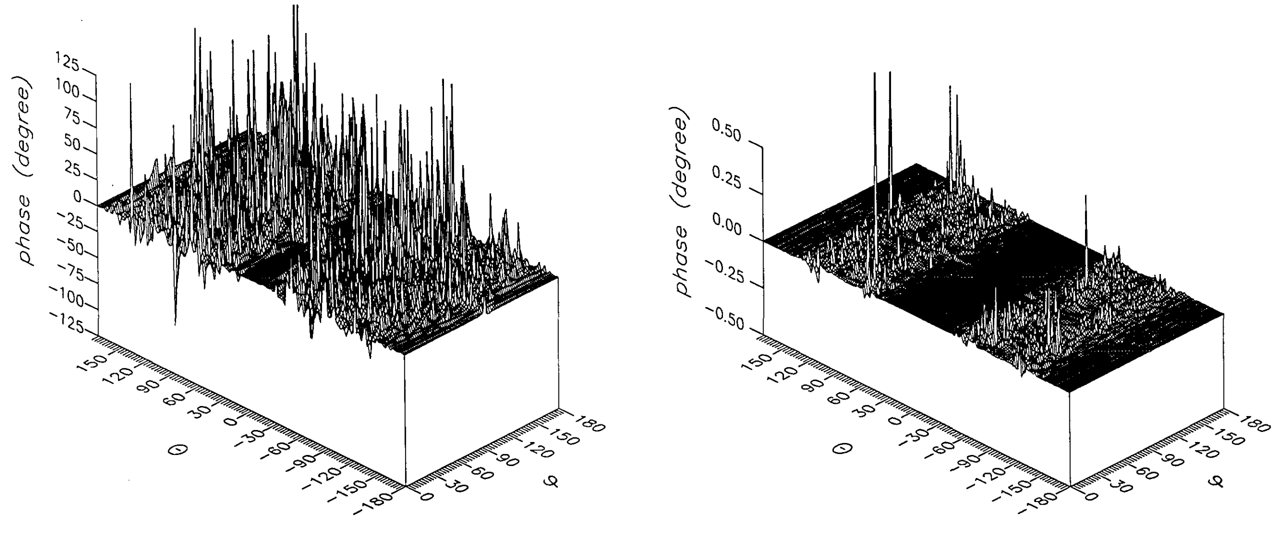

(a) (b)

Figure 26. The phase of the ϕ components of the ratios of (a) the error-contaminated and (b) the error-corrected far fields to the error-free far field in the case of errors in the ϕ coordinate.

5. References

[1] Muth, L. A., and Lewis, R. L., IEEE Trans. Ant. Prop. **38**, 1925 (1990).

[2] Muth, L. A., and Lewis, R. L., NIST Technical Note 1323, U.S. Department of Commerce (1988).

[3] Jackson, J. D., Classical Electrodynamics, John Wiley and Sons, Inc., New York (1975).

[4] Hansen, J. E., Spherical Near-Field Antenna Measurements, IEE Electromagnetic Waves Series 26, Peter Peregrinus Ltd., London, United Kingdom (1988).

[5] Edmonds, A. R., Angular Momentum in Quantum Mechanics, second edition (third printing, with corrections), Princeton University Press, Princeton, NJ (1974).

[6] Newell, A. C., IEEE Trans. Ant. Prop. **36**, 754 (1988).

[7] Muth, L. A., IEEE Trans. Ant. Prop. **36**, 581 (1988).

About the author: *Lorant A. Muth is a physicist in the Antenna Metrology Group of the Electromagnetic Fields Division, which is part of NIST Electronics and Electrical Engineering Laboratory.*

Volume 96, Number 4, July–August 1991
Journal of Research of the National Institute of Standards and Technology

[J. Res. Natl. Inst. Stand. Technol. **96**, 411 (1991)]

Data for Room Fire Model Comparisons

Volume 96 Number 4 July–August 1991

Richard D. Peacock, Sanford Davis, and Vytenis Babrauskas

National Institute of Standards and Technology,
Gaithersburg, MD 20899

With the development of models to predict fire growth and spread in buildings, there has been a concomitant evolution in the measurement and analysis of experimental data in real-scale fires. This report presents the types of analyses that can be used to examine large-scale room fire test data to prepare the data for comparison with zone-based fire models. Five sets of experimental data which can be used to test the limits of a typical two-zone fire model are detailed. A standard set of nomenclature describing the geometry of the building and the quantities measured in each experiment is presented. Availability of ancillary data (such as smaller-scale test results) is included. These descriptions, along with the data (available in computer-readable form) should allow comparisons between the experiment and model predictions. The base of experimental data ranges in complexity from one room tests with individual furniture items to a series of tests conducted in a multiple story hotel equipped with a zoned smoke control system.

Key words: accuracy assessment; data analysis; experiments; fire models; fire tests; instruments.

Accepted: April 11, 1991

Contents

Glossary

Δp	pressure difference (Pa)
σ	average specific extinction area (m^2/kg)
C	opening flow coefficient ($kg^{1/2}m^{1/2}K^{1/2}$). Typical values are 0.73 for outflow and 0.68 for inflow.
C_N	empirically determined value (typical value is 0.2)
E	net heat released by complete combustion per unit of oxygen consumed (kJ/kg of O_2). Typical values are 13100 KJ/kg for organics, 17600 kJ/kg for combustion of CO to CO_2.
g	gravitational constant (9.81 m/s^2)
h	height (m)
I	beam intensity
k	smoke extinction coefficient (m^{-1})
L	measurement path length for the smoke (m)
m	mass (kg)
$\dot{m}$	mass flow rate (kg/s)
M	molecular weight (kg/kmol). Typical value for air is 28.95 kg/kmol.
$\dot{q}$	rate of heat released from the fire room (kW)
p	pressure (Pa). Ambient value is 101325 Pa.
P	total smoke production (m^2)
R	universal gas constant (8314 J/kg mol K)
t	time (s)
T	gas temperature (K)
v	gas velocity (m/s)
$\dot{V}$	volume flow rate (m^3/s)
W	opening width (m)
X	measured concentration (mole fraction)

Subscripts used in nomenclature: ∞ – final value, a – air, b – bottom, CO – carbon monoxide, CO_2 – carbon dioxide, d – doorway, dry – dry air, e – exhaust duct, f – fuel, h – horizontal, H_2O – water, i – inside room, l – lower, max – maximum, N – at neutral plane or layer interface height, o – outside room or initial value, O_2 – oxygen, t – top, u – upper, v – vertical.

Superscripts used in nomenclature: o – ambient.

1. Introduction and Background

Analytical models for predicting fire behavior have been evolving within the fire research community for some years. Individuals have tried to describe in mathematical language the various phenomena which have been observed in fire growth and spread. These separate representations often describe only a small part of a fire experience. When combined, they create a complex computer code intended to give an estimate of expected behavior based upon given input parameters. These analytical models have progressed to the point of providing predictions of fire behavior. However, it is important to be able to state with confidence how close are the actual conditions to those predicted by the model.

The Building and Fire Research Laboratory (BFRL) has a program to develop a generic methodology for the evaluation and accuracy assessment of fire models. Our goal is to define a mechanism by which the model predictions can be assessed so that a model user can test the limits of the model predictions. A key aspect of this process is the availability of a sufficient quantity of experimental data with which to compare the performance of any given model. This report presents such a set of experimental data gathered from several sources which can be used to test the limits of a typical two-zone fire model. All of these data are available in computer readable form from the authors. The format of the data has been previously documented [1].

- The remainder of this section provides a *brief* historical perspective of room fire testing leading up to tests specifically designed for comparison with predictive computer models.

- Section 2 describes the process for assessing the accuracy of a predictive computer model. This report details one aspect of this process.

- Sections 3 and 4 present the types of analyses that can be used to examine large-scale room fire test data to prepare the data for comparison with zone-based fire models. Although not every technique was used for all data sets presented in this report, section 3 can be used for guidance in the design of future experiments. In addition, a rough guideline used to judge the quality of the data in each data set is described.

- In sections 5 to 9, five sets of experimental data are detailed. A standard set of nomenclature describing the geometry of the building and the quantities measured in each experiment is presented. Availability of ancillary data (such as smaller-scale test results) is included. These descriptions, along with the data should allow comparisons between the experiment and model predictions.

1.1 Early Developments in Room Fire Testing

Before the mid-1970s there was not much need to make experimental studies of the details of room fires. Room fire experiments were typically conducted as an adjunct to studying fire endurance [2,3]. For these experiments, it was necessary to track the average room temperature. This temperature was viewed as the prerequisite for determining the fire exposure of the room structure. Neither the heat release rate nor other aspects of the room fire, such as gas production rates, were of major interest. While as early as 1950, some investigators, conducting full-scale house burns, tried to study the gas production rates to determine how soon untenable environments might exist [4]. There was little incentive to pursue the topic quantitatively. Incentives came with the development of mathematical theories of room fires. Post flashover room fire theories were being developed throughout the 1950s, 1960s, and 1970s. The more detailed understanding necessary for the pre-flashover portion of room fires was becoming achievable by around 1975.

During the 1970s, however, empirical room fire tests were regularly being conducted at many fire research and testing facilities throughout the world. Instrumentation typically included a multiplicity of thermocouples; several probes where gas samples were extracted; smoke meters, typically located at several heights along an open burn room doorway; heat flux meters located in the walls of the burn room; and, possibly, a load platform. The load platform might register the weight of a single burning item, but was of little use when fully-furnished rooms were tested.

Despite the basic role of heat release rate in the room fire, there was no technique available to measure it. Since neither the burning item's mass loss rate nor the air and gas flows could, in most instances, be determined, the measurements of gas and smoke concentrations at isolated measuring stations were not of much use in tracking species evolution rates.

Even before the era of heat-release-rate focused studies could begin, there were at least three series of notably thorough room fire experiments. Two were conducted at Factory Mutual Research Corporation (FMRC), while a third one was at NBS (former name of NIST). The first series at FMRC [5–7] served as a basis for the Harvard Computer Fire Code. Three replicate full-scale bedroom fire tests, in which the fire grew from a small ignition in the middle of a polyurethane mattress to flashover, were studied in enough detail to define the fire as a series of loosely coupled events. As the components of the fire became better understood, a model of the entire fire growth process as a series of quantitative calculations was developed [8]. To make these tests most useful for a scientific study of fire, several hundred measurements of temperature, radiation level, gas composition, gas velocity, and weight loss were made. The mechanism of fire spread from the initial burning mattress to other room furnishings, estimates of the flow of the gases through room openings, and estimates of the energy balance of the system were all quantified. A second series of tests at FMRC [9] used a simpler test configuration—single slabs of polyurethane foam in the room, instead of fully-furnished bedrooms. A similarly fundamental series of experiments was also conducted at NBS by Quintiere and McCaffrey [10], who examined wood and polyurethane foam cribs burning in well-instrumented rooms. The largest distinction between these tests and earlier test series was the carefully defined purpose to understand the underlying principles of fire growth to be able to predict the progress of a fire in a generic building.

1.2 Measurement of Heat Release Rate in Room Fires

The first attempt to develop a technique for measuring rate of heat release in room fires was in 1978, by Fitzgerald, at Monsanto Chemical [11]. He constructed a small room (2.7 m cube) instrumented with a large number of thermocouples, located in the gas space, on the walls, and in the exhaust duct (fig. 1). The room had a forced air supply of 0.19 m^3/s, from a small 0.15 m square supply duct (later raised to 0.26 m^3/s [12]), with another duct used to exhaust the combustion products. The room was also equipped with a load cell and a port for extracting gas samples. Fitzgerald realized that a simple measurement of temperatures in the exhaust duct would not be enough to determine the heat release rate. Instead, he developed a purely statistical method—a correlation was sought between contributions from the various temperature measurements to the heat release rate. The stated capacity was 140 kW, which would not now be considered to be full-scale. This system has been sporadically in use at the Southwest Research Institute in San Antonio, Texas. The approach, however, has not been pursued by any other laboratories due to its empirical nature, its limited heat handling capacity, and to concerns about errors due to varying radiative fractions.

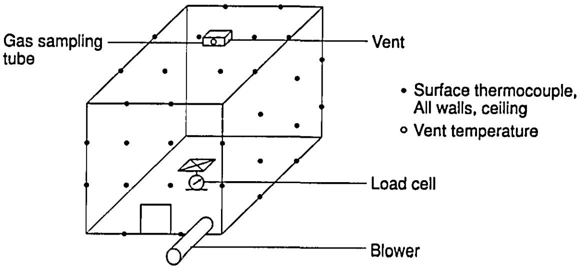

Figure 1. The Monsanto room calorimeter.

A sensible-enthalpy calorimeter, such as the Monsanto one, was not judged by the profession to be adequate for the needs. Instead, it was necessary to await the development of two measurement techniques: a robust instrument for measuring the flow rates of air and gas in a soot-laden environment; and a heat release measurement which did not depend on direct measurement of heat flow in inevitably loss-prone systems. The first was developed by Heskestad at FMRC in 1974. Conventional velocity measurement devices are normally precluded from use in fire applications due to several problems. These include clogging of small orifices (an issue with pitot/static probes) and the inability to calibrate properly for high temperature use (hot wire or disc anemometers). The new "bi-directional velocity probe" (fig. 2) solved these problems of measuring air flow rates in rooms, in corridors, and in smoke extraction systems.

By far, the most important development which was needed, however, was the principle of oxygen consumption. As early as 1917, Thornton [14] showed that for many organic fuels, a reasonably constant net amount of heat is released per unit of oxygen consumed for complete combustion. The principles have been covered in detail by Huggett [15] and Parker [16]. The application of this principle to room fires revolutionized the field. Before that, the focus was on point measurements. It is adequate to use measurements of temperatures and other quantities at individual locations in a room as a means of verifying a model if a near-ideal model is already available. Such point mea-

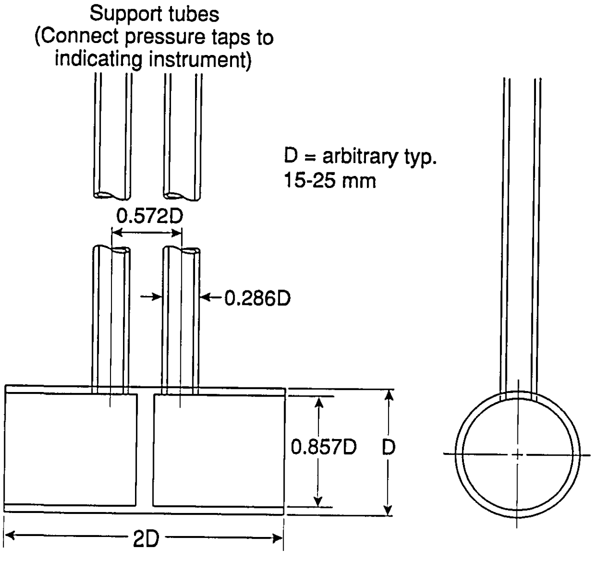

Figure 2. Bi-directional velocity probe.

surements, however, were of limited use in developing and extending the models. With the availability of oxygen consumption-based rate of heat release measurements, for the first time quantitative descriptions of fire output could be made.

1.3 Standard Room Fire Tests

During the late 1970s and early 1980s several laboratories agreed to develop a standardized method for measuring heat release rates in rooms, based on oxygen consumption. Unlike the Monsanto test, the concern here was in measuring the burning rate of combustible room linings (i.e., wall, ceiling, or floor coverings), and not furniture or other free-standing combustibles. The original development was at the University of California by Fisher and Williamson [17]. Later, extensive development also was done at the laboratories of the Weyerhaeuser Co., and at NBS [18]. The method, in its simplest form, consisted primarily of adding oxygen consumption measurements into the exhaust system attached to a room very similar to that originally used by Castino and coworkers at Underwriters Laboratories [19]. However, they did not measure heat release rates at all. The room was 2.4×3.7×2.4 m high, with a single doorway opening in one wall, 0.76×2.03 m high (fig. 3). The original studies at the University of California led to ASTM issuing in 1977 a Standard Guide for Room Fire Experiments [20]. The Guide did not contain prescriptive details on room size, ignition source, etc., but was simply a guide to good practice in designing room fire tests. ASTM then developed an actual prescriptive test method for room fire tests and published it as a "Proposed method" in 1982 [21]. The 1982 document mandated the abovementioned room size and also a standard ignition

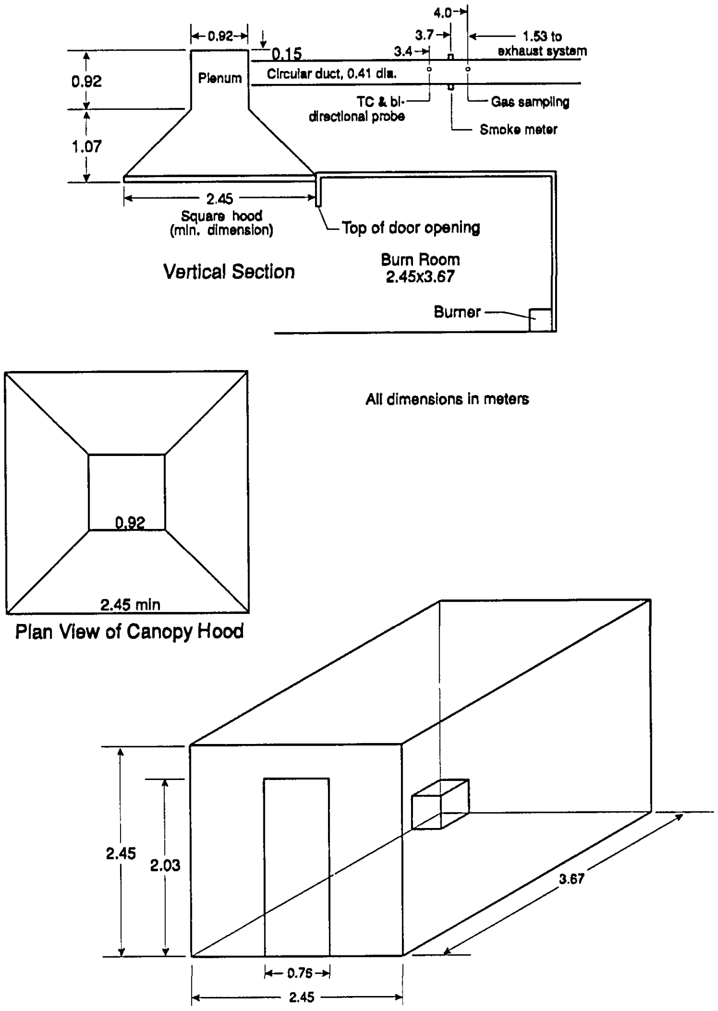

Figure 3. The original (1982) ASTM proposed room fire test.

source, which was a gas burner, placed in a rear corner of the room, giving an output of 176 kW. Since the development work at the University of California uncovered problems with a natural convection exhaust system, the actual test specification entailed a requirement to "establish an initial volumetric flow rate of 0.47 m^3/s through the duct if a forced ventilation system is used, and increase the volume flow rate through the duct to 2.36 m^3/s when the oxygen content falls below 14 percent." This specification required a complex exhaust arrangement, and it is not clear that there were many laboratories prepared to meet it. The proposed method was thus withdrawn by ASTM. However, variants of this method continue to be used by several laboratories [22].

Following ASTMs disengagement, development of a standard room fire test was accelerated in the Nordic countries, operating under the auspices of the NORDTEST organization. Development was principally pursued in Sweden, at the Statens Provningsanstalt by Sundström [23]. The NORDTEST method [24,25], as eventually published in 1986, uses a room of essentially the ASTM dimensions, 2.4 × 3.6 × 2.4 m high, with an 0.8 × 2.0 m doorway opening (fig. 4). The exhaust

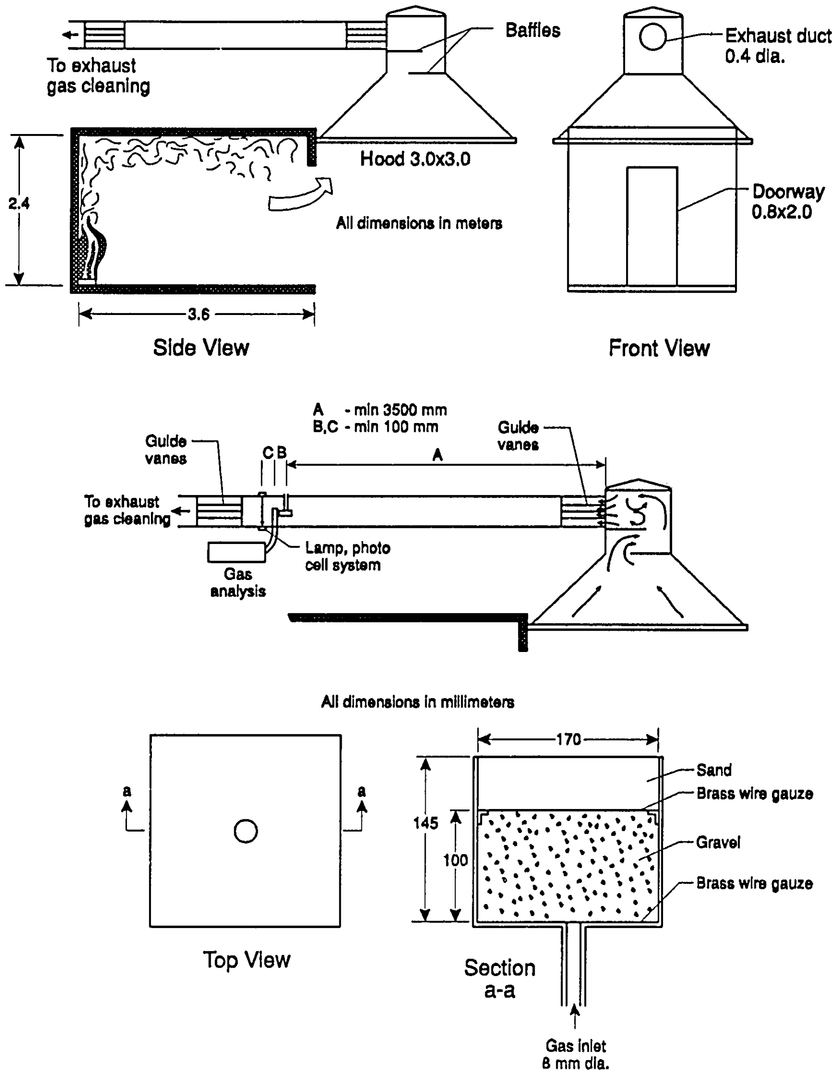

Figure 4. The NORDTEST room fire test.

system flow capability was raised to 4.0 kg/s, with the capability to go down to 0.5 kg/s to increase the resolution during the early part of the test.

A special concern in the Nordic countries has been the effect of the igniting burner. A parallel project at the Valtion Teknillinen Tutkimuskeskus (VTT) in Espoo, Finland by Ahonen and coworkers [26] developed data on three burner sizes and three burner outputs. The three burners had top surface sizes of 170×170 mm, 305×305 mm, and 500×500 mm. The energy release rates were 40, 160, and 300 kW, respectively. VTTs reported results were on chipboard room linings. They found no significant differences at all among the burner sizes. The burner output did, of course, make a difference; however, the difference between 40 and 160 kW was much larger than between 160 and 300 kW. The VTT conclusion was that either the 160 or the 300 kW level was acceptable. The NORDTEST method itself has taken an ignition source to be at the 100 kW level. If no ignition is achieved in 10 minutes, the heat output is then raised to 300 kW.

ISO (International Organization for Standardization) has adopted the NORDTEST room fire test and is finalizing the standard [27].

1.4 Room Fire Tests for Modeling Comparisons

Several systematic test series have been undertaken specifically to provide data for comparison with model predictions. In other cases, tests in which fire properties have been systematically varied (for various reasons) have been modeled using current computer fire simulations. In the first category are the study of Alpert et al. [28] for a single room connected to a short, open corridor, and that of Cooper et al. [29] or Peacock et al. [30] for gas burner fires in a room-corridor-room configuration. The second category is large, but the works of Quintiere and McCaffrey [10], and Heskestad and Hill [31] are particularly detailed.

Cooper et al. [29] report on an experimental study of the dynamics of smoke filling in realistic, full-scale, multi-room fire scenarios. A major goal of the study was to generate an experimental data base for use in the verification of mathematical fire simulation models. The test space involved 2 or 3 rooms, connected by open doorways. During the study, the areas were partitioned to yield four different configurations. One of the rooms was a burn room containing a methane burner which produced either a constant energy release rate of 25, 100, or 225 kW or a time-varying heat release rate which increased linearly with time from zero at ignition to 300 kW in 600 s. An artificial smoke source near the ceiling of the burn room provided a means for visualizing the descent of the hot layer and the dynamics of the smoke filling process in the various spaces. The development of the hot stratified layers in the various spaces was monitored by vertical arrays of thermocouples and photometers. A layer interface was identified and its position as a function of time was determined. An analysis and discussion of the results including layer interface position, temperature, and doorway pressure differentials is presented. These data were later used by Rockett et al. [32,33] for comparison to a modern predictive fire model.

Quintiere and McCaffrey [10] describe a series of experiments designed to provide a measure of the behavior of cellular plastics in burning conditions related to real life. They experimentally determined the effects of fire size, fuel type, and natural ventilation conditions on the resulting room fire variables, such as temperature, radiant heat flux to room surfaces, burning rate, and air flow rate. This was accomplished by burning up to four cribs made of sugar pine or of a rigid polyurethane foam to provide a range of fire sizes intended to simulate fires representative of small furnishings to chairs of moderate size. Although few replicates were included in the test series, fuel type and quantity, and the room door opening width were varied. The data from these experiments were analyzed in terms of quantities averaged over the peak burning period to yield the conditions for flashover in terms of fuel type, fuel amount, and doorway width. The data collected were to serve as a basis for assessing the accuracy of a mathematical model of fire growth from burning cribs.

Heskestad and Hill [31] performed a series of 60 fire tests in a room/corridor configuration to establish accuracy assessment data for theoretical fire models of multi-room fire situations with particular emphasis on health care facilities. With steady state and growing fires from 56 kW to 2 MW, measurements of gas temperatures, ceiling temperatures, smoke optical densities, concentrations of CO, CO_2, and O_2, gas velocities, and pressure differentials were made. Various combinations of fire size, door opening size, window opening size, and ventilation were studied. In order to increase the number of combinations, only a few replicates of several of the individual test configurations were performed.

2. Assessing the Accuracy of Room Fire Models

In essence, every experiment is an attempt to verify a model. In the simplest case, the model is a hypothesis which is based on some observed phenomenon—or even a single observation—and raises the question "why?" The hypothesis then needs to be tested to determine whether the observation is repeatable and to help define the boundaries of the validity of the hypothesis. In as simple a case as presented here, a yes or no answer may suffice to test the agreement between the model and experiment. For more complex models, the question is not does the model agree with experiment, but rather how close does the model come to the experiment over time. A quantification of the degree of agreement between a model and perhaps many experiments is the subject of the model accuracy assessment process. Quantification is made complicated by the transient nature of fires. Not only must a model be accurate at any point in time, but also have verisimilitude with the rate of change.

2.1 Documentation of the Model

For an analytical model designed for predicting fire behavior, the process of accuracy assessment is similar to the single observation case above, but perhaps more extensive because of the complexity of the model. The first step in the process is thorough documentation of the model so other modelers can use it and so its testing can be properly designed. The basic structure of the model, including the limitations, boundary conditions, and fundamental assumptions must be clearly described. Additionally, the functional form of the input parameters must be well-defined to allow any experiments carried out in the accuracy assessment process to be properly simulated (what are the inputs; what are the appropriate units for each). The same applies to the model outputs. In this way, the format of the experimental input and output can be defined to match that of the model.

2.2 Sensitivity Analysis

The sensitivity analysis of a model is a quantitative study of how changes in the model parameters affect the results generated by the model. The parameters through which the model is studied consist of those variables which are external to the program, (i.e., input variables), those variables which are internal to the program, (i.e., encoded in the program), and the assumptions, logic, structure, and computational procedures of the model. For this discussion, the model will be considered to be defined by its assumptions, logic, structure, and computational procedures and its sensitivity will be measured in terms of its external and internal variables. The key questions of interest to be investigated by the analyst are: 1) what are the dominant variables? 2) what is the possible range of the result for a given input that may arise from uncertainties within the model? and 3) for a given range of an input variable, what is the expected range for the result?

Sensitivity analysis of a model is not a simple task. Fire models typically have numerous input parameters and generate numerous output responses which extend over the simulation time. So multiple output variables must each be examined over numerous points in time. To examine such a model, many (likely to be more than 100) computer runs of the model must be made and analyzed. Thus, if the model is expensive to run or if time is limited, a full analysis is not feasible and the set of variables selected for study must be reduced. When the set of variables to be investigated must be reduced, a "pre-analysis" for the important variables can be performed or the important variables can be selected by experienced practitioners.

Classical sensitivity analysis examines the partial derivatives of the underlying equations behind a model with respect to its variables in some local region of interest. A complex model may be sensitive to changes in a variable in one region while insensitive in another region. In addition, it is most likely to be unfeasible to determine the intervals for each variable for which a complex model is sensitive. This suggests that stating a single value as a measure of sensitivity is not always sufficient and, consequently, some measure of its variability should be determined to make a global statement of how sensitive a model is to a variable.

Several methods for estimating the sensitivity of a model to its variables are available, each with its advantages and disadvantages. The choice of method is often dependent upon the resources available and the model being analyzed. It is beyond the scope of this paper to go into the details of any of these.

2.3 The Experimental Phase

Once an assessment has been made of the relative importance of the model parameters, a selection process is carried out to determine which parameters will be studied in the experimental phase of the accuracy assessment process. Typically, with a fixed budget for model testing, trade-offs are made in the selection of the number and range of variables to be studied, replication of the experiments, and complexity of the experiments to be performed. Elements of a well-designed experimental program, discussed below, address these trade-offs so the model assessment can be carried out with the available resources.

The number of possible tests, while not being infinite, is large. It is unreasonable to expect all possible tests to be conducted. The need exists to use reason and some form of experimental design strategy to optimize the range of results while minimizing the number of tests. While this is not the forum for a detailed discussion of experimental design, some elaboration is required. Traditionally, a latin-square arrangement or full factorial experimental design is employed to determine the effect of variations in input conditions on output results [35]. This, as expected, results in the number of tests increasing with the number of input variables and variations. However, there exists a reduced factorial experimental plan [36] called fractional replication. The basic concept behind fractional replication is to choose a subgroup of experiments from all possible combinations such that the chosen experiments are representative, amenable to analysis, and provide the maximum amount of information about the model from the number of observations available.

The choice of data to be collected during the experimental phase depends upon the model under evaluation. A description of the input and output data of the model directs the selection of the measurements to be made. The evaluator or test engineer must constrain the range of test conditions to those which apply to the fire model. The test design then includes a varied and representative set of conditions (i.e., enclosure configuration, fuel loading, fuel type, ignition mechanism) from this range.

The evaluator develops the instrumentation design by starting with the model output data and determining suitable algorithms for generating comparable data output from the large-scale tests. This defines the instrumentation requirements, and experience is used to define instrument placement. Unfortunately, any experimental design will include only a fraction of the range of conditions for all the input variables of a complex fire model. The choice of test conditions and instrumentation will, to a large extent, determine the quality and completeness of the accuracy assessment of the chosen model.

2.4 Review and Analysis of the Model and Experimental Data

Large-scale tests are performed according to the experimental plan designed by the evaluator. The individual data instrumentation, of which there may be one to two hundred, have to be carefully installed, calibrated, and documented (what they measure and where they are located). Since it is rare to find an individual raw data observation that can be compared to the model output, single data elements are combined to provide derived data which can be compared to the model. Using data collection techniques appropriate to the testing needs, the individual data points are collected and typically processed by computer to provide the desired outputs.

Expected and unexpected uncertainties will define the level of replication necessary for each set of test conditions [37]. There are many sources that can contribute to expected variation in large-scale fire tests, such as variations in the materials or assemblies to be tested, environmental conditions, instruments or apparatus, and calibration techniques used in the measuring process. Because of the nonuniformity of building materials normally encountered and the variability associated with fire exposures and combustion reactions, excellent repeatability is not expected. The development of an experimental plan is, to a large extent, the search for the major factors influencing the outcome of the measurements and the setting of tolerances for their variations [38]. Within the constraints of a fixed budget, replication is usually limited to less than that statistically desired to minimize the unexpected variations. The larger variations that result must be accepted and thus affect the level of confidence in the resulting model accuracy assessment.

As part of the data analysis of the large-scale tests, potential error sources must be quantitatively determined. There are recognized uncertainties in the instrumentation used for each data element as well as random and systematic "noise" in the data acquisition process. The unevenness of burning of a material or the turbulent nature of fluid motion in most fire situations also introduce "noise" into the data analysis process and erratic burning does so among replicate tests. Each step in the data reduction process contributes to the accumulated uncertainties.

Data analysis itself requires the development of a series of algorithms that combine individual data elements to produce the desired output parameter [39]. As can be seen from this short discussion, data analysis of the large-scale tests requires a significant effort before comparisons between the model and the large-scale tests are possible. The size of the data reduction program can be as large and complex as the model being evaluated.

3. Analyses Used for the Data

For most large-scale room fire tests, instrumentation is characterized by a multiplicity of thermocouples; several probes where gas samples are extracted; smoke meters, typically located at several heights along doorways or in rooms; heat flux meters located in the walls of the burn room; and, possibly, a load platform. Although certainly useful for evaluation the burning behavior of the specific materials studied, variables representing key physical phenomena are required for comparison with predictive room fire models. Some typical variables of interest from large-scale tests are:

• heat release rate (of fire, through vents, etc.)	(W)
• interface height	(m)
• layer temperatures	(°C)
• wall temperatures (inside and out)	(°C)
• gas concentrations	(ppm or %)
• species yields	(kg/kg)
• pressure in room	(Pa)
• mass flow rate	(kg/s)
• radiation to the floor	(W/m^2)
• mass loss	(kg)
• mass loss rate	(kg/s)
• heat of combustion	(J/kg)

To obtain these variables, a significant amount of analysis of a large-scale fire test is required. This data analysis requires the development of a series of algorithms that combine individual data elements to produce the desired output parameter. Breese and Peacock [1] have prepared a specially designed computer program for the reduction of full-scale fire test data. In addition to easing the burden of repetitive and similar calculations, the program provides a standard set of algorithms for the analysis of fire test data based upon published research results and a standard form for detailing the calculations to be performed and for examining the results of the calculations. The program combines automated instrument calibrations with more complex, fire-specific calculations such as

- smoke and gas analysis,
- layer temperature and interface position,
- mass loss and flows, and
- rate of heat release.

A description of these algorithms applicable to the analysis of large-scale fire test data is presented below along with an example of each of the algorithms. Although not every one of the techniques was applied to every test (individual measurements available for analysis varied from test to test), many of the techniques were applied to most of the data sets. Details of those applied to an individual data set are available in the sections describing the data sets in sections 5 to 9.

3.1 Smoke and Gas Analysis

In the recent past, optical smoke measurements in room fires have been made in several ways:

- vertical or horizontal beams within the room [40],
- vertical or horizontal beams in the doorway [41],
- vertical or horizontal beams in the corridor [42], and
- a diagonal, 45° beam across the doorway plume [43].

The actual measurement is typically made with a collimated light source and directly opposed photometer receiver. This provides a measure of the percentage of the light output by the source that reaches the photometer, and is typically expressed as an extinction coefficient, k, as follows:

$$k=\ln\left(\frac{I_0}{I}\right). \qquad (1)$$

Bukowski [44] has published a recommended practice for a widely-used design of photometer using an incandescent lamp source. Newer designs [45] are available, however, based on a laser source and are therefore, free of certain measurement errors [46].

Smoke measurements have been reported in a multitude of ways. Many reporting variables suffer from the drawback that the values depend as much on geometric or flow details of the apparatus, as they are on properties of the combustible being burned. Thus, it was important to arrive at a set of variables from which the apparatus influence is removed. There are two such variables. The first is the total smoke *production* for the duration of the test, P (m^2). This variable can be visualized as the area of obscuration that would be caused by the smoke produced in the experiment. The second normalizes the production by the specimen mass loss during burning to form the *yield* of smoke per kg of specimen mass lost (m^2/kg) [47]. The latter has come to be called the *specific extinction area*, σ_f. None of the measurement geometries mentioned above, however, are at all useful in characterizing these variables. Such information can be obtained by providing a photometer in the exhaust collection system [48], as, for instance, is done with the ISO/NORDTEST standard (fig. 4). Although such smoke data are sparse, encouraging progress is being made [49].

The specific extinction area is the true measure of the smoke-producing tendency of a material which can be described on a per-mass basis, for instance, wall covering materials. If a fully-furnished room is being tested, or some other configuration is examined where mass loss records are not available, then the smoke production serves to characterize the results.

The total smoke production is computed as

$$P = \int k\dot{V}\,\mathrm{d}t, \tag{2}$$

where $\dot{V}$ is the *actual* volume flow at the smoke measuring location.

The average specific extinction area is then computed as

$$\sigma_f = \frac{P}{m_0 - m_\infty}. \tag{3}$$

One of primary applications of the yield is in comparing results on the same material conducted in different test apparatus or geometries. Since the effects of specimen size, flow, etc., have been normalized out in this expression, the variable permits actual material properties to be compared.

In some cases, it is also of interest to derive the instantaneous, time-varying expression for σ_f. Its definition is analogous the one given in eq (3).

Gas measurements in the 1970s were typically made by installing probes for CO, CO$_2$, etc., analyzers in several places in the room or in the doorway. Data from such measurements had the same limitations as point measurements of temperature: only the behavior at one point was characterized, and no measurement of total fire output was available. Once measurement systems, such as the ISO/NORDTEST room fire test have been adopted which collect all of the combustion products in an exhaust hood, it became a simple manner to instrument that exhaust system for combustion gases.

Old data for gas measurements are typically reported as ppm's of a particular gas. Similar as to smoke, such measurements depend strongly on the test environment and are not very useful for describing the fuel itself. The appropriate units are very similar to those for smoke. The *production* of a particular gas is simply the total kg of that gas which flowed through the exhaust duct for the duration of the entire test. The *yield* of a particular gas (kg/kg) is the production divided by the total specimen mass lost. As for smoke, there may be scale effects applicable to a particular gas; the yield of a given gas might be expected to be similar for various apparatus and experiments where the specimen was burned under similar combustion conditions [50].

3.2 Layer Interface and Temperature

Cooper et al. [29] have presented a method for defining the height of the interface between the relatively hot upper layer and cooler lower layer induced by a fire. Since the calculation depends upon a continuous temperature profile, and a limited number of point-wise measurements are practical, linear interpolation is used to determine temperatures between measured points. The equivalent two zone layer height is the height where the measured air temperature is equal to the temperature T_N and is determined by comparison of T_N with the measured temperature profile:

$$T_N = C_N(T_{\max} - T_b) + T_b. \tag{4}$$

Once the location of the interface has been determined, it is a simple matter to determine an average temperature of the hot and cold layers within the rooms as:

$$\begin{aligned} T_u &= \int_{h_N}^{h_t} \frac{T(h)}{h_t - h_N}\,\mathrm{d}h; \\ T_l &= \int_{h_b}^{h_N} \frac{T(h)}{h_N - h_b}\,\mathrm{d}h. \end{aligned} \tag{5}$$

With a discrete vertical profile of temperatures at a given location, the integral can be evaluated numerically. The average layer temperature (either of the lower layer or the upper layer), T_{avg}, is thus simply an average over the height of the layer from the lower bound, z_l, to the upper bound, z_u, for either the upper or lower layers. Figure 5 shows the results of such a calculation of layer height and layer temperature for a set of eight replicate experiments [51]. Although systematic errors are apparent in the data (two distinct subsets of the data are apparent which may relate to seasonal temperature variations over the testing period) and the limitations inherent in two-zone fire models are equally applicable to these layer height and temperature calculations, the reproducibility of the calculation is good. For a series of large-scale test measurements in a multiple room facility, the uncertainty between 95 percent confidence limits averaged under 16 percent [51].

While the in-room smoke measurement schemes are not useful in quantifying the smoke production or yield, they can be used to deduce the location of the interface in a buoyantly stratified compartment [52]. In this method, if a two zone model is assumed (a smoke-filled upper zone and a clear lower zone), the use of a paired vertical (floor to ceiling) smoke meter and horizontal (near the ceiling) smoke meter can be used to determine the smoke layer thickness. If the smoke layer is homogeneous, $k_v/L_v = k_h/L_h$, then the height of the smoke layer L_v can be given as a simple ratio,

$$L_v = h_t - \left(\frac{\ln(I_0/I_v)}{\ln(I_0/I_h)}\right)L_h. \qquad (6)$$

where the subscripts v and h refer to the vertical and horizontal measurements.

Figure 6 presents a comparison of the smoke layer height calculated from smoke measurements and from temperature measurements for one series of tests [51]. Within experimental uncertainty, the two methods may be equivalent. However, small systematic differences exist. First, the smoke measurement estimates are typically higher than the temperature based calculations. This is consistent with the observations of others, notably Zukoski and Kubota [53], who measured temperature profiles in detail in a scale "room" measuring 0.58 m square with a doorway in one wall measuring 0.43×0.18 m. A smoke tracer was used to allow visual observation of the smoke layer thickness along with the temperature profile measurements. They concluded that, since the lower boundary layer is not steady and there are distinct gravity waves along the boundary, the smoke measurements produce a less steep boundary than would be measured from instantaneous profiles at a given instant of time. For tests where the interface height

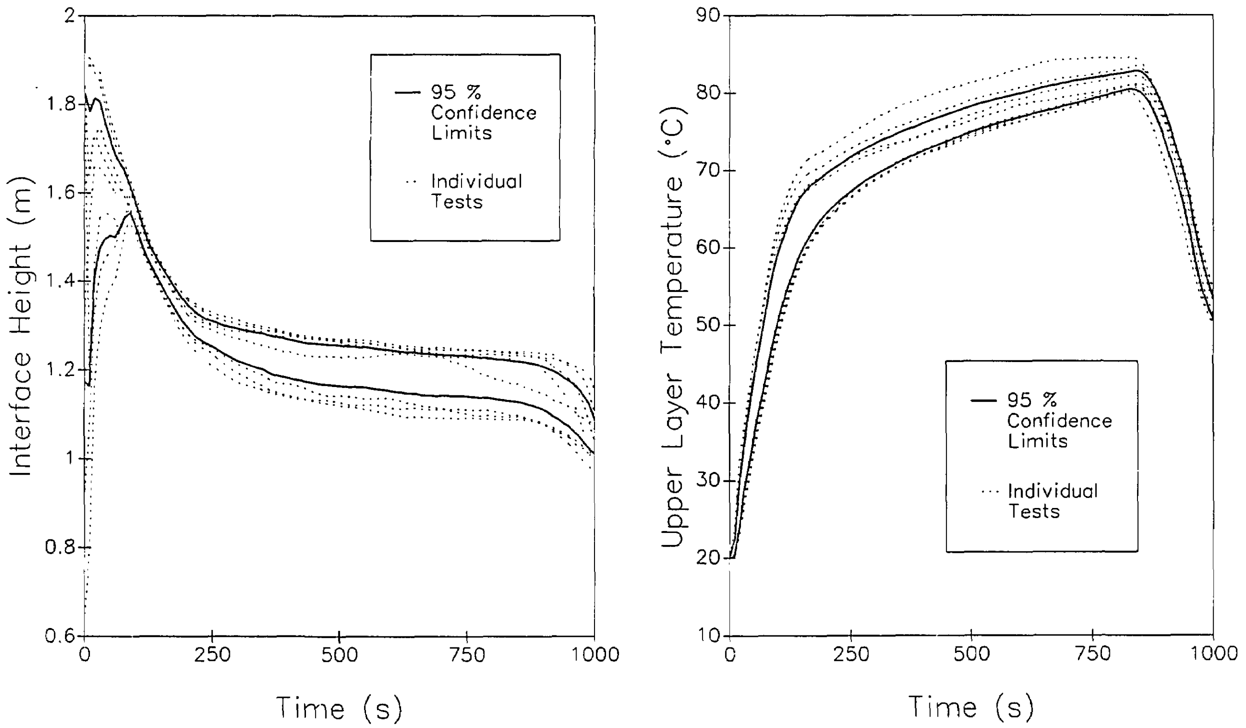

Figure 5. An example of layer interface position and layer temperature calculated from temperature profiles measured during several tests along with estimated repeatability of the measurement [51].

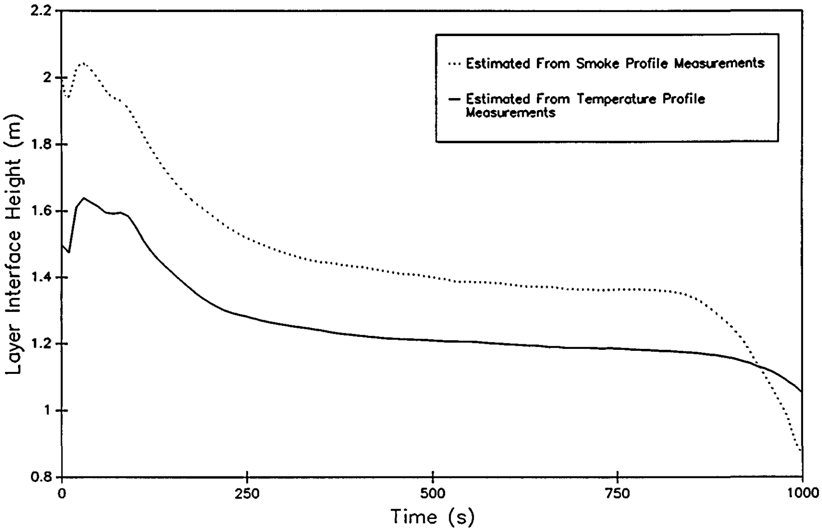

Figure 6. A comparison of hot/cold layer interface position estimated from temperature profiles and from smoke obscuration in one test series (an average of 9 individual tests) [51].

reaches the floor, the temperature based method falters since it is based upon interpolation between adjacent measurement points. Without extensive instrumentation near the floor, a bottom limit at the level of the lowest thermocouple is evident in the temperature-based calculations. However, with the typically higher uncertainty of the smoke-based measurements, the significance of any perceived difference between the two different techniques must be questioned.

3.3 Mass Flows

Computation of mass flows through openings can be accomplished through a knowledge of the velocity profile in the opening [54,55]:

$$\dot{m}_u = C \int_{h_N}^{h_t} \rho v W \, dh; \qquad \dot{m}_l = C \int_{h_b}^{h_N} \rho v W \, dh. \tag{7}$$

The velocity profile can be determined in a number of ways. In some experiments, the bi-directional velocity probes described earlier can be used to directly measure velocity in a room doorway. This is usually done by locating 6 to 12 such probes vertically along the centerline of the doorway. Mass flow rates can be computed by eq (7) and can give adequate results for steady-state fires, especially if the opening is much taller than its breadth [56]. Use of such a straightforward technique in non-steady state fires, and especially when the opening is broader than tall, has been shown to give nonsensical results [57]. Lee [56] exploits this method to calculate the mass flow using the pressure drop across the doorway to calculate the velocity. Since the pressure drop across an opening passes through zero as the flow changes direction at the height of the neutral plane, measurement of the pressure profile in a doorway is particularly difficult. Estimation of the pressure in the extreme lower resolution of the instrumentation (as the pressure drop approaches zero) yields an inherently noisy measurement. As such, these measurements are used only as an alternate to the temperature method, to provide an assessment of the consistency of the data collected. As an alternative measurement technique combined with dramatically higher instrumentation costs (several orders of magnitude higher than the temperature measurements), a less detailed profile of measurement points can be used for the pressure profile.

Steckler, Quintiere, and Rinkinen [58] use an integral function of the temperature profile within the opening to calculate the mass flow. Casting their equations in a form that can be used directly to calculate the velocity profile for use in eq (7) yields:

$$v_h = \sqrt{2g}\, T_d \int_{h_N}^{h} \left(\frac{1}{T_i} - \frac{1}{T_0}\right) dh. \tag{8}$$

The temperature profile may also be used with a single pressure measurement to determine the neutral plane height, h_N, required in eq (8). The neutral plane is obtained by solving for h_N in eq (9) [56]:

$$\Delta p_b + \frac{M_a p_a g}{R} \int_{h_b}^{h_N} \left(\frac{1}{T_0} - \frac{1}{T_i}\right) dh = 0. \tag{9}$$

Figure 7 shows the results of such a mass flow calculation for a set of eight replicate experiments. For the same set of experiments, the reproducibility of the mass flow calculation is lower than the layer height and temperature calculations, averaging 35 percent [51]. The reasons for this are at least two-fold. The technique used, as described by Steckler et al. [58] was developed for a single room exhausting into an infinite reservoir of ambient air. An extension of the technique for flow between rooms is available [59]. Since the technique depends upon the temperature gradient across the opening as a function of height, the choice of temperature conditions "outside" the opening may be important. Finally, the technique utilizes temperature changes from the neutral plane to the edges of the opening to calculate the flow. Because the smaller temperature change from the neutral plane is in the lower, cooler region, a small variation in temperature should cause more uncertainty in mass flow than in the upper, hotter region where the temperature gradient is larger.

Figure 8 shows a comparison of the mass flow through a typical doorway calculated from pressure measurements, from temperature measurements, and from velocity measurements made in the doorway for a large-scale room fire test [60]. Comparing the mass flow calculations, it is apparent that the temperature based calculations result in a slightly lower calculated mass flow into a room and correspondingly higher mass flow out of a room than for the pressure-based calculations. This is consistent with the difference in calculated neutral plane height for the two methods. As previously discussed, measurement of flows using commercially available pressure transducers is difficult due to the extremely low pressures involved. Compounding the problem for the measurement of the neutral plane height is the desire to know where the flow changes direction. Thus, the most important measurement points are those with the smallest magnitude, just on either side of the neutral plane. Since the neutral plane calculation from pressure measurements searches for the point of zero pressure from the floor up, the calculated point of zero pressure is consistently low.

The potential for multiple neutral planes within an opening further complicates the measurement of flow with pressure-based measurements. Jones and Bodart [61] have described an improved fluid transport model with up to three neutral planes within a single opening to incorporate in predictive models (see fig. 9). With potentially different layer boundaries in the two rooms connected to the opening, cross flows are possible between the layers, leading to flow reversals depending upon the relative positions of the two layer boundaries.

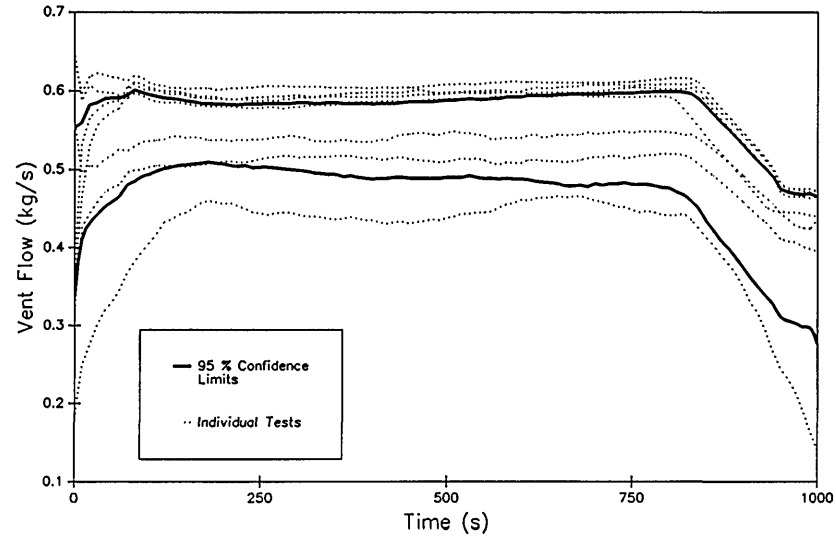

Figure 7. An example of mass flow calculated from temperature profiles measured during several tests along with estimated repeatability of the measurement [51].

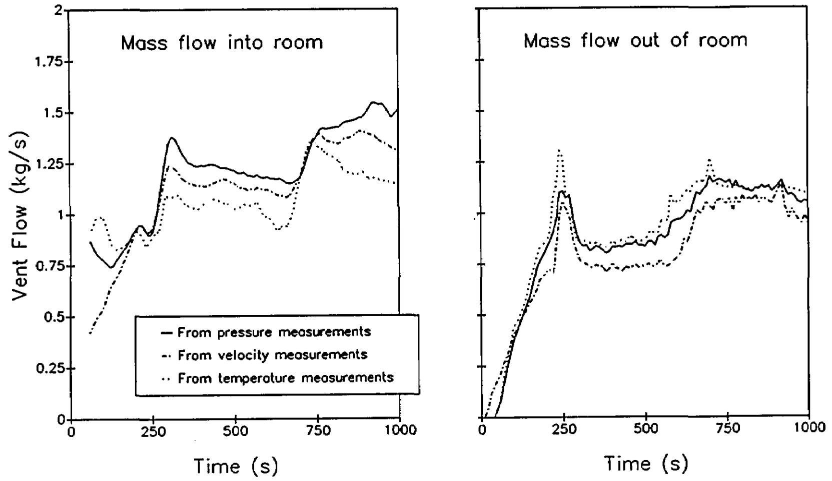

Figure 8. A comparison of calculated mass flow based upon temperature, pressure, and velocity profiles measured during a large-scale fire test [60].

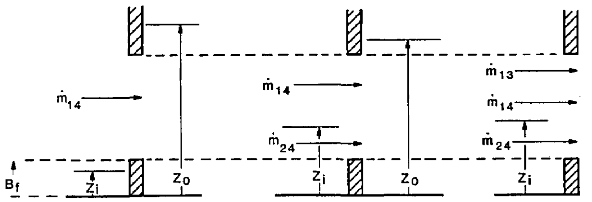

Figure 9. Flow possibilities in a single vent connected to two rooms with different layer boundaries in the rooms [61].

Temperature based measurements have far less dependency on the low flow region of the opening, relying on only one pressure measurement near the bottom (or top) of the opening where the pressure gradient is highest. Thus, for the determination of neutral plane height, the temperature based measurement technique seems preferable.

3.4 Rate of Heat Release

The large-scale measurement which has benefited the most from the emergence of science in large-scale fire testing is the measurement of the rate of heat released by a fire. With few exceptions [62,63], this is calculated by the use of the oxygen consumption principle. If all the exhaust from a room fire test is collected, measurement of temperature, velocity, and oxygen, carbon dioxide, carbon monoxide, and water vapor concentrations in the exhaust collection hood can be used to estimate the rate of energy production of the fire. With these measurements, the total rate of heat release from the room can be determined from [16]:

$$\dot{q} = \left(E\phi - (E_{CO} - E)\frac{1-\phi}{2}\frac{X_{CO}}{X_{O_2}}\right)\frac{M_{O_2}}{M_a}\dot{m}_a$$

$$(1 - X_{H_2O})X^{o}_{O_2}, \qquad (10)$$

where

$$M_e = (1 - X_{H_2O})(X_{O_2} + 4X_{CO_2} + 2.5)4 + 18; \qquad (11)$$

$$\dot{m}_e = C\sqrt{\frac{M_{dry}\Delta p}{M_e T_e}}; \qquad (12)$$

$$\frac{\dot{m}_a}{M_a} = \frac{\dot{m}_e}{M_e}\frac{(1 - X_{H_2O})(1 - X_{O_2} - X_{CO_2} - X_{CO})}{(1 - X^{o}_{H_2O})(1 - X^{o}_{O_2} - X^{o}_{CO_2})}; \qquad (13)$$

$$\phi = \frac{X^{o}_{O_2}(1 - X_{CO_2} - X_{CO}) - X_{O_2}(1 - X^{o}_{CO_2})}{X^{o}_{O_2}(1 - X_{O_2} - X_{CO_2} - X_{CO})}. \qquad (14)$$

Simplifications are available, with some loss of precision, if concentrations of some of the gas species are not measured [64].

Figure 10 shows an example of calculated heat release rate from several large scale fire tests [65]. Measurement errors in rate of heat release measurements can be higher than in other measurements, especially for smaller fires. In one study [51], coefficients of variation ranged from 4 to 52 percent. With an oxygen depletion for a 100 kW fire of only 0.26 percent, the calculation of heat release rate suffers the same fate as the calculation of mass flows with pressure probes described above, with much of the uncertainty in the heat release calculations attributable to noise in the underlying measurements.

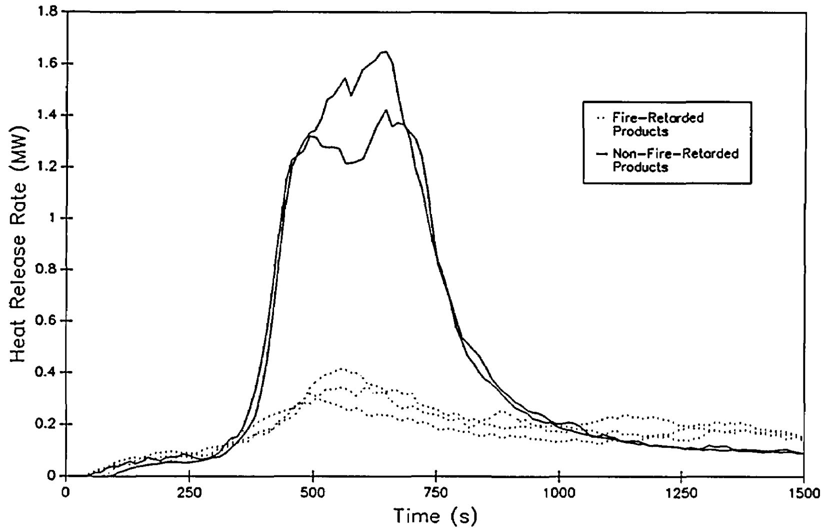

Figure 10. An example of heat release rate calculated from oxygen consumption calorimetry in several large scale fire tests [65].

This technique has been used extensively in both small- and large-scale testing [25,57,66,67]. Babrauskas [57], for instance, has demonstrated the validity of the measurements in a study of upholstered furniture fires. He provides comparisons between replicate tests in the open and enclosed in a room. He notes precision to within 15 percent for fires of 2.5 MW and consistent comparisons of heat release rate expected from mass loss measurements to those measured by oxygen consumption calorimetry.

4. Criteria Used to Judge the Quality of the Data

In order to take better advantage of the extensive library of large-scale test data presented in this report, a method of qualifying the data for fast identification was devised. This identification included the type of test that was performed (e.g., furniture calorimeter, multiple room, etc.), the major types of materials tested, the kinds of data available (e.g., gas concentrations, mass flow rates, heat release rate, etc.), and a rating of the quality of the data. This information is presented at the beginning of each section describing the data (secs. 5 to 9).

Since the rating of the data will necessarily be somewhat subjective, a simple type of rating system, one with not-too-fine distinctions, should be employed. The ratings used in this report are the following:

– data not available or not valid or of questionable validity;

± data exist but may not be appropriate for comparison to other tests (check test conditions and quality of data); and

+ data should be appropriate for comparisons.

Availability of small-scale and/or individual burning item data is identified, since these are desirable for development of model input data.

5. Single Room with Furniture

This data set describes a series of room fire tests using upholstered furniture items in a room of fixed size but with varying opening sizes and shapes. For the four tests conducted, good agreement was seen in all periods of the room fires, including post-flashover, noting that only fuel-controlled room fires were considered. It was selected for its well characterized and realistic fuel sources in a simple single-room geometry. In addition, the wide variation in opening size should provide challenges for current zone fire models.

5.1 Available Data in the Test Series

Following the subjective ratings discussed in section 4, the following set of ratings were apparent from the examination of the test data:

heat release rate (of fire, through vents, etc.)	+
interface height	+
layer temperatures	+
wall temperatures (inside and out)	−
gas concentrations	+
species yields	±
pressure in room	−
mass flow rate	±
radiation to the floor	+
mass loss	+
mass loss rate	+
heat of combustion	±

In general, the data included in the data set is consistent with the experimental conditions and expected results. Heat release rate, mass loss rate, and species yields are available for all the tests. This should allow straightforward application of most fire models.

5.2 General Description of the Test Series

This data set describes a series of room fire tests using upholstered furniture items for comparison with their free burning behavior, previously determined in a furniture calorimeter. Furniture is most often a hazard, not when burned in the open, but rather inside a room [57]. Room fire data lack generality and often cannot be extrapolated to rooms other than the test room; open burning rates have more useful generality. This work was undertaken in a room of fixed size but with varying opening sizes and shapes, in which furniture specimens identical to those previously tested in the furniture calorimeter would be burned. For the four tests conducted, good agreement was seen in all periods of the room fires, including post-flashover, noting that only fuel-controlled room fires were considered.

The conclusions from this study can be summarized as follows:

- The validity of open burning measurements for determining pre-flashover burning rates has been shown for typical upholstered furniture specimens.

- Post-flashover burning of these upholstered items was also seen not to be significantly different from the open-burning rate, for fires which are fuel limited. Fires with ventilation control, by definition, show a lower heat release rate within the room.

- The typical test arrangement of velocity probes spaced along the centerline of the window opening was found to lead to serious errors in computed mass and heat flows. Data taken in the exhaust system collecting the fire products did provide for satisfactory heat release measurements. A method is still lacking which could adequately separate the outside plume combustion heat from that released within the room itself.

- Various relationships for predicting flashover were examined considering the present data. The relationship proposed by Thomas was identified as the most useful, taking into account wall area and properties; however, this relationship may not apply to fires with a very slow build-up rate or for wall materials substantially different from gypsum wallboard.

This program was carried out at the National Institute of Standards and Technology in Gaithersburg, MD in which four experiments were conducted in a single room enclosure; ventilation to the room was provided by window openings of varying sizes. The room was equipped with an instrumented exhaust collection system outside the window opening. The exhaust system could handle fires up to about 7 MW size.

5.3 Test Facility

An experimental room with a window opening in one wall was constructed inside the large-scale fire test facility as shown in figure 11. The dimensions

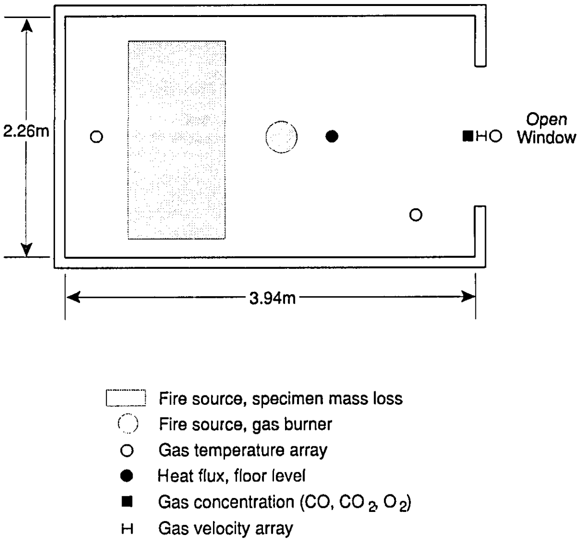

Figure 11. Plan view of experimental room for single room tests with furniture.

of the room and the window openings for the various tests is given in table 1. The soffit depth of the window opening was the same in all cases (fig. 12). For tests 1 and 2, the opening height (and therefore the ventilation parameter $A\sqrt{h}$) only was varied. For test 6, the same $A\sqrt{h}$ was retained but the shape of the opening was changed, compared to test 2. Test 5 resembled test 6, except that the armchair was used. Thus, for specimen type, ventilation factor, and opening aspect ratio, a pair of tests each was provided where these variables were singly varied, the other two being held constant.

The walls and ceiling materials in the room were 16 mm thick Type X gypsum wallboard, furred out on steel studs and joists. Floor construction was normal weight concrete.

The location of the instrumentation used in these experiments is shown in table 2 and figure 11. Two arrays of thermocouples, each consisting of 15 vertically spaced thermocouples, were installed in the room. The top and bottom thermocouples were at the ceiling and on the floor, respectively. In addition, a load cell for mass loss and a Gardon heat flux meter for measuring radiation to the floor were installed on the centerline of the room. Figure 11 also shows the location where a gas burner was used to check the calibration of the exhaust system; the gas burner was removed before testing furniture specimens.

Fifteen closely spaced velocity probes, with companion thermocouples, were located evenly spaced along the vertical centerline to facilitate accurate measurements of mass and heat flow through the opening. Two gas sampling probes were also located along the upper part of the opening centerline.

The exhaust system had an array of velocity probes and thermocouples, together with O_2, CO_2, and CO measurements to permit heat release to be determined according to the principle of oxygen consumption [13].

5.4 Experimental Conditions

Four of the six tests are listed in table 3. The test furniture included a 28.3 kg armchair (F21) and a similar 40.0 kg love seat (F31). Both were of conventional wood frame construction and used polyurethane foam padding, made to minimum California State flammability requirements, and polyolefin fabric. A single piece of test furniture and the igniting wastebasket were the only combustibles in the test room.

Table 1. Room and vent sizes for one room tests with furniture

Location[a]	Room	Vent	Dimensions (m)[b]
Room 1 (burn room)	√		2.26×3.94×2.31
Doorway or window, room 1 to ambient		√	2.0×1.13×0.31 (test 1) 2.0×1.50×0.31 (test 2) 1.29×2.00×0.31 (test 5) 1.29×2.00×0.31 (test 6)

[a] Notation used for rooms and vents were changed from the original report to be consistent throughout this report.

[b] For rooms, dimensions are width×depth×height. For vents, dimensions are width×height×soffit depth.

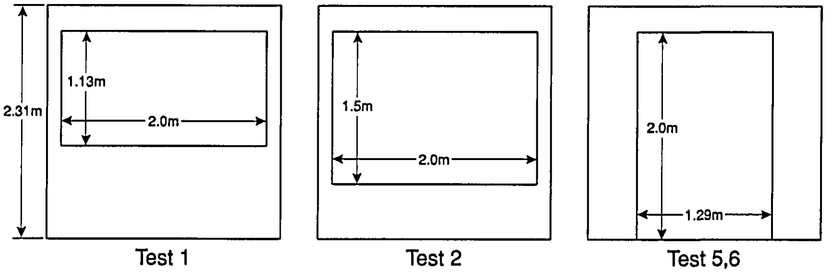

Figure 12. Elevation view of experimental room for single room tests with furniture.

Table 2. Location of instrumentation for one room tests with furniture

Room location[a]	Measurement type[b]	Position[c]
Room 1 (burn room)	Gas temperature arrays in two positions	0.17, 0.33, 0.50, 0.66, 0.83, 0.99, 1.16, 1.32, 1,49, 1.65, 1.82, 1.98, and 2.15 m
	Surface temperature in two positions	On floor and ceiling
	Heat flux	On floor
	Specimen mass loss	
Doorway, room 1 to ambient (burn room doorway)	Gas temperature array	See footnote d
	Gas concentration, CO, CO_2, and O_2	1.66 and 1.72 m
	Gas velocity array (bi-directional velocity probes)	See footnote d
Exhaust hood	Gas temperature array	Nine positions evenly spaced
	Gas velocity array	Nine position evenly spaced
	Gas concentration, CO, CO_2, and O_2	At centerline of hood
	Smoke obscuration	At centerline of hood

[a] Notation used for rooms and vents were changed from the original report to be consistent throughout this report. For reference, names used in the original report are shown in parentheses.

[b] Notation used for instrumentation was changed from the original report to be consistent throughout this report. For reference, names used in the original report are shown in parentheses.

[c] Distances are measured from floor.

[d] 15 locations spaced evenly from bottom to top of vent[c].
For test 1: 0.93, 1.00, 1.08, 1.15, 1.22, 1.29, 1.36, 1.43, 1.50, 1.57, 1.64, 1.72, 1.79, 1.86, and 1.93 m.
For test 2: 0.58, 0.67, 0.77, 0.86, 0.96, 1.05, 1.14, 1.24, 1.33, 1.43, 1.52, 1.61, 1.71, 1.80, and 1.90 m.
For tests 5 and 6: 0.13, 0.25, 0.38, 0.50, 0.63, 0.75, 0.88, 1.00, 1.13, 1.25, 1.38, 1.50, 1.63, 1.75, and 1.88 m.

Table 3. Tests conducted for one room test with furniture

Test	Chair	Soffit depth (m)	Opening width (m)	Opening height (m)	$A\sqrt{h}$ ($m^{5/2}$)
1	love seat	0.31	2.0	1.13	2.43
2	love seat	0.31	2.0	1.50	3.65
5	armchair	0.31	1.29	2.00	3.65
6	love seat	0.31	1.29	2.00	3.65

The tests in the furniture calorimeter [68,69] made use of a gas burner simulating a wastebasket fire as the ignition source. Because of practical difficulties in installing that burner in the test room, actual wastebasket ignition was used. This involved a small polyethylene wastebasket filled with 12 polyethylene-coated paper milk cartons. Six cartons were placed upright in the wastebasket, while six were torn into six pieces and dropped inside, The total weight of a wastebasket was 285 g, while the 12 cartons together weighed 390 g, for a total weight of 675 g. The gross heat of combustion was measured to be 46.32 kJ/g for the wastebasket and 20.26 kJ/g for the cartons, representing 21.10 MJ in all. Using an estimated correction, this gives a heat content of 19.7 MJ, based on the net heat of combustion. To characterize this ignition source, it seems appropriate to consider a constant mass loss rate $\dot{m} = 1.8$ g/s (equivalent to 52.5 kW) for the first 200 s and negligible thereafter.

The test room was conditioned before testing by gas burner fires where the paper facing was burned off the gypsum wallboard and the surface moisture driven off. The room was allowed to cool overnight and between tests.

Initial calibrations with gas burner flows showed adequate agreement, to within 10 to 15 percent, of window inflows and outflows, after an initial transient period of about 30 s. Similarly, during the final, smoldering stages of the furniture fires, a reasonable mass balance was obtained. During peak burning periods in the upholstered furniture tests, such agreement, however, was not obtained.

5.5 Examples of Data from the Test Series

Three examples of the data contained in this data set are shown below:

- Concentrations of O_2, CO_2, and CO in the upper gas layer in the doorway of the room (fig. 13).
- Rate of heat release from the four room burns in the test series (fig. 14.).
- Rate of mass loss of the burning furniture items for the four room burns in the test series (fig. 15).

In all three of these figures, the consistency of the data set can be seen. In figure 13, the effect of the opening can be seen along with the effect noted above for the heat release rate. For test 1, the O_2 concentration drops lower (with a concomitant rise in the CO_2 and CO concentrations) than test 3 or test 6 (the three tests with the same furniture item). However, the three peaks are similar in duration with the fourth peak for test 5 lagging slightly behind. In figure 14, three near replicate curves are seen with a fourth curve of lower peak heat release rate. This is consistent with the two different furniture items burned during the tests. In the original work, Babrauskas [57] suggests an uncertainty of ±330 kW in these heat release rate measurements. Thus, the three love seat tests (tests 1, 2, and 6) can be considered identical. Not surprisingly, the mass loss rate curves shown in figure 15 shows similar results.

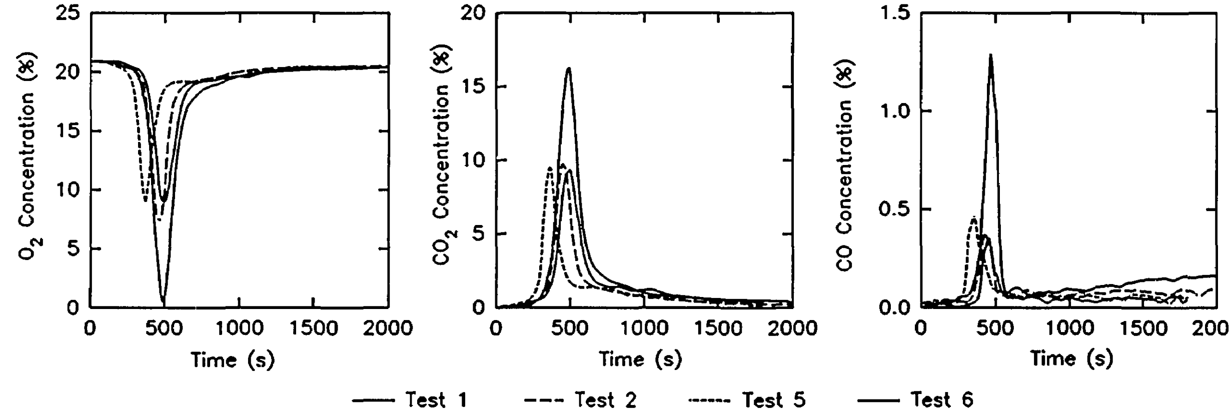

Figure 13. Gas concentrations measured during single room tests with furniture.

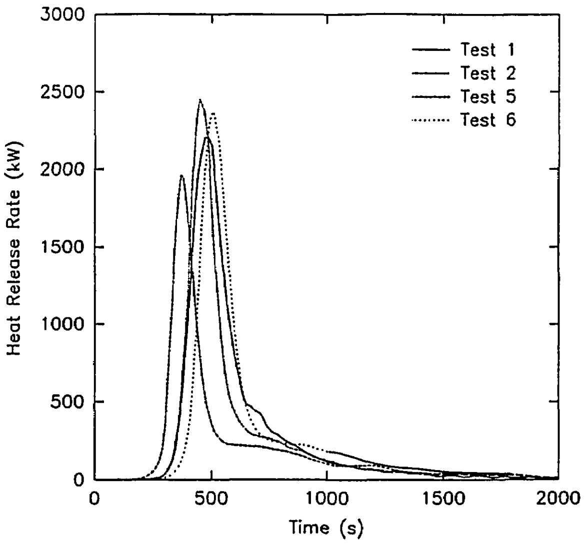

Figure 14. Heat release rate during single room tests with furniture.

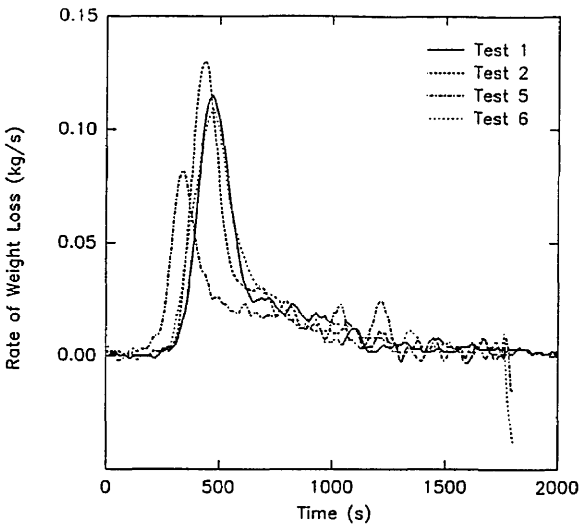

Figure 15. Mass loss rate measured during single room tests with furniture.

6. Single Room with Furniture and Wall Burning

Like the first set, this data set describes a series of single room fire tests using furniture as the fuel source. It expands upon that data set by adding the phenomenon of wall burning in some of the tests. It was chosen for examination because it provides an opportunity 1) to compare burning in the open and in a compartment using the same fuel package, and 2) to compare the effects of non-combustible wall linings versus combustible wall linings in the room [60].

6.1 Available Data in the Test Series

Following the subjective ratings discussed in section 4, the following set of ratings were apparent from the examination of the test data:

heat release rate (of fire, through vents, etc.)	+
interface height	+
layer temperatures	+
wall temperatures (inside and out)	−
gas concentrations	±
species yields	±
pressure in room	+
mass flow rate	+
radiation to the floor	±
mass loss	−
mass loss rate	−
heat of combustion	−

A few notes on the ratings are appropriate. Test 5 in the test series seems to be of questionable quality. It is the only test where the mass flow through the doorway does not exhibit a reasonable mass balance, and although a replicate, radically different than test 2. Thus, its quality must be questioned. Although no mass loss rates were obtained during the tests, the burning materials should allow estimation by the method presented by Babrauskas et. al. [70].

6.2 General Description of the Test Series

This data set was chosen for examination because it provides an opportunity 1) to compare burning in the open and in a compartment using the same fuel package, and 2) to compare the effects of non-combustible wall linings versus combustible wall linings in the room [60]. In the former case, the early stages of the fire between the open burns and the room burns are similar; however, it is possible to show how the burning regime changes when influenced by the confines of the room and when the ventilation effects take over. In the latter case, the room wall linings were well-characterized and data are available for estimating heat transfer through the walls. Peak heat release rates as high as 7 MW were measured in these tests.

The relevant conclusions from this study can be summarized as follows:

- Room flashover could occur as early as 233 s with a peak heat release rate of over 2 MW; wood paneling in the room increased the peak heat release to 7 MW.

- The presence or degree of combustibility of a wall behind the bed did not have a significant effect on the free burn rate nor on the smoke and carbon monoxide generation from the furnishing fires. Differences due to the wall were within the experimental scatter found between repeat runs of each test.

- Prior to the ignition of the exposed combustible ceiling surface (paper), the effect of the room on the rate of burning of the furnishings did not appear to be significant. However, subsequent to ceiling surface ignition, noticeable enhancement in the burning rate of furnishings was indicated in all open door room burn tests with one exception.

- Much higher concentrations of carbon monoxide occurred inside the room for a well-ventilated fire than those for a closed room fire. Higher carbon monoxide levels occurred at the 1.5 m height than at the 0.30 m height in the room.

- Mass flow out of the doorway, calculated using three computational techniques, showed good agreement with each other.

6.3 Test Facility

A furnishing arrangement typical of those in the U.S. Park Service (Dept. of the Interior) lodging facilities was evaluated for its burning characteristics and the times for sprinkler activation. Six open fire tests, i.e., unconfined fires in a large open space, and six room fire tests of one bedroom furnishing arrangement were performed. The test room and exhaust hood arrangement is shown in figure 16. The dimensions of the room and doorway are given in table 4. As can be seen, the 2.44×3.66×2.44 m high test room was located adjacent to the 3.7×4.9 m exhaust collector hood which had an exhaust flow capacity of 3 m^3/s. In the open burns, the furnishing arrangement was located directly under the hood with the headboard positioned 0.76 m away from the exterior front wall of the room. Two of the open burns had a 2.44×2.44 m free standing wall 25.4 mm behind the headboard and in front of the room. This wall was constructed from 12.7 mm gypsum board mounted on 51×102 mm steel studs 0.41 m apart. Two other open burns had 6.4 mm plywood lining the same free standing wall. For the room tests, the headboard was located 40 mm away from the back wall. The back and two side walls were 12.7 mm thick gypsum board mounted over 51×102 mm steel studs 0.41 m apart. The ceiling was fabricated from 15.9 mm thick fire resistant gypsum board over a sub-layer of 25 mm thick calcium silicate board and was attached to the underside of several steel joists spanning the side walls. The front wall, with a 0.76×2.03 m high doorway, was constructed from a single layer of calcium silicate board. Three of the room tests had 6.4 mm plywood over the gypsum board on the two side walls and back wall. In one of the gypsum board lined room tests (test 6), a 0.76 m wide×2.03 m high and 9.55 mm thick door made from transparent poly(methylmethacrylate) was used for manually closing off the room upon activation of the smoke detector.

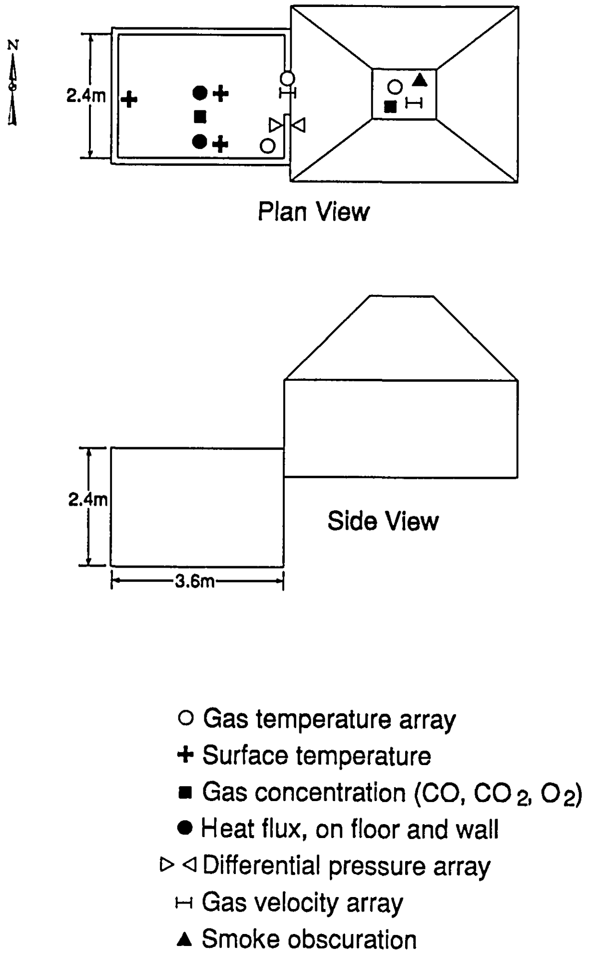

Figure 16. Test room exhaust hood arrangement and instrumentation for single room tests with wall burning.

Measurements were made in the room and doorway to characterize the fire environment and to allow calculation of the mass flow from the room. These measurements included the air temperature and pressure gradients in the room and air temperature and velocity gradients along the doorway centerline. Total incident heat flux to a horizontal target on the floor was monitored along with the thermal radiance to a vertical surface measured at a height of 0.64 m in the room, next to the left wall, facing the wastebasket. In addition, CO and CO_2 concentrations were recorded at the 0.30 and 1.5 m heights in the room for test R6. Measurements were also taken in the room to help evaluate sprinkler head and smoke detector responses to the fire environment. Temperatures, velocities, and O_2 and CO_2 concentrations in the exhaust gases in the stack were monitored to determine the mass flow through the stack and $\dot{Q}_s$, the total rate of heat production by the fire.

Table 4. Room and vent sizes for one room tests with furniture and wall burning

Location[a]	Room	Vent	Dimensions (m)[b]
Room 1 (burn room)	√		2.44×3.66×2.44
Doorway, room 1 to ambient		√	0.76×2.03×0.31

[a] Notation used for rooms and vents were changed from the original report to be consistent throughout this report. For reference, names used in the original report are shown in parentheses.

[b] For rooms, dimensions are width×depth×height. For vents, dimensions are width×height×soffit depth.

An average temperature taken across the inlet of the exhaust collection hood was used together with the mass flow in the stack to estimate h_s, the total flux of heat from the fire test room ($\dot{Q}_s$ minus the heat loss to the room boundaries). The estimated value for the quantity h_s is actually equal to h_s minus the heat loss to the surroundings between the room doorway and the inlet to the exhaust collection system. Smoke and CO also were monitored in the stack to help quantify the products of combustion from the room fires.

Location of all instrumentation in the room fires is indicated in table 5 and figure 16. Temperatures in the room and doorway were measured with chromel-alumel thermocouples made with 0.05 mm wire. Because these thermocouples were difficult to prepare and were vulnerable to breakage under normal fire test operations, more robust thermocouples fabricated from 0.51 mm chromel-alumel wires also were employed at these same locations. The larger thermocouples were more susceptible to radiation error and were used primarily as backup measurements. Pressures in the room were measured with probes mounted in one corner of the burn room, flush with the interior surface of the front wall, along the height of the room. Bi-directional velocity probes [71] were employed for measuring the air velocity in the doorway and to note the occurrence of any flow reversal along the doorway. Heat flux was monitored with water-cooled total heat flux meters of the Gardon type. Crumpled newspaper on the floor also was used to indicate if and when the irradiance was sufficient to ignite such light combustible materials in the lower half of the room. Non-dispersive infrared analyzers were used to record the concentrations of CO and CO_2 in the room and in the stack and oxygen concentration was measured with a paramagnetic type instrument. Stack velocities were measured with pitot-static probes and stack temperatures were monitored with chromel-alumel thermocouples fabricated from 0.51 mm wire. The optical density of the smoke was determined by attenuation of a light beam in the stack. Neutral optical density fil-

Table 5. Location of instrumentation for one room tests with furniture and wall burning

Room location[a]	Measurement type[b]	Position[c]
Room 1 (burn room)	Gas temperature arrays (0.51 mm and 0.05 mm thermocouple trees)	Two sets of each 0.20, 0.41, 0.61, 0.81, 1.02, 1.22, 1.42, 1.63, 1.83, 2.03, and 2.24 m
	Gas temperature	Center of room, 2.34 m
	Surface temperature (thermocouple near brass disks)	On three walls, 2.31 m
	Gas concentration, CO and CO_2	0.30 and 1.52 m
	Heat flux	On floor and 0.64 m
Doorway, room 1 to ambient (burn room doorway)	Gas temperature arrays (0.51 mm and 0.05 mm thermocouple trees)	Each set 0.10, 0.20, 0.51, 0.81, 1.12, and 1.73 m
	Differential pressure array (pressure probes)	0.20, 0.41, 0.61, 0.81, 1.02, 1.22, 1.42, 1.63, 1.83, 2.03, and 2.24 m
	Gas velocity array (bi-directional velocity probes)	0.30, 0.91, 1.22, 1.52, and 1.83 m
Exhaust hood	Gas temperature array	Nine positions evenly spaced
	Gas velocity array	Nine position evenly spaced
	Gas concentration, CO, CO_2, and O_2	At centerline of hood
	Smoke obscuration	At centerline of hood

[a] Notation used for rooms and vents were changed from the original report to be consistent throughout this report. For reference, names used in the original report are shown in parentheses.

[b] Notation used for instrumentation was changed from the original report to be consistent throughout this report. For reference, names used in the original report are shown in parentheses.

[c] Distances are measured from floor.

ters were used to calibrate the light sensor over the range of optical densities from 0.04 to 3.0. At the inlet of the exhaust hood, the average temperature was monitored with a grid of 25 chromel-alumel thermocouples arranged in parallel; each thermocouple was made from 0.51 mm diameter wire.

A sprinkler head with an activation temperature of 71 °C and two different size brass disks, used to simulate faster response sprinkler heads, were used in tests 2 to 6. The smaller disk had a diameter of 9.8 mm, was 0.8 mm thick, and weighed 0.5 g; the larger disk had a diameter of 21.6 mm, was 2.4 mm thick, and weighed 7.3 g. Each disk had a 0.51 mm chromel-alumel thermocouple soldered on its surface. Test R1 did not have a sprinkler or brass disk. The sprinkler in test R3 had a discharge rate of 1.4 L/s (22 gal/min), corresponding to an operating water pressure of 103,400 Pa (15 psi). The other room tests used a dry sprinkler where the pipe was pressured with air to 34,500 Pa (5 psi). In addition, two types of ionization smoke detectors were used in test 6.

6.4 Experimental Conditions

These tests are outlined in tables 6 and 7. The standard set of furnishings shown in figure 17 was used for these tests and was based on an inspection of some selected U.S. Park Service lodging facilities at Yosemite National Park in California and at Shenandoah National Park in Virginia. The room furnishings consisted of a 1.37 m wide × 1.91 m

Table 6. Room fire tests

					Ambient room conditions	
Test	Furnishings	Wall material[a]	Sprinkler	Test duration s	Temperature °C	Relative humidity %
R1	Std. set	12.7 mm gypsum board	None	1800	23	50
R4			Dry	1800	23	56
R6			Dry	1800	23	45
R2		6.4 mm A/D plywood over 12.7 mm gypsum board	Dry	525	23	50
R3			Wet	470	22	52
R5			Dry	1800	24	48

[a] Ceiling material was 15.9 mm fire-resistant gypsum board.

Table 7. Open burn tests

				Ambient room conditions	
Test	Furnishings	Wall behind headboard	Test duration s	Temperature °C	Relative humidity %
O4	Std. set	No wall	1800	22	32
O6			1800	21	38
O1		12.7 mm gypsum board	1800	22	50
O3			1800	21	40
O2		6.4 mm A/D plywood over gypsum board	1800	22	50
O5			1800	21	38

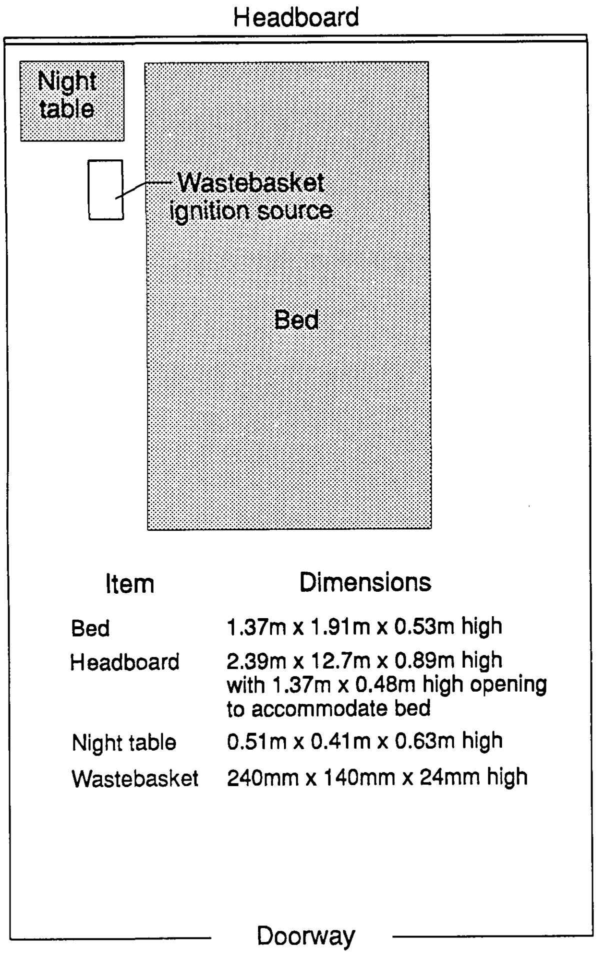

Item	Dimensions
Bed	1.37m x 1.91m x 0.53m high
Headboard	2.39m x 12.7m x 0.89m high with 1.37m x 0.48m high opening to accommodate bed
Night table	0.51m x 0.41m x 0.63m high
Wastebasket	240mm x 140mm x 24mm high

Figure 17. Fire test room arrangement for single room tests with furniture.

long × 0.53 m high double bed, a 2.39 × 0.89 m high headboard, and 0.51 m wide × 0.41 m deep × 0.63 m high night table. Both headboard and night table were fabricated from 12.7 mm thick plywood. The bedding was comprised of two pillows, two pillow cases, two sheets, and one blanket. The pillows had a polypropylene fabric with a polyester filling. The pillow cases and sheets were polyester-cotton. The blanket was acrylic material. The bedding was left in a "slept in" condition which was duplicated to the degree possible in each test. The spring mattress had the same upholstery and padding on the top as on the bottom. The upholstery was a polyester quilted cover. Padding consisted of 6.4 mm polyurethane foam over a fire-retarded cotton felt layer with sub-layers of a cotton felt and a synthetic cellulosic fiber pad. The box spring had a covering of polyester fabric over a layer of cotton felt and a sub-layer of cellulosic fiber pad. Underneath the padding was a wood frame with a steel wire grid on top and a cellulosic cloth cover on the bottom. The combustible weight of each item is given in table 8. The total combustible fire load for this arrangement was 6.0 kg/m^2 of floor area. With three walls of the room lined with 6.4 mm plywood, the room fire load came to 14.8 kg/m^2 of floor area.

In all of the tests, the fire was started with match flame ignition of a 0.34 kg (240 × 140 × 240 mm high) wastebasket, filled with 0.41 kg of trash, positioned adjacent to the night table and against the bed. The type and distribution of the contents is shown in table 9.

Duplicate experiments were performed under free-burning conditions (in the open) using three different scenarios: 1) no wall behind the bed, 2) a gypsum wall behind the bed, and 3) a plywood wall behind the bed. In all cases, the same furnishing arrangement and ignition scenario was used.

Three replicate room burns using the same furnishing arrangement and ignition scenario as in the

Table 8. Fuel loading in fire tests

Fuel item	Combustible weight, kg Open burns	 Room burns
Mattress and box spring[a]	24.7	24.7
Headboard	14.4	14.4
Night table	10.6	10.6
Bedding	3.2	3.2
Filled wastebasket	0.75	0.75
Total combustible furnishings	53.7	53.7
Plywood[b]	19.5	77.9

[a] Mattress and box spring weight excluding that of the inner springs.

[b] Only used for open burn tests 2 and 5 and for room tests 2, 3, and 5.

Table 9. Wastebasket ignition source

Wastebasket—polyethylene wastebasket
weight: 0.34 kg

Trash contents, in order of stacking

1 polyethylene liner
16 sheets of newspaper
1 paper cup, 3 oz, crumpled
2 sheets of writing paper
3 paper tissues, crumpled
1 cigarette pack, crumpled
1 milk carton, 8 oz
2 paper cups, crumpled
1 cigarette pack, crumpled
1 sheet of writing paper, crumpled
2 paper tissues, crumpled
Total weight of contents: 0.41 kg

open burns were performed in the room lined with gypsum board and three replicate room burns were carried out in the room lined with plywood. In the latter tests, one fire was extinguished early (167 s) due to sprinkler activation, a second was extinguished after 525 s, and, in the third test, the door to the room was closed after 22 s and reopened after 960 s.

6.5 Examples of Data from the Test Series

Three examples of the data contained in this data set are shown below:

- Rate of heat release from the six room burns in the test series (fig. 18).
- Position of the interface between the upper and lower layer in the doorway of the room for the six room burns (fig. 19).
- A comparison of mass flow in and out of the doorway for all six tests in the test series (fig. 20).

In figure 18, it is apparent that test 5 is significantly different than test 2, although the two tests are described in the report as replicate tests. In addition, the agreement of the mass flows shown in figure 20 shows an anomaly in the lower left hand corner of the figure also due to test 5. Thus, the quality of that test must be questioned.

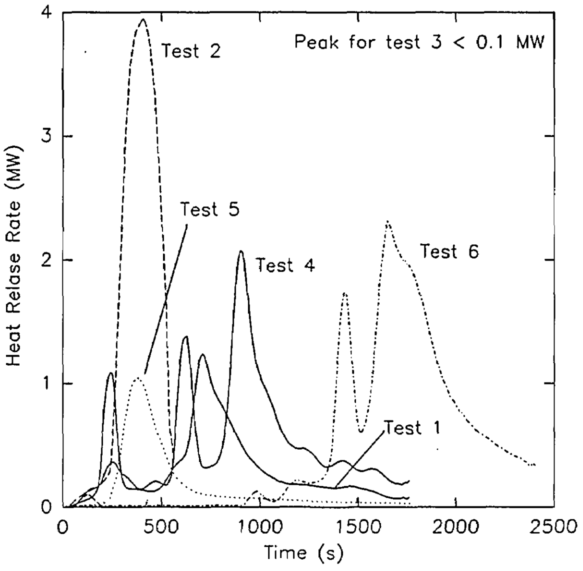

Figure 18. Heat release rate for single room test with furniture and wall burning.

The interface position displayed in figure 19 shows two of the three sets of replicates with two pairs of similar curves. Since the doorway was closed during much of test 6, it cannot be considered a replicate of test 4. However, for the two pairs of replicate tests, the agreement is seen as quite good.

Figure 20 shows a comparison of the mass flow in and out of the doorway of the test room. The

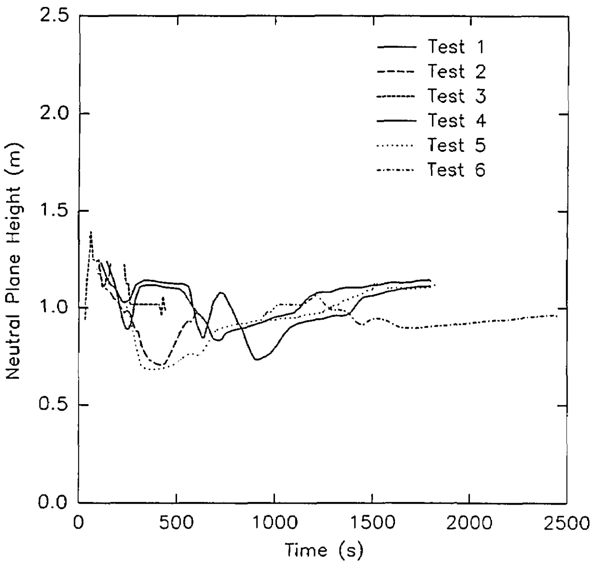

Figure 19. Position of the layer interface for single room tests with furniture and wall burning.

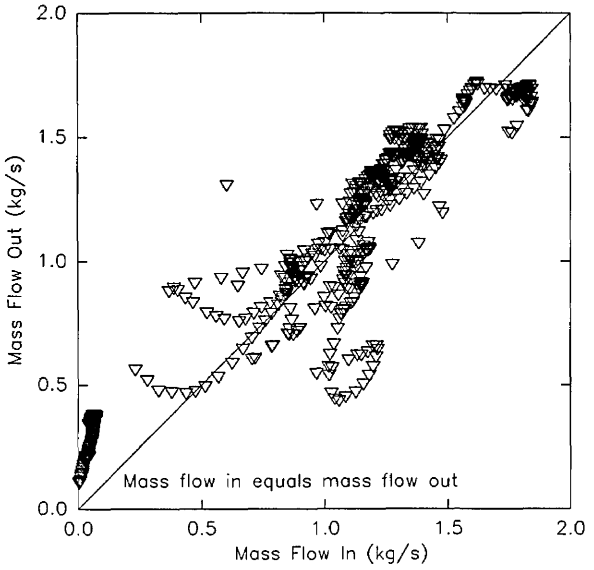

Figure 20. A comparison of mass flow in and mass flow out a doorway during single room tests with furniture and wall burning.

data for all times and all tests is shown on this figure. Although there is some divergence from the line of perfect agreement, these occur early and late in each test and may be due to the unaccounted for expansion or contraction of the gases within the room. In general, for the hundreds of individual measurements presented, the level of agreement is quite good.

7. Three Rooms Including Corridor

This data set describes a series of tests in a multiple room configuration with simple steady-state gas burner fires. It provides a basic set of quantities that are predicted by current fire models for small to medium size fires. Since all fires were gas burner fires, simulation should be straightforward. It is of particular interest since it was undertaken as a part of a program to develop a generic methodology for the evaluation and accuracy assessment of fire models [51].

7.1 Available Data in the Test Series

Following the subjective ratings discussed in section 4, the following set of ratings were apparent from the examination of the test data:

heat release rate (of fire, through vents, etc.)	+
interface height	+
layer temperatures	+
wall temperatures (inside and out)	±
gas concentrations	−
species yields	−
pressure in room	+
mass flow rate	+
radiation to the floor	−
mass loss	+
mass loss rate	+
heat of combustion	+

7.2 General Description of the Test Series

This data set is of particular interest because the study was conducted as part of a program to develop a generic methodology for the evaluation and accuracy assessment of fire models. To this end, one specific model (FAST) was chosen because it was well advanced in its development and was fairly well documented by the modeler. A carefully constructed and well-instrumented large-scale fire test facility was developed to provide experimental data for the evaluation of FAST and other models. The parameters studied were selected as the major energy-driven quantities predicted in multi-room fire models. This choice allowed the study to be limited to a manageable set of parameters while providing insight into many of the predictable quantities in room fire models. A three room configuration, with rooms of different sizes, was selected leaving three major variables whose chosen values were combined to define the experiments: fire size, room door opening size, and number of rooms. In total, nine different sets of experiments were conducted, with multiple replicates of each, for a total of 45 tests.

7.3 Test Facility

The experimental arrangement is shown in figure 21. It was a three compartment configuration, with two smaller rooms opening off a corridor 12.4 m long. Table 10 summarizes the dimensions of the three rooms and the connecting vents. The first room, where the fire source was located, had 50 mm thick ceramic fiber insulation under a calcium silicate ceiling and over fire brick walls to reduce thermal losses through these surfaces. The floor of the room was exposed fire brick. The second room ceiling and walls were constructed of steel studding with unfilled stud spaces with gypsum board sheathing and a covering of 13 mm calcium silicate board; this was to assure structural integrity during prolonged exposures to a possible post-flashover fire plume from the door between the first and second rooms. The concrete floor in the second room was covered with 13 mm gypsum board to protect the concrete. The passageway from the second room to the first and third rooms was a small corri-

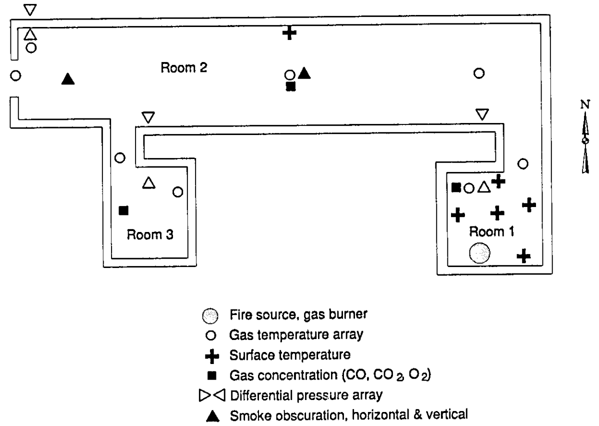

Figure 21. Test room arrangement and instrumentation for three room tests with a corridor.

Table 10. Room and vent sizes for three room tests with a corridor

Location[a]	Room	Vent	Dimensions (m)[b]
Room 1 (first room)	✓		2.34×2.34×2.16
Doorway, room 1 to room 2[c] (first room doorway)		✓	0.81×1.60×0.53
Room 2 (second room)	✓		2.44×12.19×2.44
Doorway, room 2 to room 3[d] (third room doorway)		✓	0.79×2.04×0.40
Doorway, room 2 to ambient (second room exit doorway)		✓	0.76×2.03×0.41
Room 3 (third room)	✓		2.24×0.94×2.43

[a] Notation used for rooms and vents were changed from the original report to be consistent throughout this report. For reference, names used in the original report are shown in parentheses.

[b] For rooms, dimensions are width×depth×height. For vents, dimensions are width×height×soffit depth.

[c] Doorway from room 1 to room 2 was actually 1.02×1.03×2.00 m passageway.

[d] Doorway from room 2 to room 3 was actually 0.79×0.94×2.04 m passageway.

dor (about 1 m wide×1 m deep×2 m high) constructed with the same materials as the second room. Since only warm air circulation was expected in the third room, the walls and ceiling were constructed from 13 mm gypsum board over metal studs, without the calcium silicate covering. The floor was exposed concrete. The construction materials used in this test series, together with their thermophysical properties, are given in table 11. All material properties are literature values and should be considered approximate.

Table 11. Construction materials

	Location	Material	Thickness mm	Density kg/m³	Heat capacity KJ/kg·K	Thermal conductivity W/m·K	Emissivity
Room 1	Wall substrate	Fire brick	113	750	1.04	0.36/200 °C 0.38/300 °C 0.45/600 °C	0.80
	Ceiling substrate	Calcium silicate		Same as room 2 walls			
	Walls and ceiling[a]	Ceramic fiber	50	128	1.04	0.09/300 °C 0.17/600 °C 0.25/900 °C	0.97
	Floor[a]	Fire brick		Same as wall substrate			
Room 2	Ceiling and wall substrate	Gypsum board	12.7	930	1.09	0.17	
	Ceiling and walls[a]	Calcium silicate	12.7	720	1.29/200 °C 1.33/300 °C 1.55/600 °C	0.12/200 °C 0.11/300 °C 0.12/600 °C	0.83
	Floor substrate	Concrete	102	2280	1.04	1.8	
	Floor[a]	Gypsum board	12.7	930	1.09	0.17	
Room 3	Walls and ceiling[a]	Gypsum board[b]	12.7	930	1.09	0.17	
	Floor[a]	Concrete	102	2280	1.04	1.8	

[a] Interior finish.

[b] Gypsum board over studs.

The locations of all instrumentation initially used in the rooms and adjacent exhaust collection hood are summarized in table 12. Some of the instrument locations also are shown in figure 21. Data were recorded with an automatic data logging system at a rate of 24 channels per second.

A 15.9 mm diameter orifice flow meter was used for metering the natural gas flow and a 200 SCFH gas flow meter was used to monitor the acetylene flow.

A 3.7 × 4.9 m hood, having an exhaust flow capacity of about 3 m^3/s, was located over the doorway from the second room and collected the exhaust from the fire tests. Temperatures, velocities, and O_2 and CO_2 concentrations in the exhaust collection hood were monitored with the instrumentation listed in table 12 to determine the rate of energy production of the fire based on oxygen consumption calorimetry.

Part way through the test program, the placement of thermocouples in the first and second rooms were revised to permit greater resolution of the mass flow exhausting from the rooms. At that time, thermocouples were installed also on the unexposed back side of the second room ceiling and north wall to aid in the calculation of the conductive heat losses through these surfaces.

Table 12. Location of instrumentation for three room tests with a corridor

Room location[a]	Measurement type[b]	Position[c]
Room 1 (first room)	Gas temperature array (tree 1)	0.15, 0.36, 0.66, 0.97, 1.27, 1.88, 2.03, and 2.15 m
	Surface temperature	Four walls (0.55 and 1.64 m), ceiling, and floor
Doorway, room 1 to room 2 (first room doorway)	Gas temperature array (tree 2)	0.15, 0.30, 0.61, 0.91, 1.22, and 1.52 m
	Differential pressure array (static pressure probes)	25 mm, 0.30, 0.61, 1.22, and 1.52 m
Room 2 (second room)	Three gas temperature arrays (trees 3, 4, and 5)	0.15, 0.30, 0.61, 0.91, 1.22, 1.52, 1.83, 2.13, 2.29, 2.44 m
	Surface temperature	0.61 and 1.83 m
	Smoke obscuration	Horizontal array at 0.61, 0.91, 1.22, 1.52, 1.83 and 2.29 m Vertical measurement
Doorway, room 2 to room 3 (third room doorway)	Gas temperature array (tree 7)	0.15, 0.61, 0.91, 1.07, 1.22, 1.52, 1.83, and 1.93 m
	Differential pressure (static pressure probes)	80 mm
Doorway, room 2 to ambient (second room exit doorway)	Gas temperature array (tree 6)	0.15, 0.30, 0.61, 1.22, 1.52, 1.83, and 2.13 m
	Differential pressure array (static pressure probes)	76 mm, 0.61, 1.22, 1.52, and 1.83 m
Room 3 (third room)	Gas temperature array (tree 8 in third room)	0.15, 0.61, 0.91, 1.07, 1.22, 1.52, 1.83, 2.13, 2.29, and 2.44 m
Exhaust hood	Gas temperature array	Nine positions evenly spaced
	Gas velocity array	Nine position evenly spaced
	Gas concentration, CO, CO_2, and O_2	At centerline of hood
	Smoke obscuration	At centerline of hood

[a] Notation used for rooms and vents were changed from the original report to be consistent throughout this report. For reference, names used in the original report are shown in parentheses.

[b] Notation used for instrumentation was changed from the original report to be consistent throughout this report. For reference, names used in the original report are shown in parentheses.

[c] Distances are measured from floor.

7.4 Experimental Conditions

A diffusion flame burner using natural gas, placed snugly against the middle of the back wall of the burn room, served as the fire source. The top of the burner, positioned 0.5 m above the floor, had a 0.34 m square porous ceramic surface with a perimeter of 13 mm wide steel plate. Initially, zinc chloride candles served as the smoke source. Their use was discontinued due to non-uniform time and spatial distributions of the smoke. Later experiments used a mixture of natural gas and acetylene in a heat release ratio of 77 kW of natural gas to 23 kW of acetylene (0.31 g of acetylene per g of natural gas) to achieve a concentration of smoke which provided a visible separation of the hot and cold layers during a test and provided constant smoke production throughout a test.

Gas fires with nominal heat release rates of 100, 300, and 500 kW were conducted under the following configurations:

- second room exit doorway open, third room doorway closed;
- second room exit doorway closed, third room doorway closed;
- second room exit doorway open, third room doorway closed; and
- second room exit doorway closed, third room doorway open.

All the tests are described in tables 13 and 14. Tests 50 K, 100 F, and 100 K had experimental difficulties and were excluded from the tables. For tests 50 D, 300 D, and 300 E, the fuel to the burner was cut off prematurely by the ultraviolet flame sensor.

In the tests with the second room exit doorway closed, a doorway having a realistic 20 mm undercut was used. Unfortunately, measurement or calculation of the flow under the door was difficult. In test 100 O, the undercut in the door was sealed. An opening in the floor, near the door, with an orifice having about the same area as the undercut was used to measure the equivalent flow through the latter.

Tests were initially performed with the data recording system turned on for 300 s before ignition of the gas burner, with the pilot ignited during this 300 s period. Later in the series, a 300 s baseline period, followed by a 300 s pilot flame interval before burner ignition, was also recorded for each test. This allowed an adequate time for the corridor flow behavior associated with the pilot flame to reach steady conditions. The burner was allowed to run for 900 s with data acquisition terminated after recording about 300 s of the cooling period.

To insure a self-consistent definition across the test series and to allow comparison with model predictions beginning at a preset set of conditions, the data from all tests were normalized to a standard definition. Once normalized, the repeatability of a given measurement ranged from excellent to poor. For temperature-based measurements and calculations, the repeatability, as shown by the average standard deviation during steady state burning, was good—typically less than 10 percent of the measured or calculated values. For pressure-based measurements, the repeatability was not nearly as good, at times approaching 70 percent of the values. Much of the disparity between individual tests can be traced to experimental technique, which refined as the testing progressed. The precision of some of the calculations suffers from the propagation of large errors in the individual factors. The rate of heat release or mass flow measurements could be improved by multiple measurements of the same quantity with instruments of different resolution, thus allowing more precise determination of the quantity in the range of interest. For the mass and heat balance calculations, however, such an approach would provide less improvement. Alternate techniques for such determinations should be explored which do not depend as strongly on propagated errors.

7.5 Examples of Data from the Test Series

Three examples of the data contained in this data set are shown below:

- Rate of heat release from the six open door data sets in the test series (fig. 22).
- Interface height for the nine data sets in the test series (fig. 23).
- Vertical profiles of average temperature along with layer temperatures estimated with a two zone assumption (fig. 24).

Figure 22 presents the heat release rate data. These data are only presented for the tests with an open room 2 doorway, since flow through the room 2 doorway to the collection hood was restricted by the closed door, hindering the measurement in the collection hood of the heat release rate of the fire.

Table 13. Initial conditions for tests with gas burner (third room closed)

Test	Room 2 doorway to ambient	$\dot{Q}_T$[a] kW	Smoke[b] source	P_a[c] mm Hg	T_a[d] °C	T_{out}[e] °C	RH[f] %	Room 2 lights
100 A	open	100	C					on
100 B				756	23		68	
100 C				751	23		72	
100 D			none	749	23		74	
100 E			C	760	21		58	
100 G			A	764	22		54	
100 H								off
100 I				760	20	−7	46	
100 J				755	21	2	51	
100 L	closed			751	21	2		g
100 M				749	21	4	41	off
100 N				745	21	6	45	on
100 O				740	21	11	45	g
300 A	open	300		744	21	12	63	on
300 B				754	21	8	54	off
300 C								
500 A		500	none	756	22	13	57	
500 B			A	748	22	10	50	
500 C								g
500 D				768	21	−6	31	on
500 E				748	21	4		off
500 F				755	21	6	46	

[a] Calculated gas burner heat release rate (includes acetylene).
[b] C is for candle; A is for acetylene.
[c] Ambient barometric pressure in test facility.
[d] Ambient temperature in test facility at the start of the test.
[e] Ambient outside temperature at the start of the test.
[f] Relative humidity in test facility at the start of the test.
[g] Uncertain.

Comparing the measured rate of heat release to the heat release calculated from the gas flow rate to the burner (assuming complete combustion of the gas), the measured rate of heat release is consistently low, averaging 19 percent lower than expected. While usually within the experimental uncertainty as exemplified by the average standard deviation for the data sets, the consistently lower readings deserve attention. In the test configuration, flow through the exhaust collection hood is

Table 14. Initial conditions for tests with gas burner (third room open)

Test	Room 2 doorway to ambient	$\dot{Q}_T$[a] kW	Smoke[b] source	P_a[c] mm Hg	T_a[d] °C	T_{out}[e] °C	RH[f] %	Room 2 lights	Footnotes
100 U	open	100	A	761	22	16	66	off	
100 V				747	20	2	43		
100 W				744	21	1	48		
100 X				752	23	20	61		
100 Y				751	23	26	58		
100 Z				754	22	18	61		
100 AA				752	22	30	62		
100 AB				754	22	26	55	on	
100 P	closed			749	22	24	70	off	
100 Q				749	21	21	63		g
100 R				748	22	26	67		g
100 S				749	22	30	65		g
300 F	open	300		748	22	24	70		g
300 G				754	23	19	65		
300 H				741	23	26	66		
300 D	closed			748	22		66		g,h
300 E				748	22	26	70		g,h
500 G	open	500		750	22	24	68		g

[a] Calculated gas burner heat release rate (including acetylene)—accuracy within 2%.
[b] A is for acetylene.
[c] Ambient barometric pressure in test facility at the start of the test.
[d] Ambient temperature in test facility at the start of the test.
[e] Ambient outside temperature.
[f] Relative humidity in test facility.
[g] Anemometer used to measure flow in third room doorway.
[h] Burner flames prematurely extinguished by ultraviolet sensor.

measured minimally downstream from bends in the system. For this reason, accurate measurement of the flow may be suspect.

Figure 23 presents the layer height data. From this figure, the effect of the third room on the layer height in the second room is small, whereas whether the second room exit doorway was open or closed makes a big difference. Comparing similar sets with the door open and closed shows a small time delay in the initial filling of the second room, but with a steady state layer height very similar for the sets with the second room exit doorway in the same position. This result follows logically from the added volume of the third room taking some time to fill, but allowing the second room to fill to the same depth.

Figure 24 shows the average temperature profiles from an open door and a closed door test (both 100 kW tests with room 3 open) overlaid with the upper and lower layer temperature calculated using the two-zone assumption for the test rooms. The solid line represents the average temperature

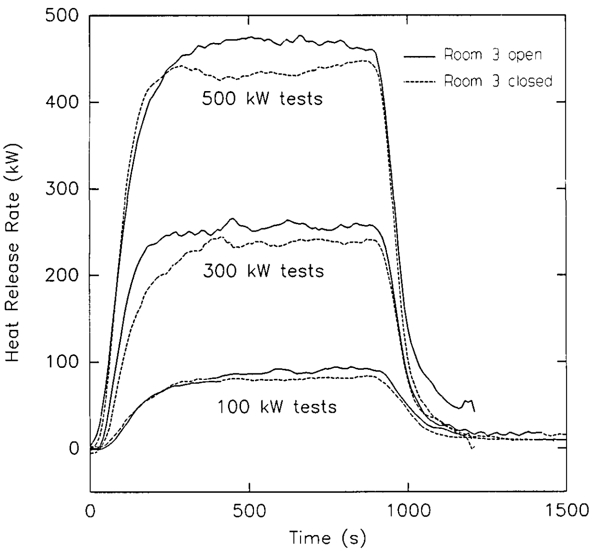

Figure 22. Heat release rate during three room tests with corridor.

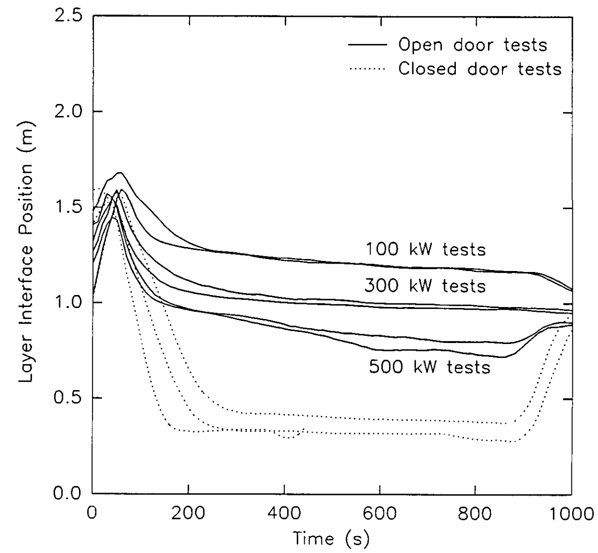

Figure 23. Layer interface heights for tests with three rooms with a corridor.

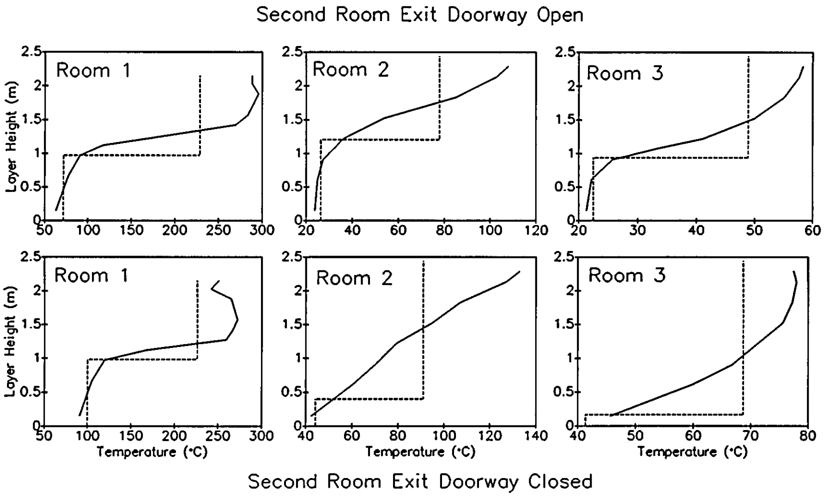

Figure 24. Average temperature profiles for open and closed door tests along with layer temperatures estimated with a two zone assumption.

profile; the dotted lines describe the results from the two-zone model. Specifically, the horizontal dotted line shows the height of the layer interface, while the two vertical dotted lines represent the lower and upper layer temperatures and extend through the heights appropriate to these layers. Temperature profiles for room 1, with the burner, are very similar for the open and closed door tests—not surprising, since the door to room 2 is open in both tests. Visually, the two-zone assumption holds better for the open door test than for the closed door test in the cooler rooms 2 and 3. No distinct layering is evident in rooms 2 or 3 in the closed door test. With the closed door, the hot gases come closer to the floor and, along with mixing as the gases reach the end of room 2, lead to a more closely linear temperature profile from the floor to the ceiling. In the test with a closed exit doorway in the second room, mixing occurs at the end of the long corridor in room 2, heating the lower air and cooling the upper air. Even with no distinct break between the layers, interface heights defined using the two-layer assumption show evidence of the mixing with a far more uniform layer thickness in the test with an open doorway in room 2.

8. Four Rooms Including Corridor

This data set describes a series of tests conducted in a multiple room configuration with more complex gas burner fires than the previous data set. This study [31] was included because, in many ways, it is similar to the smoke movement study performed at NBS, and permits comparisons between two different laboratories. In addition, it expands upon that data set by providing larger and time-varying gas burner fires in a room-corridor configuration.

8.1 Available Data in the Test Series

Following the subjective ratings discussed in section 4, the following set of ratings were apparent from the examination of the test data:

heat release rate (of fire, through vents, etc.)	+
interface height	+
layer temperatures	+
wall temperatures (inside and out)	−
gas concentrations	+
species yields	+
pressure in room	+
mass flow rate	−
radiation to the floor	−
mass loss	+
mass loss rate	+
heat of combustion	+

This data set provides a widely varied set of room configurations and quantities that could be predicted by current fire models for varied fire sizes. Since all fires were gas burner fires, simulation should be straightforward.

8.2 General Description of the Test Series

Early enclosure fire tests have been conducted for comparison with fire models involving a single room with natural ventilation through open doors and windows to a large laboratory space. This study was performed to collect data allowing for variations in fire source, ventilation, and geometry, especially for situations with closed doors. This test program was carried out at Factory Mutual Research Corporation (FMRC) in West Glocester, RI, in which 60 fire experiments were conducted in a multiple-room enclosure to furnish validation data for theoretical fire models.

This program was to furnish validation data for theoretical fire models of multiroom fire situations with particular emphasis on health care facilities and no specific conclusions were reached. The data were made available to NBS for further analysis and for making model comparisons.

8.3 Test Facility

Figure 25 shows a diagram of the basic facility with indications of instrumentation location. The facility was built on the floor of FMRC's fire test building, using part of the 67×76 m test building where the ceiling height is 18.3 m. The layout in figure 25 shows a burn room and two target rooms connected to a corridor. The corridor was 2.43 m wide×18.89 m long×2.43 m high. The burn room measured 3.63 m deep×3.64 m wide×2.45 m high; a sealable window opening, measuring 0.85 m square, was centered on the rear wall, 0.34 m down from the top, and a door, measuring 0.92×2.05 m high, was centered on the front wall (opening to the corridor). For closed window experiments, the wood-framed Marinite I™[1] window cover was pressed against a bead of caulking around the steel window frame and held by drop bars positioned into slots on the outside wall.

Room 3, located opposite the burn room, measured 3.65 m deep×3.64 m wide×2.45 m high; a

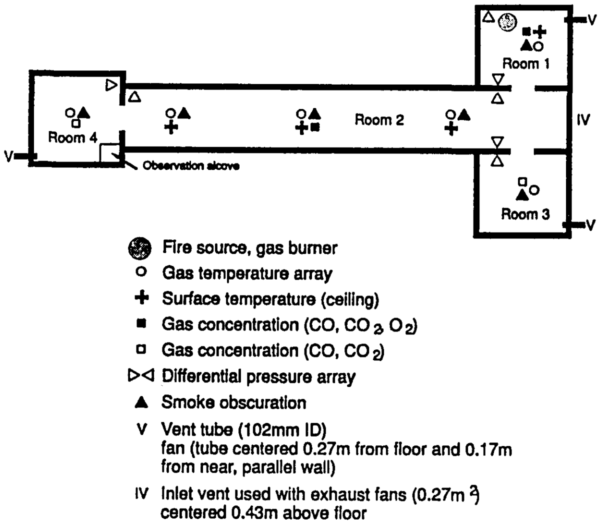

Figure 25. Schematic of facility with instrumentation for four room tests with a corridor.

---

[1] Certain commercial equipment, instruments, or materials are identified in this paper to specify adequately the experimental procedure. Such identification does not imply recommendation or endorsement by the National Institute of Standards and Technology, nor does it imply that the materials or equipment identified are necessarily the best available for the purpose.

door, measuring 0.88×2.02 m high, was centered on the front wall (opening to the corridor). Room 4, located at the opposite end of the corridor, measured 3.65 m deep×3.65 m wide×2.43 m high and had a 0.88×2.02 m high door centered on the front wall (opening to the corridor); an observation alcove, measuring 1.28×0.86×1.99 m high, was located in the front corner of room 4. Each room was equipped with a 102 mm i.d. vent tube with a 61 mm i.d. orifice meter and thermocouple, with option of exhaust fan (tube centered 0.27 m from the floor and 0.17 m from the closest parallel wall). An inlet vent (0.29 m square) used with exhaust fans was centered 0.43 m above the floor at the end of the corridor between the burn room and room 3. When not in use, the inlet vent was sealed with a gypsum board cover taped in place.

The target room doors were commercial fire doors (wood-faced composite doors with calcium silicate cores, 1½ h rated) mounted on 16 gage steel frames. The burn room door was fabricated from 12.7 mm Marinite I™, mounted in a steel frame lined with Marinite I™. Details of the doors and the spacings (cracks) are given in the original reference [31]. The reader is advised to consult that report if leakage requirements are needed. A summary of the room and door (vent) dimensions is given in table 15.

Gypsum wallboard, 12.7 mm thick, on wood studs was used throughout the experimental facility. In addition, the walls and ceiling of the burn room were overlaid with Marinite I™, also 12.7 mm thick, to harden against repeated fire exposure. The existing concrete floor of the test building was used.

In figure 26, the instrument clusters, or instrument stations, are numbered 1 through 9. This figure also shows the locations of the instrument stations along with detailed interior dimensions and placement of the fire source. The instrument locations correspond to the vertical thermocouple array of each instrument cluster; locations in the rooms were at the geometric center and, in the corridor, half way between the side walls. These are summarized in table 16.

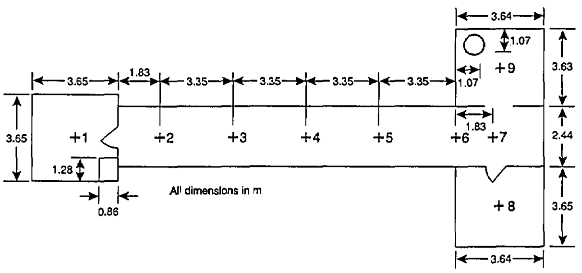

Figure 26. Locations of instrument stations and fire source for four room tests with a corridor.

Table 15. Room and vent sizes for four room tests with a corridor

Location[a]	Room	Vent	Dimensions (m)[b]
Room 1 (burn room)	√		3.64×3.63×2.45
Doorway, room 1 to room 2 (burn room doorway)		√	0.92×2.05×0.40
Window, room 1 to ambient (burn room window)[c]		√	0.85×0.85×0.34
Room 2 (corridor)	√		2.43×18.89×2.43
Doorway, room 2 to room 3 (target room 1 doorway)		√	0.88×2.02×0.43
Doorway, room 2 to room 4 (target room 2 doorway)		√	0.88×2.02×0.43
Room 3 (target room 1)	√		3.64×3.65×2.45
Room 4 (target room 2)	√		3.65×3.65×2.43

[a] Notation used for rooms and vents were changed from the original report to be consistent throughout this report. For reference, names used in the original report are shown in parentheses.

[b] For rooms, dimensions are width×depth×height. For vents, dimensions are width×height×soffit depth.

[c] Closed during some tests.

[d] An observation alcove measuring 1.28×0.86×1.99 m was located in the corner of room 4 reducing the total volume of the room.

Table 16. Location of instrumentation for four room tests with a corridor

Room location[a]	Measurement type[b]	Position[c]
Room 1 (burn room)	Gas temperature array (station 9)	0.26, 0.66, 1.07, 1.48, 1.88, 2.19, 2.34, and 2.39 m
	Surface temperature	Ceiling
	Gas concentration, CO, CO_2, and O_2	1.48 m
	Smoke obscuration array	0.26, 1.07, 1.88, and 2.39 m
	Differential pressure (wall pressure taps)	Two locations at 2.05 m
Doorway, room 1 to room 2	Differential pressure (wall pressure taps)	2.05 m
Room 2 (corridor)	Gas temperature arrays (stations 2–7) 3, 4, and 5)	0.26, 0.66, 1.07, 1.48, 1.88, 2.19, 2.34, and 2.39 m
	Surface temperatures (stations 3, 5, and 7)	Ceiling at three locations
	Gas concentration, CO, CO_2, and O_2 (station 4)	Center of corridor, CO, CO_2, and O_2 at 1.48 m, CO_2 at 0.26 and 2.39 m
	Smoke obscuration arrays (stations 2, 4, and 6)	Three locations at 0.26, 1.07, 1.88, and 2.39 m
	Differential pressure (wall pressure taps)	Corridor end near room 4 at 2.05 m
Doorway, room 2 to room 3	Differential pressure (wall pressure taps)	2.05 m
Room 3 (target room 1)	Gas temperature array (station 8)	0.26, 0.66, 1.07, 1.48, 1.88, 2.19, 2.34, and 2.39 m
	Gas concentration, CO, CO_2	1.48 m
	Smoke obscuration array	0.26, 1.07, 1.88, and 2.39 m
Room 4 (target room 2)	Gas temperature array (station 1)	0.26, 0.66, 1.07, 1.48, 1.88, 2.19, 2.34, and 2.39 m
	Gas concentration, CO, CO_2	1.48 m
	Smoke obscuration array	0.26, 1.07, 1.88, and 2.39 m
	Differential pressure (wall pressure taps)	2.05 m

[a] Notation used for rooms and vents were changed from the original report to be consistent throughout this report. For reference, names used in the original report are shown in parentheses.

[b] Notation used for instrumentation was changed from the original report to be consistent throughout this report. For reference, names used in the original report are shown in parentheses.

[c] Distances are measured from floor.

Gas phase thermocouples were chromel-alumel, 28 gage, insulated with glass braid, except in the burn room where magnesium oxide insulation in 1.6 mm diameter inconel sheathing was used. The wire bundles of the vertical thermocouple arrays entered through the ceiling and were kept taut with steel springs anchored in the concrete floor; the beads extended on horizontal wire a distance of 50 mm to the side of the wire bundles. Chromel-alumel "cement on" thermocouples were used to measure ceiling surface temperatures. All thermocouple wires were connected to 20 gage extension wire immediately outside the enclosure for connections to building signal stations.

The photometers were fabricated according to NBS design [44]. The lamp was operated at an estimated color temperature of 2425 K. The light receiver was a 1P39 phototube with a filter to correct its spectral response approximately to that of the human eye. A 1 m beam length was used and the units in a vertical array were mounted in a rack made from slotted angle framing. The phototube output was transmitted unamplified across a 167 kΩ load resistor to the data acquisition computer. The system response time to sudden blocking of the light beam was about 4 s (to 63 percent attenuation of output). The turbidimeter measured obscuration of light by smoke at three discreet wavelengths, 0.4579 μm (red), 0.6328 μm (blue), and 1.060 μm (infrared). These meters were operated with a beam length of 0.346 m. Response times to sudden obscuration have been estimated at less than 1 ms. The three-wavelength technique can be used to determine smoke particle size and concentration. Responses of photometers and turbidimeters were reduced to smoke extinction coefficient.

The bidirectional flow probe was of standard design [13] with a diameter of 22 mm; it was connected to a Datametrics™ electronic manometer.

Gases were sampled through vertical 12.7 mm o.d. and 9.4 mm i.d. stainless steel tubing, coupled to 12.7 mm o.d. and 9.7 mm i.d. polyethylene tubing above the roof of the enclosure. About 63 m of the polyethylene tubing led from each of the steel sampling tubes to a manifold in the overhead space of the test building, near the gas analyzers, the manifold being exhausted to the atmosphere at a total estimated rate of 4 L/s. Ahead of the manifold, individual sampling lines were joined to the polyethylene sampling tubes for delivering gas samples to respective gas analyzers via glass wool particulate filters, moisture condensers (ice bath), dryers, pumps, and flowmeters. Beckman™ analyzers were employed for oxygen (paramagnetic), carbon monoxide (infrared), and carbon dioxide (infrared). Analyzers were calibrated at the start of each test day. Delay times from the instant of exposure to a constant gas concentration at the open end of a sampling tube to 63 percent of full response of an analyzer were measured at the beginning of the test program and checked at intervals thereafter.

Smoke detectors selected for the program included an ionization type and a photoelectric type. Both types were mounted into separate base units in quick-connect or disconnect fashion. Both the ionization and photoelectric units were designed to alarm when smoke in the detection chamber reached a threshold density. Additionally, the photoelectric unit supposedly had a feature which would lower the threshold for fast rates of rise in smoke density, but this feature may not have been important in this test program.

All pressure differentials from wall pressure taps were recorded on Datametrics™ electronic manometers.

The 102 mm i.d. vent tubes, described above, were 1.63 m long and were provided with an orifice meter and a thermocouple. Pressure differentials across the 61 mm diameter orifice meter, positioned at mid-length and provided with flange connections, were measured with pressure transducers manufactured by Setra Systems™. The thermocouple in each tube was positioned on the tube axis, 0.51 m from the orifice away from the room. Where needed, a Dayton™ fan was coupled to the open end of each vent tube to provide forced exhaust; throttling to desired flow rate was achieved with adhesive tape across the discharge of each fan.

The data were recorded at a rate of one scan per second on the building data acquisition system. The data acquisition computer also controlled the fuel control system where required, i.e., in the automatic growing fire mode. Except thermocouple signals, reduced directly to temperatures by the building data acquisition system, all data reductions were made on computer facilities in FMRC's Norwood Laboratories from raw data tapes.

8.4 Experimental Conditions

Three types of fire sources were used: 1) steady propylene fires at 56 kW on a 0.30 m diameter (sandbox) burner and 522 kW on a 0.91 m diameter burner; 2) propylene fires on the 0.91 m diameter burner programmed under computer control to grow with the square of time, exceeding 1 MW in 1, 2, 4, or 8 min; and 3) a naturally growing fire in a configuration of so-called "Standard Plastic Commodity," a Factory Mutual test fuel consisting of corrugated boxes with polystyrene tubs in compartments (test 60 only—not discussed in this report).

The 0.91 m diameter, 0.58 m high propylene burner was used for most of the tests. Its design was adopted from D'Souza and McGuire [72] and consisted of a 12 gage steel container with a gas distributor near the bottom, filled with gravel to the 67 percent height, where there was wire mesh screen, and coarse sand to the full height of the burner. The 0.30 m diameter burner was a scaled-down version of similar design. When in use, this burner was placed in a central cavity scooped out of the sand above the screen of the larger burner so its top was level with the top of the larger burner; the sand was back-filled and screeded to present a smooth, unbroken top surface with the burner rims. Ignition was by a propane pilot flame established by a spark at the burner periphery wall before the start of a test; ignition occurred when propylene gas was admitted to the burner. Propylene was selected as a fuel because of its high production of smoke, which made the fire gases easily traceable by the eye and the optical devices.

The 0.91 m diameter propylene burner was calibrated using the FMRC fire products collector located in the fire test building. This device gathers combustion products from a test fire below an inlet cone and then conditions the flow to one of uniform velocity, temperature, and species concentrations. Single-point measurements of temperature and species concentrations, together with the known flow rate, lead to the determinations of heat release, yields of CO and CO_2, yields of particulates, and flux of optical density.

Total heat release rate ($\dot{Q}_t$) was determined from mass flow rate and generation rates of CO_2 ($\dot{m}_{CO_2}$) and CO ($\dot{m}_{CO}$). Convective heat release rate ($\dot{Q}_c$) was determined from mass flow rate and temperature rise. Particulate yield rates ($\dot{m}_p$) were established using particle mass concentrations (C_p), together with the mass flow rate. Flux of optical density in the collector was defined as $D_u \cdot \dot{v}$, where D_u is the optical density (per unit length) and is the volumetric flow rate in the collector duct. Optical density was determined from a photometer of the kind installed in the multi-room enclosure and mounted across the collector duct.

The fuel control for the burners was designed to deliver gas flow to provide energy release rate increments of 32 kW, up to a maximum of 2 MW. Combinations were provided manually with electrical switches, or controlled automatically with the data acquisition computer to generate parabolically growing fires ($\dot{Q}_t \propto t^2$). The calibrations were performed in the automatic mode. Two different automatic modes were employed, one with a design "growth time" $t_g = 240$ s and one with $t_g = 480$ s. ("Growth time" is the time for a parabolically growing fire to exceed 1 MW.)

Calibration results are presented in figure 27. Shown in this figure are the mass generation rate of particulates in ratio to the fuel mass rate and the ratio of generation rates of CO to CO_2, clearly showing an effect of fire size.

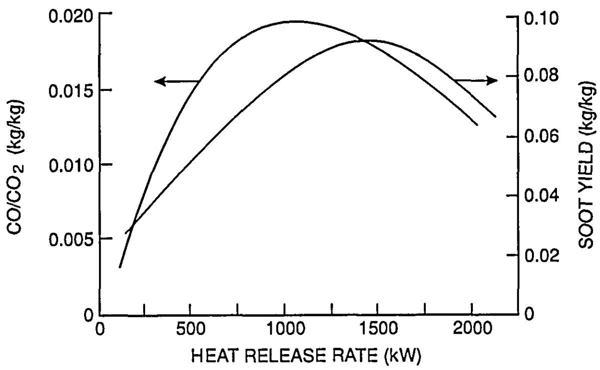

Figure 27. CO, CO_2, and soot yields from calibration of a 0.91 m gas burner used in four room tests with a corridor.

Figure 28 shows the growth of heat release rate during the calibration run for $t_g = 480$ s. Small drops in gas supply pressure occurred during the run as additional orifices were actuated, resulting in somewhat lower growth rates than would have been the case otherwise. The calibration results discussed in the preceding paragraph have been referenced to a constant gas supply pressure of 274 kPa. During fire tests, deviations of the gas supply pressure from the reference value were reduced by manual adjustments of the pressure regulator for the gas supply.

The 0.31 m diameter propylene burner did not provide enough heat output for accurate measurements in the large fire products collector. Instead, a smaller, but similar, device located at FMRC's Norwood Laboratories was used. Measurements of yield were made for 1, 2, 3 (1 and 2 flow units in parallel), and 4 nominal flow units. The results are summarized in table 17. It is seen that the total heat release rates per flow unit (FU) average about 27 kW vs 32.6 kW for the larger burner. The convective fraction, $\dot{Q}_c/\dot{Q}_t$, averages 0.59, consistent with the result for the larger burner. The mass yield ratios, $\dot{m}_{CO}/\dot{m}_{CO_2}$, and particulate yields, $\dot{m}_p/\dot{m}_f$, may be compared to the results for the larger burner (fig. 27). Only the two-flow unit orifice was used with the smaller burner in the fire tests. An output of 26.9 kW per flow unit is shown in table 17 for this orifice and, hence, the output for the nominal two-flow unit burner will be indicated as $2.10 \times 26.9 = 56$ kW.

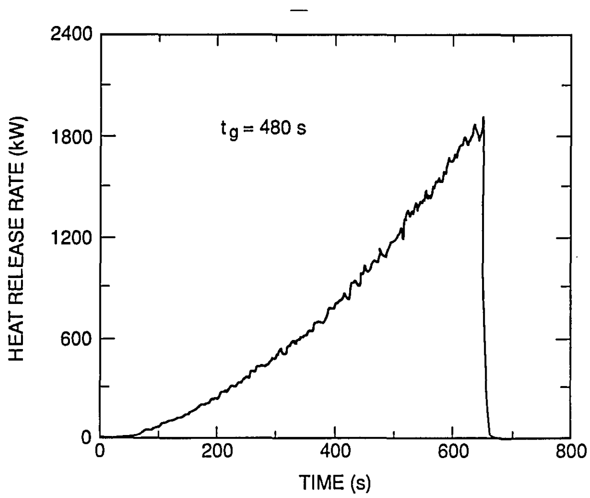

Figure 28. Parabolic fire growth during calibration of 0.91 m diameter propylene burner for four room tests with a corridor.

Table 17. Calibration of 0.31 m diameter propylene burner

Orifice normal no. of flow units	Orifice actual no. of flow units	$\dot{Q}_t$(kW)	$\frac{\dot{Q}_c}{\dot{Q}_t}$	$\frac{\dot{m}_{CO}}{\dot{m}_{CO_2}}$	$\frac{\dot{m}_p}{\dot{m}_f}$
1	0.97	25.6	0.58	0.0126	0.081
2	2.10	56.5	0.60	0.0105	0.083
3	3.07	86.3	0.60	0.0095	0.076
4	3.91	105.2	0.57	0.0094	0.071

Starting with test 38, tests were performed to investigate smoke migration in certain ventilation conditions. A sealed partition (fig. 29) was provided between stations 3 and 4 (as identified in fig. 26). Figure 29a is a plan view of the region, showing the instrument stations, the partition (gypsum board on a frame of wood studs with silicone caulking around the perimeter), and the location of ceiling diffusers. As evident in figures 29b and 29c, the diffusers were ducted together into a common horizontal duct, continued as a vertical round tube (aluminum) with an orifice meter ($\beta = 0.6$) and thermocouple, followed by horizontal and vertical round ducts (steel) into the wall of a plenum. Figure 29d is a side view of the plenum (steel pipe), showing the entering duct and the inlet of a blower being open to the building space. The blower connection just described (bottom of fig. 29d) was employed when the venting system was in the "return mode," i.e., with air being drawn into the ceiling diffusers in the corridor. Suction was provided by sub-atmospheric pressures in the plenum developed as a venturi effect by air drawn into the plenum from the building space by the blower; the air flow, suction pressure, and hence the vent flow were controlled with a louvered damper at the exit of the blower. The blower connection shown at the top of figure 29d, with the blower discharge connected via a rectangular-to-round transition to the plenum was used when the venting system was in the "supply mode," i.e., with air being discharged through the ceiling diffusers into the corridor. The discharge was observed to occur in two oppositely directed ceiling jets, away from the vent, generally

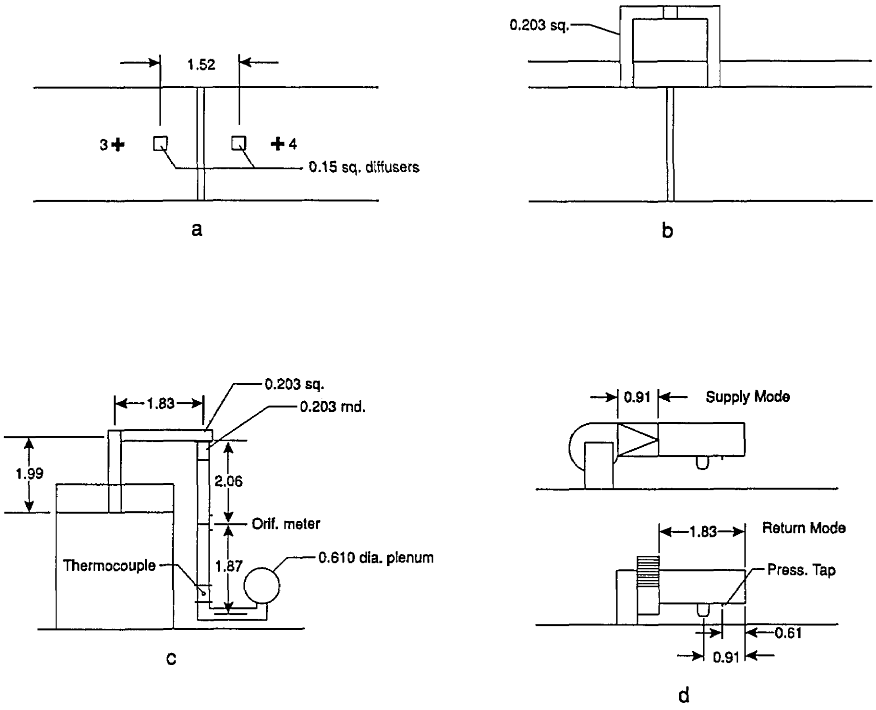

Figure 29. Corridor partition with ventilation ducting for four room tests with corridor.

aligned with the length of the corridor. At 0.20 m from the vent, the ceiling jets had a maximum depth of about 0.10 m and a width of about 0.4 m. In this case, a positive plenum pressure and the desired vent flow were generated by partially obstructing the open end of the plenum with a plate. Because the blower had to be elevated in this mode, the top section of the vertical round duct in figure 29c had to be replaced with a shorter section.

The blower capacity and plenum were so large that the plenum pressure was practically independent of any flow to and from the corridor ceiling vents. Thus, the plenum may be considered to be a constant pressure plenum in both the return and supply modes, regardless of any fire activity. Total mass venting rates were determined from the pressure differential across the orifice meter together with the flow temperature indicated by the thermocouple. Plenum pressures relative to the atmosphere were determined with a Setra Systems™ transducer connected to the plenum tap indicated in figure 29d.

When the vents were operated in a return mode at approximately 170 g/s total flow with no fire, the plenum pressure was 249 Pa below atmospheric pressure (82 Pa drop in each of the vent ducts before joining and 167 Pa pressure drop in remaining ducting to the plenum, according to experiments). When the vents were operated in a supply mode at approximately 170 g/s total flow with no fire, the plenum pressure was 284 Pa above atmospheric pressure (184 Pa pressure drop from plenum through common ducting and 100 Pa pressure drop in individual ducts to the vents, according to experiments).

A total of 60 tests were conducted over a period of 4½ months. Tables 18, 19, and 20 list the experimental conditions for each test.

The column "HRR" in table 18 indicates the heat release characteristics of the source fires. The entries 56 kW and 522 kW refer to steady total heat release rates at the levels indicated for the 0.30 m diameter and 0.91 m diameter burners, respectively. The entries 60 s, 120 s, 240 s, and 480 s refer to fires growing with the square of time (0.91 m diameter burner), exceeding 1 MW total heat release rate at the indicated growth times.

"Forced vent" indicates whether forced ventilation (exhaust) was provided for the vent tube attached to each of the three rooms. An entry of a number in units of g/s refers to the approximate mass exhaust rate set in each vent tube before each experiment.

The columns "Room 1 door" and "Room 1 window" refer to the dispositions of the door to the burn room and the burn room window, respectively, i.e., open or closed.

Tests 38 to 47 incorporated a partition in the corridor (room 2). The last column in table 20 indicates the mode in which the ceiling vents on either side of the partition were: "None" (ceiling vents blocked); "Natural" (enclosure fires to vent through venting system in response to fire pressures); "170 g/s Ret." (venting in return mode and set at 170 g/s prior to experiment); and "170 g/s Sup." (venting in supply mode and set at 170 g/s prior to experiment).

Starting with test 48 (table 19), the corridor partition was removed, the ceiling vents blocked, and the modifications made for accommodating flashover targets in the burn room (not of interest in this report and, consequently, not described).

The smoke detectors were always cleaned with a vacuum cleaner before each test or replaced with a new unit if the preceding test or a pretest with a smoke source (smoldering or flaming paper towel) indicated malfunctions. Starting with the increased heat release rate fires, test 16 onwards, the detectors in the burn room were removed in anticipation of certain destruction in each test.

After test 25, a crack was discovered in the Marinite™ ceiling over the fire source. The affected ceiling area was reinforced with an overlay of 12.7 mm thick Marinite I™, screwed through the existing ceiling into ceiling joists; the overlay measured 1.22 m × 1.65 m.

8.5 Examples of Data from the Test Series

Two examples of data from this test series are shown below:

- CO and O_2 concentrations in the four rooms of the test structure for two experiments in the test series (fig. 30).

- Pressure differences between rooms of the test structure for two experiments in the test series (fig. 31).

9. Multiple-Story Building

By far the most complex set of tests described in this report, this data set describes a series of full-scale experiments conducted to evaluate the current approach to zoned smoke control systems,

Table 18. Experimental conditions for steady state fires

Test	Burner diam.	HRR	Doors (rooms 3 & 4)	Forced vent	Room 1 door	Room 1 window	Room 2	
							Partition	Ceiling vent
1	0.30 m	56 kW	closed	none	open	closed	no	none
2								
3						open		
4					closed	closed		
5						open		
6					open	closed		
7			open					
8								
9					closed			
10						open		
11					open			
12			closed	18 g/s		closed		
13				9 g/s				
14					closed			
15				18 g/s				
16	0.91 m	522 kW		none	open			
17								
18						open		
19			open					
20			closed		closed			
21			open		open	closed		
22					closed			
23			closed	36 g/s	open			
24				72 g/s				
25				144 g/s				

with and without stairwell pressurization [73]. It was conducted in a seven story hotel with multiple rooms on each floor and a stairwell connecting to all floors. This data set was chosen because it would be considered beyond the scope of most current fire models.

9.1 Available Data in the Test Series

Following the subjective ratings discussed in section 4, the following set of ratings were apparent from the examination of the test data:

Table 19. Experimental conditions for growing fires

Test	Burner diam.	HRR	Doors (rooms 3 & 4)	Forced vent	Room 1 door	Room 1 window	Room 2	
							Partition	Ceiling vent
26	0.91 mm	240 s	closed	none	closed	open	no	none
27					open	closed		
28		120 s						
29					closed	open		
30			open		open	closed		
31		240 s						
32			closed			open		
33			open					
34		120 s						
35		240 s			closed	closed		
36		120 s	closed		open	open		
37			open		closed	closed		
48		240 s			open	closed	no	
49								
50			closed		closed	open		
51			open		open	closed		
52			closed		closed	open		
53								
54								
55			open		open	closed		
56								
57		120 s						
58		60 s						
59		480 s						

heat release rate (of fire, through vents, etc.)	–	pressure in room	+
interface height	+	mass flow rate	–
layer temperatures	+	radiation to the floor	–
wall temperatures (inside and out)	–	mass loss	–
gas concentrations	+	mass loss rate	–
species yields	–	heat of combustion	–

Table 20. Experimental conditions for tests with corridor partition

Test	Burner diam.	HRR	Doors (rooms 3 & 4)	Forced vent	Room 1 door	Room 1 window	Room 2	
							Partition	Ceiling vent
38	0.91 m	240 s	open	none	open	closed	yes	none
39								natural
40		120 s						
41		240 s						170 g/s return
42						open		natural
43								170 g/s return
44		120 s						natural
45		240 s				closed		170 g/s supply
46						open		
47								none

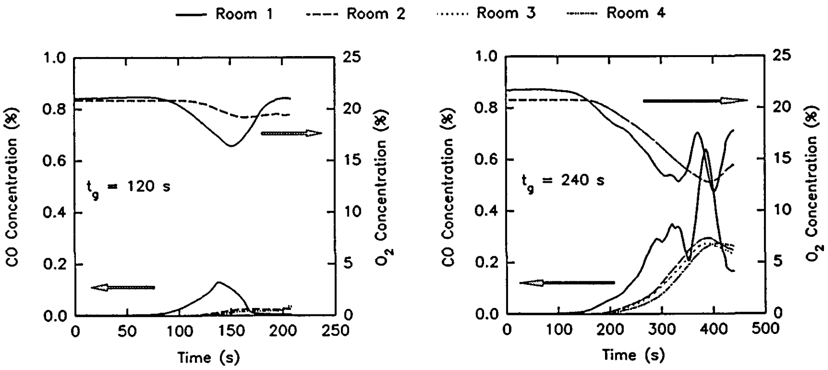

Figure 30. Carbon monoxide and oxygen concentrations in the four rooms during two experiments for four room tests with a corridor.

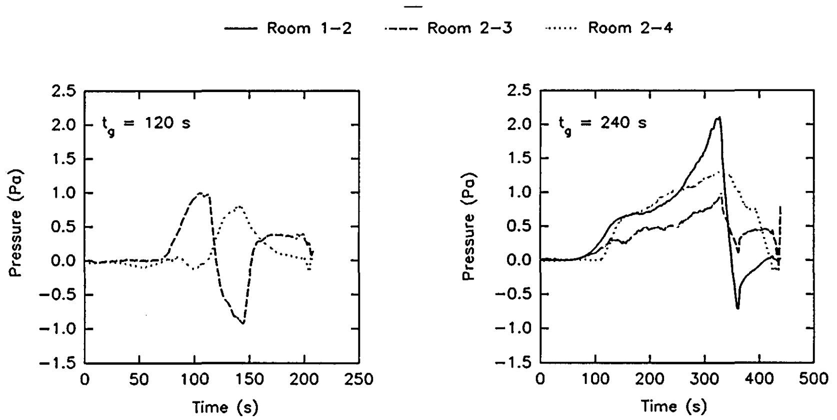

Figure 31. Pressure differences measured in room doorways during two experiments of four room tests with a corridor.

Measured pressure differences between floors of the building and between the stairwell and fire floor of the building are extensive and consistent throughout the test series. For modeling purposes, mass loss rate and heat release rate would have to be estimated. The work of Quintiere and McCaffrey [10] or Babrauskas et. al. [70] could be used to provide such estimates.

9.2 General Description of the Test Series

Smoke movement and the performance of smoke control systems were studied in a seven story building with smoke generated from wood fires and from smoke bombs. A total of 12 single experiments were conducted under a variety of conditions: two different fire sizes; sprinklered vs non-sprinklered wood fires; zoned smoke control on or off; stairwell pressurization on or off; with and without ventilation to the outside; and open and closed doors. As expected, in these experiments the zoned smoke control system prevented smoke migration beyond the fire floor.

The relevant conclusions from this study can be summarized as follows:

- For persons trapped above the neutral plane and exposed to smoke from a fire below the neutral plane, the exposure times of concern are of the order of 20 minutes to several hours.

- For fires of this experimental series, the zoned smoke control system effectively maintained positive pressurization around the fire floor.

- The change in mass (dm/dt) of the gases on the fire floor (or in the smoke zone) can have an adverse effect on smoke control system performance. This effect can be mitigated if the exhaust flow rate is sufficiently large.

- High temperature gases going through a smoke control exhaust fan can result in a significant loss in system pressurization.

- With few exceptions, smoke bombs should not be used for acceptance tests.

9.3 Test Facility

The Plaza Hotel building was a masonry structure consisting of two wings, one three stories and the other seven stories tall. The two wings were built at different times. The wings were connected to each other at only one location on each floor. The connections between the wings at each floor were sealed off, and the fires were set on the second floor of the seven-story wing (fig. 32), using the shorter wing as an instrumentation area. Areas of the second floor were fire hardened to minimize structural damage to the building. The walls were covered by a 12.7 mm layer of calcium silicate board over a 12.7 mm layer of Type X gypsum board attached to wood furring strips. The ceilings were protected by similar layers of calcium silicate and gypsum board attached to the bottom of the ceiling joists made of commercial steel studs. The floors were protected by calcium silicate board extending about 3 m outward from the fire and by Type X gypsum board for the remainder of the fire hardened areas. The dimensions of the rooms and vents are listed in table 21.

The smoke control systems were designed using the methods presented in the ASHRAE smoke control manual [74], and the design analysis is discussed in detail by Klote [75]. The minimum design pressure difference was 25 Pa (0.10 in H_2O), meaning that the system should be able to maintain at least this value without a fire. The intent was that the system should function satisfactorily under the

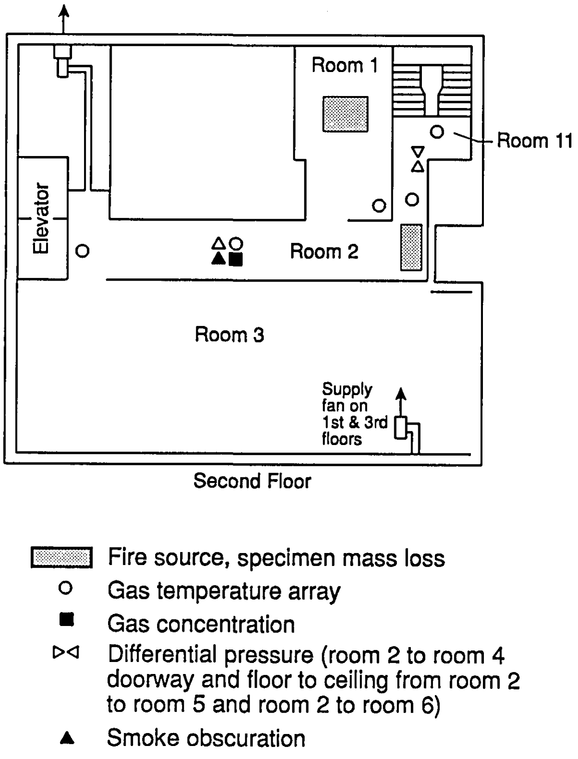

Figure 32. *Plan view of one floor for multiple-story building tests (second floor shown).*

Table 21. Room and vent sizes for multiple story building tests

Location[a]	Room	Vent	Dimensions (m)[b]
Room 1 (2nd floor burn room)	√		6.2×6.2×2.3
Doorway, room 1 to room 2 (2nd floor burn room doorway)		√	0.78×2.1×0.22
Window, room 1 to ambient[c] (burn room window)		√	1.2×1.2×0.37
Room 2 (corridor)	√		1.9×14.6×2.6
Doorway, room 2 to room 3		√	0.78×2.1×0.5
Doorway[d], room 2 to room 4 (2nd floor corridor to stairwell)		√	0.016×2.1×0.5, tests 1–3 0.03×2.1×0.5, tests 4–12
Room 3 (remainder of 2nd floor)	√		10.3×10.3×2.7
Rooms 4, 5, 6, 7, 8, 9, and 10 (basement, 1st, 3rd, 4th, 5th, 6th, and 7th floors)	√		13.3×13.3×2.6
Doorways[d], rooms 4, 5, 6, 7, 8, and 9 to room 11 (basement, 1st, 3rd, 4th, 5th, and 6th floors to stairwell)		√	0.03×2.1×0.5
Doorway[d], room 10 to room 11 (7th floor to stairwell)		√	0.016×2.1×0.5, tests 1–3, 12 0.91×2.1×0.5, tests 4–11
Room 11 (stairwell)	√		3.0×4.1×21.5
Doorway[d], room 11 to ambient (stairwell to outside at basement)			0.016×2.1×0.5, tests 1–5, 10–11 0.91×2.1×0.5, tests 6–9, 12

[a] Notation used for rooms and vents were changed from the original report to be consistent throughout this report. For reference, names used in the original report are shown in parentheses.

[b] For rooms, dimensions are width × depth × height. Room dimensions are approximate. Only total volume and ceiling heights were noted in the original report. For vents, dimensions are width × height × soffit depth.

[c] Only for test 12.

[d] An average value is used for leakage areas around doors to stairwell. Other leakage paths from floors were noted in the report but not quantified (elevator shaft, building wiring, spiral stairs). These may need to be estimated to obtain accurate model predictions.

most challenging conditions likely to occur during a fire. This level of pressurization is recommended by the National Fire Protection Association [76] for smoke control in unsprinklered buildings. The design pressure difference incorporates the effects of fire in the form of a buoyancy term plus a safety factor, as explained in the Appendix of NFPA 92A. A general discussion of design pressure differences is provided by Klote [77].

In general, the design analysis should be based on likely conditions of open doors and windows; also, the direct effects of the fire must be included in the selection of the minimum design pressure difference. This is the approach evaluated by this project. The design analysis did not include a broken fire room window as one of the likely fire conditions. The importance of this window was not apparent at the start of the project.

In zoned smoke control, the building is divided into a number of zones. These zones may be separate floors, or even a number of floors together. The zone in which the fire occurs is called the smoke zone. For the experiments of this project, each floor of the building was a smoke zone.

Exhausting air from the smoke zone results in air from the outside and from other zones being pulled into the smoke zone. This air flowing into the smoke zone can provide oxygen for the fire. Smoke control systems frequently are designed to exhaust and supply air at six air changes per hour. Most commercial air-conditioning systems are capable of moving about four to six air changes per hour, which probably accounts for the popularity of six air changes in smoke control applications. Current designs are based on the assumption that the adverse effect of supplying oxygen at six air changes per hour is not significant in comparison with the benefit of smoke control. For these reasons, the tests described in this report were conducted at six air changes per hour.

The Plaza Hotel building had no central forced-air heating, ventilating, and air-conditioning (HVAC) system, so a dedicated system of fans and ducts was installed for zoned smoke control and stairwell pressurization. The smoke control system consisted of the three 0.944 m^3/s (2000 cfm) centrifugal fans shown in figure 32, plus another centrifugal fan (not shown) located outside and supplying 4.25 m^3/s (9000 cfm) of pressurization air to the stairwell at the first floor. The smoke control system is illustrated in figure 33. All the test fires were located in the second floor smoke zone. This smoke was exhausted at about six air changes per hour. The first and second floors were pressurized at about six air changes per hour. When the stairwell pressurization system was activated, the exterior stairwell door was open. This approach is intended to minimize fluctuations due to opening and closing doors.

To measure temperatures, pressure differences, gas concentration, smoke obscuration, and wind speed and direction, over 4 km (2½ miles) of wire were installed between the instruments and a data acquisition system. The instruments used in this test series are shown in figure 32 and are listed in table 22. All instrumentation channels were recorded at 20 s intervals. More instrumentation was used than was necessary for the evaluation of the effectiveness of a smoke control system with the view that it would be valuable for later computer simulation of the experimental fires.

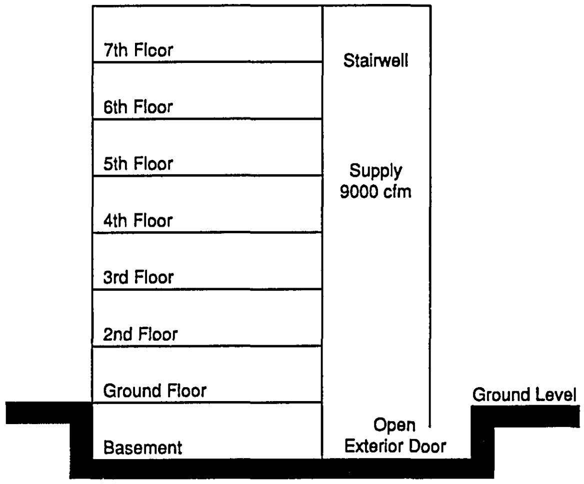

1. The second floor is the smoke zone, and it is exhausted at about six air changes per hour.
2. The first and second floors are pressurized at about six air changes per hour.
3. The stairwell is pressurized by 9000 cfm, and the exterior stairwell door remains open throughout pressurization.

Figure 33. Schematic of the smoke control system for multiple-story building tests.

Temperatures were measured on the fire floor and the other floors at locations shown in figure 32. Additionally, outside air temperature, second floor exhaust fan outlet air temperature, and inlet air temperature of second floor exhaust duct were measured. These temperatures were measured by bare beaded chromel-alumel (type K) thermocouples made from 24 gage (0.51 mm diameter) wire. The wind speed and direction were measured by a propeller-type transducer located 3 m above the roof of the seven story wing.

Smoke meters developed by Bukowski [44] were used to measure light obscuration in the corridors of floors 2, 3, and 7 1.52 m above floor level. This type of meter is an extinction beam consisting of a collimated light source and a detector separated by a path through the smoke. Smoke obscuration is expressed in terms of smoke extinction coefficient.

Carbon monoxide, carbon dioxide, and oxygen were continuously measured at three locations. On floors 2, 3, and 7, gas sampling probes were located at 1.52 m above the floor in the center of the corridor.

Pressure differences were measured by variable reluctance differential pressure transducers.

9.4 Experimental Conditions

Smoke movement and the performance of smoke control systems were studied with smoke generated from unsprinklered wood fires, sprinklered wood fires, and smoke bombs. All the windows were closed except for the window of the fire-hardened room during test 12, which was left open to simulate the effect of a broken window. For many of the tests, the second floor stairwell door was cracked open 13 mm, simulating the gap of a door warped due to high differential temperatures. The specific doors open, and other test conditions, are listed in table 23.

For the unsprinklered fires, wood sticks were arranged in geometric piles called cribs. The cribs were constructed of fir sticks 38×38 mm×0.61 m long. The sticks were fastened together with 8d

Table 22. Location of instrumentation for multiple story building tests

Room location[a]	Measurement type[b]	Position[c]
Room 1 (2nd floor burn room)	Gas temperature array (thermocouple tree)	61 mm, 0.46, 0.91, 1.37, 1.83, and 2.28 m
	Specimen mass loss	
Room 2 (corridor)	Gas temperature arrays (thermocouple trees)	Two near burn room at 61 mm, 0.48, 0.96, 1.44, 1.92, and 2.39 m near elevator at 61 mm, 0.52, 1.05, 1.57, 2.09, and 2.61 m
	Gas concentration, CO, CO_2, and O_2 (gas analysis)	Center of corridor, at 1.52 m
	Smoke obscuration (smoke meter)	Center of corridor, at 1.52 m
	Differential pressures (pressure differences)	Through floor to room 6 and through ceiling to room 7
Doorway, room 2 to room 11 (2nd floor corridor to stairwell)	Differential pressures (pressure differences)	0.15 and 2.2.3 m
Rooms 4, 5, 6, 7, 8, 9, and 10 (basement, 1st, 3rd, 4th, 5th, 6th, and 7th floors)	Gas temperature array (thermocouple tree)	61 mm, 0.65, 1.31, 1.96, and 2.61 m
	Gas concentration, CO, CO_2, and O_2 (gas analysis)	Test 3, in room 6, 1.52 m test 5, 9, 10, and 11, in room 10, 1.52 m
	Smoke obscuration (smoke meter)	In rooms 6 and 10, 1.52 m
Doorways, rooms 4, 7, and 10 to room 11, (basement, 4th, and 7th floor to stairwell)	Differential pressure (pressure difference)	1.52 m
Room 11 (stairwell)	Gas temperature array (thermocouple trees on each floor)	61 mm, 0.7, 1.4, 2.0, 2.7, 2.8, 3.4, 4.0, 4.7, 5.4, 5.5, 6.1, 6.7, 6.8, 7.4, 8.1, 8.2, 8.7, 9.4, 10.1, 10.8, 10.9, 11.4, 12.1, 12.8, 13.5, 13.6, 14.1, 14.8, 15.5, 16.1, 16.2, 16.8, 17.5, 18.2, 18.8, 18.9, 19.5, 20.2, 20.9, and 21.5 m
	Differential pressures to ambient (pressure differences)	1.5, 12.3, and 20.4 m
	Smoke obscuration array	0.26, 1.07, 1.88, and 2.39 m
Ambient	Gas temperature, wind velocity and wind direction	

[a] Notation used for rooms and vents were changed from the original report to be consistent throughout this report. For reference, names used in the original report are shown in parentheses.

[b] Notation used for instrumentation was changed from the original report to be consistent throughout this report. For reference, names used in the original report are shown in parentheses.

[c] Distances are measured from floor.

common nails. The crib illustrated in figure 34 was 24 layers high and weighed about 68 kg the 24-layer crib was used for most of the tests. The exception was for test 3 in which smaller cribs of 18 layers were used because of concern about possible damage to the building's structural system.

All of the fires used two cribs located in the second floor corridor (fig. 32), except for test 12 in which four 24-layer cribs were located in the fire-hardened room on the second floor. The cribs were stored in a room in the Plaza Hotel without humidity control. However, the moisture content was

Table 23. Experimental conditions

Test	Test type	Fire load[b] kg	Zoned smoke control[c]	Stairwell pressurization[d]	Activation time[e] min	Condition of doors in Room 11 to: Ambient	Room 2	Room 10
1	wood fire	136	off	off		closed	closed	closed
2	smoke bomb		on	″	0	″	″	″
3	wood fire	91	″	″	0	″	″	″
4	smoke bomb		off	″		″	½ inch	open
5	wood fire	136	″	″		″	″	″
6	smoke bomb		on	on	0	open	″	″
7	wood fire	136	″	″	0	″	″	″
8	smoke bomb		″	″	4	″	″	″
9	wood fire	136	″	″	4	″	″	″
10	sprinklered	136	off	off		closed	″	″
11	sprinklered	136	″	″		″	″	″
12	wood fire	272	on	on	0	open	″	closed

[a] All fires in the second floor corridor and all windows closed, except for test 12, where the fire was in the fire-hardened room on the second floor, and the window in that room was open.
[b] Fire load is approximate.
[c] Zoned smoke control consisted of pressurization of first and third floors at 0.94 m^3/s each, and the exhaust of the second floor at the same rate.
[d] Stairwell pressurization consisted of supplying 3.3 m^3/s into the stairwell at the first floor with the exterior basement door open.
[e] Activation time is the time after ignition that the smoke control system and stairwell pressurization system are turned on.
[f] Second floor door designation ½ in indicates that the door was cracked open ½ in.

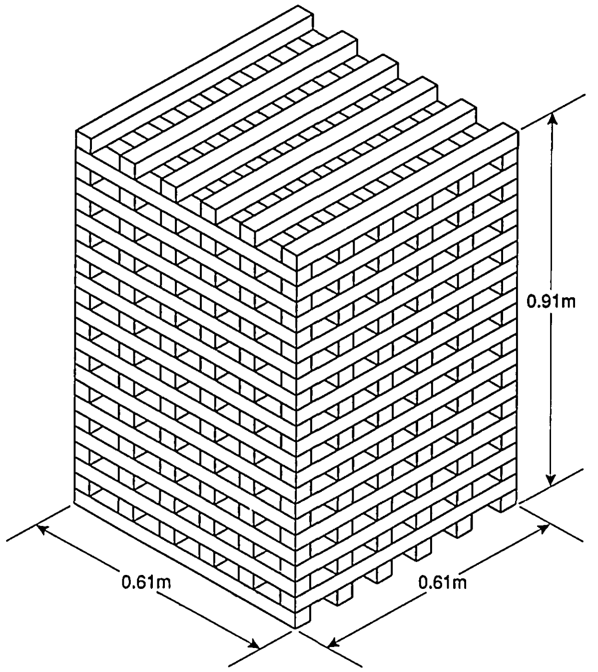

Figure 34. Configuration of nominal 68 kg wood crib used as a fire source for multiple-story building tests.

measured at less than 6 percent for all the cribs. By extrapolation of data for similar cribs burning in free air [78], it was estimated that two 24-layer cribs would have a peak energy release rate of 1.5 MW, and two 18-layer cribs would have a peak energy release rate of 1.0 MW. Four 24-layer cribs would have an energy release rate of 3.0 MW.

A 0.13 m diameter metal pan with 1 L of heptane was centered under each crib as an ignition source; the heptane was ignited with a propane torch.

The sprinklered fires were set in the corridor, as illustrated in figure 32, and two 24-layer cribs as described above were used. Test 10 was with a listed quick-response pendant sprinkler with a 71 °C operating temperature. Test 11 was with a pendant sprinkler with a fusible element operating at 63 °C and a bimetallic disk for on-off operation opening at 74 °C and closing at 35 °C. The sprinklers were located above the cribs about 0.64 m from the center of the two cribs. The deflector of the quick-response sprinkler was 0.10 m below the ceiling, and the deflector of the on-off sprinkler was 0.15 m below the ceiling. The density of spray was measured by collecting water from the sprinklers in pans located so that the pan tops were at the elevation of the top of the cribs. The quick-response sprinkler produced an average density of 0.21 L/s m^2 and the on-off head produced an average density of 0.28 L/s m^2.

The smoke bombs were ignited at the same corridor location as most of the other tests. Three smoke bombs, rated by the manufacturer for a three minute duration, were wired together, placed in a metal container, and ignited.

Because so many complicated detection and activation schemes are in common use, simulation of one particular activation approach would have been of limited value. Thus, it was decided to simulate the extreme conditions of very fast activation and delayed activation. For very fast activation, the smoke control system was activated before ignition for tests 2, 3, 6, 7, and 12. This is considered to be similar to what would happen if the smoke control system were activated rapidly enough so that very little smoke would reach the horizontal barriers of the smoke control system before ignition. A four minute time was arbitrarily selected for the delayed activation for tests 8 and 9.

9.5 Examples of Data from the Test Series

Two examples of data from this test series are shown below:

- Pressure differences between the fire floor and the floors above and below the fire floor for a test with and a test without smoke control (fig. 35).

- Upper layer temperatures for all the experiments in the test series (fig. 36).

Included in the full report of this test series [73] is an analysis of the pressure differences for the tests shown in figure 35. With a simple predictive model developed in the report, calculated pressure differences between the floors agreed quite well with measured values.

10. Summary and Conclusions

BFRL has been working to develop a generic methodology for fire model evaluation. This report has presented documentation of more than 125 individual room fire tests that can be used for comparison with zone-based predictive models. Five different test series were included in the discussion:

- A single room test series with furniture and varied opening sizes,

- A single room test series with furniture and wall burning,

- A three room test series including a corridor with multiple replicates of several different experimental conditions,

- A four room test series including a corridor with large growing fires, and

- A multiple-story building test series with a zoned smoke control system.

Derived outputs from individual raw data elements were developed for all the tests in a single, consistent format together with the mathematical treatment used to make the calculations. Geometry of the room(s) and the measurements taken for all the tests were reviewed and presented using the same nomenclature for all tests, simplifying comparison of data from different tests (from different laboratories).

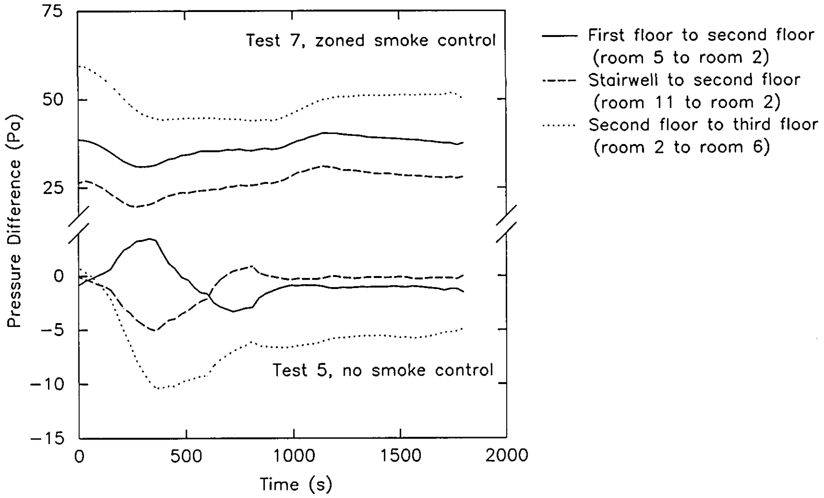

Figure 35. Pressure difference between floors in two multiple-story building tests.

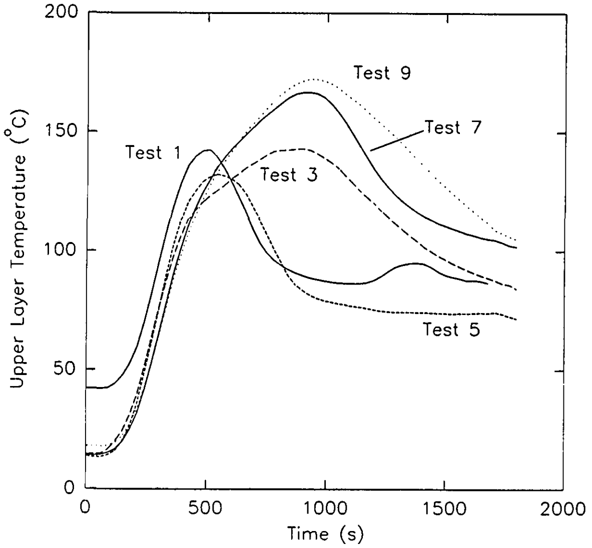

Figure 36. Upper layer temperature during tests in a multiple-story building.

Since the tests to be included in this database were chosen to present a broad range of challenges for the current generation of fire models, the comparisons with current fire models may not always be favorable. In some cases, the tests include physical phenomena not included in some models (such as forced ventilation, flow in long corridors, or multiple stories in a building). Thus this base of data can also be viewed as providing input for model developers to extend the capabilities of the models.

11. References

[1] Breese, J. N., and Peacock, R. D., A Users Guide for RAPID, Reduction Algorithms for the Presentation of Incremental Fire Data, Natl. Bur. Stand. (U.S.), NBS Spec. Publ. 722 (March 1986).

[2] Ingberg, S. H., Tests of the Severity of Building Fires, NFPA Quarterly **22**, 43–61 (1928).

[3] Fire Tests of Office Occupancies at U. S. Bureau of Standards, NFPA Quarterly **19**, 234–237 (1926).

[4] Department of Scientific and Industrial Research and Fire Offices' Committee, Report of the Fire Research Board, with the Report of the Director of Fire Research for the Year 1950, HMSO, London, UK (1951) pp. 24–28.

[5] Croce, P. A., and Emmons, H. W., The Large-Scale Bedroom Fire Test, July 11, 1973 (FMRC Serial No. 21011.4), Factory Mutual Research Corp., Norwood, MA (1974).

[6] Croce, P. A., A Study of Room Fire Development: The Second Full-Scale Bedroom Fire Test of the Home Fire Project (July 24, 1974), 2 vols. FMRC Serial 21011.4. Factory Mutual Research Corp., Norwood, MA (1975).

[7] The Third Full-Scale Bedroom Fire Test of the Home Fire Project (July 30, 1975). Vol. 1 (FMRC Serial 21011.6), authors: R. L. Alpert, A. T. Modak, and J. S. Newman (1975). Vol. 2 (FMRC Serial 21011.7), author: A. T. Modak (1976), Factory Mutual Research Corp., Norwood, MA.

[8] Emmons, H. W., The Home Fire Viewed as a Scientific System, Society of Fire Protection Engineers, SFPE Technology Report 77-5 (May 1977).

[9] Modak, A. T., and Alpert, R. L., Influence of Enclosures on Fire Growth. Vol. 1: Guide to Test Data, Alpert, R. L. et al., and Test 0 through Test 7. FMRC Serial No's. OAOR2.BU-0 through 8, Factory Mutual Research Corp., Norwood, MA (1977).

[10] Quintiere, J. G., and McCaffrey, B. J., The Burning of Wood and Plastic Cribs in an Enclosure, 2 vols., Natl. Bur. Stand. (U.S.), NBSIR 80-2054 (November 1980).

[11] Fitzgerald, W. E., Quantification of Fires: 1. Energy Kinetics of Burning in a Dynamic Room Size Calorimeter, J. Fire Flammability **9**, 510–525 (1978).

[12] Grand, A. F., and Valys, A. J., Assessment of Burning Characteristics of Aircraft Interior Materials, Task I—Analog Seat (NASA-CR-166390). National Aeronautics & Space Administration, Washington DC (1981).

[13] Heskestad, G., Bidirectional Flow Tube for Fire-Induced Vent Flows, pp. 140-5 in Large-Scale Bedroom Fire Test, July 11, 1973, Croce, P. A., and Emmons, H. W., eds. (FMRC Serial 21011.4), Factory Mutual Research Corp., Norwood, MA (1974).

[14] Thornton, W., The Relation of Oxygen to the Heat of Combustion of Organic Compounds, Philosophical Magazine Science **33**, 196 (1917).

[15] Huggett, C., Estimation of Rate of Heat Release by Means of Oxygen Consumption Measurements, Fire Materials **4**, 61–65 (1980).

[16] Parker, W. J., Calculation of the Heat Release Rate by Oxygen Consumption for Various Applications, J. Fire Sciences **2**, 380–395 (1984).

[17] Fisher, F. L., and Williamson, R. B., Intralaboratory Evaluation of a Room Fire Test Method, Natl. Bur. Stand. (U.S.), NBS-GCR 83-421 (1983).

[18] Lee, B. T., Standard Room Fire Test Development at the National Bureau of Standards, pp. 29–44 in Fire Safety: Science and Engineering (ASTM STP 882), Harmathy, T. Z., ed., American Society for Testing and Materials, Philadelphia, PA (1985).

[19] Castino, T. G., Beyreis, J. R., and Metes, W. S., Flammability Studies of Cellular Plastics and Other Building Materials Used for Interior Finishes, Subject 723. Underwriters Laboratories, Northbrook, IL (1975).

[20] Standard Guide for Room Fire Experiments (E 603), 1989 Annual Book of ASTM Standards, Vol. 04.07, American Society for Testing and Materials, Philadelphia, PA.

[21] Proposed Standard Method for Room Fire Test of Wall and Ceiling Materials and Assemblies, 1982 Annual Book of ASTM Standards, Part 18, American Society for Testing and Materials, Philadelphia, PA (1982).

[22] Beitel, J. J., Jr., ISR's Fire Research Project, ASTM Standardization News **18**, 36–38 (1990).

[23] Sundström, B., Room Fire Test in Full Scale for Surface Products (Rapport SP-RAPP 1984:16), Statens Provningsanstalt, Borås, Sweden (1984).

[24] Surface Products: Room Fire Tests in Full Scale (Nordtest Method NT FIRE 025), NORDTEST, Helsingfors, Finland (1986).

[25] Göransson, U., Nordtest Full-scale Fire Tests, Proceedings of the Flame Retardants '90 Conference, London, UK (January 1990) pp. 34–42.

[26] Ahonen, A., Holmlund, C., and Kokkala, M., On the Influence of Ignition Power and Burner Size on Fire Growth in Room Fire Experiments (VTT Report 383), Valtion Teknillinen Tutkimuskeskus, Espoo, Finland (1986).

[27] Room Fire Test in Full Scale for Surface Products, ISO DP 9705, International Organization for Standardization (1989).

[28] Alpert, R. L. et al., Influence of Enclosures on Fire Growth: Volume I: Test Data, FMRC No. OAOR2.BU-1 through 7, Factory Mutual Research Corp., Norwood, MA (1977).

[29] Cooper, L. Y., Harkleroad, M., Quintiere, J. G., and Rinkinen, W. J., An Experimental Study of Upper Hot Layer Stratification in Full-Scale Multiroom Fire Scenarios, J. Heat Trans. **104**, 741–749 (1982).

[30] Peacock, R. D., Davis, S., and Lee, B. T., An Experimental Data Set for the Accuracy Assessment of Room Fire Models, Natl. Bur. Stand. (U.S.), NBSIR 88-3752 (April 1988).

[31] Heskestad, G., and Hill, J. P., Experimental Fires in Multiroom/Corridor Enclosures, contract to the Natl. Bur. Stand. (U.S.), NBS-GCR 86-502, CIB W14/85/10 (USA) (January 1986).

[32] Rockett, J. A., Morita, M., and Cooper, L. Y., Comparisons of NBS/Harvard VI Simulations and Full-scale Multi-room Fire Test Data, in Proceedings of 2nd International Symposium of Fire Safety Science, Tokyo, Japan (1988) pp. 481–490.

[33] Rockett, J. A., Morita, M., and Cooper, L. Y., Comparisons of NBS/Harvard VI Simulations and Data from all Runs of a Full-scale Multi-room Fire Test Program, Fire Safety J. **15**, 115–169 (1989).

[34] Rockett, J. A., and Morita, M., The NBS Harvard VI Multi-room Fire Simulation. Fire Sci. Technol. **5**, 159–164 (1985).

[35] Freund, J. E., Livermore, P. E., and Miller, I., Manual of Experimental Statistics, Prentice-Hall, Englewood Cliffs, NJ (1960).

[36] Zelen, M., Introductory Lectures on the Statistical Design of Experiments, U. S. Army Mathematics Research Center, NTIS, AD707613 (November 1981).

[37] Davies, A. D., Some Tools for Fire Model Validation, Fire Technology **23**, 95–114 (1987).

[38] Fang, J. B., Repeatability of Large-Scale Room Fire Tests, Fire Technology **17**, 5–15 (1981).

[39] Peacock, R. D., and Babrauskas, V., Analysis of Large-Scale Fire Test Data, Accepted for publication in the Fire Safety Journal.

[40] Budnick, E. K., Mobile Home Living Room Fire Studies: The Role of Interior Finish, Natl. Bur. Stand. (U.S.), NBSIR 78-1530 (September 1978).

[41] Babrauskas, V., Combustion of Mattresses Exposed to Flaming Ignition Sources, Part I. Full-Scale Tests and Hazard Analysis, Natl. Bur. Stand. (U.S.), NBSIR 77-1290 (1977).

[42] Heskestad, G. and Hill, J. P., Propagation of Fire Smoke in a Corridor, Proceedings of the 1987 ASME·JSME Thermal Engineering Joint Conference, Honolulu HI, March 22–27, 1987, pp. 371–379 (1987).

[43] Woolley, W. D., Raftery, M. M., Ames, S. A., and Murrell, J. V., Smoke Release from Wall Linings in Full-Scale Compartment Fires, Building Research Establishment, Borehamwood, UK, Current Paper CP 56/78 (July 1978).

[44] Bukowski, R. W., Smoke Measurement in Large and Small Scale Fire Testing, Fire Technol. Part I **15**, 173–179; Part II **15**, 271–281 (1979).

[45] Upton, S., Fire Testing Technology, Ltd., private communication.

[46] Mulholland, G., How Well Are We Measuring Smoke?, Fire Materials **6**, 65–67 (1982).

[47] Babrauskas, V., Effective Measurement Techniques for Heat, Smoke, and Toxic Fire Gases, pp. 4.1 to 4.10 in Fire: Control the Heat ... Reduce the Hazard, QMC Fire and Materials, London (1988).

[48] Atkinson, G., and Drysdale, D. D., A Note on the Measurement of Smoke Yields, Fire Safety J. **15**, 331–335 (1989).

[49] Mulholland, G. M., Henzel, V., and Babrauskas, V., The effect of scale on smoke emission, in Proceedings of 2nd International Symposium of Fire Safety Science, Tokyo, Japan (1988).

[50] Braun, E., Gann, R. G., Levin, B. C., and Paabo, M., Combustion Product Toxic Potency Measurements: Comparison of a Small-Scale Test and "Real-World" Fires, J. Fire Sci. **8**, 63–79 (1990).

[51] Peacock, R. D., Davis, S. and Lee, B. T., An Experimental Data Set for the Accuracy Assessment of Room Fire Models, Natl. Bur. Stand. (U.S.), NBSIR 88-3752 (April 1988).

[52] Bukowski, R. W., Quantitative Determination of Smoke Toxicity Hazard—A Practical Approach for Current Use, in Proceedings of the First International Symposium of Fire Safety Science, Gaithersburg, MD (June 1986) pp. 1089–1100.

[53] Zukoski, E. E., and Kubota, T., An Experimental Investigation of the Heat Transfer from a Buoyant Gas Plume to a Horizontal Ceiling—Part 2, Effects of Ceiling Layer, Natl. Bur. Stand. (U.S.), NBS-GCR 77-98 (September 1975).

[54] Emmons, H. W., The Flow of Gases Thru Vents, Home Fire Project Technical Report No. 75, Harvard University, Cambridge, MA (March 1987).

[55] Emmons, H. W., Vent Flows, Section 1, Chapter 8 in The SFPE Handbook of Fire Protection Engineering, Beyler, C. L., ed., National Fire Protection Association, Quincy, MA (1988).

[56] Lee, B. T., Effect of Ventilation on the Rates of Heat, Smoke, and Carbon Monoxide Production in a Typical Jail Cell Fire, Natl. Bur. Stand. (U.S.), NBSIR 82-2469 (March 1982).

[57] Babrauskas, V., Upholstered Furniture Room Fires—Measurements, Comparison with Furniture Calorimeter Data, and Flashover Predictions, J. Fire Sci. **4**, 5–19 (1984).

[58] Steckler, K. D., Quintiere, J. G. and Rinkinen, W. J., Flow Induced by Fire in a Compartment, Natl. Bur. Stand. (U.S.), NBSIR 82-2520 (September 1982).

[59] Nakaya, I., Tanaka, T., Yoshida, M., and Steckler, K., Doorway Flow Induced by a Propane Fire, Fire Safety J. **10**, 185–195 (1986).

[60] Lee, B. T., Effect of Wall and Room Surfaces on the Rates of Heat, Smoke, and Carbon Monoxide Production in a Park Lodging Bedroom Fire, Natl. Bur. Stand. (U.S.), NBSIR 85-2998 (September 1985).

[61] Jones, W. W., and Bodart, X., Buoyancy Driven Flow As the Forcing Function of Smoke Transport Models, Natl. Bur. Stand. (U.S.), NBSIR 86-3329 (1986).

[62] Smith, E. E., Fire Safety Evaluation of Rapid Transit Systems, Proceedings of the Eighth International Conference on Fire Safety, Millbrae, CA, January 17–21, 1983, pp. 85–94 (1983).

[63] Kaufman, S., Smith, E. E., Przybyla, L. J., and Williams, J. L., Large Scale Fire Tests of Building Riser Cables, Proceedings of the Eighth International Conference on Fire Safety, Millbrae, CA, January 17–21, 1983, pp. 105–112 (1983).

[64] Janssens, M., Measuring Rate of Heat Release by Oxygen Consumption, to be published in Fire and Materials.

[65] Babrauskas, V., Harris, Jr., R. H., Gann, R. G., Levin, B. C., Lee, B. T., Peacock, R. D., Paabo, M., Twilley, W., Yoklavich, M. F., and Clark, H. M., Fire Hazard Comparison of Fire-Retarded and Non-Fire-Retarded Products, Natl. Bur. Stand. (U.S.), NBS Spec. Publ. 749 (July 1988).

[66] Babrauskas, V., Development of the Cone Calorimeter—A Bench Scale Heat Release Rate Apparatus Based on Oxygen Consumption, Fire Materials **8**, 81–95 (1984).

[67] Karlson, B., Room Fires and Combustible Linings (Report SE-LUTVDG/TVBB-3050). Department of Fire Safety Engineering, Lund University, Lund, Sweden (1989).

[68] Babrauskas, V., Lawson, J. R., Walton, W. D., and Twilley, W. H., Upholstered Furniture Heat Release Rates Measured with a Furniture Calorimeter, Natl. Bur. Stand. (U.S.), NBSIR 82-2604 (1982).

[69] Babrauskas, V., Upholstered Furniture Heat Release Rates: Measurements and Estimation, J. Fire Sci. **1**, 9–32 (1983).

[70] Babrauskas, V., Harris, R. H., Braun, E., Levin, B. C., Paabo, M., and Gann, R. G., The Role of Bench-Scale Test Data in Assessing Real-Scale Fire Toxicity, Natl. Inst. Stand. Technol, Tech. Note 1284 (February 1990).

[71] McCaffrey, B. J., and Heskestad, G., A Robust Bidirectional Low-Velocity Probe for Fire and Flame Application, Combustion Flame **26**, 125–127 (1976).

[72] D'Souza, M. V., and McGuire, J. H., Development of a 4-ft Corner Wall Fire Test Apparatus, Report 432, National Research Council, Ottawa, Canada (November 1976).

[73] Klote, J. H., Fire Experiments of Zoned Smoke Control at the Plaza Hotel in Washington, DC, Natl. Inst. Stand. & Tech. (U.S.), NISTIR 90-4253 (February 1990).

[74] Klote, J. H., and Fothergill, J. W., Design of Smoke Control Systems for Buildings, American Society for Heating, Refrigerating, and Air-Conditioning Engineers, Atlanta, GA.

[75] Klote, J. H., Project Plan for Full Scale Smoke Movement and Smoke Control Tests, Natl. Bur. Stand. (U.S.), NBSIR 88-3800 (June 1988).

[76] NFPA 92A, Recommended Practice for Smoke Control Systems, National Fire Protection Association, Quincy, MA (1988).

[77] Klote, J. H., An Overview of Smoke Control Technology, ASHRAE Transactions **94**, Part 1 (1988).

[78] Walton, W. D., Suppression of Wood Crib Fires with Sprinkler Sprays: Test Results, Natl. Bur. Stand. (U.S.), NBSIR 88-3696 (January 1988).

About the authors: Richard D. Peacock is a chemical engineer in the Fire Measurement and Research Division of the NIST Building and Fire Research Laboratory. Sanford Davis is retired. Vytenis Babrauskas is head of the Fire Toxicity Measurement Group in the Fire Measurement and Research Division of the NIST Building and Fire Research Laboratory.

Volume 96, Number 4, July–August 1991
Journal of Research of the National Institute of Standards and Technology

[J. Res. Natl. Inst. Stand. Technol. 96, 463 (1991)]

Numerical Modeling of Silicon Photodiodes for High-Accuracy Applications
Part I. Simulation Programs

Volume 96 Number 4 July–August 1991

Jon Geist and
Deane Chandler-Horowitz

National Institute of Standards and Technology,
Gaithersburg, MD 20899

and

A. M. Robinson and
C. R. James

University of Alberta,
Alberta, Canada T6G 2G7

The suitability of the semiconductor-device modeling program PC-1D for high-accuracy simulation of silicon photodiodes is discussed. A set of user interface programs optimized to support high-accuracy batch-mode operation of PC-1D for modeling the internal quantum efficiency of photodiodes is also described. The optimization includes correction for the dark current under reverse- and forward-bias conditions before calculating the quantum efficiency, and easy access to the highest numerical accuracy available from PC-1D, neither of which is conveniently available with PC-1D's standard user interface.

Key words: high accuracy; internal quantum efficiency; PC-1D; photodiode modeling; silicon photodiodes.

Accepted: May 29, 1991

1. Introduction

PC-1D[1] [1,2] is a computer program for numerical modeling of the electrical performance of one-dimensional semiconductor devices including photogeneration. It is optimized for solar cell modeling, and runs on IBM PC-compatible computers equipped with a numerical coprocessor. Version 2 of PC-1D includes realistic models of most of the semiconductor material and device properties that are important for high-accuracy applications of photodiodes. Consequently, Version 2 of PC-1D has the potential to be a tool for supporting these applications.

Unfortunately, for reasons that have to do with the difference between the applications for high-accuracy photodiodes and those for solar cells, it is not easy to achieve the highest accuracy of PC-1D through its standard user interface. Luckily, the designer of Version 2 of PC-1D anticipated this sort of problem and included the option to run it in batch mode in a way that does allow access to the highest levels of numerical precision and accuracy that are available from PC-1D.

This paper reports the development of a program shell for PC-1D that provides a batch-mode user interface optimized for high-accuracy modeling of photodiodes. The shell consists of three programs. The first is a program that prepares the input for PC-1D, the second is a program that reads the output from PC-1D, and the third is a MS-DOS batch file program that supervises the sequential execution of PC-1D and the other two programs.

The remainder of Part I of this series of papers reviews PC-1D and describes the new program shell for high-accuracy modeling of photodiodes. Typical applications are described in Parts II and III of this series of papers.

---

[1] Certain commercial equipment, instruments, or materials are identified in this paper to specify adequately the experimental procedure. Such identification does not imply recommendation or endorsement by the National Institute of Standard and Technology, nor does it imply that the materials or equipment identified are necessarily the best available for the purpose.

2. Description of PC-1D

PC-1D is an interactive, graphical, semiconductor-device simulation program that solves the fully-coupled, drift-diffusion (electron and hole transport) equations in one dimension. Its principal limitations are that it supports no more than three regions of possibly different materials, and that it is a one-dimensional model with a maximum of 150 finite elements. Within these constraints, the program is very versatile. It is well beyond the scope of this paper to describe its various capabilities.

Both the IBM Pascal source code and executable code are available. The latter requires an IBM PC-compatible computer equipped with at least 512 Kbytes of random access memory (RAM), a 80×87 coprocessor chip, a CGA, VGA, or EGA compatible graphics adapter, and a matching display. To use the shell described in this paper, batch-mode operation is necessary which requires an MS-DOS compatible operating system (Version 3.1 or greater).

Only one of the interactive modes of PC-1D is of interest for the purposes of this paper, the one that allows the creation and saving of parameter files. Parameter files contain all of the information needed by PC-1D to model a specific, user-defined device. These files are stored in binary format under user-defined names with .PRM as their extension. Included in the parameter file are the names of other data files needed by PC-1D to model the device.

2.1 Opening Menu

Figure 1 shows the opening menu when PC-1D is run in the interactive mode. An overview of the options mentioned in this menu is appropriate for what follows. The first, second, and fourth options, "Proceed with Solution," "Preview / Examine," and "Output Graphs:" are used in the interactive modeling mode, and are of no concern here. The "Solution Mode:," "Base Voltage:," "Collector Voltage:," and "Light:" options are used to set the electrical and optical conditions under which the simulation will be run. For the purposes of this paper, it does not matter what selections are made for these options, because they will be set to the correct values by the high-accuracy photodiode modeling shell when it is run.

The "Simulation Parameters:" option is used to load parameter files in the interactive mode, but it is also used to save parameter files, which is of interest to the use of PC-1D in batch mode. The "Reinitialize:" and "Number of Finite Elements:" options allow details of the numerical procedures to be modified to a certain extent. Normally, 150 finite elements, the maximum allowed, will be needed for high-accuracy modeling. It will sometimes be necessary to use this menu option in order to force PC-1D to use all 150 elements. Reinitialization is probably desirable except, perhaps, when simulating a reverse-bias experiment.

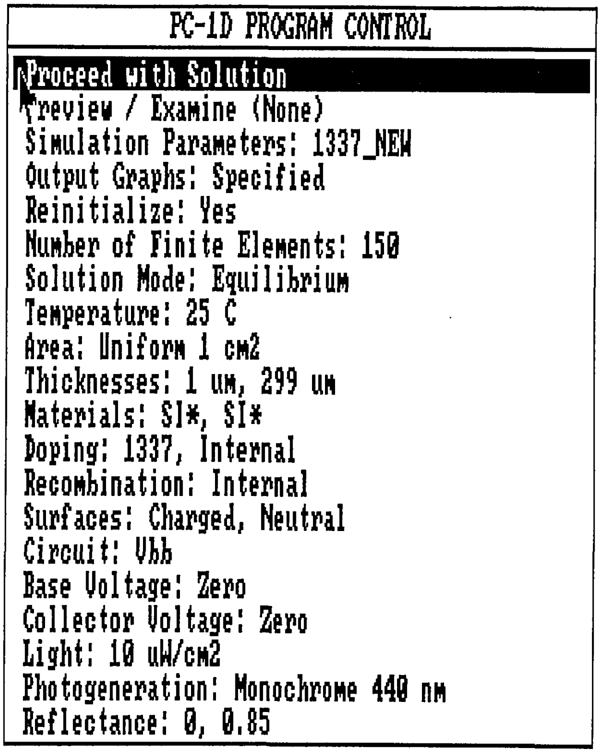

```
PC-1D PROGRAM CONTROL
Proceed with Solution
Preview / Examine (None)
Simulation Parameters: 1337_NEW
Output Graphs: Specified
Reinitialize: Yes
Number of Finite Elements: 150
Solution Mode: Equilibrium
Temperature: 25 C
Area: Uniform 1 cm2
Thicknesses: 1 um, 299 um
Materials: SI*, SI*
Doping: 1337, Internal
Recombination: Internal
Surfaces: Charged, Neutral
Circuit: Vbb
Base Voltage: Zero
Collector Voltage: Zero
Light: 10 uW/cm2
Photogeneration: Monochrome 440 nm
Reflectance: 0, 0.85
```

Figure 1. The opening menu of PC-1D when run in the interactive mode.

The remaining options define the detailed nature of the device and external circuit to be modeled. All of the parameters obtained from the internal models built into PC-1D are adjusted to the values appropriate for the temperature entered following the "Temperature:" heading at the bottom of the opening menu. The user, of course, must assure that any user-defined parameters or data files are consistent with the chosen temperature. The "Area:" option is straightforward. The "Thickness:" option allows three different regions to be defined, each having its own thickness, material, and doping properties. If the thickness of a region is set to zero, it is not included in the solution, and it is not explicitly indicated following the "Thickness:" heading.

2.1.1 Materials Properties Selection of the "Materials:" heading of the opening menu allows such properties as the carrier mobilities, band-gap narrowing, Auger recombination cross sections, and absorption coefficient to be adjusted. For each region, a set of three files having the extensions .MAT, .INR, and .ABS are needed. These files are 1) an ASCII file that is the main material file, 2) an ASCII file containing wavelength versus real index of refraction data, and 3) an ASCII file containing wavelength versus absorption-coefficient data, respectively. All of the file names are stored in the parameter (PRM) file. In default operation, the INR and ABS files will have the same name as the MAT file. The user has the option of associating alternate ABS and INR files with a given MAT file in a particular parameter file, even though they have different names. If this is done, asterisks follow the MAT file names in the "Materials:" option heading, as shown in figure 1. Other material properties are included in internal models. Some of these allow the user to specify the values of the parameters in the equations defining the models, and most can be replaced by user-supplied ASCII files having the appropriate extensions. The internal model of the absorption coefficient of silicon, which is discussed next, is an example.

The default absorption-coefficient data in the SI.ABS file of Version 2 of PC-1D are not accurate enough for high-accuracy modeling of silicon photodiodes over the 400 to 900 nm spectral region [3]. Therefore, two data sets of higher accuracy were calculated and stored in files named SIL_WEAK.ABS and SIL_PHIL.ABS. The first data set was calculated by using eq (1) of reference [3], which was fitted to the data of reference [4] over the spectral range from 470 to 1180 nm. The second data set was calculated by interpolation of the data of reference [5]. The first set is expected to be more accurate at longer wavelengths, and the second at shorter wavelengths.

The ratios of the data in SIL_PHIL.ABS to that in SIL_WEAK.ABS are plotted over the 400 to 900 nm spectral range in figure 2. The difference can be characterized as 12% ± 4% over the spectral region from 440 to 780 nm, growing much larger outside that spectral region. The value of 12% is a convenient average offset because it is the difference between the two data sets at 633 nm. At that wavelength, the value calculated from eq (1) of reference [3] agrees with a recent measurement [6] to within the ±2% uncertainty associated with the measurement.

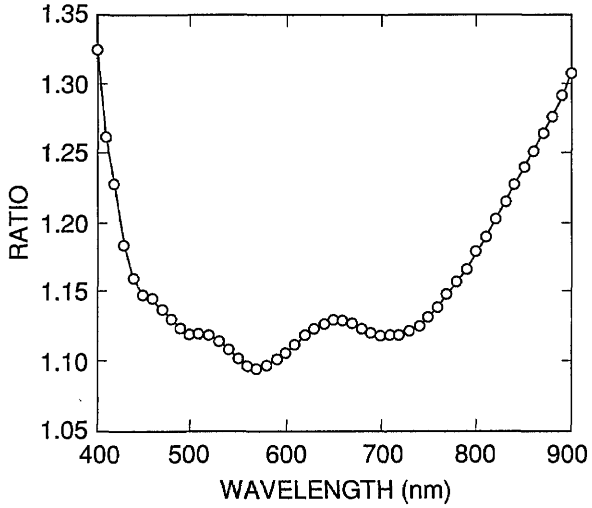

Figure 2. Ratios of the absorption-coefficient data interpolated from reference [5] to those calculated from eq (1) of reference [3] that were fitted to the data of reference [4].

One material property not modeled by PC-1D is the quantum yield for electron hole pair production [7]. This quantity may differ significantly from unity outside the 400 to 900 nm spectral region [8], but no high accuracy models currently exist [7,9]. This is the main reason that the modeling described in Part II of this series of papers is confined to the 400 to 900 nm spectral region. However, other problems, such as larger uncertainties in the available absorption-coefficient data at shorter wavelengths and uncertainties in the fraction of the radiation reflected by the rear surface of the photodiode at the longer wavelengths, also contribute to a significant deterioration in accuracy outside that spectral region.

2.1.2 Device Properties The "Doping:" heading of the opening menu of PC-1D allows either an internal doping model or an external file containing doping concentrations for each region of the device being modeled. The internal model consists of two front and two rear dopant distributions, as well as a uniform background dopant. The distributions can be chosen from uniform, complementary error, and Gaussian functions, and the parameters defining the maximum value, its location, and the width of the distributions can be adjusted. If tabular doping data are to be used, they are read from a user-generated ASCII file containing a depth, an n-type dopant concentration, and a p-type dopant concentration on each line, and having .DOP as its extension.

The shape of the equilibrium majority-carrier concentration near the front-surface oxide-silicon interface is very important to high-accuracy photodiode modeling [10]. It is necessary to use external files to model the front region doping in p^+n-type photodiodes to force PC-1D to devote enough finite elements to the front region to approximate accurately the majority-carrier concentration there.

The "Recombination:" heading of the opening menu of PC-1D allows the defect-related recombination in the volume and at the surfaces of the device to be modeled. (Auger recombination is considered a material property and is covered under the "Materials:" heading.) Shockley-Read-Hall (SRH) recombination through a single energy-level trap state is used as the model for volume recombination. Either an internal model or a user-defined table of depths and electron and hole lifetimes (equivalent to cross sections in the SRH model) in an external ASCII file with the extension .TAU can be used to model the volume recombination. With the internal model, the user may choose a single electron lifetime, a single hole lifetime, and a single trap energy relative to mid-gap for each region. With the external model, a trap level at mid-gap is used with the lifetime data in the external ASCII file.

The restriction of the SRH model to a single-energy state prevents PC-1D from accurately fitting the measured [11] variation of quantum efficiency with flux (i.e., nonlinearity) at 950 nm for an EG&G UV444B photodiode as illustrated in figure 3. The simulated data in figure 3 were calculated using a mid-gap state with equal electron and hole lifetimes. Even though the simulated and experimental data agree in the low flux limit and again at a high flux level, their shapes are very different. Better agreement can be achieved at low flux levels at the cost of a worse fit at the higher flux levels by moving the state away from mid-gap, and by using different electron and hole lifetimes as illustrated in figure 4. It is expected that the proper distribution of SRH trap levels over the band gap would result in an accurate simulation of the nonlinearity of this type of photodiode.

It should be possible to develop an external lifetime model based on a parameterized distribution of SRH recombination states, and to adjust the parameters to fit the nonlinearity data shown in figures 3 and 4. However, it would be necessary alternately to run PC-1D to calculate the carrier concentrations and then the external model to calculate the lifetimes appropriate to these carrier concentrations, and to iterate to self-consistency. This is beyond the scope of the work reported in this paper.

The failure of the model to describe the nonlinearity of this type of photodiode casts some doubt on its ability to model accurately the reverse-bias self-calibration experiment [12-13]. This point is addressed in more detail in Part II of this series of papers.

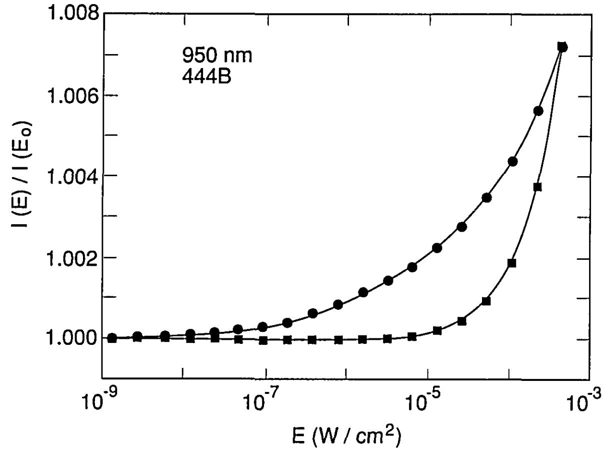

Figure 3. Comparison of experimental (filled circles) and simulated (filled squares) linearity measurements on an EG&G UV444B photodiode at 950 nm using a single SRH trap level at mid-gap with electron and hole lifetimes of 74.04 μs.

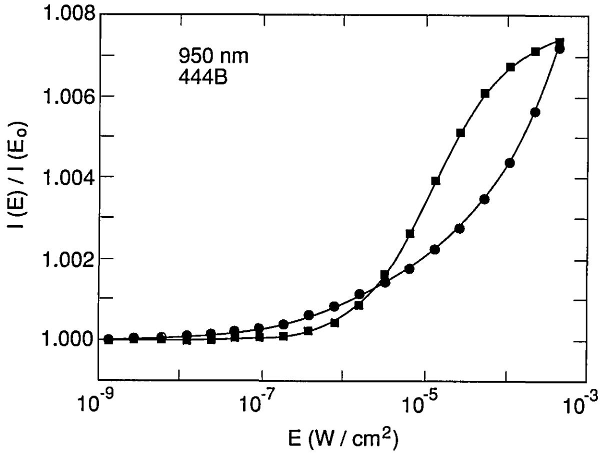

Figure 4. Comparison of experimental (filled circles) and simulated (filled squares) linearity measurements on an EG&G UV444B photodiode at 950 nm using a single SRH trap level 0.1796 eV above mid-gap with electron and hole (check for vice versa) lifetimes of 900 and 700 ms, respectively.

In the case of surface recombination, the "Recombination:" option allows the choice of one of two internal models, a surface-recombination velocity model, and a saturation-current density model, but does not accommodate a user-defined data file. The choice of the surface-recombination velocity model allows the user to adjust the hole- and electron-recombination velocities as well as the energy-level of a single-energy surface state.

The "Surfaces:" option allows the user to choose the surface charge at the front and back surfaces of the device. For modeling the oxide-bias self-calibration experiment [12-13], the surface charge is the algebraic sum of any charge trapped in the oxide as a result of thermal oxidation and the charge stored on the oxide surface by the voltage applied to the transparent electrode.

The "Circuit:" option of the main menu of PC-1D allows the user to define a circuit in which the device is to operate. For the case of a photodiode, the emitter and base are connected, the collector is disconnected, and the connections to the device are made at the front and back surface. Keeping the collector disconnected forces the "Collector Voltage:" option to zero, as shown in figure 1. Setting the internal resistance R_b to some non-zero value allows the effect of series resistance to be simulated.

3. The Photodiode Modeling Shell Programs

The photodiode modeling shell for Version 2 of PC-1D is designed to allow simulation of oxide-bias and reverse-bias, self-calibration experiments, nonlinearity measurements, and internal quantum efficiency spectra, while accessing the highest accuracy and precision available from PC-1D. It consists of three program files. The first program, a short MS-DOS Batch program named RUN_PC1D.BAT, is listed in figure 5. The other two programs, MAKE_PRM.EXE and READ_PDF.EXE, were complied with Version 5.5 of Turbo Pascal. Listings of the source code for these programs are given in reference [14].

3.1 Operation of RUN_PC1D.BAT

The first thing that RUN_PC1D.BAT does when run is to test whether or not the files MAKE_PRM.EXE, PC-1D.EXE, and READ_PDF.EXE all exist. If not, it issues an error message, and terminates execution at :STOP. If all three files do exist, RUN_PC1D deletes the temporary file TEMP.DAT. This is a precaution in case a previous nonstandard termination left this file in existence. RUN_PC1D then enters the loop between :LOOP and GO TO LOOP. Once in this loop, it transfers control to MAKE_PRM.EXE.

```
IF NOT EXIST MAKE_PRM.EXE GOTO ERROR1
IF NOT EXIST PC-1D.EXE GOTO ERROR2
IF NOT EXIST READ_PDF.EXE GOTO ERROR3
DEL TEMP.DAT
:LOOP
  MAKE_PRM.EXE
   IF NOT EXIST TEMP.DAT GOTO STOP
  PC-1D TEMP TEMP
  READ_PDF.EXE
  GOTO LOOP
:ERROR1
  REM MAKE_PRM.EXE not found.
  GOTO :MESSAGE
:ERROR2
  REM PC-1D.EXE not found.
  GOTO MESSAGE
:ERROR3
  REM READ_PDF.EXE not found.
  GOTO MESSAGE
:MESSAGE
  TYPE RUNPC1D.DOC
  GOTO STOP
:STOP
```

Figure 5. Listing for the MSDOS batch file RUN_PC1D.BAT that supervises the execution of the programs MAKE_PRM.EXE, PC-1D.EXE, and READ_PDF.EXE for high-accuracy photodiode modeling.

The first thing that MAKE_PRM.EXE does is to test the existence of TEMP.DAT. If TEMP.DAT does not exist, then MAKE_PRM.EXE prompts the user to define the photodiode experiment to be simulated. Examples of the questions and typical answers are shown in Appendix A. The questions and answers are straightforward and require no explanation. If the file option rather than the keyboard option is chosen to define the independent variables for the experiment to be simulated, then the program asks for the file name instead of the start, stop, and step values for the independent variable. Once MAKE_PRM.EXE has obtained all of the necessary information, it writes that information into the file TEMP.DAT, creates the temporary parameter file TEMP.PRM, and passes control back to RUN_PC1D.BAT.

RUN_PC1D.BAT now tests the existence of TEMP.DAT. If it does not exist, RUN_PC1D terminates execution. If TEMP.DAT does exist, then RUN_PC1D passes control to PC-1D.EXE. This program reads TEMP.PRM (the first TEMP on the command line following PC-1D), carries out the simulation defined therein, writes a table having a depth, an electron current, a hole current, and a total current on each line in the file TEMP.PDF (the second TEMP on the command line), and returns control to RUN_PC1D.BAT. Note that PDF files are the standard ASCII format HP plotter output files generated by PC-1D.

RUN_PC1D.BAT now passes control to READ_PDF.EXE. This program reads the total photocurrent at the depth specified in the definition of the experiment to be simulated (see Appendix A) from file TEMP.PDF, and appends it to the output file specified in response to the prompt from MAKE_PRM.EXE. READ_PDF.EXE then returns control to RUN_PC1D.BAT.

On subsequent passes through the loop, MAKE_PRM.EXE finds that TEMP.PRM does exist, reads the necessary information from this file, and writes updated TEMP.DAT and TEMP.PRM files. The information about when to exit the loop is in TEMP.DAT, and when MAKE_PRM.EXE determines that this time has come, it deletes TEMP.DAT, triggering RUN_PC1D.BAT to terminate execution.

3.2 Features of MAKE_PRM and READ_PDF

A few points about MAKE_PRM.EXE and READ_PDF.EXE are in order. First, these two programs are designed to compensate for traits of PC-1D that make it less than ideal for high-accuracy modeling of photodiodes. The first of these is that PC-1D.EXE calculates the internal quantum efficiency from the sum of the photocurrent and the dark current occurring under reverse or forward bias. This may not be a problem in solar cell modeling, but it is not correct for photodiode modeling. As a result, MAKE_PRM.EXE calculates and stores the appropriate dark currents for all simulations that have a nonzero bias voltage V_{bb}, and READ_PRM.EXE reads them and subtracts them from the appropriate total currents when calculating the quantum efficiency. This is simulated as a shutter-closed/shutter-open measurement sequence by MAKE_PRM.EXE.

Even though the total current is a constant throughout a photodiode, it must be calculated at each finite element in the photodiode. The numerical precision with which it can be calculated depends upon the majority-carrier concentration in the element where it is being calculated due to the nature of the numerical algorithm, which involves the difference of two large numbers that scale with doping concentration. This is illustrated in figure 6, which shows the variation in the total current computed by PC-1D as a function of depth in the front region of a $p+n$-type photodiode irradiated by 1 μW/cm^2 of 440 nm radiation. This result was obtained by running PC-1D through its standard user interface and could not be obtained by running PC-1D with the shell just described, since carrier concentration as a function of depth is not an output supported by the shell. The decrease in the noise in the data with increasing distance from the front surface of the photodiode is evident in the figure.

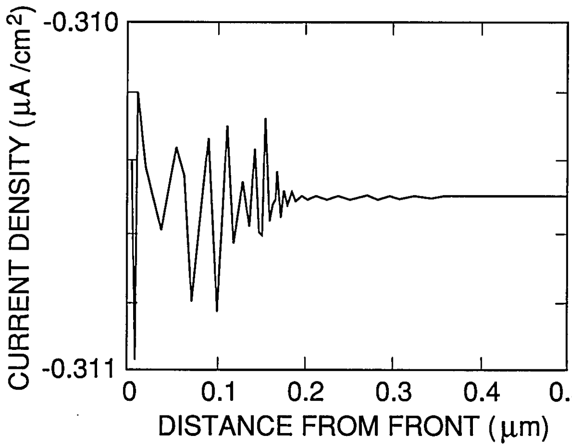

Figure 6. Variation in the total photocurrent calculated by PC-1D as a function of position in the front region of a Hamamatsu 1337 type photodiode due to the effect of the high front region doping concentration.

PC-1D.EXE calculates the quantum efficiency from the total current at either the front or the rear of the photodiode at the discretion of the user. Since these are usually the regions where the majority-carrier concentration is greatest, PC-1D often calculates the quantum efficiency from values of the total photocurrent that are not the most precise available to it. This loss of precision, which occurs even in the absence of dark current, is the reason that MAKE_PRM.EXE asks the user to choose the depth at which the total photocurrent will be read from the TEMP.PDF file. This depth should be somewhere in the interior of the photodiode where the doping concentrations are low and the effect of surface fields on the carrier concentrations is small or negligible.

Very high precision is available under these conditions. The internal quantum efficiency calculated by RUN_PC1D for the same type of photodiode used to generate the data in figure 6, but with all loss (recombination) mechanisms set to zero, is 6 parts per million (ppm) above unity ±1 ppm for 1 μW/cm^2 irradiation anywhere within 400 to 900 nm spectral region. This result was obtained by assuming the somewhat large thickness of 400 mm for this photodiode to minimize the fraction of the incident radiation penetrating to the rear of the photodiode. Since PC-1D does not permit a reflectance of 100% at the rear surface of the diode, a more typical 300 mm thick photodiode would show a loss of a few ppm at the longest wavelengths.

Since PC-1D does not model the oxide passivation on the front surface of the photodiode, it is necessary to vary the oxide trapped charge N_{ss} to simulate the effect of applying a voltage across the oxide in the silicon self-calibration experiment. First, the value of N_{ss} must be chosen to simulate the oxide-fixed charge. To this value must be added the charge appropriate to the application of oxide bias according to the formula for the charge density stored on a capacitor as a function of thickness, dielectric constant, and applied voltage. It is this sum that PC-1D must use as N_{ss} when simulating the effect of oxide bias on a photodiode. The bookkeeping for the values of N_{ss} chosen to simulate the oxide-fixed charge and the values of N_{ss} needed to simulate the combined effect of the fixed charge and the applied oxide bias are handled by MAKE_PRM.EXE.

4. Conclusion

The semiconductor device modeling program PC-1D and some programs to enhance its use in the high-accuracy modeling of silicon photodiodes have been described. The features of PC-1D that suit it for high-accuracy photodiode modeling have been described, and the features of the support programs that compensate for features of the PC-1D user interface that are less than ideal for this application have also been described. Examples of the use of these programs in photodiode modeling in different types of high-accuracy applications are given in Parts II and III of this series of papers.

5. Appendix A

A Sample of the Screen Produced by MAKE_PRM.EXE When RUN_PC1D.BAT is Executed.

```
Parameter file (including PRM extension) defining photodiode:
1337_new.prm
Complete path to file in which to store QE results:
test.dat
Type of experiment to simulate?
(O)xide bias (Volts) scan?
(R)everse bias (Volts) scan?
(W)avelength (nm) scan?
(P)hoton energy (eV) scan?
(L)inearity (W/cm^2) scan?
Enter letter here: w
Start, stop, and stop values from (K)eyboard or all values from (F)ile? k
First value for scanned parameter: 400
Stop value for scanned parameter: 900
Step size for scanned parameter: 10
Incident irradiance (W per sq. cm): 1e-5
Oxide bias voltage (V): 0
Reverse bias voltage (V): 0
Non-zero thickness of front surface oxide (nm): 25
Depth at which to get total photocurrent (um): 100
```

About the authors: Jon Geist and Deane Chandler-Horowitz are physicists in the NIST Semiconductor Electronics Division, and A. M. (Sandy) Robinson and C. R. (Bob) James are Professors of Electrical Engineering at the University of Alberta in Edmonton, Alberta, Canada. Prof. James is presently Vice-President (Research) at the University.

6. References

[1] Available from ISU Extension Software, 108 Atanasoff Hall, Iowa State University, Ames, IA 50011, (505) 294-8658.

[2] Basore, P. A., 20th IEEE Photovoltaic Specialists Conference – 1988, pub. # 0160-8371/88/0000-0389 (IEEE, NY, 1988) p. 389.

[3] Geist, J., Migdall, A., and Baltes, H. P., Appl. Opt. **27**, 3777 (1988).

[4] Weakliem, H. A., and Redfield, D., J. Appl. Phys. **50**, 1491 (1979), and personal communication from H. A. Weakliem.

[5] Philipp, H. R., J. Appl. Phys. **43**, 2835 (1972), and personal communication.

[6] Geist, J., Schaefer, A. R., Song, J-F., Wang, Y. H., and Zalewski, E. F., J. Res. Natl. Inst. Stand. Technol. **95**, 549 (1990).

[7] Geist, J., and Wang, C. S., Phys. Rev. **B27**, 4841 (1983).

[8] Geist, J., Gladden, W. K., and Zalewski, E. F., J. Opt. Soc. **72**, 1068 (1982).

[9] Geist, J., Gardner, J. L., and Wilkinson, F. J., Phys. Rev. **B42**, 1262 (1990).

[10] Geist, J., and Baltes, H., Appl. Opt. **26**, 3929 (1989). Note that there is an error in eq (31) of this reference. The plus sign in the numerator of the first term in eq (31) should be replaced by a minus sign.

[11] Stock, K. D., Appl. Opt. **25**, 830 (1986), and personal communication.

[12] Zalewski, E. F., and Geist, J., Appl. Opt. **19**, 1214 (1980).

[13] Geist, J., Zalewski, E. F., and Schaefer, A. R., Appl. Opt. **19**, 3795 (1980).

[14] Geist, J., Robinson, A. M., James, C. R., Chandler-Horowitz, D., Köhler, R., and Goebel, R., NISTIR 4592 (1991).

Volume 96, Number 4, July–August 1991
Journal of Research of the National Institute of Standards and Technology

[J. Res. Natl. Inst. Stand. Technol. 96, 471 (1991)]

Numerical Modeling of Silicon Photodiodes for High-Accuracy Applications Part II. Interpreting Oxide-Bias Experiments

Volume 96 Number 4 July–August 1991

Jon Geist
National Institute of Standards and Technology,
Gaithersburg, MD 20899

Rainer Köhler and
Roland Goebel
BIPM, F-92310 Sèvres, France

and

A. M. Robinson and
C. R. James
University of Alberta,
Alberta, Canada T6G 2G7

The semiconductor device modeling program PC-1D and the programs that support its use in high-accuracy modeling of photodiodes, all of which were described in Part I of this series of papers, are used to simulate oxide-bias self-calibration experiments on three different types of silicon photodiodes. It is shown that these simulations can be used to determine photodiode characteristics, including the internal quantum efficiency for the different types of photodiodes. In the latter case, the simulations provide more accurate values than can be determined by using the conventional data reduction procedure, and an uncertainty estimate can be derived. Finally, it is shown that 0.9997±0.0003 is a nominal value for the internal quantum efficiency of one type of photodiode over the 440 to 460 nm spectral region.

Key words: induced junction photodiode; inversion layer photodiode; numerical modeling; numerical simulation; oxide-bias experiment; quantum efficiency.

Accepted: May 29, 1991

1. Introduction

Part II of this series of papers presents the results of high-accuracy simulations of various oxide-bias experiments performed on silicon photodiodes. The simulations were carried out by using the semiconductor device modeling program PC-1D[1] and a set of three programs designed to support the use of PC-1D in this specific application. Both PC-1D and the support programs are described in Part I of this series of papers.

The oxide-bias experiment [1-3] consists of recording the ratio of the photocurrent as a function of oxide-bias voltage to the zero-bias photocurrent during irradiation of the photodiode with a stable photon flux. The oxide bias is usually applied with a transparent water-drop electrode. A review is given in reference [3].

Part II is organized as follows: Section 2 describes the simulation of an oxide-bias, self-calibration experiment on an EG&G UV444B type photodiode. The purpose of this simulation is to demonstrate the derivation of an accurate value for the zero-bias quantum efficiency including an uncertainty estimate. Section 3 describes the simulation of an oxide-bias experiment on a Hamamatsu 1337 type photodiode. The purpose of this simulation is to determine nominal values for the charge trapped in the oxide covering the front surface of the photodiode, and for the surface recombination velocity at the oxide-silicon interface. Section 4 describes the simulation of an oxide-bias experiment on a

---

[1] Certain commercial equipment, instruments, or materials are identified in this paper to specify adequately the experimental procedure. Such identification does not imply recommendation or endorsement by the National Institute of Standard and Technology, nor does it imply that the materials or equipment identified are necessarily the best available for the purpose.

UDT UV100 type photodiode. The purpose of this simulation is to determine a nominal high-accuracy value for the internal quantum efficiency of this type of photodiode and the nominal wavelength region where this value is valid. Section 5 gives the conclusions of Part II.

2. EG&G UV444B Photodiode

The EG&G UV444B silicon photodiode was the first of its type to be self-calibrated by using the oxide-bias experiment [2]. This type of photodiode consists of a 300 μm thick, 300 Ω cm, phosphorus-doped, n-type silicon substrate with an n^+-type phosphorus diffusion in the rear surface, a p^+-type boron diffusion in the front surface, and a nominally 120 nm thick, thermally grown oxide-passivation layer over the front surface. Figure 1 shows the front-region doping profile that was obtained from spreading resistance measurements on a representative UV444B photodiode. Figure 1 also shows the equilibrium hole concentration calculated for this doping distribution by using PC-1D.

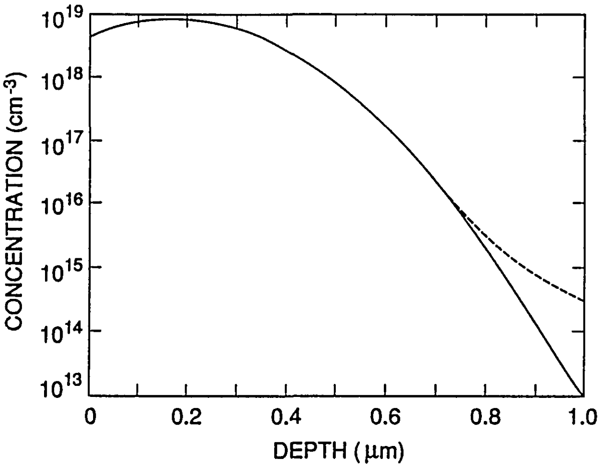

Figure 1. The front-region boron concentration (continuous line) and the equilibrium hole concentration (dashed line) calculated by PC-1D for a typical EG&G UV444B type photodiode.

The rear-region, n^+-type diffusion in the UV444B was not modeled; instead it was assumed that the recombination velocity at the rear of the device was zero. This assumption is not physically realizable, but it results in a mirror for minority carriers at the rear of the device, just as does the n^+-type diffusion. This assumption is useful because it requires fewer finite elements, thereby leaving more of them available for modeling the front region and depletion region.

Figure 2 compares simulated and experimental results of an oxide-bias experiment on a UV444B photodiode for irradiation by a 3 mm diameter spot of 476.2 nm laser radiation through a water-drop electrode. Reference [4] describes the apparatus used to obtain the experimental data. The absorption-coefficient data in the file SIL_WEAK.ABS used for this simulation were calculated from eq [5] that was fit to the data measured by Weakliem and Redfield [6]. These data are described in Part I. Both the surface recombination velocity S and the number density N_{ss} of the oxide fixed charge were adjusted in the simulation to obtain a good fit to the experimental data in figure 2.

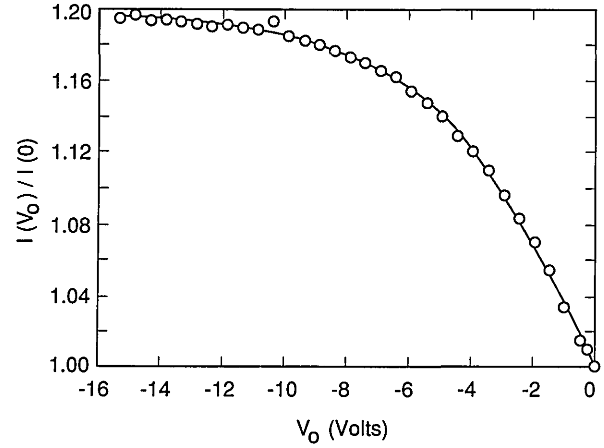

Figure 2. Ratio of the photocurrent $I(V_0)$ as a function of oxide-bias voltage V_0 to the photocurrent $I(0)$ at zero-bias voltage as measured on an EG&G UV444B silicon photodiode and as calculated with PC-1D with a front-surface recombination velocity $S = 6000$ cm/s and an oxide trapped charge number density $N_{ss} = 1.942 \times 10^{12}$ cm^{-2}.

The procedure used to fit the simulated data to the experimental data shown in figure 2 was as follows: first, a value of S was chosen, then the value of N_{ss} was adjusted until the average residual of the fit to the photocurrent ratio was zero for the last two data points in the figure. This gave a value of N_{ss} for each value of S that was chosen. The best combination of S and N_{ss} was then obtained by minimizing the residual standard deviation over all of the data shown in figure 2.

Figures 3, 4, and 5 plot the residuals (differences) between the results of the fits and the experimental results, and table 1 lists the residual standard deviation for three different choices of S and N_{ss}. It is clear by inspection of the figures that the combination of S and N_{ss} used for figure 3 gives a better overall fit than either of the other choices, even though the residual standard deviation for figure 3 is not very much lower than that for figure 4 or figure 5. One reason for the relatively small decrease in residual standard deviation with the best fit is the effect of the apparent outlier points near −1 and −10.5 V oxide bias.

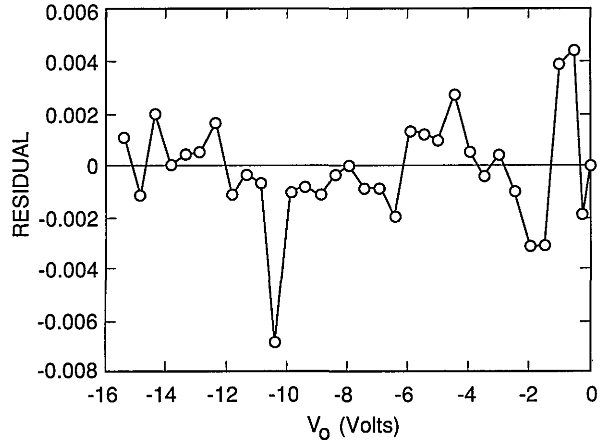

Figure 3. The residuals between the experimental data of figure 2 and the simulated data calculated by PC-1D when $S = 6000$ cm/s and $N_{ss} = 1.942 \times 10^{12}$ cm^{-2}.

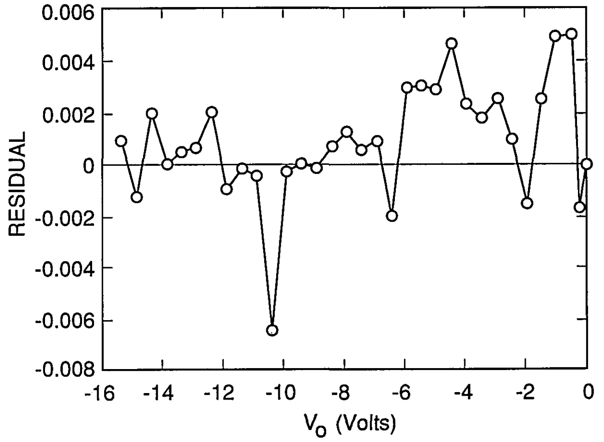

Figure 4. The residuals between the experimental data of figure 2 and the simulated data calculated by PC-1D when $S = 5000$ cm/s and $N_{ss} = 2.011 \times 10^{12}$ cm^{-2}.

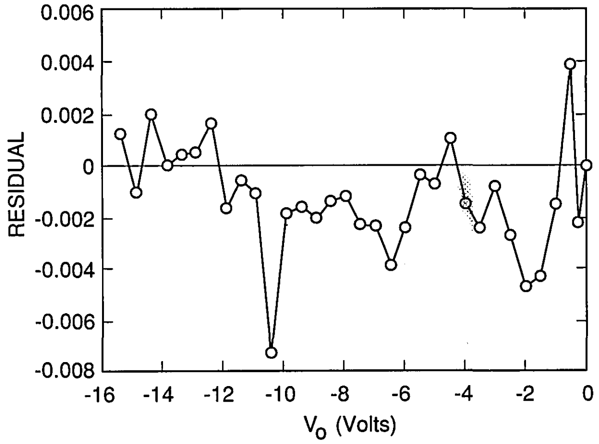

Figure 5. The residuals between the experimental data of figure 2 and the simulated data calculated by PC-1D when $S = 7000$ cm/s and $N_{ss} = 1.883 \times 10^{12}$ cm^{-2}.

Table 1. Comparison of simulated oxide bias results with experimental results for a UV444B type photodiode where Res. std. dev. is the standard deviation of the difference between simulated and experimental results

S (cm/s)	N_{ss} (10^{12} cm^{-3})	Res. std. dev.
5000	2.011	0.002233
6000	1.942	0.002076
7000	1.883	0.002093

The assignment of $S = 6000$ cm/s and $N_{ss} = 1.942 \times 10^{12}$ cm^{-2} with estimated uncertainties of ± 1000 cm/s and $\pm 0.070 \times 10^{12}$ cm^{-2}, respectively, is justified by figures 3, 4, and 5. This assignment corresponds to an internal quantum deficiency (one minus the internal quantum efficiency) at zero oxide bias of 0.1690 ± 0.0021. The stated uncertainty is the maximum difference between the internal quantum deficiency calculated for the combination of S and N_{ss} used in figure 3, and those calculated for the combinations of S and N_{ss} used for figures 4 and 5.

The assumption that the average of the last two data points in figure 3 corresponds to 100% internal quantum efficiency gives a zero-bias internal quantum deficiency of 0.1634 with no reliable way to estimate the uncertainty associated with that value. This assumption, which is usually used with the oxide-bias, self-calibration experiment, produces a result that differs from the more accurate value determined from the fit by 0.0056. This difference is about 3.3% of the effect being calculated, and more than 2.5 times the uncertainty associated with the more accurate value.

It must be emphasized that the results reported here are illustrative rather than definitive since the doping distribution data in figure 1 were obtained from one photodiode, and the oxide-bias data in figure 2 were obtained from a different photodiode. An additional uncertainty associated with the effect of variations in doping distribution would be needed, or the doping distribution must be measured on the actual photodiode used in the self-calibration.

Because oxide-bias voltages large enough to nearly saturate the photodiode response are also large enough to change S or N_{ss}, the oxide-bias measurement is already destructive to a certain extent, and it must be carried out as described in reference [7] in order to yield the highest accuracy of which it is capable. Therefore, the sacrifice of the photodiode for a spreading resistance measurement is not as impractical as it might at first seem. Nevertheless, it is inconvenient, and more convenient approaches are being developed [3].

The results reported here might be considered illustrative for another reason. The fitting and uncertainty analysis were carried out by hand in a somewhat subjective manner. Ideally, the fitting and uncertainty analysis would be carried out automatically by a fitting routine incorporated into the set of programs used to run PC-1D for photodiode modeling. However, this task might not be as straightforward as it first would seem because the fit should be constrained to pass through the mean of the last few data points at the highest oxide-bias voltage, as it was in the hand fit reported here. Without this constraint, the minimum residual standard deviation might be obtained for a choice of parameters that clearly does not fit the data well at the highest oxide-bias voltages. It is clear that the data at the highest oxide-bias voltages should be weighted more heavily in the fit, but it is not clear how much more heavily. Therefore, an automated program does not eliminate the subjectivity, but only transfers it to the weighting of the data.

3. Hamamatsu 1337 Photodiode

Like the EG&G UV444B photodiode, the Hamamatsu 1337 is a p^+nn^+ photodiode, but its front-region doping profile is shallower, its background n-type dopant concentration is 5×10^{12} cm^{-3}, and its oxide-passivation layer has a nominal thickness of 25 nm. Figure 6 shows relative front-region doping profiles for six different Hamamatsu 1337 photodiodes taken from four different batches. The curves in figure 6 were normalized to unity at the oxide-silicon interface because it is the shape of the doping profile rather than the magnitude that has the major effect on the internal quantum efficiency [8]. The measured dopant concentrations at the oxide-silicon interface varied between 2×10^{18} and 1×10^{19} cm^{-3} for the six photodiodes of figure 6.

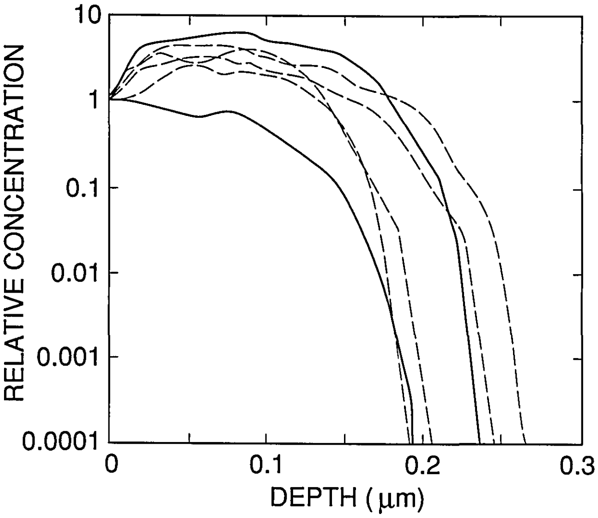

Figure 6. The relative front-region boron concentration for six typical Hamamatsu 1337 type photodiodes. The two profiles shown with solid lines bracket the other four in their effect on the shape of the internal quantum-deficiency spectrum.

Figure 7 shows the results of modeling an oxide-bias experiment on a 1337 type photodiode at 476.2 nm by using the doping profile that corresponds to the lower solid curve in figure 6. The fit shown in figure 7 was obtained with $N_{ss}=-3.0\times10^{12}$ cm^{-2} and $S=1.835\times10^5$ cm/s, and gave a zero-bias internal quantum deficiency of 0.003199. A fit that looked virtually identical to that shown in figure 7 was obtained for the doping profile corresponding to the upper solid curve in figure 6 by using $N_{ss}=-4\times10^{12}$ cm^{-2} and $S=1.56\times10^5$ cm/s. This fit gave a zero-bias internal quantum efficiency of 0.003280. As in the case of the UV444B type photodiode, the SIL_WEAK.ABS absorption-coefficient data were used, and the rear of the photodiode was modeled as uniformly doped with zero recombination velocity.

Figure 8 compares the internal quantum deficiencies calculated from the doping profile corresponding to the solid curves in figure 6 by using the values of N_{ss} and S that were obtained from the

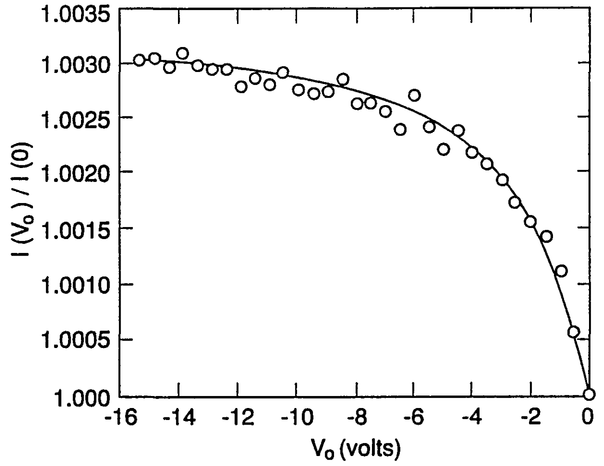

Figure 7. Ratio of the photocurrent $I(V_0)$ as a function of oxide-bias voltage V_0 to the photocurrent $I(0)$ at zero-bias voltage as measured on a Hamamatsu 1337 silicon photodiode and as calculated with PC-1D for the doping distribution corresponding to the upper solid curve in figure 6 with $S=1.835\times10^5$ cm/s and $N_{ss}=-3.0\times10^{12}$ cm^{-2}.

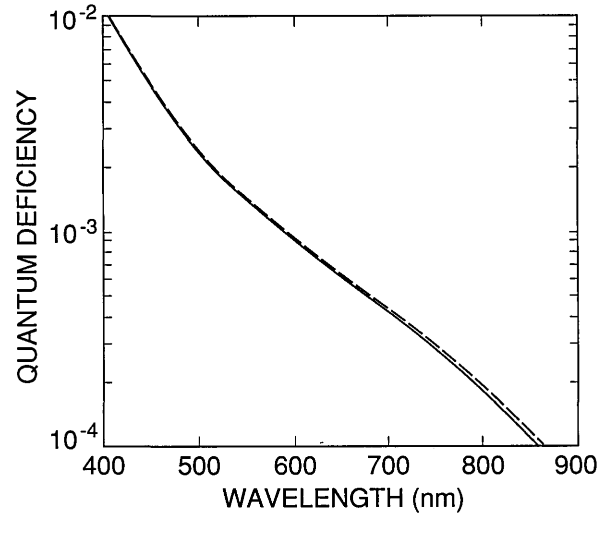

Figure 8. Simulated internal quantum deficiencies for the 1337 type photodiode having the oxide-bias data shown in figure 7: (solid curve) for the doping profile that corresponds to the lower solid curve in figure 6 with $N_{ss}=-3.0\times10^{12}$ cm^{-2} and $S=1.835\times10^5$ cm/s, and (dashed curve) for the doping profile that corresponds to the upper solid curve in figure 6 with $N_{ss}=-4\times10^{12}$ cm^{-2} and $S=1.56\times10^5$ cm/s.

simulated oxide-bias experiments based on each of those profiles. The fact that the two curves have very similar shapes is very important. It suggests that a single function of wavelength might be used to extrapolate the internal quantum efficiency of any 1337 type photodiode, rather than a different function for each different photodiode. This possibility is examined in detail in Part III of this series of papers.

Notice that the sign of the trapped charge in the 1337 type photodiode is the opposite of that for the UV444B photodiode, and that the interface recombination velocity is much larger. Both the sign of the trapped charge and the large value of the recombination velocity are consistent with an oxide prepared by chemical vapor deposition rather than by thermal oxidation, because the former is known to produce trapped positive charge and a low surface recombination velocity. The modeling carried out here shows that a large negative charge in the oxide more than makes up for the greater surface recombination velocity by repelling minority carriers from the surface.

The fact that the 1337 type photodiode has negative rather than positive charge trapped in its oxide is important for its possible use in quantum-efficiency interpolation and extrapolation. If the oxide contained a significant amount of positive charge, as assumed in reference [9], the oxide-silicon interface would be depleted of holes, leading to a very large decrease in the energy needed to impact-ionize a valence band electron. However, since the oxide contains negative charge, the interface is accumulated. In this case, even though the charge density is quite large, there is little or no decrease in the energy needed to impact-ionize a valence band electron [9]. This is important because a large decrease in the energy required to impact-ionize a valence band electron might cause the quantum yield [10] for electron-hole pair production of the silicon near the front surface to exceed unity at wavelengths as long as 450 nm. This would limit the usefulness of this type of photodiode for extrapolating and interpolating quantum-efficiency calibrations. If this limitation were encountered, it could only be overcome with a very accurate model of the quantum yield in the presence of surface fields. Such a model appears well beyond the current state of the art [9].

Even though the uncertainties in the internal quantum deficiency associated with the diode-to-diode variations in doping profile are quite small for the 1337 type photodiode, the oxide-bias experiment is still less than ideal for self-calibration [3]. However, since the 1337 is so well suited for interpolating and extrapolating internal quantum-deficiency data, as shown in Part III, all that is needed are ways to calibrate the photodiode that work over limited spectral regions near 450 nm and near 900 nm. The next section illustrates how simulation can be used to predict the internal quantum efficiency of a different type of photodiode with an uncertainty of about 0.0003 at 450 nm.

4. UDT UV100 Photodiode

The UDT UV100 type photodiode is usually assumed to have an internal quantum efficiency of unity in the short wavelength portion of the visible [11]. In fact, this assumption is the basis for the use of the QED 100 and QED 200 multiple reflection radiometers [12], which contain modified UV100 photodiodes, as high-accuracy absolute radiometric standards.

As the state of the art in absolute radiometry improves with time, the assumption of unity quantum efficiency for the UV100 type photodiode becomes more questionable. What is needed is a nominal internal quantum-deficiency spectrum accompanied by a reliable uncertainty spectrum. Since the 1337 type photodiode can be used to interpolate or extrapolate internal quantum-efficiency calibrations, as shown in Part III, it is only necessary to have these spectra over a limited spectral region above 400 nm. (Below 400 nm, the non-unity quantum yield would be a problem.) One way to obtain these spectra is to calculate them from nominal characteristics of the UV100 type of photodiode. The pertinent characteristics can be obtained by fitting numerical simulations of oxide-bias measurements to experimental results as demonstrated in the preceding sections.

The UV100 type of photodiode is quite different from the UV444B and 1337 type photodiodes. Its n^+p junction is not formed by introducing a front-region dopant, but is induced in a 100 Ω cm p-type (approximately 1.3×10^{14} cm^{-3}, boron-doped) silicon substrate by the growth of an oxide passivation layer having a large concentration of trapped positive charge [13].

Figure 9 compares the results of simulated and experimental oxide-bias experiments on a UV100 type photodiode. Here again, the absorption-coefficient data in SIL_WEAK.ABS were used, and the rear of the photodiode was modeled as uniformly doped with a surface recombination velocity of zero. Since the UV100 type photodiode is an n^+p type rather than a p^+n type, the effect of increasing negative bias is to decrease rather than increase the photocurrent. However, because the zero-bias quantum efficiency is so close to unity, this procedure samples the portion of the curve with the most information about the values of N_{ss} and S, as can be seen in the figure.

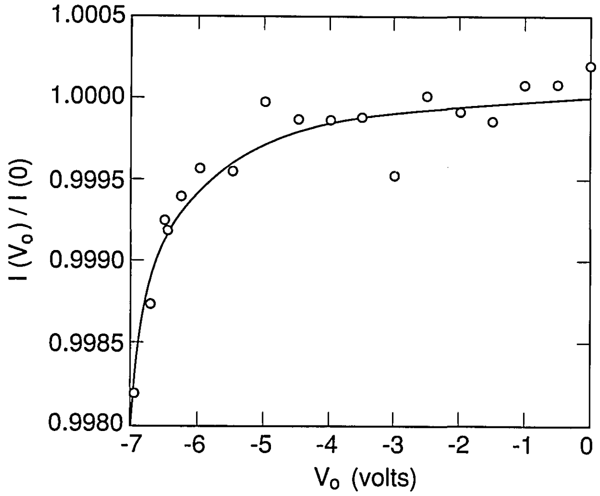

Figure 9. Ratio of the photocurrent $I(V_0)$ as a function of oxide-bias voltage V_0 to the photocurrent $I(0)$ at zero-bias voltage as measured on a typical UDT UV100 silicon photodiode and as calculated with PC-1D for $S=3.0\times10^5$ cm/s and $N_{ss}=1.38\times10^{12}$ cm^{-2}.

These values of N_{ss} and S are used to simulate the internal quantum-deficiency spectra for a nominal UV100 photodiode in figure 10. The three different curves shown in figure 10 correspond to minority carrier lifetimes τ of 1 μs, 10 μs, and 81 ms, respectively, in the rear region of the photodiode. The lifetimes of 1 and 10 μs give internal quantum deficiencies at 700 nm that bracket the range measured for six typical UV100 type photodiodes [14], and the 81 ms lifetime is the longest lifetime that the default silicon material model of PC-1D will allow for 100 Ω cm, p-type silicon with a recombination trap at mid-gap.

The region between the curves corresponding to $\tau=1$ and $\tau=10$ μs in figure 10 is a nominal internal quantum-deficiency spectrum that applies to UV100 type photodiodes and to QED 100 and QED 200 radiometers at zero reverse bias [3,12]. Figure 11 compares the spectrum for $\tau=1$ μs around its minimum in the 400 to 500 nm spectral region with spectra obtained for the cases where either the front-region surface recombination velocity is doubled, or the positive charge trapped in the oxide is halved. These are conservative limits to associate with the mass production of photodiodes in a controlled planar-silicon fabrication process. These should also be conservative limits for the effects of environmental stress, such as humidity, temperature, and irradiation with ultraviolet radiation, for UV100 photodiodes [15-16] made after 1986.

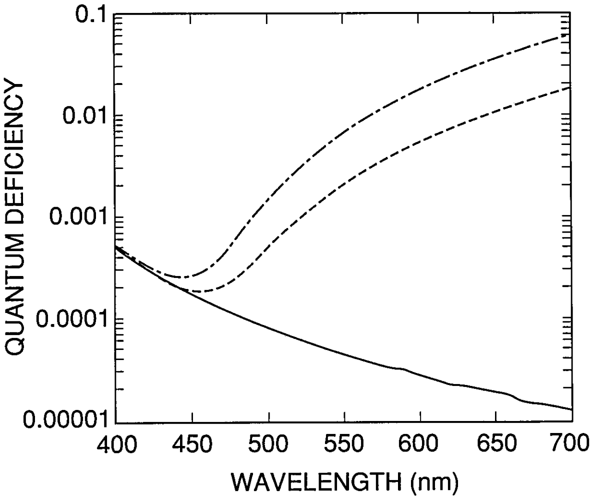

Figure 10. Internal quantum-deficiency spectra calculated by PC-1D for $S=3.0\times10^5$ cm/s, $N_{ss}=1.38\times10^{12}$ cm^{-2}, and rear-region lifetimes τ of 81 ms (solid line), 10 μs (dashed line), and 1 μs (dot-dashed line).

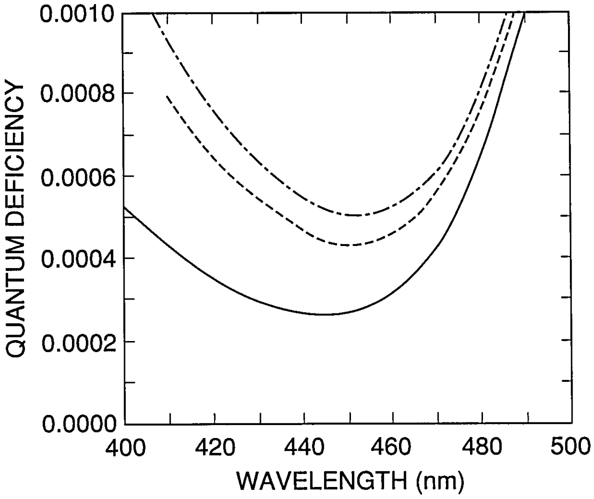

Figure 11. Internal quantum-deficiency spectra calculated by PC-1D for a rear-region lifetime $\tau=1$ μs with $S=3.0\times10^5$ cm/s and $N_{ss}=1.38\times10^{12}$ cm^{-2} (solid line), with $\tau=1$ μs with $S=6.0\times10^5$ cm/s and $N_{ss}=1.38\times10^{12}$ cm^{-2} (dashed line), and with $\tau=1$ μs with $S=3.0\times10^5$ cm/s and $N_{ss}=0.69\times10^{12}$ cm^{-2} (dot-dashed line).

The curves in figure 11 can be used to estimate uncertainties to be associated with the nominal values of the internal quantum efficiency of the UV100 type photodiode. Summing in quadrature the differences between the nominal spectrum and the other two spectra in figure 11 produces a somewhat conservative estimate since increases in surface recombination velocity tend to be correlated with increases in trapped charge. In the region from 440 to 460 nm, a nominal value of 0.0003 ± 0.0003 is a practical summary of the results of such an analysis. This result should be considered a one-standard-deviation equivalent, rather than a limit of error, since the whole analysis is based on the results obtained for a single device. Outside the 440 to 460 nm spectral region, the uncertainties grow so rapidly that they are not really practical for high-accuracy applications.

There are a number of sources of error not yet considered, but since their effect scales with the magnitude of the internal quantum deficiency, they are all negligible with respect to ±0.0003. This is illustrated in figure 12 for the uncertainty associated with the absorption coefficient of silicon in the 440 to 460 nm spectral region, which is the largest uncertainty not considered so far.

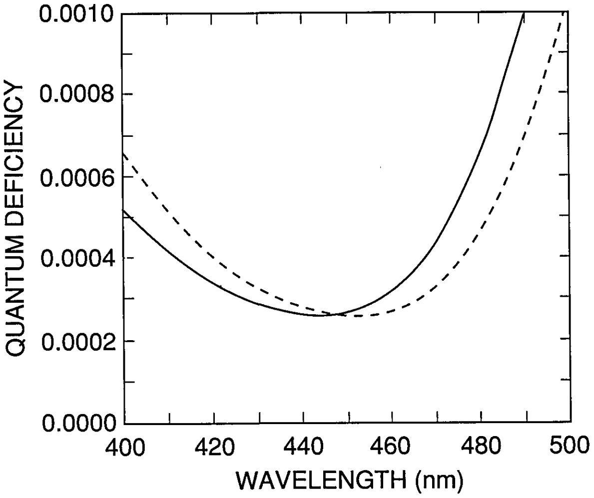

Figure 12. Comparison of the internal quantum-deficiency spectra calculated for a UV100 type photodiode for a rear-region lifetime $\tau=1$ μs with $S=3.0\times10^5$ cm/s and $N_{ss}=1.38\times10^{12}$ cm^{-2} with the absorption-coefficient data in the SIL_WEAK.ABS file (solid line), and with the absorption-coefficient data in the SIL_PHIL.ABS file (dashed line). The data in these files are described in more detail in Part I of this series of papers.

Figure 12 compares the spectrum of figure 11 for $\tau=1$ μs, which was based on the absorption-coefficient data in SIL_WEAK.ABS, with the same spectra calculated for identical parameters, but based on absorption-coefficient data (measured by Philipp [17], and described in Part I) that is stored in SIL_PHIL.ABS. When added in quadrature to the ±0.0003 assigned to the variations in N_{ss} and S from diode to diode, the effect of the uncertainty in the absorption coefficient is negligible. This might not remain true if a much larger wavelength interval were considered.

Because of the large long-wavelength quantum deficiency shown in figure 10, reverse bias is often applied to UV100 photodiodes and QED 100 and 200 radiometers when they are used at the longer wavelengths. By moving the depletion region toward the rear of the photodiode, the reverse bias forces the internal quantum deficiency to approach the lower quantum deficiency limit given by the 81 ms curve in figure 10 [12,18-19]. Reverse bias is also applied to eliminate the saturation type nonlinearity that is sometimes observed with photocurrents above a few microamperes. However, recent results [4] suggest that moderate bias levels can cause gain, resulting in an internal quantum efficiency in excess of unity. This effectively precludes the application of moderate reverse bias in high-accuracy applications.

Figure 13 plots a simulation of the decrease in the internal quantum deficiency as a function of reverse bias for the UV100 type photodiode at the 442, 476, and 514 nm laser lines. The feature in the curves for reverse-bias voltages less (more negative) than −3.5 V is a symptom of a problem with PC-1D. It may mean that more than 150 finite elements are needed to maintain the level of accuracy achieved as the reverse bias is increased, but this is not certain. In any case, it not only invalidates the data for reverse-bias voltages more negative than −3.5 V, but it also casts some doubt on any conclusions drawn about the data at the less negative bias voltages as well. At best, figure 13 suggests that 480 nm is a practical upper limit to the wavelength at which reverse bias can be used to eliminate the effect of recombination in the rear region of the photodiode without risking gain. However, the best advice would be never to use a UV100 photodiode or QED radiometer with a bias voltage without first assuring experimentally that gain is not a problem.

5. Conclusion

Part II of this series of papers has demonstrated the use of Version 2 of PC-1D.EXE, RUN_PC1D.BAT, MAKE_PRM.EXE, and READ_PDF.EXE to simulate various oxide-bias experiments of interest to high-accuracy applications of silicon photodiodes. In each case, the simulation was used to interpret an oxide-bias experiment, with different sorts of information being sought from the different experiments.

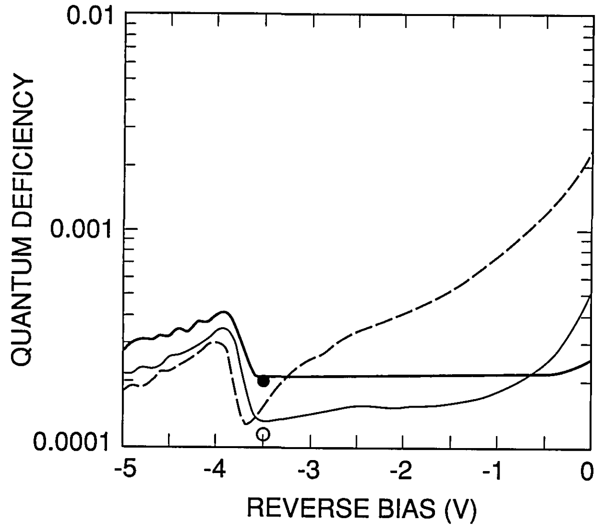

Figure 13. Simulation of the decrease in internal quantum-deficiency of a UV100 type photodiode with reverse bias at 442 nm (heavy solid line), 476 nm (light solid line), and 514 nm (dashed line). The values of N_{ss}, S, and τ are as in figure 12. The feature near −3.5 V is an artifact of the simulation. The open circle and closed circle are the internal quantum deficiencies at 442 nm and 476 nm, respectively, for $\tau = 81$ ms. The internal quantum deficiency at 514 nm for the same condition is too small to appear on the graph.

It was shown that the simulations can be used to derive a more accurate internal quantum-deficiency value from an oxide-bias experiment than that available from the conventional data reduction, and that an uncertainty can be associated with the value derived from the simulation based on how well the simulated oxide-bias data can be fitted to the experimental data. It was also shown that simulations can be used to determine nominal values for the front-surface recombination velocity and for the charge trapped in the front-surface oxide, and that values for these parameters can be used to determine nominal internal quantum-deficiency spectra for various types of silicon photodiodes.

As well as illustrating these general ideas, some more specific results were also obtained. First, it was shown that a nominal internal quantum deficiency of 0.0003 ± 0.0003 is appropriate for the unbiased UDT UV100 type photodiode in the 440 to 460 nm spectral region. Second, it was shown that the shape of the internal quantum-deficiency spectrum of the 1337 type photodiode is quite independent of typical variations in doping profile. This result suggests that the 1337 type photodiode might serve to extrapolate high-accuracy calibrations obtained from cryogenic absolute radiometers or from QED type radiometers in the 440 to 460 nm spectral region to longer wavelengths with little or no loss of accuracy. Part III of this series of papers shows that this is the case. Finally, it was shown that reverse-bias simulations based on the programs described in Part I of this series of papers do not work well enough with inversion layer (induced junction) photodiodes to be useful for high-accuracy applications.

About the authors: Jon Geist is a physicist in the NIST Semiconductor Electronics Division, Rainer Köhler and Roland Goeble are physicists at the Bureau International des Poids et Mesures in Sèvres, France, while A. M. (Sandy) Robinson and C. R. (Bob) James are Professors of Electrical Engineering at the University of Alberta in Edmonton, Alberta, Canada. Prof. James is presently Vice-President (Research) at the University.

5. References

[1] Geist, J., J. Appl. Phys. **51**, 3993 (1980).
[2] Zalewski, E. F., and Geist, J., Appl. Opt. **19**, 1214 (1980).
[3] Geist, J., SPIE **1109**, 246 (1989), provides a review of the oxide-bias, self-calibration technique.
[4] Köhler, R., Pello, R., and Bonhoure, J., Appl. Opt. **29**, 4212 (1990).
[5] Geist, J., Migdall, A., and Baltes, H. P., Appl. Opt. **27**, 3777 (1988).
[6] Weakliem, H. A., and Redfield, D., J. Appl. Phys. **50**, 1491 (1979), and personal communication.
[7] Key, P. J., Fox, N. P., and Rastello, M. L., Metrolgia **21**, 81 (1985).
[8] Geist, J., and Baltes, H. P., Appl. Opt. **28**, 3929 (1989).
[9] Geist, J., Gardner, J. L., and Wilkinson, F. J., Phys. Rev. **42B**, 1262 (1990).
[10] Geist, J., and Wang, C. S., Phys. Rev. **27B**, 4841 (1983).
[11] Geist, J., Liang, E., and Schaefer, A. R., J. Appl. Phys. **52**, 4879 (1981).
[12] Zalewski, E. F., and Duda, C. R., Appl. Opt. **22**, 2867 (1983).
[13] Hansen, T., Phys. Scr. **18**, 471 (1978).
[14] Houston, J. M., and Saunders, R. B., personal communication of data.
[15] Korde, R., and Geist, J., Solid-State Electronics **30**, 89 (1987).
[16] Korde, R., and Geist, J., Appl. Opt. **26**, 5284 (1987).
[17] Philipp, H. R., J. Appl. Phys. **43**, 2835 (1972), and personal communication.
[18] Geist, J., Zalewski, E. F., and Schaefer, A. R., Appl. Opt. **19**, 3795 (1980).
[19] Schaefer, A. R., Zalewski, E. F., and Geist, J., Appl. Opt. **22**, 1232 (1983).

Volume 96, Number 4, July-August 1991
Journal of Research of the National Institute of Standards and Technology

[J. Res. Natl. Inst. Stand. Technol. 96, 481 (1991)]

Numerical Modeling of Silicon Photodiodes for High-Accuracy Applications Part III: Interpolating and Extrapolating Internal Quantum-Efficiency Calibrations

Volume 96 | Number 4 | July-August 1991

Jon Geist

National Institute of Standards and Technology,
Gaithersburg, MD 20899

and

A. M. Robinson and
C. R. James

University of Alberta,
Alberta, Canada T6G 2G7

The semiconductor device modeling program PC-1D and the programs that support its use in high-accuracy modeling of photodiodes, all of which were described in Part I of this series of papers, are used to simulate the interpolation of high-accuracy internal quantum-efficiency calibrations in the spectral region between 450 nm and 850 nm. Convenient interpolation formulae that depend only upon wavelength are derived. Uncertainty spectra for a number of sources of error are also derived. The formulae are normalized to experimental internal-quantum efficiency calibrations in the 440 to 470 nm spectral region and at 860 nm and are used to interpolate the calibration values between these wavelengths. The results of the interpolations are compared with experimental calibration data that are available at a few wavelengths between 440 and 860 nm. The disagreement between the interpolated and measured internal quantum-efficiency data is never worse than 0.0003.

Key words: extrapolation; internal quantum-efficiency; interpolation; photodiode; silicon; visible.

Accepted: May 29, 1991

1. Introduction

Part II of this series of papers suggested that the Hamamatsu[1] 1337 type photodiode might be conveniently used for interpolating or extrapolating high-accuracy quantum efficiencies in the 400 to 900 nm spectral region. The idea of quantum-efficiency extrapolation was implicit in the first detailed description of how a silicon photodiode could be used (in this case in conjunction with a thermal detector having a spectrally flat responsivity) to realize a scale of absolute spectral responsivity [1], and interpolation was explicitly considered in reference [2]. Beyond these two publications, however, little progress has been reported in this area until recently.

Hoyt et al. [3] (using early results of the work described here) used three Hamamatsu 1337 type photodiodes to extrapolate a quantum-efficiency calibration obtained at 441.6 nm with a UDT QED 100 radiometer to 633.0 nm, and reported an average difference of 0.04% compared to independent measurements based on their electrically calibrated cryogenic cavity radiometer. Even though 0.04% is quite good by conventional radiometric standards, it was a factor of two larger than the combined uncertainty estimate for the two measurement techniques being compared, and further study was proposed by Hoyt et al. More recently, Zalewski and Hoyt [4] have reported a more direct test of the accuracy of the use of the Hamamatsu 1337 type photodiode to extrapolate quantum-efficiency values. The results of this test agreed to within the combined estimated uncertainty, and two errors were discovered in the earlier work. When these

---

[1] Certain commercial equipment, instruments, or materials are identified in this paper to specify adequately the experimental procedure. Such identification does not imply recommendation or endorsement by the National Institute of Standards and Technology, nor does it imply that the materials or equipment identified are necessarily the best available for the purpose.

errors were corrected, agreement within the estimated uncertainty of the earlier intercomparison was obtained.

The purpose of Part III of this series of papers is to develop formulae and uncertainty estimates for interpolating and extrapolating internal quantum-efficiency calibrations with Hamamatsu 1337 photodiodes. It will be shown that this type of photodiode has characteristics that suit it particularly well for this task over the 440 to 860 nm spectral region. The remainder of Part III is organized as follows: Section 2 investigates the errors associated with the use of relations that are only approximate for the 1337 type photodiode, but which simplify interpolation and extrapolation of the internal quantum deficiency (one minus the internal quantum efficiency) for this type of photodiode. Section 3 investigates the various sources of error associated with the actual calculation of internal quantum-deficiency spectra using the semiconductor-device modeling program PC-1D and the support programs described in Part I. Finally, section 4 compares the results obtained here with experimental measurements and demonstrates agreement within 0.0003.

2. Errors Associated with the Quantum-Deficiency Approximations

For the purposes of extrapolating and interpolating the internal quantum efficiency of Hamamatsu 1337 type photodiodes, the internal quantum deficiency can be approximated by a function $\delta(\lambda, N_{ss}, S, \tau_r)$ of wavelength λ and of three recombination-related variables: N_{ss} the charge number density stored in the front-surface oxide, S the surface recombination velocity at the oxide-silicon interface, and τ_r the minority-carrier lifetime in the rear region.

For silicon photodiodes, $\delta(\lambda, N_{ss}, S, \tau_r)$ can be approximated by a function that has properties that make it particularly useful for extrapolating and interpolating quantum-deficiency measurements. The approximate equation for $\delta(\lambda, N_{ss}, S, \tau_r)$ is

$$\delta(\lambda, N_{ss}, S, \tau_r) = K_f(N_{ss}, S)\ \delta_f(\lambda) + K_r(\tau_r)\ \delta_r(\lambda), \tag{1}$$

where

$$\delta_r(\lambda) = 0, \tag{2}$$

for λ less than some wavelength λ_0.

To see how this is useful for interpolating quantum-deficiency values, suppose that $\delta(\lambda_f, N_{ss}, S, \tau_r)$ has been measured at wavelength $\lambda_f < \lambda_0$, and $\delta(\lambda_r, N_{ss}, S, \tau_r)$ has been measured at wavelength $\lambda_r > \lambda_0$. The values for $K_f(N_{ss}, S)$ and $K_r(\tau_r)$ can then be determined from

$$K_f(N_{ss}, S) = \frac{\delta(\lambda_f, N_{ss}, S, \tau_r)}{\delta_f(\lambda_f)}, \tag{3a}$$

and

$$K_r(\tau_r) = \frac{\delta(\lambda_r, N_{ss}, S, \tau_r) - K_f(N_{ss}, S)\delta_f(\lambda_r)}{\delta r(\lambda_r)}, \tag{3b}$$

and these values can be used in eq (1) to interpolate the quantum deficiency between λ_f and λ_r. In the above equations, $\delta_f(\lambda)$ and $\delta_r(\lambda)$ are functions only of wavelength, λ_f and λ_r are the wavelengths at which the internal quantum deficiency is to be normalized, and λ_0 will generally fall between 600 and 650 nm. The subscript f stands for the front of the photodiode since this is the location of the recombination mechanisms that cause $\delta_f(\lambda)$ to exceed zero. The subscript r stands for the rear of the photodiode since this is the location of the recombination mechanism that cause $\delta_r(\lambda)$ to exceed zero. Therefore, $\delta_f(\lambda)$ and $\delta_r(\lambda)$ will be called the front-region and rear-region internal quantum-deficiency spectra, respectively. The functional dependence of K_f and K_r will be dropped from the notation for the remainder of this paper.

Exactly how accurate eqs (1–3) are depends upon the particular type of photodiode and the range covered by the parameters. Figure 1 illustrates the accuracy of eq (1) for the 1337 type photodiode (modeled as described in Part II of this series of papers) over the 400 to 900 nm spectral region for an internal quantum-deficiency spectrum that is a practical upper limit for this type of photodiode. Figure 1 compares the internal quantum-deficiency spectra $\delta(\lambda, 0, 71264\ \text{cm/s}, \infty)$ and $\delta(\lambda, 0, 0, 1\ \text{ms})$ with their sum, and with the internal quantum-deficiency spectrum $\delta(\lambda, 0, 71264\ \text{cm/s}, 1\ \text{ms})$. The latter spectrum and the sum of the two first spectra differ by less than 2×10^{-5} over the entire 400 nm spectral region, and cannot be distinguished at the scale of the figure. (Any errors with absolute values less than 2×10^{-5} are negligible for the purposes of this paper.)

Figure 2 illustrates the accuracy of eqs (1–3) over the 400 to 900 nm spectral region for the case where $\tau_r = \infty$. The spectra in figure 2 were calculated for the range of parameters listed in table 1.

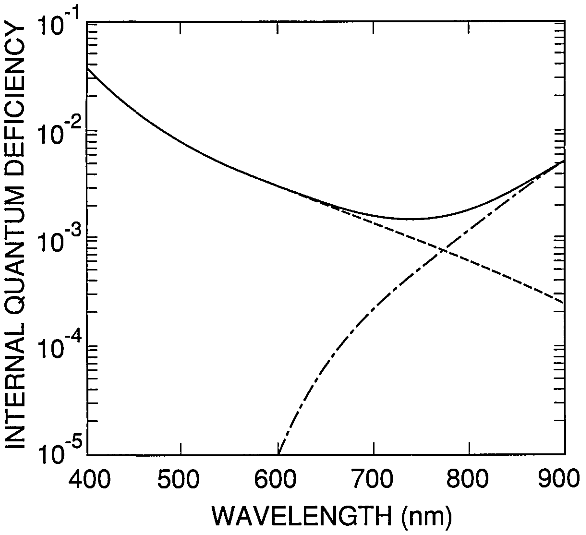

Figure 1. The quantum-deficiency spectra $\delta(\lambda,0,71264\ \mathrm{cm/s},\infty)$ (dashed line) and $\delta(\lambda,0,0,1\ \mathrm{ms})$ (dot-dashed line) and their sum (solid line).

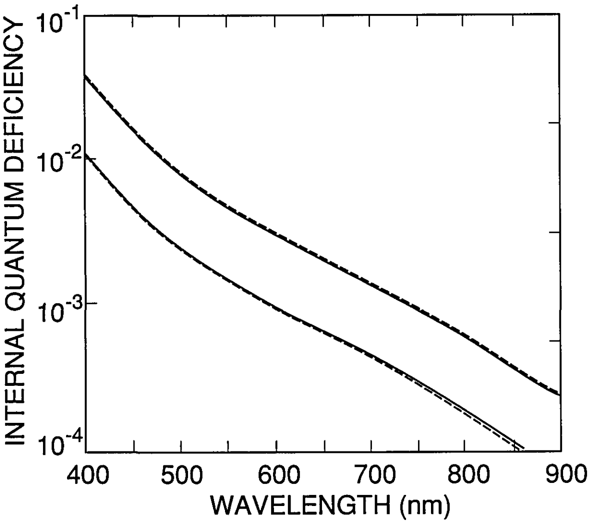

Figure 2. The quantum-deficiency spectra $\delta(\lambda,N_{ss},S,\tau_r)$ for the conditions (Case 1—upper dashed line; Case 2—lower dashed line; Case 3—upper solid line; Case 4—lower solid line) listed in table 1.

Table 1. Recombination related parameters used with the doping distributions shown in figure 3 to model the quantum-deficiency spectra of Hamamatsu 1337 type photodiodes

Case	N_{ss} (cm^{-3})	S (10^5 cm/s)	τ_r (s)	$N_A(x)$
1	0	0.71264	∞	dashed curve
2	-3×10^{12}	1.83500	∞	dashed curve
3	-1×10^{13}	100.000	∞	dashed curve
4	-4×10^{12}	1.56000	∞	solid curve

Cases 1–3 in that table are based on the front-region doping distribution $N_A(x)/N_A(0)$ shown as the dashed curve in figure 3, and Case 4 is based on that shown as the solid curve in the same figure. Of six doping distributions measured for different 1337 type photodiodes, the two shown in figure 3 produce the largest change in shape of the internal quantum-deficiency spectrum.

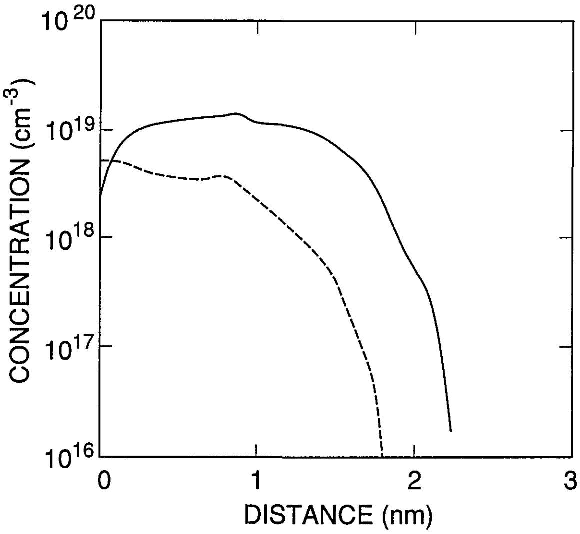

Figure 3. The front-region doping distributions $N_A(x)$ used to calculate the front-region internal quantum-deficiency curves in figure 2.

The shapes of the front-region internal quantum-deficiency spectra in figure 2 are compared in figure 4 by normalizing all of the spectra to 0.01 at 440 nm and by plotting their differences relative to the normalized spectrum for Case 2. Cases 1 and 3 compared with Case 2 shows how the shape of $\delta_f(\lambda)$ changes when its magnitude is increased by over a factor of three in association with either a substantial decrease or a substantial increase in N_{ss}. (Cases 1 and 3 bracket a number of cases that were examined in which N_{ss} and S were independently varied within the range of values shown in table 1.)

Case 4 compared with Case 2 shows how the shape of $\delta_f(\lambda)$ changes when the dopant distribution is changed from the dashed curve to the solid curve in figure 4. This effect is much larger than that associated with varying N_{ss} and S.

The three spectra in figure 4 characterize the uncertainties to be associated with the diode-to-diode variations in N_{ss}, S, and $N_A(x)$ when any one of the spectra in that figure is used as $\delta_f(\lambda)$ with $K_f=0.01$ in eqs (1) and (3). These spectra should be multiplied by $K_f/0.01$ if $K_f \neq 0.01$. For the purposes of this paper, the $\delta(\lambda, N_{ss}, S, \infty)$ spectrum corresponding to Case 4 in table 1 will be used for $\delta_f(\lambda)$ in eqs (1) and (3).

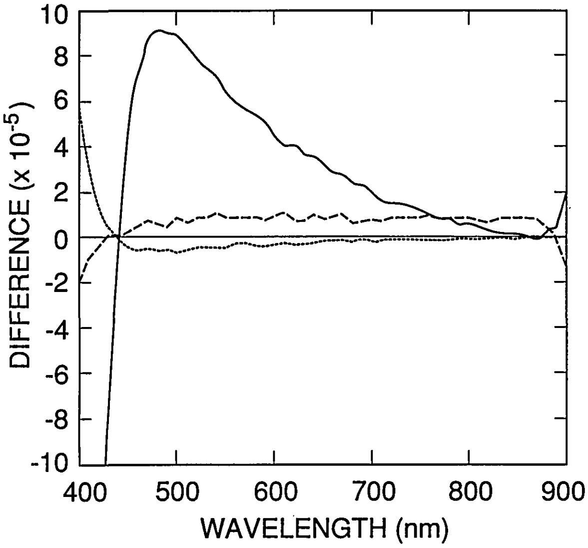

Figure 4. Differences between the internal quantum-deficiency spectra of figure 2 for Cases 1 (dashed line), 3 (dotted line), and 4 (solid line) when normalized to 0.01 at 440 nm, and that for Case 2 when normalized to 0.01 at 440 nm.

The front-region internal quantum deficiency also depends upon two front-region recombination mechanisms not considered above. These are the Auger and band-to-band mechanisms that become important in the heavily doped front region of the photodiode. Both effects were included in all of the spectra described so far by using the default cross sections that are built into PC-1D for these recombination mechanisms. The PC-1D default values for the Auger recombination cross sections give an internal quantum-deficiency spectrum with a value of 9×10^{-6} at 400 nm. The shape of this spectrum is well modeled by $\delta_f(\lambda)$ [5]. In fact, an uncertainty of ±100% can be tolerated in the Auger cross sections without causing an error as large as 2 times 10^{-5} anywhere within the 400 to 900 nm spectral region.

For the doping profile shown as the solid curve in figure 3, the PC-1D default values for the band-to-band recombination cross sections give the lifetimes shown in figure 5 as a function of distance from the oxide-silicon interface in the photodiode. These lifetimes give an internal quantum-deficiency spectrum with a value of 6×10^{-5} at 400 nm. This spectrum is not as well modeled by $\delta_f(\lambda)$ as is the spectrum for Auger recombination, but an uncertainty of ±50% in the band-to-band recombination cross sections can be tolerated without raising the error associated with this uncertainty to 2×10^{-5} anywhere in the 400 to 900 nm spectral region.

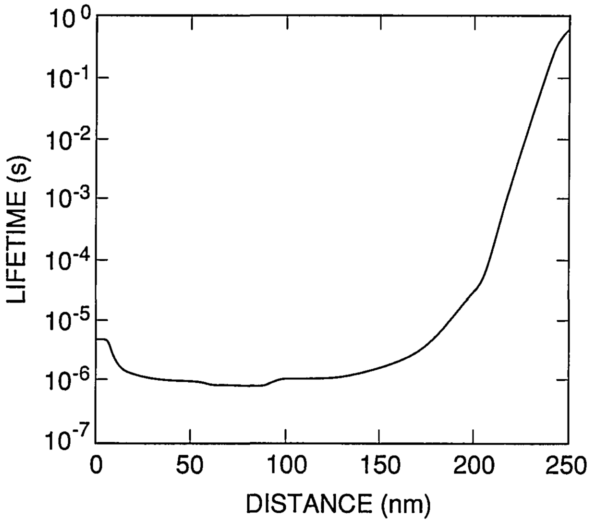

Figure 5. The default, band-to-band recombination lifetime profile calculated by PC-1D for the doping distribution shown as the solid curve in figure 3.

Now consider $\delta_r(\lambda)$. Figures 6 and 7 illustrate the accuracy of eqs (1) and (3) over the 400 to 900 nm spectral region for the case where $S = 0$. (Note that when $S = 0$, the internal quantum-deficiency spectrum is independent of N_{ss}.) The spectra in figure 6 were calculated for $\tau_r = 1$ ms and 10 ms, with $N_{ss} = S = 0$. For the purposes of this paper, $\delta_r(\lambda)$ will be set to zero in eqs (2) and (3) for $\lambda \leq 610$ nm, and the spectrum for $\tau_r = 1$ ms will be used for $\delta_r(\lambda)$ for $\lambda > 610$ nm.

The shapes of the spectra in figure 6 are compared in figure 7 by normalizing them to 0.002 at 860 nm and plotting their differences relative to the spectrum for $\tau_r = 1$ ms. The normalization value of 0.002 was chosen as a practical upper limit. The difference spectrum in figure 7 characterizes the uncertainties to be associated with the variations in rear-region lifetime when the spectrum for $\tau_r = 1$ ms is used as $\delta_r(\lambda)$ with $K_r = 0.002$ in eqs (2) and (3). This spectrum should be multiplied by $K_r/0.002$ if $K_r \neq 0.002$.

A convenient function of wavelength has been fitted to the spectrum corresponding to Case 4 in table 1, and another to the spectrum for $\tau_r = 1$ ms in figure 6. These functions are

$$\delta_f(\lambda) = A_0 \left[X(\lambda) + A_1 X^2(\lambda) + A_2 Y(\lambda)\right], \qquad (4)$$

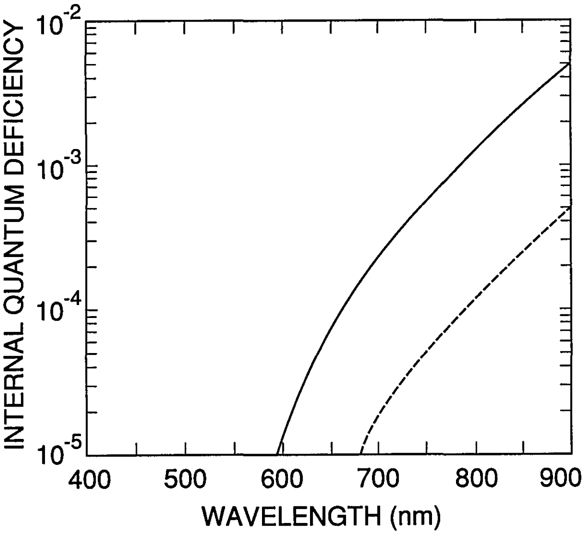

Figure 6. The internal quantum-deficiency spectra $\delta(\lambda, N_{ss}, S, \tau_r)$ for $\tau_r = 1$ ms (solid line), and $\tau_r = 10$ ms (dashed line) with $N_{ss} = S = 0$.

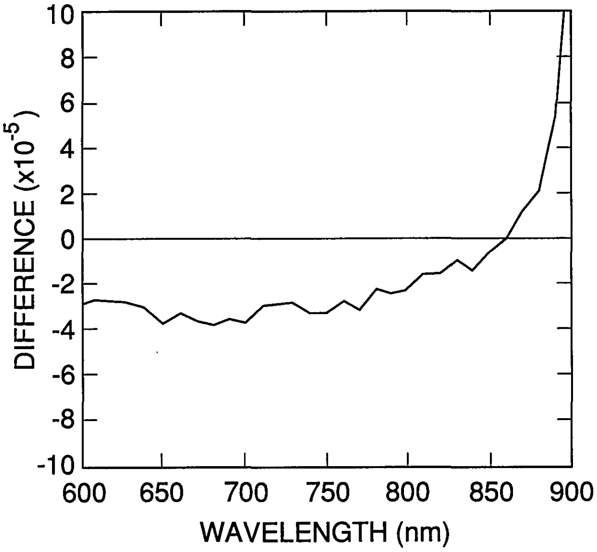

Figure 7. Differences between the internal quantum-deficiency spectra of figure 6 when normalized to 0.002 at 860 nm.

and

$$\delta_r(\lambda) = A_0\,[1/X(\lambda) - A_2/Y(\lambda)], \tag{5}$$

respectively, where

$$X(\lambda) = \exp(-\lambda/\lambda_0), \tag{6}$$

and

$$Y(\lambda) = \exp(-(\lambda/\lambda_2)^2). \tag{7}$$

The appropriate values for A_0, A_1, A_2, λ_0, and λ_2 for eqs (4) and (5) are listed in table 2. The function in eq (5) becomes negative for $\lambda < 620$ nm, in which case eq (5) is replaced with $\delta_r(\lambda) = 0$ as mentioned earlier. The values of A_0 in table 2 normalize $\delta_f(\lambda)$ to 0.01 at 440 nm, and $\delta_r(\lambda)$ to 0.002 at 860 nm, respectively.

With $K_f = 0.5516405$, eq (4) fits the spectrum for $N_{ss} = -3\times10^{12}$ cm/s in figure 4 with a residual standard deviation of 2.9×10^{-6} over the 420 to 900 nm spectral region and never differs from that spectrum by more than 7×10^{-6} over the same spectral region. This translates to less than 10 ppm when the internal quantum deficiency is normalized to 0.01 at 440 nm; thus the error associated with the use of eq (4) is negligible for the purposes of this paper. The larger variations below 420 nm are negligible with respect to uncertainties already identified and others discussed below.

With $K_r = 1.685081$, eq (5) fits the spectrum shown as a solid line in figure 6 with a residual standard deviation of 1.4×10^{-5} over the 610 to 900 nm spectral region, and never differs from that spectrum by more than 2.5×10^{-5} over that same spectral range. This translates to less than 1.7×10^{-5} when the quantum deficiency is normalized to 0.002 at 440 nm; thus the error associated with the use of eq (5) is also negligible for the purposes of this paper.

Table 2. Values of the parameters to be used in eq (4) for extrapolating a short wavelength internal quantum-deficiency value to longer wavelengths and in eq (5) for extrapolating a long wavelength internal quantum-deficiency value to shorter wavelengths

Parameter	eq (4)	eq (5)
A_0	1.38002×10^{2}	2.02157×10^{-8}
A_1	1.47530×10^{2}	3.51764×10^{3}
A_2	8.07476×10^{-5}	0.0
λ_9	4.39312×10^{1} nm	7.53991×10^{1} nm
λ_2	4.27998×10^{2} nm	1.66889×10^{8} nm

3. Errors Associated with Quantum-Deficiency Calculations

Two types of error associated with the quantum-deficiency values calculated by PC-1D can be distinguished: 1) numerical errors associated with the algorithms used by PC-1D and the limited number of finite elements available to PC-1D, and 2) physical errors associated with approximations and simplifications in the physical models used with, or built into, PC-1D. Both types are considered in this section.

It was shown in reference [5] that $\delta_f(\lambda)$ is well approximated by

$$\delta_f(\lambda)=\frac{\Gamma\{I(0)-I[\alpha(\lambda)]\}}{1+\Gamma I[\alpha(\lambda)]}, \tag{8}$$

$$I[\alpha(\lambda)]\int_0^{x_1}\hat{k}(x)\exp(-\alpha(\lambda)x)\mathrm{d}x, \tag{9}$$

$$\hat{k}(x)=k(x)/k(0), \tag{10}$$

$$k(x)=1/[m_0(x)D_m(x)], \tag{11}$$

$$\Gamma=S/D_m(0), \tag{12}$$

where $\alpha(\lambda)$ is the absorption-coefficient spectrum of silicon, x is the distance from the oxide-silicon interface toward the rear of the photodiode, $m_0(x)$ is the equilibrium minority-carrier concentration at the point x in the front region of the photodiode, and $D_m(x)$ is the equilibrium diffusion constant for the minority carriers at the point x. Note that the sign in the numerator in eq (8) is correct and that the sign is incorrect in reference [5]. Also, note that $f(\lambda)$ becomes very insensitive to x_1 as x_1 increases beyond some critical value. The point where the electron and hole concentrations cross is a convenient choice for x_1, but smaller values would work as well.

From the point of view of PC-1D, the kernel $k(x)$ in eq (11) is given by

$$k(x)=qM_0(x)/[n_{ie}^2(x)kT\mu_m(x)], \tag{13}$$

where $M_0(x)$ is the equilibrium majority carrier concentration in the front region, $n_{ie}(x)$ is the effective intrinsic carrier concentration [6], which in PC-1D includes the effect of Fermi-Dirac statistics, $\mu_m(x)$ is the minority-carrier mobility as a function of position in the front region, k is the Boltzmann constant, and T is the temperature of the photodiode.

Figure 8 compares $\exp(-\alpha(400\ \mathrm{nm})x)$ with the equilibrium functions $M_0(x)$, $n_{ie}(x)$, and $\mu_m(x)$ as calculated by PC-1D over the range $0<x<200$ nm for the same photodiode model used to calculate the quantum-deficiency spectra in figure 3 for Case 2 of table 1. Equations (8–12), figure 8, and figure 3 show why the shape of $\delta_f(\lambda)$ is very insensitive to N_{ss} while being quite sensitive to the shape of $N_A(x)/N_A(0)$. Since the width of the accumulation layer created by N_{ss} is small compared to the distance over which $\exp(-\alpha(\lambda)x)$ changes significantly for $\lambda\geq 400$ nm, changes in N_{ss} have the effect of multiplying the integral in eq (9) by a constant factor independent of $\lambda\geq 400$ nm. On the other hand, the changes in $N_A(x)/N_A(0)$ shown in figure 3 extend well into the region where $\exp(-\alpha(\lambda)x)$ varies significantly from unity for $\lambda=400$ nm. As λ is increased above 400 nm, the shape of $\delta_f(\lambda)$ will become less dependent on the shape of $N_A(x)/N_A(0)$ because $\alpha(\lambda)$ decreases with increasing λ.

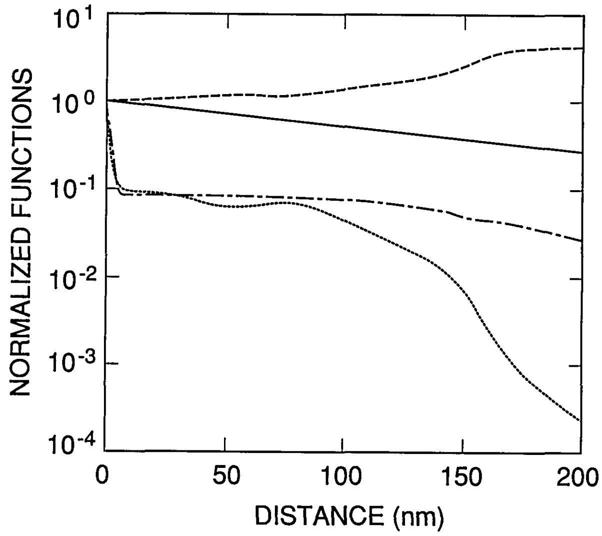

Figure 8. Comparison of $\hat{M}_0(x)$ (dotted line), $\hat{n}_{ie}(x)$ (dashed line), $\hat{\mu}$ (dot-dashed line), and $\exp(-\alpha(400\ \mathrm{nm})\,x)$ (solid line) for a 1337 type photodiode with N_{ss}, S, and τ_r set as defined in Case 2 of table 1. The tildes in the preceding expressions indicate that these expressions have been normalized to unity at $x=0$, as shown for $k(x)$ in eq (10).

The numerical accuracy with which PC-1D calculates $M_0(x)$ within the framework of the drift-diffusion approximations for the conditions of charge accumulation at an oxide-silicon interface as shown in figure 8 has been studied previously and found to be quite good [7]. With a uniform doping density of 10^{19} cm^{-3} and an oxide charge density of 10^{13} cm^{-2}, PC-1D overestimates $M_0(x)$ by about 9% at $x=0$, decreasing to within ±1% for $x>1$ nm. The uncertainty in $k(x)$ due to this source of error will be modeled by replacing $k(x)$ by

$$k_1(x)=k(x)/(1-0.1\,x/x_0), \tag{14}$$

for $x<x_0$, and

$$k_1(x)=k(x)/0.9, \tag{15}$$

for $x > x_0$ in the kernel of the integral in eq (9), where $x_0 = 1$ nm.

Another source of error that must be considered is the numerical accuracy with which PC-1D would calculate the steady-state photocurrent if the equilibrium carrier concentration were exact. The uncertainty associated with this source of error was estimated as follows: 1) The internal quantum-deficiency spectrum was calculated directly from the PC-1D solution of the steady-state drift-diffusion equations for the total current flowing in the photodiode for the conditions described by Case 2 of table 1. 2) Equations (8–13) were used to calculate the internal quantum-deficiency spectrum from the equilibrium values of $M_0(x)$, $n_{ie}(x)$, and $\mu_m(x)$ calculated by PC-1D for the same conditions as in 1) above. The integration in eq (9) was carried out using a generalization of Simpson's rule for nonequidistant points. 3) Both spectra were normalized to 0.01 at 440 nm, and the differences calculated. There is no reason to believe that these differences, which exceed 2×10^{-5} only at 400 and at 900 nm, are caused by errors associated with PC-1D. It is just as likely that they are associated with eqs (8–12) since these equations were derived from a number of assumptions that are not rigorously satisfied. The important point is that it is unlikely that either calculation is in error by much more than the differences between them. This verifies the numerical accuracy of the photocurrents calculated by PC-1D to the level of accuracy required in this paper.

There are a number of other errors, which are associated with incomplete or approximate physical models built into PC-1D, that also affect the accuracy with which PC-1D calculates the functions defining $k(x)$ in eq (13). These include quantum-mechanical effects (tunneling) [8] that change the shape of $M_0(x)$ from that calculated from the drift-diffusion approximation for $x < 1$ nm, band-gap narrowing effects [9] associated with heavy doping and large surface-fields [10] that cause $n_{ie}(x)$ [6] to depend upon position in the photodiode, and carrier-carrier and carrier-ion scattering mechanisms that cause $\mu_m(x)$ to depend upon position [11]. It is beyond the scope of this paper to investigate each of these sources of error in detail, but the uncertainty in $k(x)$ due to this source of error will be modeled by replacing $k(x)$ by

$$k_2(x) = k(x)\{1 - 0.1 \log[\hat{k}(x)]\} \qquad (16)$$

in the kernel of the integral in eq (9). This allows an error of 10% per decade change in $k(x)$.

The differences between the internal quantum-efficiency spectrum calculated from eqs (8–13) by replacing $k(x)$ with either $k_1(x)$ or $k_2(x)$ in eq (9) and the spectrum calculated using $k(x)$ were calculated after all three spectra were normalized to 0.01 at 440 nm. Neither difference exceeded 2×10^{-5} over the entire 400 to 900 nm spectral region. Therefore, all of these sources of error are considered negligible for the purposes of this paper.

Another source of error that is obvious in eqs (8–12) is the uncertainty associated with the absorption-coefficient data used in the simulations. As described in Part I, the absorption-coefficient data were calculated from an equation [12] fitted to the data of Weakliem and Redfield [13]. An alternate set of absorption-coefficient data was described by Philipp [14]. Figure 9 plots the differences between the internal quantum-deficiency spectra normalized to 0.01 at 440 nm for Case 2 of table 1 when based on the absorption-coefficient data in reference [14] and when based on the equation in reference [12]. These differences will be used as the estimated uncertainties arising from the uncertainties in the silicon absorption-coefficient spectrum when $\delta_f(\lambda)$ is used to extrapolate an internal quantum deficiency of 0.01 from 440 nm to longer wavelengths with a 1337 type photodiode. A similar calculation was carried out for the case where $S = 0$ and $\tau_r = 1$ ms. Both spectra were normalized to 0.002 at 860 nm. The differences, which are shown in figure 10, are taken as the estimated uncertainties arising from the uncertainties in the silicon absorption-coefficient spectrum where $\delta_r(\lambda)$ is used to extrapolate an internal quantum deficiency of 0.002 from 860 nm to shorter wavelengths with a 1337 type photodiode.

Figures 11 and 12 plot the quadrature sum of the difference spectra plotted in figures 4 and 9 and in figures 7 and 10, respectively. The spectrum in figure 11 plots the estimated (one standard deviation) uncertainty as a function of wavelength that is associated with the use of $\delta_f(\lambda)$ in eq (4) to extrapolate a measured internal quantum deficiency of 0.01 from 440 nm to longer wavelengths. The major sources of error contributing to the uncertainty spectrum in figure 11 are the diode-to-diode variations in $N_A(x)/N_A(0)$ and the uncertainty in the absorption-coefficient spectrum for silicon, but a number of other sources of error were identified with the help of eqs (8–12), and any that produced differences greater than 2×10^{-5} for 400 nm $< \lambda < 900$ nm are included in figure 11.

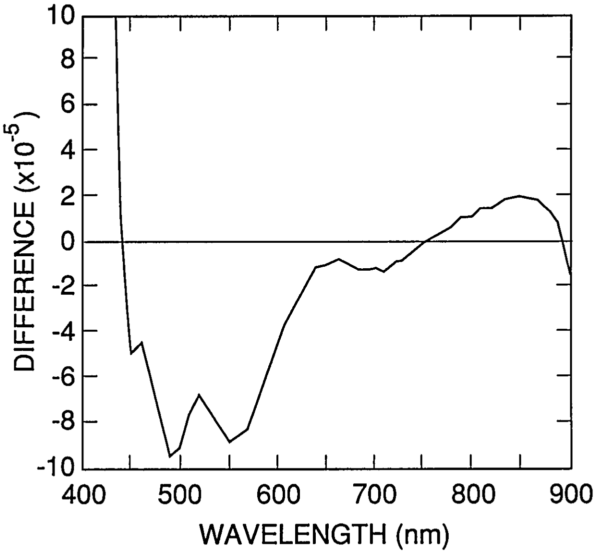

Figure 9. Differences between the internal quantum-deficiency spectrum for a 1337 type photodiode satisfying the conditions defined in table 1 for the absorption-coefficient data of reference [14] and for the absorption-coefficient data of reference [12].

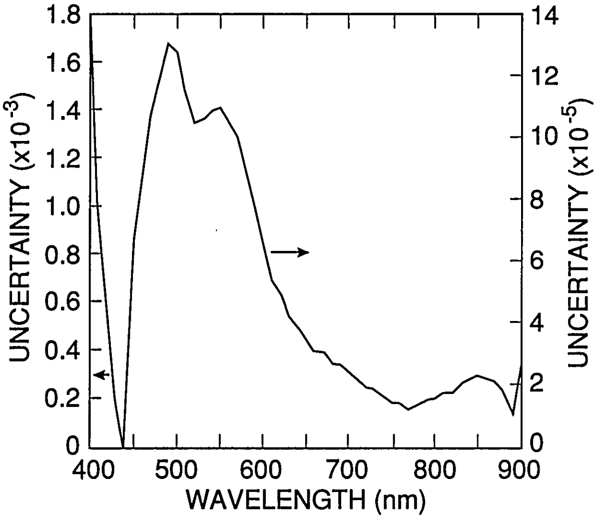

Figure 10. Differences between the internal quantum-deficiency spectra for a 1337 type photodiode with $S=0$ and $\tau_r=1$ ms for the absorption-coefficient data of reference [14] and for the absorption-coefficient data of reference [12].

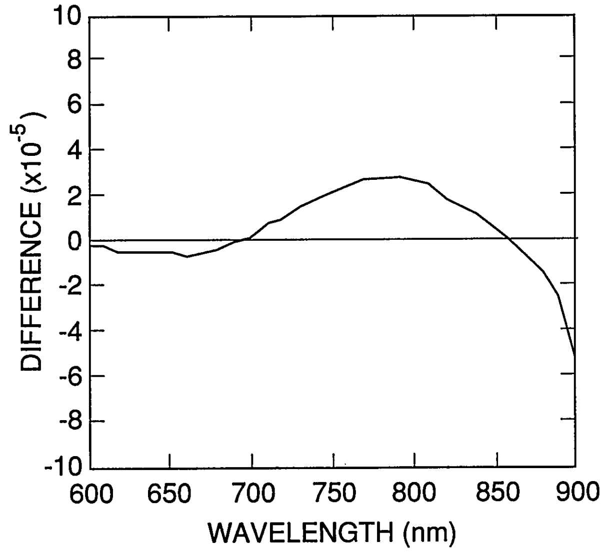

Figure 11. Sum in quadrature of the curves in figures 4 and 9. This curve is the nominal uncertainty associated with the use of eq (4) in eq (2) to extrapolate a quantum deficiency of 0.01 at 440 nm to any other wavelength between 400 and 900 nm. Notice that the sum is plotted on different scales below and above 440 nm.

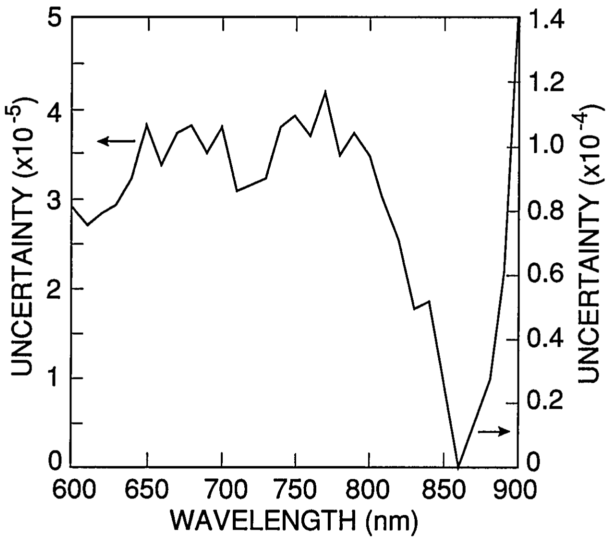

Figure 12. Sum in quadrature of the curves in figures 7 and 10. This curve is the nominal uncertainty associated with the use of eq (5) in eq (2) to extrapolate a quantum deficiency of 0.02 at 860 nm to any other wavelength between 400 and 900 nm. Notice that the sum is plotted on different scales below and above 440 nm.

The spectrum in figure 12 plots the estimated (one standard deviation) uncertainty as a function of wavelength that is associated with the use of $\delta_r(\lambda)$ in eq (5) to extrapolate a measured internal quantum deficiency of 0.002 from 860 nm to shorter wavelengths. The major sources of error contributing to the uncertainty spectrum in figure 12 are the change in shape of $\delta_r(\lambda)$ with τ_r and the uncertainty in the absorption-coefficient spectrum for silicon. All other sources of error considered were negligible with respect to 2×10^{-5} for 400 nm $<\lambda<900$ nm.

No equivalents to eqs (8–12) were used to guide the error analysis for $\delta_f(\lambda)$. The results of the uncertainty analysis of $\delta_f(\lambda)$ show that numerical accuracy of PC-1D will be a negligible source of error. This leaves the errors associated with the approximations in the physical models that are built into PC-1D. Some of these were tested, but no tests were possible for the use of a single SRH trap level to model the recombination in the rear region of the photodiode. This approximation could be a non-negligible source of error; it was shown in Part I that this approximation introduced errors of the order of the effect being modeled in nonlinearity simulations on a UV444B type photodiode. A more complete model might make τ_r depend upon position in the photodiode, which might modify the shape of $\delta_r(\lambda)$ and add an uncertainty that is not included in figure 12.

4. Comparison with Experiment

To use the results developed thus far, it is necessary to define the internal quantum-deficiency interpolating function $\delta(\lambda)$, and to assume that it exactly satisfies eqs (1–3), which can be rewritten in more compact form as

$$\delta(\lambda)=$$

$$\delta_x(\lambda_f)\,\frac{\delta_f(\lambda)}{\delta_f(\lambda_f)}+\delta_x(\lambda_r)\left[1-\frac{\delta_f(\lambda_r)}{\delta_r(\lambda_r)}\right]\frac{\delta_r(\lambda)}{\delta_r(\lambda_r)}, \tag{17}$$

where $\delta_x(\lambda_f)$ and $\delta_x(\lambda_r)$ are the measured values of the internal quantum deficiency at the wavelengths λ_f and λ_r, respectively; $\delta_f(\lambda)$ and $\delta_r(\lambda)$ are defined in eqs (4) and (5), respectively, and the constants used in these equations are defined in table 2. The uncertainty associated with $\delta(\lambda)$ due to the sources of error considered in the last two sections of this paper can be obtained by summing in quadrature each of the terms on the right-hand side of the differential of eq (17). That differential is given by

$$d\delta(\lambda)=d\delta_x(\lambda_f)\left[\frac{\delta_f(\lambda)}{\delta_f(\lambda_f)}\right]$$

$$+d\delta_x(\lambda_r)\left[\frac{\delta_r(\lambda)}{\delta_r(\lambda_r)}\right]\left[1-\frac{\delta_f(\lambda_r)}{\delta_r(\lambda_r)}\right]$$

$$+d\delta_f(\lambda)\left[\frac{\delta_x(\lambda_f)}{\delta_f(\lambda_f)}\right]$$

$$+d\delta_r(\lambda)\left[\frac{\delta_x(\lambda_r)}{\delta_r(\lambda_r)}\right]\left[1-\frac{\delta_f(\lambda_r)}{\delta_r(\lambda_r)}\right]. \tag{18}$$

The differentials $d\delta_f(\lambda)$ and $d\delta_r(\lambda)$ are plotted in figures 11 and 12 for $\lambda_f=440$ nm, and for $\lambda_r=860$ nm, respectively.

There are not many data available against which to test eqs (17) and (18), but there are some. For instance, Zalewski and Hoyt [4] have reported the internal quantum efficiencies at 441.6 nm and the spectral responsivities and absorptances at 633.0 nm for five multiple reflection (trap) [4,15–17] radiometers based on Hamamatsu 1337 photodiodes at 441.6 and 633.0 nm. Similarly, Fox [17] has reported the average internal quantum efficiency of 10 trap radiometers also based on Hamamatsu 1337 photodiodes at six Ar^+ ion laser lines, and he has also measured the oxide-bias correction for a single Hamamatsu 1337 photodiode at four Ar^+ ion laser lines. Zalewski and Hoyt [4] presented their data, which are summarized in bold face type in table 3, as an intercomparison of spectral responsivity. Since the internal quantum deficiency is the quantity of interest in this paper, it is necessary to compute this quantity from the data reported by Zalewski and Hoyt as shown in table 3. The corrections for nonlinearity that Zalewski and Hoyt derived from reverse-bias measurements also eliminate any effects of recombination in the rear region of the photodiodes.

Table 3. Average values of, and uncertainty estimates for, the internal quantum efficiency ϵ_f, spectral responsivity R, one minus the reflectance $(1-\rho)$ and nonlinearity correction $(1-NL)$ reported in reference [4] (bold face type) at wavelength λ for five multiple-reflection radiometers based on 1337 type photodiodes, and internal quantum-deficiency values $\delta_x(\lambda)$ calculated from the reported data

λ (nm)	ϵ_f	R (A/W)	$(1-\rho)$	$(1-NL)$	$\delta_x(\lambda)$
441.6	**+0.99347** **±0.00040**				+0.00653 ±0.00040
633.0	**+0.50840**	**+0.99704** **±0.00009**	**+0.99972** **±0.00014**	**+0.00097** **±0.00004**	±0.00023

Fox's [17] oxide-bias data, which are summarized in table 4, were measured at 10 V, and were reported as a fractional increase in photocurrent I given by $\gamma_o = I(10\text{V})/I(0) - 1$. The oxide-bias experiment reported in Part II shows that the internal quantum efficiency at zero bias δ_x is given by

$$\delta_x = 1 - 1/(1 + 1.13\ \gamma_o), \tag{19}$$

where the maximum oxide bias-voltage is 10 V. The average internal quantum efficiencies reported by Fox are also shown in table 4, and the internal quantum deficiencies calculated from them are also shown there.

Table 4. Oxide-bias data γ_o reported in reference [17] for a single 1337 type photodiode, the average internal quantum-efficiency data ϵ_x reported in reference [17] for ten multiple-reflection radiometers based on 1337 type photodiodes, and the quantum deficiencies $\delta_x(\lambda)$ calculated from these sets of data

λ (nm)	oxide bias γ_o	$\delta_x(\lambda)$	iqe ϵ_x	$\delta_x(\lambda)$
406.85	+0.0126 ±0.00015	+0.01404 ±0.00017	+0.9867 ±0.0002	+0.0133 ±0.0002
468.18	+0.0044 ±0.00015	+0.00495 ±0.00017	+0.9934 ±0.0003	+0.0066 ±0.0003
568.35			+0.9977 ±0.00020	+0.0023 ±0.0002
647.30	+0.0007 ±0.00015	+0.00079 ±0.00017	+0.9986 ±0.0002	+0.0014 ±0.0002
799.54			+0.9989 ±0.0002	+0.0011 ±0.0002
859.07	+0.0000 ±0.00015	+0.00000 ±0.00017	+0.9987 ±0.0002	+0.0013 ±0.0002

Equation (17) was normalized to the results of Zalewski and Hoyt at $\lambda_f = 441.6$ nm, and the predictions of that equation are compared with the results of Zalewski and Hoyt at 633 nm in table 5. Note that $\delta_x(\lambda_r) = 0$ for this data set due to the application of reverse bias. Equation (17) was also normalized to the oxide-bias results of Fox at $\lambda_f = 468.18$ nm, and the predictions of that equation are compared with the oxide-bias results in table 6. Again note that $\delta_x(\lambda_r) = 0$ because oxide-bias measurements are not sensitive to recombination in the rear of the photodiode.

The uncertainty estimates for eq (17) in tables 5 and 6 made use of the data in figure 11 even though those data apply to $\lambda_f = 440$ nm rather than 441.6 or 468.2 nm. This does not distort the estimated uncertainty significantly because the terms are added in quadrature, and the first term on the right-hand side of eq (18) is larger than the second term for both sets of data. Fox's data point at 406.85 nm was included in table 6 even though the uncertainties associated with extrapolating $\delta_f(\lambda)$ to wavelengths shorter than λ_f are very unfavorable for high-accuracy applications. The good agreement at this wavelength must be considered fortuitous considering the uncertainty associated with the predicted value. The differences at the other wavelengths never exceed 0.00015, and they fall within the estimated uncertainty for the differences.

Table 5. Comparison of predictions of eq (17) with measured internal quantum-deficiency data $\delta_x(\lambda)$ in table 3 for $\lambda_f = 441.6$ nm and $\delta_x(\lambda_r) = 0$

Prediction wavelength (nm)	Measured value reference [4]	Predicted value eq (17)	Difference
633.0	+0.00097 ±0.00023	+0.00089 ±0.00007	−0.00008 ±0.00024

Table 6. Comparison of predictions of eq (17) with internal quantum-deficiency data $\delta_x(\lambda)$ derived from oxide-bias data in table 4 for $\lambda_f = 468.18$ nm and $\delta_x(\lambda_r) = 0$

Prediction wavelength (nm)	Measured value reference [15]	Predicted value eq (17)	Difference
406.85	+0.01404 ±0.00017	+0.01321 ±0.01144	−0.00083 ±0.01144
647.30	+0.00079 ±0.00017	+0.00090 ±0.00030	+0.00010 ±0.00034
859.07	+0.00000 ±0.00017	+0.00015 ±0.00005	+0.00015 ±0.00018

Table 7 and figure 13 compare the internal quantum-deficiency results of Fox [17] with the predictions of eq (17) when normalized at $\lambda_f = 468.18$ nm and at $\lambda_r = 859.07$ nm. The data in figures 11 and 12 that apply for $\lambda_f = 440$ nm and for $\lambda_r = 860$ nm, respectively, are used with eq (18) to estimate the uncertainties assigned to the predictions of eq (17). The difference at 406.85 nm is much larger than that obtained with the oxide-bias data but still falls within the estimated uncertainty. Because the oxide-bias experiment is not sensitive to the quantum yield for electron-hole pair production, it is tempting to imagine that the discrepancy

Table 7. Comparison of predictions of eq (17) with measured internal quantum-deficiency data in table 4 for $\lambda_f = 468.18$ nm and $\lambda_r = 859.07$ nm

Prediction wavelength (nm)	Measured value reference [15]	Predicted value eq (17)	Difference
406.85 nm	+0.0133 ±0.00025	+0.01744 ±0.01000	+0.00414 ±0.01000
568.35 nm	+0.0023 ±0.00030	+0.00224 ±0.00007	−0.00006 ±0.00031
647.30 nm	+0.0014 ±0.00020	+0.00121 ±0.00004	−0.00019 ±0.00020
799.54 nm	+0.0011 ±0.00021	+0.00082 ±0.00009	−0.00028 ±0.00023

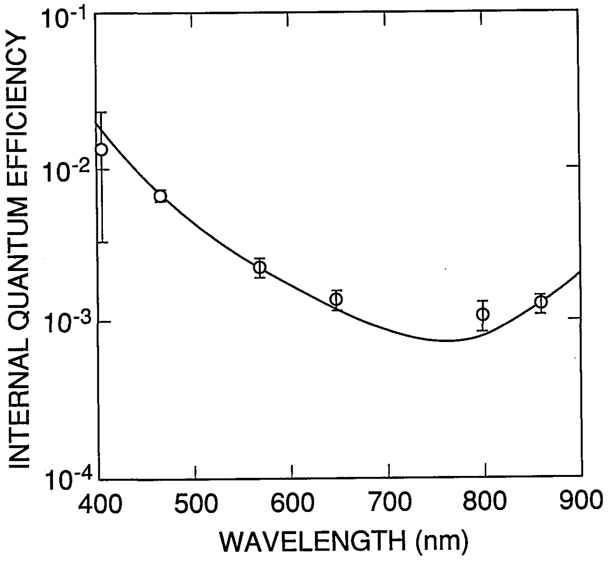

Figure 13. Comparison of measured data of reference [17] (open circles) with eq (17) (solid line) normalized to pass through the measured point at 468.18 and 859.1 nm. At these wavelengths the error bars are the uncertainties in the measured values; at the other wavelengths the error bars are the quadrature sum of the uncertainties in the measured values and those associated with the use of eq (17).

between the oxide bias and internal quantum efficiency reflects the fact that the quantum yield for the 1337 type photodiode is greater than unity at 406 nm. However, the fact that this discrepancy is not statistically significant at the one-sigma level shows that this conclusion cannot be drawn from the data presented here. The differences at the other wavelengths never exceed 0.0003, and only fall outside the estimated uncertainties for the differences at 799.54 nm.

The results shown in tables 5–7 and figure 13 verify that the internal quantum-deficiency spectrum of multiple-reflection radiometers based on Hamamatsu 1337 photodiodes can be interpolated over the 440 to 860 nm spectral region from only two measured quantum deficiencies, one at each end of the region. This greatly reduces the number of measurements needed for high-accuracy spectral calibrations of these photodiodes and radiometers. Furthermore, the theoretical uncertainty analysis suggests that the uncertainties in the interpolated values will be less than or equal to the uncertainties in the measured values, at least as long as the latter are greater than ±0.0001. The results in tables 5 to 7 and figure 13 do not contradict this idea, but the experimental data are not accurate enough to confirm it. On the other hand, the experimental data do confirm that an uncertainty of ±0.0003 is obtainable.

4. Conclusion

Part III of this series of papers has shown that Version 2 of the semiconductor-device modeling program PC-1D can be used to model the spectral shape of the internal quantum deficiency of 1337 type photodiodes with very small uncertainty over the 440 nm spectral region. The largest uncertainties are caused by uncertainties in the absorption-coefficient spectrum of silicon, diode-to-diode variations in the shape of the front-region dopant distribution, and diode-to-diode variations in the position-independent rear-region minority-carrier lifetime. It was not possible to estimate the uncertainty caused by approximating the rear-region minority-carrier lifetime as being independent of position.

Simple formulae were derived that allow high-accuracy internal quantum-efficiency calibrations on 1337 type photodiodes to be interpolated from measured values at the ends of the 440 to 860 nm spectral region over the interior of that region. The uncertainties that can be obtained with these formulae are comparable to those that can be obtained with the highest accuracy measurements currently available.

5. References

[1] Geist, J., Appl. Opt. **18**, 760 (1979).
[2] Geist, J., Zalewski, E. F., and Schaefer, A. Appl. Opt. **19**, 3795 (1980).
[3] Hoyt, C. C., Miller, P. J., Foukal, P. V., and Zalewski, E. F., SPIE **1109**, 236 (1989).

[4] Zalewski, E. F., and Hoyt, C. C., Metrologia **28**, 203 (1991).
[5] Geist, J., and Baltes, H., Appl. Opt. **28**, 3929 (1989).
[6] Slotboom, J. W., and de Graaff, H. C., Solid-State Electron. **19**, 857 (1976).
[7] Geist, J., Lowney, J. R., James, C. R., and Robinson, A. M., J. Appl. Phys. **70**, 236 (1991).
[8] Ohkura, Y., Solid-State Electron. **33**, 1581 (1990).
[9] Bennett, H. S., and Lowney, J. R., Solid-State Electron. **33**, 675 (1990).
[10] Girisch, R. B. M., Mertens, R. P., and Verbeke, O. B., Solid-State Electron. **33**, 85 (1990).
[11] Bennett, H. S., Solid-State Electron. **26**, 1157 (1983).
[12] Geist, J., Migdall, A., and Baltes, H. P., Appl. Opt. **27**, 3777 (1988).
[13] Weakliem, H. A., and Redfield, D., J. Appl. Phys. **50**, 1491 (1979), and personal communication.
[14] Philipp, H. R., J. Appl. Phys. **43**, 2835 (1972), and personal communication.
[15] Zalewski, E. F., and Duda, C., Appl. Opt. **22**, 2867 (1983).
[16] Fox, N. P., and Martin, J. E., Appl. Opt. **29**, 4686 (1990).
[17] Fox, N. P., Metrologia **28**, 197 (1991), and personal communication.

About the authors: Jon Geist is a physicist in the NIST Semiconductor Electronics Division, and A. M. (Sandy) Robinson and C. R. (Bob) James are Professors of Electrical Engineering at the University of Alberta in Edmonton, Alberta, Canada. Prof. James is presently Vice-President (Research) at the University.

Volume 96, Number 4, July–August 1991
Journal of Research of the National Institute of Standards and Technology

Conference Report

WORKSHOP ON ASSESSMENT OF TESTING METHODOLOGY FOR GLASS, GLASS-CERAMIC, AND CERAMIC MATRIX COMPOSITES

Gaithersburg, MD
February 8, 1990

Report prepared by

David C. Cranmer

Ceramics Division,
National Institute of Standards and Technology,
Gaithersburg, MD 20899

A workshop on mechanical testing methodology for glass, glass-ceramic, and ceramic matrix composites was held at NIST on February 8, 1990. The purpose of the workshop was to assess room- and elevated-temperature measurement techniques for whisker- and continuous-fiber reinforced ceramic composites and their constituents. Techniques being used for metal- and polymer-matrix composites as well as those developed exclusively for use with ceramic composites were discussed. Important points included the use of tensile tests, not flexure, for strength and creep measurements; the need for different tests for material development and for system design; the need to precisely control test parameters; and the importance of specimen preparation. Additional conclusions were that the same tests used for monolithic ceramics can be used for whisker-reinforced materials with few or no changes, and that interlaboratory round robin tests were needed to determine both the reproducibility and limitations of the methodologies as well as material behavior. Additional research areas identified included long-term deformation behavior of composites, environmental effects on material behavior, and the relation of constituent properties to composite properties.

1. Introduction

This paper summarizes a workshop on testing methodology for glass, glass-ceramic and ceramic matrix composites held at the National Institute of Standards and Technology on February 8, 1990. For brevity, the term "ceramic" refers to glass, glass-ceramic, and ceramic materials. The purpose of the workshop was to review and discuss mechanical property measurement techniques for whisker- and continuous-fiber reinforced ceramic composites and their constituents. A series of nine papers was presented detailing various aspects of mechanical testing of these materials. More details for each paper can be found in reference [1]. Prior to discussing the workshop, it is appropriate to review several salient features of composites testing. First, testing of polymer and metal matrix composites has a long history compared to ceramic matrix composites. Some of the test methods used for metal and polymer composites can be directly applied to the testing of ceramic matrix materials, while others can be adapted for use at elevated temperatures. One group of presentations was, therefore, selected to provide a background of standard and commonly used tests for evaluating polymer and metal matrix composites. A second group of presentations related the government and industrial experience with fracture of fiber-reinforced ceramics, primarily at room temperature. Finally, since there is little knowledge of the long-term deformation characteristics of these composite materials [2], a third group of presentations was selected to address long-term deformation.

The expectations for the workshop were fourfold. First, that appropriate measurement techniques suitable or adaptable for determination of the properties of the composites would be identified. Second, that appropriate measurement techniques suitable or adaptable for determination of the properties of the components (i.e., fiber, whisker, interface, and matrix) of the composites would be identified. Third, that areas where additional research and development were required to meet the needs for appropriate measurement techniques would be identified. Fourth, that techniques would be identified which are or can be made suitable as standard measurement methods. As will be shown below, each of these objectives were met. The following sections give synopses of the presentations and discussion for the various areas of composite testing.

2. Available Test Methods for Polymer and Metal Matrix Composites

A number of test methods have been used to evaluate the mechanical, thermal, and physical properties of polymer and metal matrix composites. The properties of interest are ultimate strength, yield strength, elastic moduli, strain to failure, fatigue life, creep, thermal expansion, thermal conductivity, thermal diffusivity, electrical conductivity, dielectric constant, and chemical resistance. The mechanical tests are almost exclusively destructive, while the physical tests can be either destructive or non-destructive. There are ASTM standard tests [3] for fiber density (D-276, D-792, D-1505, D-3800), fiber tensile properties (D-3379, D-3544, D-4018), composite tensile strength and modulus (D-638, D-3039), composite compressive strength and modulus (D-695, D-3410), flexural strength and modulus (D-790), composite shear strength and modulus (D-2344, D-3518, D-4255, E-143), composite tensile fatigue (D-3479), dielectric constant and dissipation factor (D-150), and dielectric strength (D-149). In addition, there are commonly used tests for shear strength and modulus such as the Arcan [4] and Iosipescu [5] methods.

3. Tensile Testing for Strength of Ceramic Matrix Composites

There are several significant issues to be considered in designing a tensile strength test, including specimen design, specimen grip-ping arrangements, load train design, heating method, temperature measurement, and strain measurement. All the issues must be addressed properly to obtain a valid tensile test result. Failure to correctly implement them in the test will result in useless numbers for tensile strength. Additional details of the tensile test are in reference [6]. One viable tensile test uses a dogbone-shaped specimen containing three holes in the tab end. The three holes used to pin the specimen in the grips are the means by which the load is applied to the gage section. The remainder of the load train consists of a load cell, pullrods, universal joints and a chain to control alignment and prevent introduction of bending moments into the system (fig. 1).

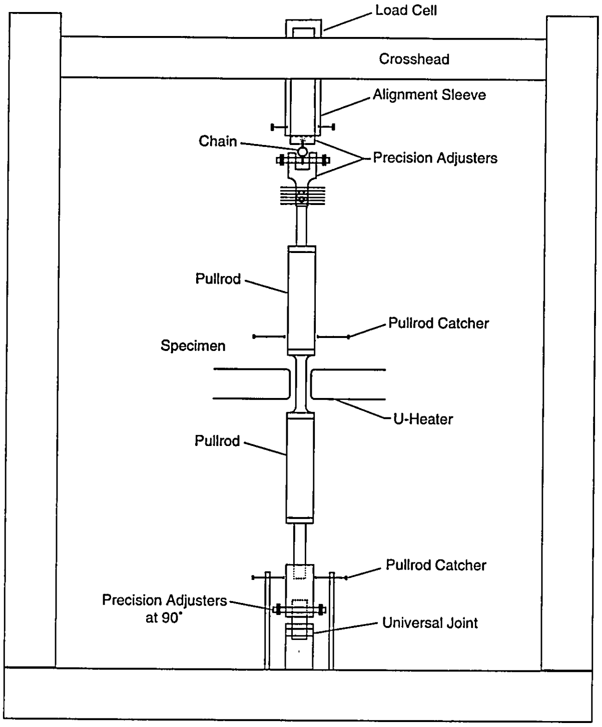

Figure 1. Schematic of tensile strength test apparatus using flexible load train.

Another tensile test configuration which works well utilizes a rigid grip system (see reference [1]). Rigid grips have the advantages of staying aligned during the test; no "pre-load" is required to remove any slack in the load train; test specimens can be consistently and correctly mounted using simple tools such as calipers and depth gages; the rigid load train provides a stable platform for instrumentation (e.g., extensometer cables, thermocouples); and the degree of bending introduced into the specimen remains nearly constant throughout the complete load range. The specimen remains nearly constant throughout the complete load range. The specimen geometry can be straight-sided or dogbone-shaped, and can be tabbed or untabbed. Specific specimen dimensions depend on the test geometry, test conditions, and material availability. The tabbed, straight-sided specimen is the only one suitable for use with a unidirectionally reinforced composite with this configuration. Other specimens must use cross-plied material.

A third configuration discussed in more detail below applies the load to the shoulders of the tab section. This configuration uses dogbone-shaped specimens, and requires very tight tolerances on both the specimen and the loading fixture. Depending on the testing requirements, this configuration can be operated with either hot or cold grips.

Specimen preparation is a critical part of specimen design. Machining can have a significant impact on the behavior of the material, particularly where fibers are not parallel to the tensile axis. Improper grinding can lead to broken, debonded, and/or improperly aligned fibers during the test, resulting in inaccurate or incorrect numbers for the tensile strength. The degree of inaccuracy will also depend on fiber alignment (layup), fiber volume fraction, and relation of the tensile stress axis to the fiber orientation.

Strain can be measured using strain gages, laser sensors, clip-on extensometers, or high temperature rod extensometers. The choice of strain measurement tool depends on the specimen geometry, and the test geometry and conditions, as well as the degree of precision desired. Time can also be a significant factor in deciding on the precision required in the strain measurement. In practice, for strength measurements, the clip-on extensometers and laser dimension sensors do not have the required precision, and attention should be focussed on the high temperature rod extensometers. The contact point on the specimen for the rod extensometers is a critical area. Three methods can be used to ensure that the specimen deformation is transferred to the contact rods: pin holes, grooves in the material, and grooves in a paint overcoat. All three work satisfactorily under some conditions, but the choice depends on the specimen and the temperature of the test. Since introduction of bending moment is a concern, strain should be measured on more than one side of the specimen. This is necessitated by the fact that the specimens are heterogeneous and may be bent or warped as a result of the manufacturing or fabrication process.

There have been no studies yet which compare the same material using all three of the configurations mentioned above. While all three can be expected to provide good results, an interlaboratory comparison of at least two continuous fiber-reinforced composites is needed to discern testing reproducibility and limitations, as well as material behavior including reproducibility. Testing laboratories and suitable materials remain to be identified.

4. Tensile Testing for Creep of Ceramic Matrix Composites

Evaluation of creep and creep rupture of ceramic matrix composites is a relatively recent development, as most researchers and material developers have concentrated their efforts on more critical fabrication and strength issues. However, as the materials evolve, there will be a greater need for information about the long-term deformation characteristics including fatigue, creep and slow (or subcritical) crack growth. Several tensile tests are available with which to evaluate the properties of ceramic composites as well as monolithic ceramics.

A typical tensile creep test specimen and set-up are shown in figure 2. The holes in the tab sections of the specimen are tapered to minimize strains due to bending. The load train is similar to that described for the tensile strength test above in that it consists of loading rods to which the specimen is pinned. The loading rods are attached to universal joints, which in turn are connected to either the load cell (at the bottom) or to the air piston which provides the load (at the top). The entire specimen is located in the hot section of the furnace.

Changes in the gage length of the specimen are monitored via an optical telescope or a laser dimension sensor. Flags (with or without Pt wires attached) are fixed to the specimen to provide the measure of the gage length. A laser dimension sensor can provide an accuracy of ± 2 μm and acquires much more data than the optical telescope method. This degree of accuracy and data acquisition ability means that all three stages of creep can be monitored continuously, resulting in better measurements of rupture life, and hence better predictions of component reliability and lifetime.

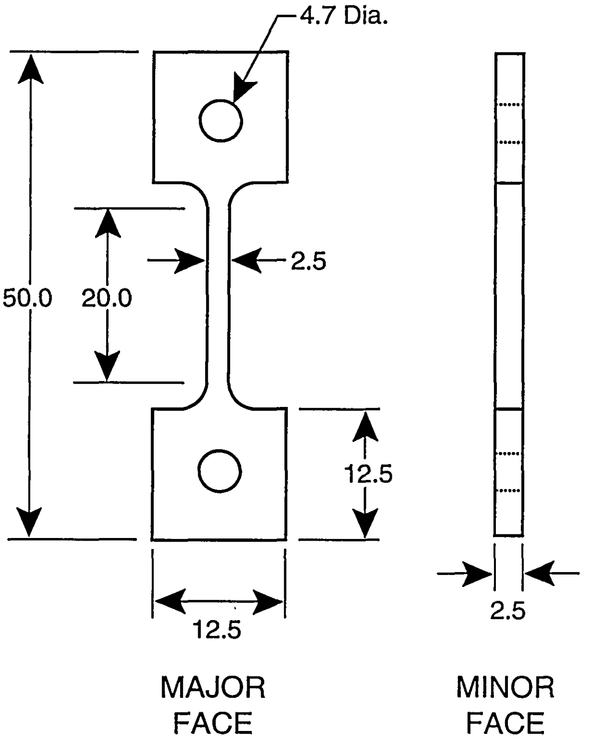

Figure 2. Typical dogbone specimen geometry used for tensile creep testing. Dimensions are in mm. The holes in the specimen are tapered to minimize bending strains.

Another test geometry for measuring tensile creep and strength has been developed at Oak Ridge National Laboratory [7]. The specimen has a cylindrical geometry with a machined buttonhead end for gripping. The shape is simple but requires very precise tolerances which are achievable with computer numerical controlled (CNC) grinding equipment. The technique has several advantages: symmetrical loading on the specimen, a simple gripping arrangement, relatively uniform load transfer which minimizes the bending moment on the specimen, and the ability to achieve large volume-to-surface area ratios. There are, however, at least two difficulties with this specimen: the cost associated with machining of the material, and the large amount of material required for each specimen. This test can be used to obtain design data, but, given the machining requirements, it may not be appropriate for fiber reinforced materials because of fiber breakage and misalignment.

A different tensile creep (and fatigue) test [8] for ceramic matrix composites has also been developed. The apparatus is similar to that used for the shoulder-loaded tensile strength test described in the previous section. The grips can be either ceramic (e.g., SiC) for high temperature use, or superalloy for intermediate temperatures. A schematic of the gripping arrangement is shown in figure 3. Front-to-back alignment in the fixture is controlled by precision-machined inserts which are fastened to the body of the fixture after the specimen is in place. This configuration has been used to evaluate tensile strength, tensile creep, and tension-tension fatigue of fiber-reinforced ceramic composites.

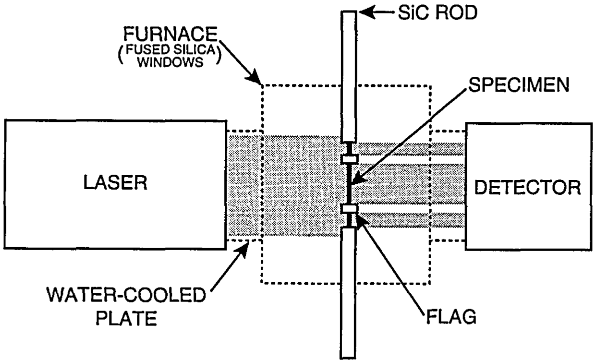

Figure 3. Schematic of tensile creep apparatus.

The experimental data must be accompanied by proper microstructural evaluation to more fully understand the strength, creep, and fatigue failure mechanisms, and be able to make changes to the microstructure to enhance the desired properties while minimizing degradation of the remaining ones. As an example, for creep, in the case of a SiC_w-Si_3N_4[9], it was found that the initial transient was dominated by devitrification of a glassy interfacial phase, and that cavitation at the SiC_w/Si_3N_4 interface enhances the creep rate, thus reducing the composite's lifetime. Compared to an unreinforced Si_3N_4, there was no increase in creep resistance as a result of introducing the whiskers. This unexpected result is explained by cavitation which occurs at the SiC_w/Si_3N_4 interface, and may possibly be altered by changing the initial glassy phase composition or content, or by appropriate surface treatment of the whiskers to minimize cavitation.

5. Determination of Fiber/Matrix Interfacial Properties

The strength of the fiber-matrix interface is one of the key parameters responsible for the stress-strain behavior and damage tolerance of ceramic composites. Two different types of tests are available to measure the fiber/matrix interfacial properties in fiber-reinforced ceramic composites. The first is based on an indentation technique to either push the individual fiber into the matrix or push the fiber through the matrix. The second relies on pulling a single fiber out of a matrix. These methods have been compared [10] to one another for a glass matrix material, and show similar results.

The indentation tests were performed using an instrumented indenter, allowing for independent determinations of force and displacement during the complete loading and unloading cycle. A schematic of the test apparatus is shown in figure 4. Displacement was determined using a pair of capacitance probes; the change in capacitance in a probe varies as it approaches a fixed target. Targets were fixed with respect to the specimen surface, and each probe was initially calibrated using a laser interferometer. Specimens for which indentation results have been obtained include 1 and 2 mm thick multifilament SiC/glass-ceramic and 0.3 mm thick monofilament SiC/borosilicate glass. The samples were at least partially flat and polished so that the capacitance probes did not have to be adjusted frequently.

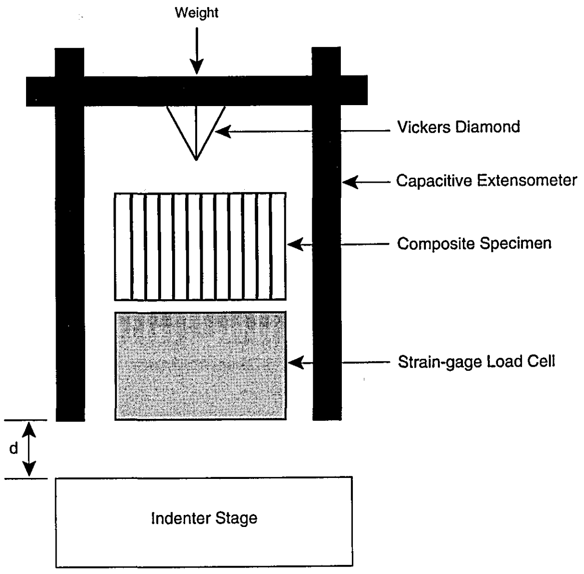

Figure 4. Schematic of instrumented indentation apparatus.

For the SiC monofilament/borosilicate glass system, the push-out test can exhibit two plateaus in the (force)^2-displacement curve (fig. 5). The force at the first plateau gives a value of τ of 36 MPa for the carbon core slipping in SiC and the force at the second plateau gives a value of τ of 10 MPa for the SiC slipping in the matrix. Tests on additional fibers gave an average value of τ of 30 ± 9 MPa for the core in SiC. The value of τ for SiC in the matrix is in reasonable agreement with τ_{debond} obtained from the single fiber pull-out test.

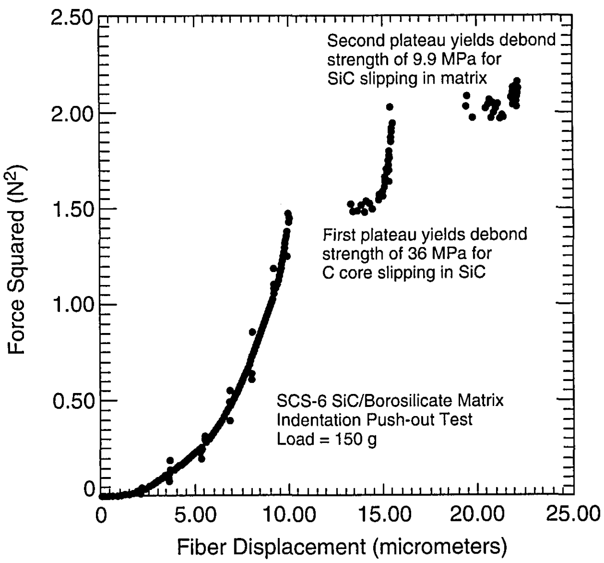

Figure 5. Force^2-displacement curve from indentation test for SiC monofilament/borosilicate matrix composite. First plateau is for carbon core debonding from SiC, second plateau is for SiC debonding from borosilicate glass matrix.

Examination of the SiC/glass-ceramic system shows that τ is dependent on the investigator as well as the technique [11]. The indentation push-in results yield τ's varying from 1 to 10 MPa, and from 1 to 100 MPa, depending on the heat treatment. The discrepancy in heat treated materials is due to differences in the fiber-matrix interface bonding with some fibers being more tightly bound than others. This would lead to differences in both debond strength and frictional pull-out. The discrepancy in various untreated materials is due to both differences in the fiber-matrix bond and fiber misorientation with respect to the applied force.

The indentation tests use a minimal amount of material and can be performed on samples containing either large monofilaments or small diameter multifilament tows but provide information on only τ_{friction} (push-in) or τ_{friction} or τ_{debond} (push-out), depending on indenter geometry and material characteristics. The push-out test can be performed at slower loading rates and with a different indenter geometry, thus allowing separation of the debonding strength from the interfacial friction stress in the force^2-displacement curve. Preparation of push-out samples is more difficult than for push-in samples but the analysis is simpler and the results appear to be more reproducible. An additional potential advantage of the indentation method is that it may be adaptable for use as a quality assurance tool, since it can be used on small pieces of the as-fabricated composite. This application may not be realized until a clearer relationship is established between the debond strength/frictional shear stress and the macroscopic properties of the composite, such as strength.

6. Single Fiber Testing

There is a need for testing of the composite components, namely, the starting fibers, the matrix material, and the fiber/matrix interface. Test methods for determining the interface properties were discussed in the previous section. For the matrix material, recourse can be had to a large number of techniques developed over several decades. Several comprehensive reviews of these techniques have been published in the past 10-15 years [12, 13].

Determination of the properties of the starting fibers is a difficult task, particularly at elevated temperatures. Among the factors to be considered are testing of a single filament versus a multifilament yarn, test system compliance, gauge length, strain rate, grip material and pressure, strain measurement technique, and fiber diameter measurement. Each of these factors can significantly affect the measured result. As an example, when considering the measurement of a single fiber, it matters whether the fiber was indeed single or removed from a larger tow. For those removed from a multifilament tow, the fiber selection process itself may be expected to bias the results toward a higher strength, as fibers that break during removal from the tow would be discarded, not tested. This will affect not only the average strength, but any measures of strength distribution such as standard deviation and the Weibull modulus.

Room temperature testing can be accomplished using standard fiber tensile tests such as ASTM D-3379, D-3544, and D-4018. Elevated temperature testing provides a host of new considerations including furnace design, vertical versus horizontal testing, hot versus cold grips, grip materials, and temperature measurement and uniformity. The furnace design must consider chimney effects and the resultant difficulties associated with temperature stability and thermal gradients. An additional consideration is the effect of time at temperature, and the length of time required to thermally equilibrate the fiber prior to testing. The small diameter fibers typically are composed of small grains, which can grow rapidly when exposed to elevated temperatures. If it takes too long to perform the test, the material tested may no longer be representative of the initial fiber.

7. Fracture Toughness Determinations

One of the advantages of reinforced ceramics is that of increased damage tolerance. It has been shown [14] that inclusion of whisker reinforcement in a ceramic can result in as much as a four-fold increase in fracture toughness (K_{Ic}). It can also result in an increase in fracture resistance with increasing crack length, known as R-curve behavior. In the case of whisker-reinforced materials, the R-curve is due to changes in fracture behavior as a result of crack interactions with the whiskers, wherein the whiskers bridge the crack behind the crack tip. Similar observations have been made in some monolithic ceramics such as alumina [15] except that whisker bridges behind the crack tip are replaced by grain bridges which exist as a result of the anisotropic microstructure.

The R-curve can be evaluated using an indentation-strength method wherein the strength of the composite is measured as a function of indentation load. The resulting curve is analyzed by assuming a power-law representation of the R-curve. This analysis in turn yields information about both the strength and toughness of the composite. When coupled with microstructural observations, it is then possible to determine the cause of the increase in toughness, and begin to make changes to the processing of the composite to take advantage of the bridging phenomenon and produce a more damage tolerant material. This may provide a useful method for developing a hybrid composite containing both whiskers and fibers, wherein the whiskers enhance the toughness of the matrix while the fibers provide the necessary directional tailoring of the composite properties.

8. Industrial Experience in Composites Testing

This section covers the experiences of two industrial firms, one a materials manufacturer, the other a materials user. One of the problems identified earlier is the need for a low cost, simple, reliable tensile test procedure for determining composite properties. Another problem is related to oxygen embrittlement. An example of this behavior is the reaction of carbon interfaces with environmental oxygen after first matrix microcracking has occurred. A number of currently available ceramic composites rely on a carbon or carbon-rich interface to obtain the debonding and sliding necessary to achieve the damage tolerance shown in figure 6. As shown there, a change in slope representative of first matrix microcracking is evident. At this point, the composite interface and fibers become exposed to the environment (generally including oxygen) and chemically react with that environment, thus adversely changing the properties of the interface and/or fiber. For example, the carbon layer can form CO or CO_2, which outgasses from the interface. The underlying fiber (such as SiC) then can react to form an oxide which bonds tightly to the matrix, thus eliminating fiber sliding as a toughening mechanism.

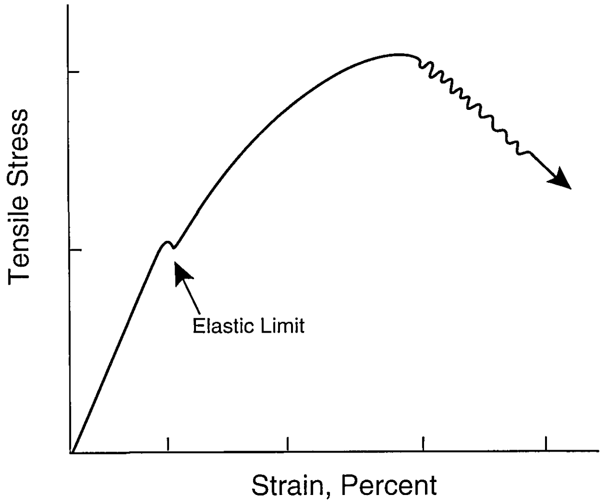

Figure 6. Typical stress-strain behavior of ceramic composite.

Corning, Inc. has developed a simple test whereby the mechanical behavior of a representative composite can be characterized, and which complements the indentation tests described above. The method uses a simple rectangular parallelopiped (similar to a flexure bar), which is mounted in hydraulic wedge grips (as described in the tensile strength tests above) with metal foil shims. The mounted specimen is loaded until matrix microcracking is observed (precracking), then removed from the grips, exposed to the desired environmental conditions (temperature, atmosphere). The post-exposure specimen is reloaded in the grips and pulled to failure. This method has been applied to materials such as Corning's calcium aluminosilicate (CAS) reinforced with Nicalon SiC and having a carbon fiber/matrix interface with the results showing a significant reduction in strength after exposure. When the interface is changed to a micaceous material, the post-exposure strength is much nearer to the pre-exposure strength, indicating an enhancement in properties due to the interface. The test has some limits at present, especially in that it has not been adapted for elevated temperature use, but for purposes of material development and the indication of trends in behavior, it is an acceptable test. Another limitation exists in the detection of initial microcracking of the matrix, which at present is detected using the deviation from linearity of the stress-strain curve. A more sophisticated approach would use acoustic emission, real-time microscopy, or other more sensitive techniques to determine the onset of microcracking. Additional cooperation is also required between the mechanical test experimenter and the chemical analysis person to ensure that the chemistry of the interface is known, both before and after exposure, in order to properly guide the changes required for improvements.

Areas which have not yet been addressed by the materials' manufacturers are the effects of long term exposure (similar to the tests described above for creep) and the actual service geometries and conditions (rig tests). These are dealt with to a certain extent below.

The kind of information obtained on ceramic matrix composites by materials' users can be dictated by external constraints, and have resulted in a collection of wisdom related to design practice such as MIL-HDBK-17 [16]. This handbook mandates requirements that must be met before a structure can be placed in service. The result is a series of design allowables. A typical requirement is that the strength of the material shall be such that it is sufficient to sustain the ultimate load without failure. A similar requirement for damage tolerance is that the structure shall be capable of performing its function in the presence of expected manufacturing and service induced damage.

Additional factors that must be taken into account are environmental effects (thermal as well as chemical), effects of defects, statistical variability of the material, long term behavior, and cyclic versus static loading effects. Assessment of these effects requires the user to conduct a large series of tests using multiple specimens. A typical series will examine a unidirectional material in tension in the 0, 90, and cross-ply directions; 0, 90, and cross-ply in compression; and 1-2, 1-3, and 2-3 shear at seven different temperatures ranging from −54 °C to the expected service temperature; creep rupture at elevated temperatures up to the expected service temperature; and fatigue at room and elevated temperature. This series of tests requires as many as 405 specimens.

Generic test method requirements to meet the testing needs cited above are that 1) the test be appropriate for the materials of interest, 2) the test be uniform and repeatable, and have a stable hot section, 3) the strain be measured accurately and precisely, 4) the test method be easy and repeatable, 5) the test be cost effective and have a reasonable turnaround time, and 6) the test efficiently use the available material. In attempting to meet these generic requirements, General Electric's experience has resulted in use of number of test methods for determining the necessary properties. These include ASTM D-638 and D-3039 test methods, as well as the tensile test methods developed by Southern Research Institute and the Cortest to measure tensile strength; ASTM D-695 and D-3410 test methods to measure compressive strength; ASTM D-3518 and D-3518(C) test methods as well as an asymmetric four-point bend (AFPB) test (a variation of the Iosipescu test) and saddle geometries to determine in-plane shear strength; and ASTM D-3846 and D-2344 test methods as well as the AFPB to measure interlaminar shear strength. The Cortest for tension relies on shoulder loading of a dogbone-type specimen, as contrasted to the tab-pinned geometries of the other tensile tests.

A number of future testing needs to obtain basic properties and general test requirements were also identified. For basic properties, the desired information includes flatwise tension, flatwise compression, interlaminar shear modulus, long cycle fatigue, and modes I and II interlaminar fracture toughness. The general test requirements include the need for interlaboratory standardization and vendor qualification, a notched tension/compression/long cycle fatigue test, a biaxial test method, a pin bearing test, characterization of joints, and residual properties as a result of impact, erosion, and wear.

9. Summary and Conclusions

A number of techniques are available for measurement of the mechanical properties of ceramic matrix composites. An assessment was made of techniques for measuring strength, creep, and fatigue. For whisker-reinforced materials, test techniques can be the same as those used for monolithic ceramics. For continuous fiber-reinforced composites, specialized tensile test techniques must be used. There is a need for different tests for material development and system design, a need to control test parameters including temperature, and temperature and stress gradients, and a need to properly prepare specimens for testing. Flexural testing generally is inappropriate for determining the mechanical properties of the fiber-reinforced composites. There is also a need to develop standard tests and reporting information in order to facilitate comparison of data from one laboratory to another. Toward that end, an interlaboratory comparison of continuous fiber-reinforced composites is needed to determine reproducibility and limitations of the methodology, as well as material behavior.

Additional research areas were identified including long term (>1000 h) deformation behavior of all of these materials (whisker- and fiber-reinforced), the changes in material behavior due to the test and/or service environment, and the relation of subcomponent tests (e.g., on fibers) to the composite properties especially in view of the fact that rule of mixtures does not adequately predict properties of these materials.

Acknowledgments

This work would not have been possible without the contributions of the workshop presenters and participants. Additional discussions with Drs. Steve Freiman and Shelley Wiederhorn are greatly appreciated.

10. References

[1] Cranmer, D. C., Testing Methodology for Glass, Glass-Ceramic, and Ceramic Matrix Composites, NIST Special Publication, in press, 1991.

[2] Wiederhorn, S. M., to be published in Flight Verhicle Materials, Structures, and Dynamics Technologies—Assessment and Future Directions, S. R. Levine, ed.

[3] For ASTM standards, refer to the appropriate Annual Book of ASTM Standards, ASTM, Philadelphia, PA.

[4] Arcan, M., Hashin, Z., and Voloshin, A., Exp. Mech. **18** (1978).

[5] Walrath, D. E., and Adams, D. F., NASA-CR-174346, June 1984.

[6] Starrett, H. S., A Test Method for Tensile Testing Coated Carbon-Carbon and Ceramic Matrix Composites at Elevated Temperature in Air, Ceram. Eng. Sci. Proc. **11**, 1281-1294 (1990).

[7] Jenkins, M. G., Ferber, M. K., and Martin, R. L., Evaluation of the Stress State in a Buttonhead, Tensile Specimen for Ceramics, Ceram. Eng. Sci. Proc. **11**, 1346-1363 (1990).

[8] Holmes, J. W., A Technique for Tensile Fatigue and Creep Testing of Fiber-Reinforced Ceramics, submitted to J. Comp. Matls., 1991.

[9] Hockey, B. J., Wiederhorn, S. M., Baldoni, J. G., and Buljan, S. T., Tensile Creep of Whisker-Reinforced Silicon Nitride, accepted for publication in J. Mat. Sci., 1991.

[10] Cranmer, D. C., Deshmukh, U. V., and Coyle, T. W., in Thermomechanical Properties of Metal Matrix and Ceramic Matrix Composites, ASTM STP 1080, ASTM, Philadelphia (1990), p. 124.

[11] Cranmer, D. C., Determination of Fiber/Matrix Interfacial Properties of Ceramic and Glass Matrix Composites, NISTIR 89-4079, February 1990.

[12] Freiman, S. W., and Hudson, C. M., Methods for Assessing the Structural Reliability of Brittle Materials, ASTM STP 844, ASTM, Philadelphia, PA (1984).

[13] Freiman, S. W., Fracture Mechanics Applied to Brittle Materials, ASTM STP 678, ASTM, Philadelphia, PA (1979).

[14] Becher, P. F., Tiegs, T. N., Ogle, J. C., and Warwick, W. H., in Fracture Mechanics of Ceramics, Volume 7, Bradt, R. C., Evans, A. G., Haddelman, D. P. H., and Lange, F. F., Plenum Press, New York (1986), p. 61.

[15] Chantikul, Prapaipan, Bennison, Stephen J., and Lawn, Brian R., Role of Grain Size in the Strength and R-curve Properties of Alumina, to be published in Journal of the American Ceramic Society, 1990.

[16] Mil Handbook 17.

Volume 96, Number 4, July–August 1991
Journal of Research of the National Institute of Standards and Technology

Conference Report

WORKSHOP ON NEW MEASUREMENT TECHNOLOGY FOR POLYMER PROCESSING
Gaithersburg, MD
December 3–4, 1990

Report prepared by

Anthony J. Bur

Polymers Division,
National Institute of Standards and Technology,
Gaithersburg, MD 20899

Pawan Handa

The Goodyear Tire & Rubber Co.,
Goodyear Research,
142 Goodyear Blvd.,
Akron, OH 44305

and

Chris Grudzien

Dynisco Inc.,
Four Commercial St.,
Sharon, MA 02067

This report describes activity at a workshop on New Measurement Technology for Polymer Processing which was held at the National Institute of Standards and Technology on December 3-4, 1990. The workshop was attended by 19 industry scientists and engineers from polymer processing and instrumentation manufacturing companies. The objective was to seek industry responses to the question: what in-line or on-line, real-time measurements do you need to make during polymer processing but are unable to do so because the measurement technology does not exist? Processors identified their measurement problems and needs by describing various processing operations. Tire and rubber manufacturing, thermoplastic compounding, injection molding, film processing, and reactive processing were described with respect to related measurement problems. Workshop discussions yielded a consensus of the following measurement needs: (a) in-line rheological measurements; (b) improved in-line temperature measurements; and, (c) in-line and on-line measurements of polymer morphology. An ongoing NIST measurement development program, which focuses on temperature and rheological measurements, was described. The NIST program is based on optical and fluorescence measurement techniques which have been used both for laboratory experiments and for instrumenting process machinery. The workshop is being used as a basis for developing NIST/industry collaboration on measurement technology development.

1. Introduction

The National Institute of Standards and Technology (NIST) was host to industry scientists and engineers at two recent workshops on technical problems associated with polymer processing. These workshops, held at NIST in September 1988 and December 1990, focused on obstacles and challenges which prevent polymer processors from utilizing the full potential of microprocessor based control to effect process control and thereby improve product quality and processing productivity.

The **1988** workshop had rather broad objectives:

- To identify processing methods that would benefit from automation and improved understanding of the process;
- To isolate important generic problems that limit the automation and productivity and impede the processing of high quality polymer materials;
- To identify technical and scientific barriers that must be overcome in order to solve processing problems;
- To identify concepts, measurement techniques, and other tools that can be applied to these problems; and
- To define the respective roles of NIST and the industrial sector in solving these problems and to establish communication between NIST and the U.S. polymer processing community.

A consensus regarding the technical barriers which face the processing industry unfolded from the discussions and presentations at the **1988** workshop. They are:

- On-line and in-line, real-time measurements;
- Process models;
- Fundamental theoretical understanding of the physics, rheology, and chemistry of polymer processing;
- Rheological understanding and structure/property relationships of new materials; and
- Materials databases.

Improvements in all of the above areas are needed in order to effectively employ program and microprocessor control based on artificial intelligence. It was agreed that the first two items, on-line measurements and process models, were the areas of most immediate need. Within the context of process control, the measurement problem was stated as follows: (a) The control of a process parameter first requires its measurement; and, (b) The importance of a process parameter will be identified by its expression in a mathematical process model. Improved and new measurement technology is of primary importance because process control cannot be achieved without it and because measurements are needed to test process models. A detailed report of the 1988 workshop is available from NIST [1].

The **1990** workshop on *New Measurement Technology for Polymer Processing* was held at NIST on December 3-4, 1990. This workshop had a single focus:

- **On-line and in-line measurement problems associated with polymer processing.**

In attendance were 19 representatives from the polymer processing and instrument manufacturing industries. The theme of the workshop centered around the question: what in-line or on-line measurements do processors wish to make but are unable to do so because the technology does not exist? The answer to this question emerged from presentations by workshop participants, from open discussions, and from responses to a questionnaire. Measurement problems were highlighted during industry presentations about injection molding, compounding, extrusion, reactive processing and film processing. Also, information was acquired by distributing a questionnaire through which we posed questions to processors concerning process problems and real-time measurement needs. Three areas of measurement needs evolved: *in-line rheological measurements*, *improved in-line temperature measurements*, and *in-line and on-line morphology measurements*. Of somewhat less importance was the need for chemical analysis during reactive processing.

The 1990 workshop activity was scheduled in four sessions:

- Measurement Needs of the Polymer Processing Industry;
- The NIST Polymer Processing Measurement Program;
- Measurement Technologies from the Instrument Manufacturer's Perspective;
- Future NIST/Industry Collaboration on Measurement Development Programs.

2. Measurement Needs, an Industry Perspective

The rationale for performing accurate and reliable on-line and in-line processing measurements was stated in a number of different ways by industry processors. For example, measurements are needed in order to: save money on post processing characterization, maintain and improve product quality, reduce off-specification products, control process, control materials properties of product, reduce time for off line post characterization, improve yield and cycle time, maintain product uniformity, control melt flows, monitor process and correct deviations from specification quickly, control reactive processing, and continuously improve product. All of these reasons can be condensed into one phrase: *product quality and process productivity*. All workshop participants recognized that improved process measurement and control are the principal means for achieving their quality and productivity objectives.

Industry scientists described a number of processing methods for which outstanding measurement problems exist: tire and rubber processing, polymer compounding, injection molding, film processing, and reactive processing. Several common themes of measurement needs emerged from these talks, namely, measurements of rheological and flow properties; temperature and temperature gradients; morphological parameters such as composition, degree of mix and domain size; and chemical analysis of reactive processing. This list is essentially the same as that which developed from the 1988 workshop. It is recognized that new measurement technology development is necessary because existing capabilities do not fulfill current requirements. Some participants stated needs for good processing models, in agreement with comments made at the 1988 workshop. Although processing models are of large importance to the processing industry, the primary focus of the 1990 workshop was on-line and in-line processing measurements.

The most frequently mentioned measurement need was for in-line, real-time rheological measurements. An important distinction was made between in-line and on-line measurements of rheological parameters. On-line refers to measurements made on a sub-stream of material diverted from the main process line, whereas in-line refers to measurements made on the material while it is in the main process line. The consensus communicated by the workshop participants was that in-line measurements are the more important in terms of monitoring and controlling the process. For rheological measurements, *on-line* observations will yield materials data for the polymer being processed, but do not describe the manner in which the polymer expresses itself rheologically in response to the processing stresses imposed on it.

Several processing operations, film extrusion, rubber manufacturing and extrusion, and injection molding, were presented as processing operations which would benefit from in-line rheological measurements. For film extrusion, uniform thickness and mechanical properties of the final product depend on the volume throughput rate, temperature, and viscosity of the resin as it moves through the exit die. Changes in resin viscosity during this operation influence the volume flow rate so that the pull-off rate must be adjusted accordingly. In the case of tire and rubber manufacturing, several steps in the process would benefit from a real time viscosity and viscoelastic measurements. Knowledge of viscoelastic properties is a prominent requirement during mixing of rubber elastomer with fillers and during extrusion and calendering of the sheeted gum product. During injection molding, high volume flow rates are accompanied by shear rates which are normally not available with standard laboratory equipment. Thus, the viscosities expressed by the flowing resin are not known from an established calibration curve but are assumed from an extrapolation of data from lower shear rates. The direct, in-line measurement of viscosity, i.e., the ratio of shear stress to shear rate, will permit a test of the extrapolation accuracy and provide a method to detect shear degradation. Volume flow rate and its relationship to viscosity are fundamental process parameters which govern continuous processing of films and extrusion of rubber. Maintaining an optimum balance between temperature, volume flow rate, viscosity, shear stresses and shear rate is a primary objective. During reactive processing viscosity is a specifying materials property by which the chemical reaction or polymerization is monitored.

An extended discussion about the measurement and control of temperature and temperature gradients transpired. Temperature not only determines the rheology of the processed material but also polymer degradation and reaction kinetics during reactive processing. The measurement of temperature gradients, particularly during molding operations, is also required. The main point of concern is that temperature measurements need to reveal the temperature of the material itself without influence from temperature conditions of the machine. In order to avoid machine influences, probes are often inserted into the flow stream which can cause breakage. Mold cavity temperatures are particularly difficult to measure because of the large thermal mass of the mold which is held at a low temperature by a circulating coolant. During batch mixing, temperature measurement and control of the actual mix compound is desirable in order to avoid hot spots due to high shear loading and to minimize the energy expended on the mixing process. Processors related their experience dealing with all types of temperature sensors, thermocouples, semiconductor devices, resistive elements, and infrared radiometry. The consensus of the processing community was that there are many manufacturing situations where the existing technology is inadequate because a precise and accurate temperature of the polymer resin is not known.

The current emphasis on reactive processing, compounding, alloying and blending has created requirements for on-line and in-line morphological measurements. In particular, processors expressed a need to know molecular weight, molecular weight distribution, domain size in mixtures of immiscible resins, filler orientation, molecular orientation, and polymer microstructure. Classical morphological measurement techniques such as low angle x-ray scattering, neutron scattering, and electron and optical microscopy are not adaptable to processing operations. Advances in fundamental science and the development of new and creative measurement concepts are needed in order to meet this challenge.

Some discussion on pressure measurements and associated problems ensued, but the general view was that, while some problems exist here, they do not severely affect product quality and productivity. Some problems experienced with pressure measurements are slow response time compared to changes which occur in injection molding, fouling of the sensor by the resin so that true pressure is not transferred to the sensor, difficulty incorporating the sensor into the mold cavity, susceptibility to damage in the manufacturing environment.

3. The NIST Measurement Program

The direct transfer of information between NIST and industry at the 1988 and 1990 workshops provided a framework within which the NIST measurement program is defined. This program, based on the application of fluorescence spectrometry and optical measurement methods, addresses two industry measurement needs: in-line rheological and in-line temperature measurements. Optical measurements, particularly fluorescence spectrometry, offer new, unexplored opportunities for polymer processing. Although a large foundation of fundamental fluorescence and optical science exists, very few attempts to apply this knowledge to processing measurement problems have been carried out. Developing measurement instrumentation for the processing environment will require significant applied research and engineering. The ready availability of optical fibers, which can be placed in existing instrumentation ports on processing equipment, will facilitate the transfer of this technology.

Highlighted at the workshop were two successful applications to the processing environment, measurement of quality-of-mix of polymer resin with particulate filler, and monitoring the glass transition of polystyrene. For the quality-of-mix experiments, laboratory development was undertaken and a subsequent technology transfer to a processing facility was carried out. A twin screw extruder was instrumented with optical fibers and associated optics detection equipment in order to monitor the quality-of-mix, concentration, and residence time distribution of a resin/particulate mixture. The glass transition of polystyrene was monitored using a viscosity sensitive fluorescent dye which produced distinct fluorescence intensity changes associated with the onset of the glassy state. The measurement method can be applied to processing where a liquid to crystal or glass phase transition needs to be monitored.

For rheological measurements, a polymeric dye, which can engage in the entanglement network of the host matrix polymer, has been used [2]. Under the application of shear stress, the resulting molecular orientation was measured by observing the fluorescence anisotropy of the incorporated polymeric dye. A polymeric dye consisting of anthracene tagged to polybutadiene was synthesized and doped into a polybutadiene host. Simultaneous fluorescence, shear stress, and shear rate measurements, which were made using an optically instrumented cone and plate rheometer, showed that fluorescence anisotropy is dependent on shear stress. The application of this phenomenon to the processing line will permit the observation of shear stress from a measurement of fluorescence anisotropy.

For temperature measurements, temperature sensitive dyes such as molecular rotors or excimer producing dyes will be used. The fluorescence intensity of these dyes is dependent on temperature and microviscosity in their molecular neighborhood. A molecular probe will reflect the temperature of the host polymer resin without influence from the temperature of the processing machine. An additional advantage of this temperature measurement is its fast response time, typically 10^{-4} s. The inherent limitation of the fluorescence response time is on the order of 10^{-8} s. Two types of temperature sensitive fluorescent molecules will be used:

- Molecular rotor dyes [3,4];
- Excimer producing dyes [5].

The measurement of temperature using these dyes will rely on a calibration function which is obtained for the particular polymer system being monitored. It is not expected that a universal calibration curve will emerge.

The rheological and temperature measurements programs form the core of the ongoing NIST development work.

4. Instrument Manufacturer's Perspective

Representatives from the instrument manufacturing community presented an assessment of morphology and mixing measurements, infrared analytical measurements, and temperature and pressure measurements. Generally, speakers at this session of the workshop described in detail the measurement capabilities of instruments from their companies. In particular, the presentations on morphology and mixing, infrared measurements, and infrared radiometric temperature measurements were company and instrument specific and will not be described in detail here. The reader is referred to companies manufacturing these instruments for additional information.

Pressure measurements and pressure transducers for polymer processing were described in general, generic terms. The different types of pressure transducers and their pros and cons were evaluated. In most cases, the transducer consists of a flexing diaphragm which, under pressure, imposes a load on a strain sensitive electrical component such as a resistive element, a semiconducting element or a capacitor. Pressure ranges and sensitivities are controlled by varying the rigidity of the diaphragm and the sensitivity of the electrical component. Temperature compensation is usually required and is incorporated in the electronic package. High temperature applications require special designs such as a mercury filled transducer in which the electronics are separated from the high temperatures at the sensing end. Dynamic pressure transducers based on the response of a piezoelectric material are also available. The trend for future pressure transducer development is to use fiber optics with which the problem of electrical interference in the manufacturing plant is eliminated.

5. NIST/Industry Collaboration

The workshop succeeded in achieving direct communication between NIST and industry concerning existing measurement problems. Strong support was communicated for the NIST rheological and temperature measurements programs. In order to maintain and utilize these lines of communication, an invitation to industry to collaborate with NIST was issued, and positive responses were expressed by most of the processing industry representatives present. It was agreed that a plan for a joint program would be developed and presented to those who wish to participate in ongoing research based on optical measurement methods. The objective of this research is to develop in-line, real-time instrumentation for rheological and temperature observations.

6. Summary

This report describes the activity at a workshop on *New Measurement Technology for Polymer Processing* which was held at NIST on Dec. 3-4, 1990. In attendance were representatives from NIST and polymer processing and measurement instrumentation companies. The theme of the workshop centered around the question: what on-line or in-line, real-time measurements of processing parameters do you need to make but are unable to because the technology does not exist? Industry participants highlighted their measurement problems during discussions about injection molding, compounding, extrusion, reactive processing, and film processing. Three areas of measurement needs emerged from these discussions: in-line rheological measurements, improved in-line temperature measurements, and in-line and on-line morphology measurements.

The direct transfer of information between NIST and industry at this and another workshop held in 1988 has provided a framework within which the NIST measurement program is defined. This program, based on the application of fluorescence spectrometry and optical measurement methods, addresses two industry measurement needs: in-line rheological and in-line temperature measurements. Optical measurements, particularly fluorescence spectrometry, offer new, unexplored opportunities for polymer processing.

Strong support for the NIST measurement program was expressed by most of the processors attending the workshop. Based on this positive response, industry collaboration with NIST was invited. Information about this program may be obtained by contacting Anthony J. Bur at 301-975-6748.

7. References

[1] Bur, A. J., and Miller, J. W., in *Intelligent Processing of Materials*, Yolken, H. T., editor, Natl. Inst. Stand. Technol., NISTIR 89-4024, January 1989.

[2] Bur, A. J., Lowry, R. E., Roth, S. C., Thomas C. L., and Wang, F. W., Macromolecules **24**, 3715 (1991).

[3] Loutfy, R. O., Macromolecules **14**, 270 (1981).

[4] Loutfy, R. O., and Arnold, B. A., J. Phys. Chem. **86**, 4205 (1982).

[5] Wang, F. W., Lowry, R. E., and Franconi, B. M., Polymer **27**, 1529 (1986).

News Briefs

General Developments

Inquiries about News Briefs, where no contact person is identified, should be referred to the Managing Editor, Journal of Research, National Institute of Standards and Technology, Administration Building, A635, Gaithersburg, MD 20899; telephone: 301/975-3572.

REPORT RECAPS BALDRIGE AWARD'S FIRST 3 YEARS

"... Interest in the award and in quality management is growing faster than any of us had imagined. The award is quickly becoming the most coveted prize in U.S. industry and symbolizes a renewed resurgence in quality," says Commerce Secretary Robert A. Mosbacher in Interim Report to the President and to the Congress on the Malcolm Baldrige National Quality Award. The report summarizes the award program's first 3 years and discusses the possibility of expanding award categories as well as the use of advertising by winners. The award program is managed by NIST with active involvement by the private sector. Copies are available from the National Technical Information Service, Springfield, VA 22161. Order by PB #91-167833 for $23 prepaid.

FASTENER ADVISORY COMMITTEE APPOINTED

A 15-member committee has been appointed to advise NIST and the secretary of commerce on accreditation of laboratories that test certain nuts, bolts, and other fasteners. The Fastener Advisory Committee is mandated by the Fastener Quality Act of 1990, which requires the secretary to establish a program to accredit or recognize laboratories to test fasteners. The purpose is to protect public health and safety by ensuring that critical fasteners conform to specifications. The statute sets civil and criminal penalties for failure to comply with its provisions. The program will be set up under the already existing National Voluntary Laboratory Accreditation Program.

FIRST LABS ACCREDITED FOR POSIX CONFORMANCE TESTING

The first laboratories to be accredited under the National Voluntary Laboratory Accreditation Program (NVLAP) to test computer operating system interfaces for conformance with the standard for Portable Operating System Interface for Computer Environments (POSIX) were announced by NIST. Compliance with the POSIX standard provides greater assurance that a computer program written for one machine will work on another. Under the NVLAP program, administered by NIST, the laboratories are accredited in the field of computer applications testing to use NIST POSIX Conformance Test Suite (NIST-PCTS: 151-1). The suite is used to test computer operating system interfaces for compliance with the POSIX standard, which has been issued as Federal Information Processing Standard (FIPS) 151-1. For information on NVLAP, contact Jeffrey Horlick, A124 Building 411, NIST, Gaithersburg, MD 20899, 301/975-4020, fax: 301/975-3839. For information on the POSIX validation program, contact James A. Hall, B266 Technology Building, NIST, Gaithersburg, MD 20899, 301/975-3273, fax: 301/590-0932.

THE CREEP OF COPPER STUDIED

Copper is used extensively as a stabilizing material for superconducting magnets and as a conductor in high-field, cryogenic magnets. Operating such magnets puts the conductor under intense pressure for extended periods of time. To assure reliable performance, users need to know the dimensional stability of the conductor. NIST researchers have made creep measurements at 295, 76, and 4 K of 99.9 percent pure, oxygen-free copper. Paper No. 9-91 describes the NIST study. Available from Jo Emery, Div. 104, NIST, Boulder, CO 80303, 303/497-3237.

NIST SIGNS AGREEMENT FOR FIPS BASIC TEST SUITE

NIST has signed a Cooperative Research and Development Agreement (CRADA) to develop a test suite for FIPS 68-2, BASIC programming language. The agreement with private industry marks the first time that a CRADA has been used to obtain the needed tests for federal programming language standards. The result of this cooperative effort will be an automated system for testing BASIC language processors for conformance to FIPS 68-2 BASIC. Under the terms of the CRADA, NIST will provide the administrative and scientific direction, while private industry will develop and maintain the test suite. The private company will own and market the resulting BASIC test suite. NIST will receive a nonexclusive, paid-up license to use the suite for testing BASIC implementations for conformance to FIPS 68-2, BASIC. For technical details, contact L. Arnold Johnson, A266 Technology Building, NIST, Gaithersburg, MD 20899, 301/975-3247.

VIDEO HIGHLIGHTS 1990 WINNERS OF BALDRIGE AWARD

To help companies better understand the Malcolm Baldrige National Quality Award and what it takes to improve quality, a new five-part, 35 minute video features the four 1990 winners. They are: Cadillac Motor Car Division and IBM Rochester (manufacturing category), Federal Express Corp. (service category), and Wallace Co. Inc. (small business category). The award, named for the late secretary of commerce, was established by legislation in August 1987. It promotes national awareness about the importance of improving quality management and recognizes quality achievements of U.S. companies—although the award is not for specific products or services. So far, nine U.S. companies have won the award. For 1991, 106 are in the running. The award program is managed by NIST with active involvement of the private sector, including the American Society for Quality Control (ASQC). The video is available from ASQC for $15, including shipping and handling. Item T992 in ASQC's inventory, it can be ordered by calling 1-800/248-1946.

NEW APPARATUS TO AID IN AEROSPACE VEHICLE DESIGN

Designers of future high-speed aircraft and aerospace vehicles have some formidable challenges, not the least of which are thermal insulation systems. These vehicles will be propelled by supercold (cryogenic) fuels; they also will generate tremendous heat as they hurtle through the atmosphere at 20 times the speed of sound. Thermal insulation systems will have to work in both extreme temperature ranges—as well as meet weight and volume restrictions. NIST scientists have developed an apparatus that can test insulation systems under conditions similar to actual use and more accurately predict in-use performance. The apparatus can measure thermal conductivity across enormous temperature differences—from 27 to 1,100 K. It is also built to withstand tremendous mechanical loads and gas pressures. Paper No. 15-91 describes the apparatus. Available from Jo Emery, Division 104, NIST, Boulder, CO 80303, 303/497-3237.

ENERGY-EFFICIENT LIGHTING TESTS PROPOSED

Technical experts, manufacturers, and others concerned with the performance of lighting equipment are asked to comment on proposed test methods and standards for a new program to accredit laboratories to test the energy efficiency of electric lighting products. The program was recently established by NIST under the National Voluntary Laboratory Accreditation Program at the request of the National Electrical Manufacturers Association. Laboratories will be accredited to test such products as indoor and outdoor luminaries, lamps, ballasts, and systems using test methods and performance criteria developed by standards-making organizations. For a copy of the proposed test methods and standards, contact Lawrence S. Galowin, A124 Building 411, NIST, Gaithersburg, MD 20899, 301/975-4022, fax: 301/975-3839.

INFORMATION SYSTEMS DICTIONARY ADOPTED AS FIPS

The American National Dictionary for Information Systems (ANSI X3.172-1990) has been adopted as a FIPS (Federal Information Processing Standard) Guideline. The dictionary consists of an alphabetic listing of terms and their definitions. The FIPS provides a reference within the Federal government for terms and definitions used in such fields of information systems as computers, data communications, and data processing. The publication is available from the National Technical Information Service, Springfield, VA 22161. Order by FIPSPUB11-3 for $45 prepaid.

NEW FACILITY TO SUPPORT SIGNAL-PROCESSING RESEARCH

A new research facility at NIST is built around a "video supercomputer" to study signal-processing techniques needed for future high-performance computer displays and video-imaging systems. Featuring a "Princeton Engine" video computer created by the David Sarnoff Research Center in Princeton, NJ, the facility is funded in part by the Defense Advanced Research Projects Agency. "The computer is an extremely useful adjunct to our existing research programs, which address the mathematics of signal processing and the testing and evaluation of electronic circuitry," said institute Director John W. Lyons in recent congressional testimony. "This facility will be used both for defense-related research and to support NIST's programs. It should save researchers both time and money and help move products to the defense and commercial markets more quickly."

ELECTRIC FIELDS MAY HELP UNLOCK MEMBRANE FUNCTIONS

Proteins embedded within the fluid membranes of our cells sense the tug of surrounding electric fields and respond differently to various frequencies. Now, researchers are becoming aware of possible effects that such fields could have on the assorted functions of membrane proteins. NIST scientists have formulated a theory for electroconformational coupling, which is a fundamental process of cellular energy and signal conversion. The theory offers a possible explanation of how membranes use energy from electric fields to perform certain functions. For example, a protein, by changing back and forth through different shapes that are differentially sensitive to an electric field, can use energy from that field to drive chemical reactions away from equilibrium.

SETTING COMPUTER CLOCKS IN A NETWORK ENVIRONMENT

NIST is developing methods for synchronizing the clocks of networked computers and setting them accurately to standard time. This will benefit companies in industries such as banking, transportation and manufacturing, which connect computers together to share data and conduct operations. Most computers have internal clocks, which need to be synchronized throughout the network to time stamp important data and prevent operational problems. The NIST service would synchronize the server computer (which controls the network and provides centralized services to client computers) to a NIST time source by telephone, radio signal, or through a higher-level network. Client computers would then be synchronized to that server. Accuracy for a packet-switched system might be ±10 ms, depending on configuration. This type of synchronization might be provided through a wide-area network if there is sufficient user interest and support. Contact Judah Levine, Div. 847.10, NIST, Boulder, CO 80303, 303/497-3903, e-mail: judah@india.colorado.edu.

INTRODUCTION TO U.S. LAB ACCREDITATION PUBLISHED

Laboratory Accreditation in the United States (NISTIR 4576) is designed for users who may not be familiar with this important conformity assessment activity. The report is a sequel to ABC's of Standards-Related Activities in the United States and ABC's of Certification Activities in the United States. Information is provided so users may make informed decisions on the selection and use of accredited laboratories and accreditation programs. To order, send a self-addressed mailing label to Standards Code and Information Program, A633 Administration Building, NIST, Gaithersburg, MD 20899, 301/975-4031.

GATT STANDARDS ACTIVITIES REPORTED FOR 1990

During 1990, NIST Standards Code and Information (SCI) program staff responded to more than 400 requests for information on proposed foreign regulations from the Secretariat of the General Agreement on Tariffs and Trade (GATT) in Geneva. Regulations on telecommunications equipment, chemicals, ozone layer depleting substances, metric use, medical products, and electrical equipment were most often requested. GATT Standards Code Activities of the National Institute of Standards and Technology 1990 (NISTIR 4559) describes NIST's role in support of the GATT Agreement on Technical Barriers to Trade (Standards Code), which includes operating the U.S. inquiry point for information on standards and certification activities that might affect U.S. trade. SCI also coordinates comments on foreign regulations, arranges for translations of texts, and maintains the GATT hotline (301/975-4041, not toll free). To order, send a self-addressed mailing label to SCI, A163 Building 411, NIST, Gaithersburg, MD 20899, 301/975-4037.

"SUPERCHAMBER" TO EVALUATE EM COMPATIBILITY

NIST is pioneering a new concept in test chambers for evaluating the electromagnetic (EM) compatibility of a wide range of electronic products. Such chambers are used to measure the immunity of systems and devices to electromagnetic fields by exposing them to known fields in the chamber and to measure the EM energy radiated from systems and devices. The new chamber combines the features of two systems commonly used for this type of testing—a transverse electromagnetic (TEM) cell and a reverberating chamber. This combination provides a test capability over the frequency range 10 kHz to 40 GHz, far exceeding capabilities of any other EM test facility. The method also will provide great cost savings in performing these critical measurements. NIST has developed the first combined chamber for the U.S. Army; it measures 1.3×2.4×3.9 m. While this chamber will be used for testing Army electronic equipment, the concept has direct application to commercial products. Much larger chambers may be possible where automobiles, helicopters, aircraft, or other large systems could be tested. Measurement and Evaluation of a TEM/Reverberating Chamber (TN1342) summarizes results. Available from the Superintendent of Documents, U.S. Government Printing Office, Washington, DC 20402. Order by stock no. 003-003-030355-4 for $5.50 prepaid.

HEAT SHOCK PROTEINS HELP MAKE NEW DNA

When the temperature rises, heat shock proteins go to work to keep normal cellular proteins from collapsing under the stress, research over the past decade has shown. Now scientists have discovered a new role taken on by one family of heat shock proteins in non-stress conditions. They perform an essential role in DNA replication, the way living things create new copies of genetic information. Even more surprising is the mechanism the heat shock proteins use in their new role, says a NIST research chemist at the Center for Advanced Research in Biotechnology (CARB). They split an otherwise inactive protein into two identical subunits, which are now active and able to bind to DNA. The NIST scientist collaborated with University of Maryland and National Cancer Institute scientists on this work described earlier this year in Nature. CARB was established in 1984 by NIST, the University of Maryland, and Montgomery County, MD, as a unique center for government, academic, and industry scientists.

BIOLOGICAL DATABASE MERGED TO ROBOTIC SOFTWARE

A new commercially available robotic system for protein crystallization experiments now includes the recipes for protein crystals of more than 600 biological macromolecules. The crystallization database and robotic system were joined through a Cooperative Research and Development Agreement between the Center for Advanced Research in Biotechnology (CARB) and private industry. The system will help scientists studying crystallization of proteins or other biological macromolecules. "This is particularly useful to assist in drug design, protein engineering, protein folding, or protein stability studies," the NIST scientist said. He and colleagues at CARB developed the NIST/CARB Biological Macromolecule Crystallization Database in 1988. After signing the agreement in January 1991, the CARB team integrated the database into the robotic system's memory. CARB was established in 1984 by NIST, the University of Maryland and Montgomery County, MD, as a unique center for government, academic, and industry scientists.

METHOD PINPOINTS TOXIC INSULATOR BYPRODUCT

For the first time, NIST researchers have measured a previously undetected toxic material—disulfur decafluoride (S_2F_{10})—produced when a common gas used for insulating electrical power equipment degrades. NIST has created a swift, sensitive method for gauging S_2F_{10} at environmentally important trace (parts per billion) levels. The method employs an instrument found in most analytical chemistry labs—a gas chromatograph/mass spectrometer, outfitted with modifications. An analysis takes about 5 min. Toxic S_2F_{10} develops when the non-toxic compressed insulating gas sulfur hexafluoride (SF_6) decomposes chemically in the electrical discharges typical in transformers and other power components. NIST tests show the toxic gas is produced under conditions like those found at power stations and substations. Whether S_2F_{10} presence poses a hazard to utility workers working around SF_6 remains undetermined. Scientists say more research is needed to learn what happens to S_2F_{10} once it is formed. NIST intends to participate in a planned government/industry consortium that aims to measure SF_6 byproducts at utility sites.

SPACE-GROWN CRYSTALS SURPRISE RESEARCHERS

A researcher with NIST has grown zeolites—inorganic crystals with many commercial applications—in the zero-gravity environment of space for the first time. The experiment was performed to see what effect gravitation has on the crystal growth of this class of technologically important materials. In collaboration with private industry the NIST researcher grew the porous crystals in an experiment aboard the Atlantis space shuttle flight April 5-11, 1991. While assuming the crystals grown in space would be shaped like a cube, as those that are grown on the Earth, the NIST scientist discovered something unexpected: They in fact were rod shaped. Zeolites are a class of minerals composed mainly of silicon, aluminum, oxygen, cations, and water. They are full of extremely tiny holes, 3 to 10 Å in size—about the size of a very small molecule—making them attractive commercially, such as in the catalytic cracking of petroleum.

FIRE HAZARDS OF WIRES AND CABLES UNDER STUDY

Thousands of miles of wires and cables snake through the walls of our offices and homes making possible such conveniences as electricity and communications. But are these products also a hidden threat during a fire? Researchers at NIST are working with the National Electrical Manufacturers Association (NEMA) to get a better picture of the behavior of these products during a fire. The researchers will be using a NIST-developed computer model to simulate how the product would burn, how much smoke would be produced, and how the smoke would move through a building. In addition, and perhaps most importantly, the model can keep track of how much toxic smoke these materials produce relative to the smoke produced by other combustible items involved in the fire. NEMA hopes this project will result in more realistic test methods.

NIST/U.S.S.R. ACADEMY RENEW SCIENCE AGREEMENT

The renewal of a Memorandum of Understanding between NIST and the U.S.S.R. Academy of Sciences on Cooperation in the Physical, Chemical, and Engineering Sciences was signed May 13, 1991, during the Second Joint Commission Meeting of the U.S./U.S.S.R. Basic Sciences Agreement in Moscow. The memorandum outlines scientific cooperation that may be conducted in theoretical and experimental physics, chemistry, and the basic scientific aspects of engineering. Topics of cooperation will be selected by both parties to cover areas of mutual interest in which both sides have active work in progress. NIST also has agreements for similar scientific cooperation with Japan, France, China, and South Korea.

PUBLIC-KEY CRYPTOGRAPHY REVIEWED

A new report, Public-Key Cryptography (NIST SP 800-2), presents a state-of-the-art survey of public-key cryptography from 1988–1990. (Cryptography covers the transformation of ordinary text into coded form and vice versa; the goal is security for transmissions over insecure channels.) This report compares public-key to conventional (secret-key) cryptography, surveys the major existing public-key systems, and examines criteria for systems and protocols for use. The information will be useful to systems implementors. The frameworks developed are versatile enough for a variety of systems, such as electronic mail and electronic fund transfer. Available from the Superintendent of Documents, U.S. Government Printing Office, Washington, DC 20402. Order by 003-003-03078-3 for $9 prepaid.

FEDERAL ROLE IN CONFORMITY ASSESSMENTS SUGGESTED

Private-sector panelists from two NIST/industry workshops—on pressure vessels and electromagnetic compatibility—made several common recommendations to assist in conformity assessment activities to gain acceptance of U.S. products in international markets such as the European Community (EC). The recommendations: the U.S. government should assume an active role in representing their respective industries in negotiations with the EC with the goal of designating notified bodies within the United States; the U.S. government should sponsor advisory committees to deal with issues of interest specific to their sectors; and NIST should assume a proactive role in disseminating information about draft regional and international standards concerning their sectors. Conformity Assessment Workshop on Pressure Vessels (NISTIR 4542) and Conformity Assessment Workshop on Electromagnetic Compatibility (NISTIR 4611) are available prepaid for $26 each, including handling, from the National Technical Information Service, Springfield, VA 22161. Order NISTIR 4542 by PB #91-192997 and NISTIR 4611 by PB #91-192989.

ARCTIC POLLUTION: NEW WAYS TO TRACK ITS EFFECTS

Studies of contaminant levels in marine mammal tissues give scientists a picture of how pollution affects the marine ecosystem over time. Now a new publication on tissue collection procedures should help marine biologists refine their studies. The 33-page document describes how marine mammal tissues are collected for long-term storage as part of the Alaska Marine Mammal Tissue Archival Project (AMMTAP) at the National Biomonitoring Specimen Bank at NIST's Gaithersburg, MD laboratory. These procedures can be applied to other marine mammal research projects. NIST, the National Oceanic and Atmospheric Administration, and the Minerals Management Service for the Interior Department started the AMMTAP project in 1987 with the goal of documenting long-term trends in environmental quality. Alaska Marine Mammal Tissue Archival Project: Revised Collection Protocol is available from the National Technical Information Service, Springfield, VA 22161. Order by PB #91-184796/AS for $15 prepaid.

CONSORTIUM TO HELP U.S. METAL POWDERS INDUSTRY

Three manufacturers that produce or use metal powders and an office of the Department of Energy that is concerned with the energy efficiency of industrial processes are joining NIST in a project to improve the competitiveness of the U.S. metal powders industry. The focus will be on the intelligent processing (IPM) of rapidly solidified metal powders by high-pressure, inert gas atomization. The program is open to researchers from industry and government who are concerned about quality in the production of rapidly solidified metal powders and IPM technology. For information, contact Dr. John P. Gudas, Deputy Chief, Office of Intelligent Processing of Materials, B344 Materials Building, NIST, Gaithersburg, MD 20899, 301/975-5727.

SUCCESSFUL PROGRAM TESTS THE TESTERS

In 1989 NIST took over the world's first program for certifying impact-testing machines from the U.S. Army. Since then, the program—termed Charpy V-notch testing—has been streamlined substantially. The program is important because manufacturers of military hardware, for instance, need to know the impact resistance of the sides of a tank. NIST researchers have developed a computer software program that has increased efficiency by 40 percent, allowing NIST staff the time to respond more rapidly to individual customer inquiries and problems. Customers generally receive their results within 2 weeks of submitting the data. Since the NIST program is recognized worldwide, 30 percent of the certification requests come from other countries. More than 1,000 Charpy V-notch testing machines are certified annually. For information, contact Dominique Shepherd, Div. 853, NIST, Boulder, CO 80303, 303/497-3211.

REPORT ON JAPANESE BUILDING TECHNOLOGY

The Japanese government and institutions such as banks are working hard to put the country at the forefront of intelligent building technology, says a NIST researcher who visited Japan to assess the state-of-the-art there in intelligent buildings. He found the Japanese quickly install new systems and products into buildings. Among the technologies used are earthquake and sway monitoring systems; infrared sensors to regulate HVAC, lighting, and Venetian blinds; fiber-optic systems to send sunlight to windowless offices; and robots for cleaning and inspecting for structural damage. A major problem shared by both the United States and Japan is a lack of standards for hardware and software that makes it difficult to integrate equipment from different manufacturers and, in some cases, equipment from the same manufacturer. Intelligent Building Technology in Japan (NISTIR 4546) is available by sending a self-addressed mailing label to Arthur Rubin, A313 Building Research Building, NIST, Gaithersburg, Md. 20899.

U.S.–U.S.S.R. STANDARDS WORKING GROUP

Under the auspices of the Joint U.S.-U.S.S.R. Commercial Commission, a Standards Working Group (SWG) was established and recently held its first meeting in Washington, DC. The chairman of Gosstandart, led the Soviet delegation that met with representatives of NIST, other federal agencies, and the U.S. private sector. The major aim of the SWG is to explore mutually advantageous avenues of cooperation, including promotion of international standards and product acceptance criteria. At the first session, emphasis was placed on exchange of information about standards and conformity assessment practices in the two countries. The second meeting of the group will be hosted by the Soviets this fall.

CAD/CAM DEMONSTRATION FACILITY IS ON-LINE

The Northeast Manufacturing Technology Center (NEMTC) located in Troy, NY, at the Rensselaer Polytechnic Institute, has established a CAD/CAM demonstration facility designed to assist small manufacturing firms in their quest for automating their manufacturing facilities. NEMTC is one of the five NIST Manufacturing Technology Centers currently in operation throughout the United States.

The staff at the demonstration facility at NEMTC has compiled a large database of CAD/CAM software products and has set up a variety of computer workstations that can be used by small firms to gain hands-on experience with different CAD/CAM packages before any purchase is actually made. The demonstration facility currently has over 40 software packages on-line, and the database is growing at the rate of one to two new packages per week. In the current mode of operations, the NEMTC staff consults with personnel from the small firms and then recommends several software packages on a case-by-case basis. The firms' staff can then experiment with the most appropriate software packages for 1 or 2 days before the final choice is made.

WORKSHOP INTRODUCES INDUSTRY TO NIST TESTING STRATEGIES FOR ANALOG AND MIXED-SIGNAL PRODUCTS

NIST recently held a 3 day workshop to introduce representatives from industry to the NIST strategy, methodology, and analytical tools for developing and implementing efficient tests for analog and mixed-signal devices and instruments. Testing is expensive; many of these products are sufficiently complex or have so many operating states that it is not physically or economically feasible to perform exhaustive testing. NIST has responded to the need for reliable cost-effective testing by developing methods for identifying a reduced set of test points that effectively yields the same information as if comprehensive testing had been carried out and in some cases, improves the prediction of performance. The reductions are significant; in one example of a 13 bit analog-to-digital data converter the reduction factor is 16. Eleven companies sent representatives to learn about NIST procedures such as determining the linearity of data converters, the frequency response of amplifier/attenuator networks, the time response of filters, and the measurement errors of a multirange ac voltmeter.

NIST SCIENTISTS RESOLVE FUEL DENSITY DISCREPANCY

NIST scientists recently resolved a controversy involving jet fuel density measurements as performed in the aircraft industry. A commercial avionic liquid density transducer had been used for monitoring the quantity of fuel carried on a commercial intercontinental aircraft with a quoted accuracy of ±0.4 percent. This device is provided by the manufacturer of a fuel monitoring system for large sectors of the aircraft industry. The NIST scientists designed a special density testing program where a hydrocarbon liquid of unknown density was used as a benchmark; the density of this liquid could be determined by NIST with an accuracy of better than ±0.1 percent. The NIST-prepared testing program was developed and presented to representatives from several interested firms. The comparison testing was performed with several density measurement devices used by the interested parties concurrently with three different instruments used by NIST. A total of 22 measurements of density were performed over 5 days of testing and over a temperature range of 10 to 35 °C. The overall accuracy of the NIST system, which was substantiated at ±0.06 percent, resolved the controversy to the satisfaction of all the test participants. The resulting improvements in measurement uncertainty can change the carrying capacity of a single fully loaded aircraft by more than 500 kg.

X-RAY DETECTOR INCORPORATES DIFFRACTION

NIST has received a patent on a new type of x-ray detector, which combines the functions of diffraction with detection.

The device consists of a large single crystal of semiconductor, which is doped with a photovoltaic detector at a precise depth beneath the surface. Changes in the depth distribution and quantity of radiation occur at the Bragg condition at which diffraction takes place. The photovoltaic detector perceives these changes, and the resulting electrical current indicates the absence or presence of the Bragg condition.

Applications of the new detector are likely to involve stabilizing the monochromatic high-energy x-ray radiation which is produced in synchrotron light sources for angiography and diffraction from biochemical molecules. The device is presently being tested as an x-ray energy standard at the synchrotron light source HASYLAB in Hamburg, Germany, for use on all of the x-ray beamlines there.

INFRARED CHARACTERIZATION OF AN OPEN-SHELL FREE-RADICAL COMPLEX

An understanding of the phenomenon of bonding is of fundamental importance in chemistry, and it has proven convenient over the years to classify bonds as covalent, ionic, hydrogen, van der Waals, etc., depending on the nature of the bond in question.

NIST scientists reported on the first infrared study of the class of bonding that takes place between one closed-shell partner (containing an even number of electrons, all of which are paired) and one open-shell partner (containing an odd number of electrons, so that complete pairing is impossible). Since traditional ideas of the chemical bond are based on the concept of electron pairs, it was speculated that a completely new type of bonding might arise when full pairing was impossible. The present work, however, suggests strongly that rather conventional ideas taken from the literature on van der Waals bonding will suffice to explain most of the essential features of the bond between the closed-shell HF partner and the open-shell NO partner.

The study involved both theoretical and experimental contributions at NIST. The NO-HF complex was formed in a supersonic jet, and an infrared spectrum was recorded using a newly constructed molecular-beam optothermal spectrometer with a color-center-laser excitation source and a liquid-helium-cooled bolometer detector. The spectral data on NO-HF could not be understood by conventional methods but were successfully treated using a computer program containing new interaction terms specifically developed to take into account most of the important vector-coupling effects associated with the unpaired electron.

WEAR TRANSITION DIAGRAMS FOR ADVANCED CERAMICS

Advanced structural ceramics are used in diverse applications requiring resistance to abrasion and erosion, resistance to corrosive wear, wear resistance at elevated temperatures, low density, and unique electrical, thermal, and magnetic properties. Limited knowledge in the tribological performance is one of the major technical barriers that must be overcome before the full potential of ceramics in tribological applications is realized. The tribology program at NIST has addressed this issue by compiling data and mechanistic information assembled in simple diagrams, which show the range of wear rates and friction coefficients as a function of load, temperature, and speed. These "wear transition diagrams" and "wear maps" are useful for design and material selection for tribological applications. These diagrams and the models that are being developed can be utilized to suggest guidelines for the control of the coefficient of friction and the reduction of the rate of wear in advanced ceramics.

INDUSTRIAL WORKSHOP ON SMALL ANGLE X-RAY SCATTERING

NIST recently hosted a workshop for users of the NIST 10 m small angle x-ray scattering (SAXs) facility. Representatives from 10 industrial organizations joined NIST staff members in this workshop. The session featured speakers from industry, academia, and NIST who presented research accomplished using this facility. Also discussed were technical issues that confront the users and operators of the facility. This information will be used in planning future improvements to the facility. The 10 m SAXS camera, in operation for nearly 4 years, has been used by a variety of academic, industrial, and government workers to study microstructure in polymeric materials and biological systems. The facility is available for proprietary as well as collaborative research.

INTERCOMPARISON STUDY OF ROCKWELL HARDNESS TEST BLOCKS

An intercomparison study of Rockwell hardness test blocks marketed in the United States has been completed by NIST in collaboration with ASTM. Three hardness levels for each of four of the most commonly used Rockwell scales—namely C, B, 30N and 30T—were considered. Hardness measurements were made on commercial hardness testers. For each series of tests comparing similar blocks, all measurements were made on one machine, all measurements were made by one person, and all measurements were made with the same indenter and supporting anvil.

Under these nearly ideal test conditions, it was found that there are some significant differences among hardness test blocks of different manufacturers. These differences demonstrate the need for national hardness standards in the United States. NIST has committed to develop some of these standards.

In addition to the differences among blocks of different manufacturers, the measurement results in a number of cases do not satisfy ASTM requirements for test block uniformity. Re-evaluation of brass test blocks after several years indicates significant instability over time for some of them, which suggests the need to develop test block material with improved stability as well as more consistent uniformity.

NEW CARBON MOLECULE STUDIED WITH NEUTRONS

The vibrational spectrum of a remarkable new molecule, carbon-60, has been measured using a neutron scattering technique at the NIST research reactor. Often referred to as "buckminsterfullerene" or "buckyballs" because of their unusual geodesic-sphere structure, C_{60} molecules constitute, when solidified and purified, a new kind of solid carbon very different from the well-known forms, diamond and graphite. Each molecule is a 60-atom spherical hollow framework, which closely resembles the seaming on a soccerball.

In a collaboration involving scientists from NIST, Ohio University, and Penn State University, the energy loss spectrum of monoenergetic neutrons scattered from a buckyball sample was measured. Unlike more common methods such as Raman scattering and infrared absorption, which permit one measurement of only a few of the vibrational energies, neutron scattering yields a distribution that accurately reflects all the vibrational modes of a molecule. When the new data were compared with existing theories, it became evident that more accurate quantum mechanical calculations would be necessary in order to predict the properties of C_{60}. Basic understanding of the molecule will undoubtedly be useful in developing new carbon chemistry with buckyballs as the starting material. Collaborative experiments involving additional university and industrial groups are planned.

NIST BEGINS CIGARETTE FIRE SAFETY PROGRAM

Cigarette-initiated furniture fires continue to be the leading cause of fire deaths in the United States. The Fire-Safe Cigarette Act of 1990 (P.L. 101-352) directs an assessment of the practicability of developing a performance standard to reduce cigarette ignition propensity. NIST has begun research on two of its three specified tasks: (a) development of a standard test method for cigarette ignition propensity; and (b) developing experimental understanding and computer modeling of the ignition process. Upon completing these, NIST is to compile performance data on currently sold cigarettes. The project will be completed by August 1993.

NIST PRODUCES STANDARD REFERENCE MATERIAL (SRM) FOR MAGNETIC TAPE CARTRIDGES

NIST Special Publication 260-115, *Standard Reference Materials: Calibration of NIST Standard Reference Material 3201 for 0.5 Inch (12.65 mm) Serial Serpentine Magnetic Tape Cartridge*, describes the test system design and operation for the calibration of the NIST secondary standard reference tapes SRM 3201 for 0.5 in (12.65 mm) 22 and 48 track serial serpentine magnetic tape cartridges. The production of an SRM for these cartridges promotes the ability to interchange data both within and among various computer systems. When the media is designed and manufactured on the basis of a comparison to a known and accepted standard reference media, reliable interchange is assured.

REFERENCE MATERIAL 8455—PYRITE ORE FOR BIOLEACHING STUDIES

The Standard Reference Materials Program announces a new reference material (RM) for use in determining the rate of biological attack on pyrite and for use as a bioleaching substrate. The rate of bioleaching of iron from the pyrite by Thiobacillus ferrooxidans, 12.4 ± 4.0 mg Fe per L per h, is reported for information only and is not certified. This rate was determined by NIST and eight cooperating laboratories in accordance with ASTM Method E 1357-90. The composition of the material, also reported for information and not certified, is 47.0 ± 0.94 percent Fe and 49.6 ± 2.13 percent S. The RM is available in 100 g bottles of the -165, $+250$ mesh fraction of the mineral (which was washed, rinsed, and dried under nitrogen before grinding), bottled in a high-purity nitrogen atmosphere, with the bottles vacuum-sealed in foil pouches.

NIST STRUCTURES AND PROPERTIES DATABASE

Standard Reference Database 25—NIST Structures and Properties Database and Estimation Program is now available from the Standard Reference Data Program. This unique database contains data for nearly 5,000 compounds from three well-established and widely used databases—NIST Positive Ion Database, NIST Chemical Kinetics Database, and NIST JANAF Thermochemical Tables. It combines a database of properties and structures, a data prediction program, and an easy-to-use structural drawing module. It also features a complete implementation of Benson's Group Additivity estimation for gas phase heats of formation, entropies, and heat capacities, as well as a structure-based method for estimating vapor pressures and boiling point. The database is already generating great interest.

MAGNETIZATION STUDIES OF SINTERED HIGH-TEMPERATURE SUPERCONDUCTOR $YBa_2Cu_3O_7$ CONTRIBUTE TO UNDERSTANDING OF GRAIN BOUNDARIES

NIST scientists have completed a study of the intergranular magnetic properties of the sintered, high-temperature superconductor $YBa_2Cu_3O_7$. Practical applications of high-temperature superconductors require these materials to support usefully high transport currents; grain boundaries in sintered materials are known to limit the transport current. To measure the intergranular magnetization directly, the researchers designed and constructed a field-compensating Hall-probe magnetometer; the results show that the magnetic properties of the intergranular material are analogous to those of proximity-coupled niobium-titanium filaments embedded in a copper matrix. This finding suggests that superconductor-normal-superconductor junctions exist at the $YBa_2Cu_3O_7$ grain boundaries. The magnetization of sintered materials has two components: one arising from the intrinsically superconducting grains and the other from the material that separates the grains. This intergranular material behaves as a weak type-II superconductor as a result of microbridges or proximity coupling between the grains. The team also measured the effect of transport current and applied fields on magnetic flux creep. They found that flux creep is very small at the grain boundaries and that it increases rapidly with small transport currents or applied magnetic fields. These results are significant because they provide detailed information on the flux pinning mechanisms at the grain boundaries.

HARD DISK RECORDING HEAD APPLIED TO EDDY-CURRENT PROBING

A NIST scientist has constructed and tested a novel eddy-current probe made from a computer hard-disk drive recording head. He demonstrated the capability of the probe by measuring a 2 mm long fatigue crack in 7075-T6 aluminum and two electrical-discharge-machined notches in Inconel 718 having lengths of approximately 0.5 and 0.25 mm. Advantages of the design include commercial availability of the critical sensing element and capability to detect small flaws in low-conductivity alloys. Non-destructive eddy-current flaw detection methods are becoming increasingly important in the early detection of fatigue cracks in aircraft structures and critical components such as engine fan disks.

STEP ON-LINE INFORMATION SERVICE DEMONSTRATED

The Information Services Center of the National PDES Testbed at NIST demonstrated the "STEP On-Line Information Service" at the joint IPO/ISO meeting, recently, in San Diego, CA. The IGES/PDES Organization (IPO) and the International Organization for Standardization (ISO) are two of the major organizations involved in developing an international standard for sharing digital product data for manufactured parts, the Standard for the Exchange of Product Model Data, or "STEP." Two other key organizations involved are the National PDES Testbed at NIST and PDES Inc., an industrial consortium. The STEP On-Line Information Service provides electronic access to the latest copies of the developing standard and related information. Three access methods are provided: a bulletin board system (bbs), a network file transfer protocol (anonymous ftp), and an electronic mail server. A help sheet is also provided on-line. The complete system documentation is contained in NISTIR 4491, *STEP On-Line Information Service User's Guide, and NISTIR 4508, The National PDES Testbed Mail Server User's Guide.*

SUPERCONDUCTING YBACUO PRODUCED IN AN AEROSOL FLAME REACTOR

Aerosol routes to the production of powders are increasing in importance due to their inherent advantages in product purity and process scale-up. Work at NIST has demonstrated the production of submicron $YBa_2Cu_3O_7$ particles in a diffusion flame reactor. The particles were unagglomerated and had a critical superconductivity temperature T_c of 92 K.

In this new flame synthesis method, droplets of an aqueous solution of yttrium, barium, and copper nitrates are entrained into the flame reactor by a dried stream of oxygen gas. A hydrogen-oxygen coannular diffusion flame, with the oxidant in the inner stream, produced the desired yttrium-barium-copper oxide. This configuration provided the best control of residence time and time-temperature history in the flame reactor. Premixed flames were also studied; but they did not produce the desired oxides, presumably because of the long residence time of the particles in an environment with a high-water concentration. These novel processing techniques are critical to the production of superconducting oxides in bulk quantities.

CONCENTRATION HISTOGRAM IMAGE TECHNIQUE

NIST researchers have adapted a scatter diagram technique to help characterize the chemistry of materials by means of compositional mapping techniques. These mapping techniques involve analytical electron microscopes, electron probe microanalyzers, and other instruments that yield images depicting the microstructure and concentrations of the elemental or molecular constituents in the specimen. The spatial relationships among the constituents and their concentrations are difficult or impossible to deduce from gray level images alone, but these relationships appear at a glance in the concentration histogram image (CHI), a transformation of the images. The CHI is much like a bivariate or trivariate histogram of the images but is displayed using a modified hot-body color scale to indicate the areas in the histogram that correspond to a particular chemical composition. The CHI has structures like blobs or stripes that correspond to particular phases, phase boundaries, or diffusion zones in the material under examination. The CHI aids in discovering concentration relationships not easily found using conventional numerical statistical methods. Research continues on methods for displaying CHIs of more than three constituents and for discovering CHI features characteristic of various types of specimens and instrumental artifacts.

MAGNETIC COUPLING IN THIN FILMS STUDIED WITH "ATOMIC WEDGE"

Scientists at NIST have discovered a new effect that may affect our understanding of exchange coupling in thin-film magnetic structures and the application of the giant magnetoresistance effect to magnetic recording devices. The antiferromagnetic exchange coupling in transition metal multilayer structures has recently caused much excitement because of the resulting giant magnetoresistance and its potential application to magnetic recording. Oscillations, ferromagnetic to antiferromagnetic, in the exchange coupling between two iron (Fe) layers separated by an "atomic wedge" of chromium (Cr) were investigated by scanning electron microscopy with polarization analysis (SEMPA). The direction of the magnetic field on the upper Fe layer reversed periodically as the thickness of the Cr layer increased by multiples of 10-12 atomic layers. The magnetic oscillations persist for a startling six periods, i.e., through 70 atomic layers with a total thickness of about 100 Å. Additional, secondary oscillations with a period of two Cr layers were also observed for the first time. This observation of oscillations, with both a long and a short period, provides a fascinating set of clues for advanced theories of the exchange coupling in these structures.

COINCIDENT FRAGMENTS OBSERVED IN UNIMOLECULAR DECOMPOSITION REACTIONS

Using pulsed nanosecond lasers, NIST scientists have measured recoil velocities with unprecedented resolution for fragments produced in molecular decomposition reactions. Measurements of this type are of great importance because they elucidate the forces acting in molecules at energies where chemical reactions occur. These forces are ultimately responsible for the rates and products of chemical reactions. In diverse fields such as atmospheric and biological chemistry, it has generally been assumed that forces acting in vibrationally energized molecules would scramble quantum states of the separating fragments, producing no particular product state correlations, with no dependence upon initial vibrational motion. The results contradict previous intuition. Analogous to coincidence measurements in particle physics which have advanced understanding of subatomic structure, these chemical coincidence experiments challenge our understanding of unimolecular decomposition and should lead to greater insight into chemical processes.

In the experiment, the nitric oxide dimer (ON–NO) is excited to specific vibrational levels sufficiently energetic to lead to dissociation, producing two NO fragment molecules. The recoil velocities of the fragments are determined by measuring their Doppler-shifted absorption spectra. The extraordinary spectral resolution of the measurements allows a determination of the relationship between the energy states of related fragments and thus provides a remarkably detailed picture of the mechanics of the dissociation event. A most surprising observation is that there is a pronounced correlation of the electronic states of coincident fragments, e.g., the electronic motion observed in one fragment is always associated with a distinct electronic motion in that fragment's separating partner. The specific correlation observed represents a unique reaction path and depends upon the vibrational motion which is initially excited in the dimer.

NEUTRON SPECTROMETER DEDICATED

On May 10, the first participating research team (PRT) instrument of the Cold Neutron Research Facility was dedicated. The instrument, the 30 m small-angle neutron scattering (SANS) spectrometer, will provide the first state-of-the-art high-resolution SANS capability for U.S. researchers. Direct application to research and development on advanced materials in such areas as new polymer blends, microemulsions, packaging materials for electronics, and new metal alloys is under way.

PRT instruments are those in which organizations provide initial funding for instrument development, and continuing support for operation and upgrades in return for a share of scheduled instrument time. One-fourth of instrument time on PRT instruments is allocated to the U.S. scientific community by a program advisory committee through a proposal review system.

NANOMATERIALS AND PROCESSING

Recent research at NIST has shown that small metallic clusters of nanometer dimensions can be dispersed in dielectric or dissimilar metallic matrices by sol-gel and controlled precipitation techniques. Many of the resultant bulk materials, referred to as functional nanocomposites, show interesting properties as a result of selection of the matrix in combination with the oxidation state, small crystallite size, and distribution of the functional component. The prototype systems under study suggest that the properties of these materials can be engineered toward specific applications through judicious chemical design. Functional nanocomposite materials are projected to have significant future applications in high-density magnetic recording, magnetic refrigeration, microwave communications components, electric motor and transformer cores, as well as in magneto-optical and electro-optical devices.

EDDY-CURRENT SENSING OF OXYGEN IN HIGH-T_C SUPERCONDUCTING OXIDES DURING PROCESSING

The important low-temperature superconducting properties of high-T_c ceramic oxides are strongly dependent on parameters of the high-temperature processing of these materials. In particular, oxygen content, which affects the superconducting transition temperature, is determined not only by the detailed thermal history and surrounding atmosphere during processing but also by the porosity and surface conditions of the ceramic. This complicated situation suggests a need for sensors that can monitor the oxygen content during heat treatment. Scientists at NIST have devised a non-contacting eddy-current technique, which uses measurements of normal-state resistivity as a monitor of oxygen in cylindrical samples. The sensor consists of a coil that surrounds the sample and is connected in parallel with a capacitor. Measurements of the impedance of this circuit at resonance are used to calculate the resistivity of the sample. The physical simplicity of this device allows it to be easily incorporated into most existing research furnaces used for processing high-T_c ceramics.

NIST ASSISTS HUD IN REVISION OF MANUFACTURED HOUSING STANDARD

Researchers at NIST have completed analyses and recommended that all single-wide and double-wide mobile homes be equipped with mechanical ventilation having a minimum capacity of 0.026 m^3/s of outdoor air in future versions of the HUD standard. The analysis was completed for all geographic locations in the continental United States. Results indicate that natural ventilation was inadequate to provide the fresh air requirements specified in the latest standard of the American Society of Heating, Refrigerating, and Air-Conditioning Engineers, Standard 62-1989, "Ventilation for Acceptable Indoor Air Quality." Additionally, considerably larger ventilation rates than were recommended would be needed to prevent condensation on single-pane windows during the heating season. Consequently, NIST recommended double-pane windows be required in all heating climates. The recommendations are currently under consideration by HUD. Additional analyses are near completion on attic ventilation requirements to prevent condensation problems.

NIST COMPLETES PREOCCUPANCY TESTING IN NEW GSA BUILDING

As part of a multiyear investigation of the thermal and indoor air quality performance of three advanced technology government office buildings, NIST researchers have just completed preoccupancy testing of the new Federal Records Center in Overland, MO. Under NIST guidance, GSA has equipped the building with a "diagnostic center," with test equipment and a terminus for sensor lines transmitting building performance data from throughout the building to monitors and data acquisition systems. The unique aspect of this building is that the occupants are moving from an existing facility that is physically linked to the new building. After moving, the old building will be renovated and the indoor air quality in the new building is expected to be affected by the construction activity. To date, measurements have indicated a surprisingly leaky (air), but otherwise thermally efficient building envelope. Also, pollutant levels of radon, formaldehyde, volatile organic compounds, carbon monoxide, and carbon dioxide are generally below acceptable limits. Several episodes of elevated levels of CO_2 and CO have occurred during the evening due to elevated levels outdoors that are still under investigation. This study will continue through the first year of occupancy to observe the effects of new building materials outgassing and occupant activities.

NIST GIVES GSA TECHNICAL BASIS FOR USE OF ADVANCED BUILDING CONTROLS

NIST staff have provided GSA with both a design guideline and a specification in the format of MASTERSPEC so GSA personnel and their design contractors can use direct digital controls (DDC) in all future buildings. Direct digital control of heating, ventilating, air conditioning, fire safety, and building security systems has great promise over more conventional analog control systems in providing reliability, versatility, and improved performance. Because their costs have been reduced significantly during the 1980s, they are now an attractive alternative. The documents were developed based on NIST studies with DDC in laboratory experiments on commercial building heating and cooling equipment and with computer simulation models of mechanical systems and their control.

WORKSHOP FOCUSES ON APPLICATIONS PORTABILITY AND OPEN SYSTEMS ENVIRONMENTS

NIST sponsored the seventh in a series of Applications Portability Profile/Open Systems Environment (APP/OSE) Users' Forum Workshops recently. The semiannual workshops provide users and suppliers with status updates on the various functional areas of the APP and on NIST proposals regarding the adoption of an integrated set of nonproprietary standards to support applications portability. Over 230 users and vendors attended the 1 day workshop.

Highlights included specific reports by NIST personnel on the status of the APP/OSE effort; an overview of the philosophy behind a new publication, NIST Special Publication 500-187, *Application Portability Profile, The U.S. Government's Open System Environment Profile – OSE/1 Ver 1.0*, and the rationale of decisions made about comments received on the draft document; a presentation on the European view of conformance testing by members of the National Computing Centre in the United Kingdom; and a report on the newly available Portable Operating System Interface for Computing Environments (POSIX) Conformance Testing for Federal Information Processing Standard (FIPS) 151-1. The next APP/OSE workshop will be held Nov. 12, 1991.

GAMS CLASSIFICATION SYSTEM ADOPTED BY NAG LTD.

The NIST Guide to Available Mathematical Software (GAMS) Problem Classification System has been adopted by the Numerical Algorithms Group (NAG) Limited of Oxford, U.K., for use in documenting their principal mathematical software library product. NAG develops and markets mathematical and statistical software worldwide.

The GAMS Problem Classification System is a taxonomy of mathematical and statistical problems amenable to solution by existing software. It was initially developed by NIST in the early 1980s and has been periodically revised since then. It is now used widely as a tool by commercial vendors as well as in government, industrial, and university computer centers.

REFERENCE MATERIALS 8495 AND 8496 – NORTHERN SOFTWOOD AND EUCALYPTUS HARDWOOD BLEACHED KRAFT PULP

The NIST Standard Reference Materials Program announces the availability of two new Kraft Pulp Reference Materials (RMs) intended primarily for use in fundamental studies on the physical properties of fibers and paper sheets. RM 8495 is a Northern Softwood Bleached Kraft Pulp and RM 8496 is a Eucalyptus Hardwood Bleached Kraft Pulp. The materials selected for these two RMs are bleached dried lap pulp, each from a single lot of a standard commercial production run. The materials were selected because of their differing fiber size, differing papermaking properties, and similarity to commercially available materials.

RMs 8495 and 8496 were developed and prepared with input and support from the Pulp Material Research Committee, a sub-committee of the Fundamental Research Committee.

The two pulp RM were donated by Aracruz Celulose S. A. and the Procter and Gamble Cellulose Company. At this time no extensive property measurements have been made on these materials beyond ensuring they were within the control limits of the normal production run. A measurement error study is in progress with participation by international paper technical laboratories. As results become available, they will be published and added to the Report of Investigation that accompanies each of these materials.

Each RM package contains 10 standard lap sheets, each sheet weighing approximately 0.5 kg (1 lb), dry weight. The sheets are hermetically-sealed in a film foil barrier bag and packaged in a 200 lb C flute carton with dust flaps.

LITHOGRAPHED ANTENNAS PROVIDE 15×INCREASE IN EFFICIENCY AT INFRARED WAVELENGTHS

NIST scientists have developed and demonstrated the operation of a lithographed log-periodic antenna for infrared radiation that offers about a 15 times higher efficiency than the best previous measurements at the wavelength of interest and extends the wavelength range of lithographed antennas to shorter wavelengths by a factor of almost ten, toward the near infrared. The lithographic methods used are based on those used in the semiconductor industry to pattern planar integrated circuits. The team has demonstrated 50 percent efficiency in collecting a single mode of 300 K blackbody radiation, a band from about 50 to 30 μm wavelength. The thin-film antenna elements are made from a high-conductivity normal metal in a toothed spiral configuration with an overall diameter of about 60 μm, about the diameter of a human hair. The antenna fabrication method and design offers the possibility of radical new approaches to infrared detection, using detectors much smaller than the infrared wavelength. The antenna was initially designed to be used in conjunction with a kinetic photoinductive detector at its feed.

OPTICAL MODELERS COMPARE RESULTS

Modeling is one way to achieve resolution in optical metrology that exceeds the classical resolution limits of the microscope used. The modeling effort, however, is not trivial because the complete optical instrument must be analyzed including the illumination optics, the optical scattering (or diffraction) at the object, and the imaging optics. If done properly, one can achieve meaningful measurements with precisions in the nanometer range and accuracies limited by the imperfect geometry of the actual present-day micrometer- and submicrometer-sized objects. Thus the end product of a recent optical metrology workshop at NIST was an agreed upon set of structures for which the scattered optical field will be computed by the different methods currently being studied throughout the world and then compared. Any significant differences will then be analyzed and, if necessary, corrections made to the present algorithms of computation. Once theoretical agreement is obtained for the scattering portion of the problem, real images will be computed and compared with experimental data. This comparison will require identifying, measuring, and then modeling all the imperfections of the actual experiment. Since this will be difficult, it was decided to perform a "theoretical round-robin" first.

NIST, APL EXTEND STUDY OF AUTOMATED ELECTRONICS ASSEMBLY

NIST and the Applied Physics Laboratory (APL) of the Johns Hopkins University have agreed to extend a cooperative research and development agreement to study the design of a computer-integrated small-batch manufacturing system for electronics and microelectronic parts. The study focuses on surface-mount printed-circuit boards. The project includes specification of process and quality control techniques and strategies, computer hardware and software data requirements, and interface and support standards, such as the Department of Defense CALS standards. New concepts for process control sensors will be emphasized. The joint project draws on NIST expertise in sensors and standards technology and APL skills in applications and electronics manufacture.

SIMS COMPOSITIONAL MAPPING OF ALUMINUM-LITHIUM ALLOYS

Aluminum-lithium alloys represent promising materials for aerospace applications because of their favorable mechanical properties, particularly the strength-to-weight ratio. Unfortunately, these alloys are more susceptible to oxidation than Li-free Al alloys, because the oxides of Al-Li alloys are non-protective and spall during temperature cycling. Preferential oxidation of Li at the alloy solutionizing temperature creates a Li-depleted layer extending several tens of micrometers into the metal below the oxide. The nature of this solute-depleted layer has been studied by compositional mapping secondary ion mass spectrometry (SIMS) in a collaboration involving scientists from NIST and Lehigh University. Because the depth of solute depletion (10–100 μm) is too great to apply conventional SIMS sputter depth profiling, lateral profiling in the ion microscope imaging mode has been used to examine the extent of Li depletion, and to monitor changes in other alloying elements, including Mg and Cu. SIMS compositional mapping has enabled measurement of diffusion coefficients for the alloying elements under realistic processing conditions. This information is critical for developing thermal processing strategies for these advanced alloys.

ULTRACOLD ATOMIC COLLISIONS

Rapid advances in laboratory techniques for laser cooling and trapping of neutral atoms at temperatures below 1 mK offer many new opportunities to science and technology, including greatly improved time and frequency standards and the ability to study the very novel physics which characterizes the collisions of such atoms. A NIST scientist has just completed a detailed study of how atomic collisions cause leaks in ultracold atom traps. Otherwise contented, laser-trapped atoms can suddenly find themselves leaving their happy home due to molecular processes that heat them up during the course of an ultracold collision. The most prominent cause of heating is a change in the fine structure state of the upper level of the laser cooling transition. The colliding atoms pick up kinetic energy equal to the energy of the fine structure splitting. This energy is much larger than the trap depth and the hot atoms escape. The calculated rate of the fine structure changing process for cesium atom collisions agrees well with experimental data at 300 K and 300 μK. The rate at 300 μK, more than 2 orders of magnitude smaller than expected, is explained by a new low-temperature effect, the suppression of an excited state collision rate due to radiative decay during the long time of the collision. There is a wide range of variation in mechanism and magnitude of the predicted loss rates for traps of lithium, sodium, potassium, and rubidium. These predictions will be tested by experiments at NIST and other laboratories in the future.

COMPOSITE MATERIALS

Composite technology under study at NIST involves electrochemically depositing a sequence of alloys at high speed on moving continuous fibers which are either single or in the form of twos. The final form of the composite is achieved by hot isostatic pressing or hot pressing. The matrix material which is in general an alloy of aluminum with titanium constitutes the dominate coating and is electrochemically produced from chloroaluminate-based fused salt electrolytes. Recently NIST has demonstrated the technology to deposit aluminum alloys on over 300 m of single fiber from the fused salt. The coated fiber, a tungsten wire 15 μm in diameter, was subsequently consolidated by hot isostatic pressing into a composite.

CATHODOLUMINESCENCE IMAGES OF CVD DIAMONDS

Cathodoluminescence (CL) imaging and spectroscopy in the scanning electron microscope provides information about the spatial distribution and atomic structure of defects in chemical vapor deposited diamond. Defect luminescence may provide the basis for visible light-emitting display applications; also, defects that are observable by luminescence may affect the electronic properties of diamond. Images of the CL from two separate spectral regions, corresponding to two distinct defect luminescence bands, were obtained and examined by NIST scientists in a number of diamond particles. In some particles, CL images viewed in the two spectral regions show complementary intensities; that is, the bright areas in one spectrally resolved image are dark in the other spectrally resolved image, and vice versa. In other particles, the images viewed in the two spectral regions are similar in appearance. A model of competing recombination centers has been developed to explain this result. In a given particle, the observation of complementary images implies that only two types of defects provide the dominant decay paths for excited electrons. Noncomplementary images imply that additional decay paths due to other types of defects, not observed by CL, are also present.

HAZARD I, VERSION 1.1 COMPLETED

NIST has prepared the first update to its prototype methodology to assess the relative contributions of potentially flammable commercial products (e.g., furniture, beds) to deaths in building fires. Over 400 copies of the original version, released in mid-1989, are in use worldwide. The method is designed for single-family homes, where 80 percent of the U.S. fire deaths occur, but is adaptable to other buildings. It helps the user define first the fire problem of concern and then the specific fire factors contributing to the problem. NIST-developed (PC compatible) software then calculates the outcome of each of the fires, enabling the user to analyze the impact of making changes in the product or other features of the fire. The new modifications allow for more complex fuels, enable hydrogen chloride to deposit on walls, and include the effects of forced ventilation on smoke transport, as well as a number of improvements in the user-friendly software. A fully revised user's guide and technical reference are included. The new version will be issued as NIST Handbook 146-1 and will be distributed by the National Fire Protection Association and the National Technical Information Service.

U.S.-JAPAN COLLABORATION ON EARTHQUAKE FIRE SAFETY OF WOOD-FRAME HOUSING

Under the sponsorship of a trade association, NIST scientists will be participating with Japanese colleagues on fire testing of wood-frame structures. Under a U.S.-Japan treaty, the Japanese are modifying the earthquake-safety provisions in their building code to allow wood-frame construction for buildings up to three stories. There is, however, a concern that the damage from an earthquake might reduce the fire resistance of the walls, floors, and/or ceilings. This would, in turn, increase the likelihood of a room fire growing to involve a full "subdivision" of closely-spaced houses. NIST staff will work with the Japanese in planning and instrumenting a fire test of a dwelling with simulated earthquake damage and then interpreting the results. It is anticipated that a successful test program will help increase U.S. wood exports.

Standard Reference Materials

STANDARD REFERENCE MATERIAL 2136—CHROMIUM/CHROMIUM MARKER LAYER THIN-FILM DEPTH PROFILE STANDARD

The Standard Reference Materials Program announces the availability of SRM 2136. It is intended primarily to provide a means for determining sputtered depths as well as sputter erosion rates in surface analysis. It was specifically developed for use in secondary ion mass spectrometry but can be used with other surface analysis techniques as well. Determinations of sputtered depth can be made at seven depths with this one SRM using chromium oxide interfaces of known spacings. The calibrated structure of this SRM makes it useful for verifying correct instrument operation, monitoring ion beam current-density stability, and producing sputtering conditions that achieve maximum interface resolution. The very thin oxide interfaces provide a means for assessing instrumental sensitivity as well as the quality of the spectral data analysis. The SRM was fabricated at the Jozef Stefan Institute, Ljubljana, Yugoslavia, and was jointly certified by NIST.

It consists of eight chromium (Cr) thin-film layers on a polished Si(100) substrate; each interface between these chromium layers is composed of a thin chromium oxide layer. This oxide marker layer is estimated to be 2 to 3 monolayers thick. The seven outermost chromium layer thicknesses are certified; the thickness of each layer is nominally 30 nm.

STANDARD REFERENCE MATERIAL 2098—CERTIFIED SAMPLES FOR CHARPY V-NOTCH TESTING MACHINES

The Standard Reference Materials Program announces the availability of super high-energy samples for Charpy V-Notch testing machines. SRM 2098 is intended primarily for checking the accuracy of large-capacity Charpy V-Notch (CVN) testing machines. These higher energy samples extend the range over which the machine performance can be evaluated and will eventually be used to join the approximately 15 and 95 J specimens now used to certify the machine performance. SRM 2098 consists of five 10×10×54 mm bars of a high-strength maraging steel. The bars were fabricated from vacuum melted, vacuum arc remelted steel rods. The bars were cut to finished lengths, machined, and heat treated in SRM "lots" of 1,200 specimens. Impact energy will range between 210-224 J. NIST will evaluate the results of the test and issue a report of its findings. This report will document conformance of machine operation.

This SRM can be used as a reference material until ASTM Standard E-23 has been modified to include the use of super high-energy specimens for machine certification.

STANDARD REFERENCE MATERIAL 1474—POLYETHYLENE RESIN

The Standard Reference Materials Program announces the availability of SRM 1474. It is intended primarily for use in calibration and performance evaluation of instruments used in polymer technology and science for the determination of the melt flow rate.

This material is certified for melt flow rate using procedure A as described in Section 8 of ASTM Method D-1238-86. Standard test condition 190/2.16 was used. Thus, the flow rate was determined at 190.0±0.1 °C using a load of 2.16 kg. The flow rate of the melt was measured by a manually operated extrusion plastometer. Under this condition the melt flow rate of this material is 5.03g/10 min with a standard deviation for a single measurement of 0.037g/10 min.

The SRM is supplied as white pellets of polyethylene in a 60 g unit.

STANDARD REFERENCE MATERIAL 710a—SODA-LIME-SILICA GLASS

The Standard Reference Materials Program announces the availability of SRM 710a. It is for use in measuring the viscosity of glass in accordance with ASTM Procedure C965. Viscosities are certified over the temperature range 918–1464 °C, and the consensus fit of the viscosity-temperature data provided by 10 cooperating laboratories to the Fulcher equation are given. The softening point temperature of 730.6 1.3 °C of the glass as measured by ASTM Test Method C338 is also certified. The SRM is available as a glass plate 100×100 ×40 mm (4×4×1.5 in).

STANDARD REFERENCE MATERIALS 1084a AND 1085a—WEAR METALS IN LUBRICATING OIL

The Standard Reference Materials Program announces the availability of two renewal SRMs for use in the calibration of apparatus and in the evaluation of methods used in the analysis of engine lubricating oils for metal content. SRMs 1084a and 1085a consist of a blend of 14 constituent elements in a base oil with a nominal concentration of 100 and 300 μg/g, respectively. A unit of each SRM consists of five ampoules each containing 1.6 g of the respective oil blends. Spectrometric analysis of lubricating oils for wear metal content is being used extensively in large sectors of the transportation industries and in the three branches of the military. All major airlines in the United States monitor engine wear status through spectrometric oil analysis of engine oils. All major railroads in the United States monitor the wear status of diesel engines. The Department of Transportation (DOT) monitors the wear status of bus engines for vehicles owned or subsidized by DOT. The accuracy of the analysis is dependent on numerous experimental factors, however, the principal condition is the accurate knowledge of the concentration of metals in the reference material used for standardization. Thus, SRMs 1084a and 1085a become very important to the transfer of accuracy for wear metal analyses. The preparation and certification of these SRMs were performed in the NIST Ceramic and Inorganic Analytical Research Divisions.

STANDARD REFERENCE MATERIAL 2694a—SIMULATED RAINWATER

The Standard Reference Materials Program announces the availability of a renewal lot of SRM 2694a, Simulated Rainwater. The SRM consists of four 50 mL solutions, two at each level of acidity, in polyethylene bottles. It was carefully prepared by the dissolution of NIST high-purity salts and acids in high-purity distilled, deionized water. SRM 2694a is intended to aid in the analysis of acidic rainwater for measurements of pH, acidity, electrolytic conductivity, nitrate, sulfate, and a selected number of the alkali metals. In addition to the certified constituents and parameters, the SRM is accompanied by a document which provides guidelines for the accurate measurement of pH in acidic rainwater. The intent of the guidelines is to improve the accuracy and precision of the pH measurement with special emphasis on reducing the effect of the residual liquid junction potential. This was the first certified reference material of its kind and is a widely accepted measurement transfer standard for aqueous deposition research. The renewal certification of this SRM was performed in the Inorganic Analytical Research Division.

STANDARD REFERENCE MATERIAL 1963—POLYSTYRENE SPHERES, 0.1 μm DIAMETER

The Standard Reference Materials Program announces the availability of SRM 1963, Polystyrene Spheres, 0.1 μm diameter. The SRM is intended primarily for use as a primary reference standard for the calibration of particle-size-measuring instruments, including optical and electron microscopes. The SRM consists of 5 mL of carboxylated polystyrene spheres in water at a weight concentration of about 5 percent. The certified number average particle diameter (0.1007±0.0020 μm) was measured in air as an aerosol by electrical mobility measurements. The size distribution of the polystyrene spheres, as determined by electrical mobility measurements, is narrow with a standard deviation of 0.0018 μm excluding outliers.

This SRM completes the series of seven NIST particle size SRMs that provide a nominal size range of 0.1–30 μm. The certification measurements for this SRM was a collaborative effort between the NIST Fire Measurement and Research Division and the Particle Technology Laboratory at the University of Minnesota.

Standard Reference Data

FIRST MANUFACTURER'S USE OF NIST PC DATABASE

The NIST/EPA/MSDC Mass Spectral Database for personal computers (PCs) is the first PC version of a standard reference data product to be licensed for use by industry in a commercial instrument. A private company has incorporated the database in a new line of gas chromatography/mass spectrometers. A major international resource for analytical chemists to use in identifying unknown substances, the database contains electron mass spectra of approximately 54,000 chemical compounds and the chemical structures of more than 52,000 of these compounds. The PC version, first issued in 1987, was prepared from the NIST/EPA/MSDC Mass Spectral Database used worldwide in computer-magnetic tape format. For information contact the Standard Reference Data Program, A320 Physics Building, NIST, Gaithersburg, MD 20899, 301/975-2208, fax: 301/926-0416.

PC DATABASE ON REFRIGERANTS AND MIXTURES EXPANDED

Three refrigerant materials, R115, R125, and RC270, have been added to the NIST Thermodynamic Properties of Refrigerants and Refrigerant Mixture Database (REFPROP). The database is a personal computer (PC) software package for producing tables of the thermodynamic properties of 18 pure refrigerants, including the ethane-based compounds, and 24 of their mixtures. The software has been expanded to permit calculations of mixtures with up to five components. Some of these materials are possible replacements for environmentally unacceptable refrigerants. Users may also consider other mixtures of the 18 refrigerants. Designed for any AT- or XT-Class PC where it occupies 512 kilobytes, NIST Standard Reference Database 23, REFPROP, Version 2.0 is available for $340 from the Standard Reference Data Program, A320 Physics Building, NIST, Gaithersburg, MD 20899, 301/975-2208, fax: 301/926-0416. Users of Version 1.0 may upgrade for $90.

PRINT OPTIONS ADDED TO CHEMICAL KINETICS DATABASE

New printer and plotter options for producing high-quality, hard-copy graphics have been added to the expanded NIST Chemical Kinetics Database for personal computers. The database contains information on the rates of more than 5,700 chemical reactions, with more than 16,700 individual entries that include data on 2,800 compounds which are reactants or products. An important research tool for modeling combustion systems, gas phase reactors, chemical processes occurring in the atmosphere, and chemical vapor deposition, the database is designed for any computer using DOS 2.1 or later versions and requires a hard disk with 4 megabytes of memory. A graphics board must be used to show graphs of the reaction rate constants. Version 3.0 of NIST Standard Reference Database 17 is available for $340 from the Standard Reference Data Program, A320 Physics Building, NIST, Gaithersburg, MD 20899, 301/975-2208, fax: 301/926-0416. Users of 1.0 may upgrade for $150; users of 2.0 for $100.

ERRATA

In the previous issue of the Journal (Volume 96, Number 3, May–June 1991), the page number 385 was missing from the page due to a printing error. Also, the following two sentences of the last paragraph in the first column were partially obscured. They should read as follows: It has been maintained and modernized by Statistical Engineering since about 1966. The system provides statistical analysis, numerical analysis, matrix/array analysis, and plotting capabilities.

Volume 96, Number 4, July–August 1991
Journal of Research of the National Institute of Standards and Technology

Calendar

October 1–4, 1991
NORTH AMERICAN ISDN USER'S FORUM (NIU-FORUM)

Location: National Institute of
Standards and Technology
Gaithersburg, MD

Purpose: To develop user-defined applications, implementation agreements for existing standards, and tests needed for a transparent, ubiquitous, and user-driven integrated services digital network (ISDN).
Topics: ISDN-related subjects.
Format: Tutorials, users' and implementors' workshops, and working group meetings.
Audience: ISDN users, implementors, and service providers.
Sponsors: NIST.
Contact: Dawn Hoffman, B364 Materials Building, NIST, Gaithersburg, MD 20899, 301/975-2937.

October 22–25, 1991
ANALYTICAL LABORATORY MANAGERS ASSOCIATION (ALMA) ANNUAL MEETING

Location: National Institute of
Standards and Technology
Gaithersburg, MD

Purpose: To facilitate annual interchange between laboratory managers to discuss mutual problems associated with running analytical laboratories.
Topics: Quality assurance at NIST, quality assurance in an industrial research facility, quality assurance in the European Community; and the role of information management systems in quality assurance.
Format: Technical talks followed by a panel discussion and roundtables.
Audience: Laboratory managers of analytical labs in industry, academia, and government.
Sponsors: NIST and ALMA.
Contact: Barry Diamondstone, A309 Chemistry Building, NIST, Gaithersburg, MD 20899, 301/975-3146.

November 14–15, 1991
25/90th NIST SYMPOSIUM ON SCIENCE TECHNOLOGY AND COMPETITIVENESS

Location: National Institute of
Standards and Technology
Gaithersburg, MD

Purpose: To provide a forum to discuss the contribution of science and technology in solving the problems of international competitiveness on the occasion of the 90th anniversary of NIST and the 25th anniversary of the NIST Gaithersburg site.
Topics: Emerging technologies, proprietary vs. non-proprietary research, education and the workforce, and the congressional viewpoint.
Format: Symposium.
Audience: Managers and researchers from industry and small businesses, science policy experts, technology transfer executives, and representatives of the academic community.
Sponsors: NIST.
Contact: Karl Kessler, A505 Administration Building, NIST, Gaithersburg, MD 20899, 301/975-3089 or Sara Torrence, A903 Administration Building, NIST Gaithersburg, MD 20899, 301/975-2774.